Quantitative MRI for measuring myelin content in human spinal cord

Marco Battiston

A dissertation submitted in partial fulfillment

of the requirements for the degree of

Doctor of Philosophy

of

University College London.

Department of Neuroinflammation, Institute of Neurology

University College London

March 28, 2018

I, Marco Battiston, confirm that the work presented in this thesis is my own. Where information has been derived from other sources, I confirm that this has been indicated in the work.

Abstract

The aim of this thesis is to progress the state-of-the art of quantitative Magnetic Resonance Imaging (MRI) in the human spinal cord, with particular focus on methods sensitive to myelin content.

Myelin is a fundamental structure of the central nervous system, ensuring the correct transmission of action potentials along neuronal axons, affected in a number of neurological disorders, first and foremost Multiple Sclerosis (MS).

MRI methods to assess myelin in the spinal cord have found limited development, despite the primary involvement of the spinal cord in demyelinating diseases, such as MS where the characterization of spinal cord pathology is key for a better diagnosis, understanding of pathological processes, and evaluation of neuroprotective and reparative treatments.

In this thesis, we develop novel methods for the spinal cord to measure parameters that are known to correlate with myelin content, namely the longitudinal relaxation time (T_1) and quantitative Magnetization Transfer (qMT) parameters, and we compare them with a large set of myelin sensitive MRI indices in the post mortem MS spinal cord.

The thesis is structured as follows: chapter 1 states the problem this thesis attempts to address and provides background information regarding the involvement of the spinal cord in MS; chapter 2 reviews the basic principles of MRI and introduces the theory behind the measurement of surrogate indices of myelin content with MRI; chapter 3 reviews an existing imaging sequence for the spinal cord, extends its use for measuring myelin sensitive parameters and discusses potential improvements for in vivo applications; chapter 4 and chapter 5 propose novel efficient methods to measure T_1 and qMT parameters in vivo in the spinal cord; and chapter 6 evaluates the performance of the methods developed in the previous chapter, together with other prospective myelin mapping methods, in the healthy and MS post mortem human spinal cord.

Acknowledgements

I struggle to find the words to express my gratitude to my supervisor, Dr. Rebecca Samson. I am grateful to Becky for the constant help and total support given to me, for making easier and softer my introduction to a new world, and relaxed and pleasant the atmosphere of the Thursday morning meetings, and for being, simply, the best supervisor I could have ever wished for.

I would like to thank Prof. Claudia Gandini Wheeler-Kinghsott for the countless advice and the incredible amount of time dedicated to me over the past years and, ultimately, for being an unequalled example of enthusiasm and positivity.

I would also like to thank Prof. Alessandra Bertoldo and Dr. Marco Castellaro for their unconditional support, without them this would have not been possible.

There are two people who have been a constant presence since I started my experience at UCL. I want to thank the *great beauty*, that not even the most talented of the writer would have been capable of, that decided I had to stumble across them: Torben Schneider and Francesco Grussu. It is thank to them if I haven't drowned in this chaos of crashing CPUs, howling rear fans, sweat, tears, hair, muscles, coffee spots, and working-class nights. Thank you, Torben and Francesco.

A very special thanks goes to Giulio Ferrazzi for being a friend in this foolish city where human relationships get blurred too easily. In particular, I thank Giulio for the inglorious rides across south London on the Thursday nights, chasing the passing clouds and talking about improbable steady-states, dangerous gradients, quirky susceptibilities, rotten plans and, in general, life.

I would also like to thank Thalis Charalambous for chats and parameter inferences over coffees.

Thanks to Andrea Aggio, Simone Ceccato and Cristina Rech, for all the good time and the support during the toughest periods, and to my brother Paolo and my cousin Andrea for voluntarily mistaking Ryanair for the CTM.

Infine, per quella strana legge secondo la quale cio' che ci arriva immancabile e constante ogni giorno, senza prenotazione o lista di attesa, scade muto e scontato in fondo alla fila, vorrei ringraziare i miei genitori, Luigino e Diana, per avermi aiutato e sostenuto in questa esperienza nel modo piu' totale, come sempre hanno fatto; per aver, nell'assecondare le mie scelte, silenziato la loro piu' intima volnta', e sinceramente gioito e sofferto con me, da lontano, di *fallimenti* e *successi* difficilmente comprensibili; e per essere, di fronte a centinaia di citazioni e qualche tesi, la mia unica vera fonte di insegnamento.

Contents

List of Figures

List of Tables

List of Abbreviations

ADC	Apparent diffusion coefficient
AFI	Actual flip angle imaging
BPF	Bound pool fraction
BSA	Bovine serum albumin
CEST	Chemical exchange saturation transfer
CNR	Contrast to noise ratio
CNS	Central nervous system
COV	Coefficient of variation
CPGM	Carr-Purcell-Meiboom-Gill
CRLB	Cramer-Rao lower bound
CSF	Cerebro-spinal fluid
CW	Continuous wave
DAM	Double angle method
DC	Dorsal column
DKI	Diffusion kurtosis imaging
DTI	Diffusion tensor imaging
DWI	Diffusion Weighted Imaging
EPI	Echo Planar Imaging
FOV	Field of view
FT	Fourier transform
GE	gradient echo
GM	Grey matter
GRAPPA	Generalized auto-calibrating partially parallel acquisition
GRASE	Gradient and spin echo
ICC	Intra-class correlation coefficient

ihMT	Inhomogeneous magnetization transfer
ihMTR	Inhomogeneous magnetization transfer ratio
IR	Inversion Recovery
IV	Inner Volume
IVI	Inner Volume Imaging
LCL	Left lateral column
LCR	Right lateral column
LL-IR	Look-Locker Inversion Recovery
LS	Least squares
M	Frequency encoding
MAMT	Minimal approximation magnetization transfer
MBP	Myelin basic protein
MRI	Magnetic resonance imaging
MS	Multiple sclerosis
msh-EPI	Multi shot echo planar imaging
MT	Magnetization transfer
MTI	Magnetization transfer imaging
MTR	Magnetization transfer ratio
MTV	Macromolecular tissue volume
MWF	Myelin water fraction
NAGM	Normal appearing grey matter
NAWM	Normal appearing white matter
NMR	Nuclear magnetic resonance
NNLS	Non-negative least squares
NODDI	Neurite orientation dispersion and density imaging
OVS	Outer volume suppression
P	Phase Encoding
PBS	Phosphate buffered saline
PLP	Proteolipid protein
PNS	Peripheral nervous system
PD	Proton density
PGSE	Pulsed gradient spin echo

qMT	Quantitative magnetization transfer
R_{PI}	Parallel imaging acceleration factor
RD	Radial diffusivity
RF	radio-frequency
rFOV	Reduced field of view
ROI	Region of interest
S	Slice Encoding
SAR	Specific absorption rate
SE	spin echo
SENSE	Sensitivity encoding
SMASH	Simultaneous acquisition of spatial harmonics
SMS	Simultaneous multislice
SNR	Signal to noise ratio
SOMA	Self-organizing migratory algorithm
ssh-EPI	Single shot Echo Planar Imaging
ssh-SE-EPI	Single shot spin echo planar imaging
TI	Inversion time
TE	Echo time
TR	Repetition time
UTE	Ultra-short echo time
VFA	Variable flip angle
WM	White matter
ZOOM	Zonally oblique magnified multislice
ZTE	Zero echo time

List of Publications

Journal publications

Yiannakas, Marios C., Francesco Grussu, Polymnia Louka, Ferran Prados, Rebecca S. Samson, Marco **Battiston**, Daniel R Altmann, Sebastien Ourselin, David H Miller, and Claudia AM Gandini Wheeler-Kingshott. **Reduced field-of-view diffusion-weighted imaging of the lumbosacral enlargement: a pilot in vivo study of the healthy spinal cord at 3T**. *PloS one* 11, no. 10(2016): e0164890.

Battiston, Marco, Torben Schneider, Ferran Prados, Francesco Grussu, Marios C. Yiannakas, Sebastien Ourselin, Claudia AM Gandini Wheeler-Kingshott, and Rebecca S Samson. **Fast and reproducible in vivo T_1 mapping of the human cervical spinal cord**. *Magnetic resonance in medicine* (2017), doi:10.1002/mrm.26852.

Battiston, Marco, Francesco Grussu, Andrada Ianus, Torben Schneider, Ferran Prados, James Fairney, Sebastien Ourselin, Daniel C Alexander, Mara Cercignani, Claudia AM Gandini Wheeler-Kingshott, and Rebecca S Samson. **An optimized framework for quantitative magnetization transfer imaging of the cervical spinal cord in vivo**. *Magnetic resonance in medicine* (2017), doi:10.1002/mrm.26909.

Conference abstracts

Battiston, Marco, Marios C Yiannakas, Jia Newcombe, Claudia AM Gandini Wheeler-Kingshott, and Rebecca S Samson. **Multi-parameter mapping of post-mortem lumbar spinal cord tissue in multiple sclerosis**. *Proceedings of 23rd Annual Meeting of ISMRM (2015)*, Toronto, Canada. p.n. 1745.

Battiston, Marco, James Fairney, Marios C Yiannakas, Claudia AM Gandini Wheeler-Kingshott, and Rebecca S Samson. **Optimisation of Magnetisation Transfer Ratio sequence acquisition parameters: application to the spinal cord**. *Proceedings of 23rd Annual Meeting of ISMRM (2015)*, Toronto, Canada. p.n. 3359.

Battiston, Marco, Francesco Grussu, James Fairney, Ferran Prados, Sebastien Ourselin, Mara Cercignani, Claudia AM Gandini Wheeler-Kingshott, and Rebecca S Samson. **In vivo quantitative Magnetization Transfer in the cervical spinal cord using reduced Field-of-View imaging: a feasibility study**. *Proceedings of 24th Annual Meeting of ISMRM (2016)*, Singapore. p.n. 306.

Battiston, Marco, Torben Schneider, Claudia AM Gandini Wheeler-Kingshott, and Rebecca S Samson. **In vivo T_1 mapping of the spinal cord using a reduced Field-of-View Inversion Recovery sequence (IR-ZOOM-EPI)**. *Proceedings of 24th Annual Meeting of ISMRM (2016)*, Singapore. p.n. 4390.

Samson, Rebecca, Marco **Battiston**, Claudia AM Gandini Wheeler-Kingshott, and Marios C Yiannakas. **Magnetisation Transfer Ratio (*MTR*) measurements in the lumbar cord: a pilot study using ZOOM-EPI at 3T**. *Proceedings of 24th Annual Meeting of ISMRM (2016)*, Singapore. p.n. 4395.

Yiannakas, Marios, Louka Polymnia, Francesco Grussu, Ferran Prados, Rebecca S Samson, Marco **Battiston**, Sebastien Ourselin, David Miller, and Claudia AM Gandini Wheeler-Kingshott. **Reduced field-of-view diffusion-weighted imaging of the lumbosacral enlargement: a pilot in vivo study of the healthy human spinal cord using a clinical 3T MR system**. *Proceedings of 24th Annual Meeting of ISMRM (2016)*, Singapore. p.n. 4402.

Battiston, Marco, Francesco Grussu, Andrada Ianus, Torben Schneider, Ferran Prados, James Fairney, Sebastien Ourselin, Daniel C Alexander, Mara Cercignani, Claudia AM Gandini Wheeler-Kingshott, and Rebecca S Samson. **Optimal quantitative Magnetization Transfer Imaging of small structures**. *Proceedings of 25th Annual Meeting of ISMRM (2017)*, Honolulu, USA. p.n.473.

Battiston, Marco, Torben Schneider, Ferran Prados, Francesco Grussu, Marios C Yiannakas, Sebastien Ourselin, Claudia AM Gandini Wheeler-Kingshott, and Rebecca S Samson. **Reproducible fast T_1 mapping of human cervical spinal cord in vivo**. *Proceedings of 25th Annual Meeting of ISMRM (2017)*, Honolulu, USA. p.n. 2510.

Grussu, Francesco, Marco **Battiston**, Ferran Prados, Torben Schneider, Enrico Kaden, Sebastien Ourselin, Rebecca S Samson, Daniel C Alexander, and Claudia AM Gandini Wheeler-Kingshott. **A unified signal readout for reproducible multimodal characterisation of brain microstructure**. *Proceedings of 25th Annual Meeting of ISMRM (2017)*, Honolulu, USA. p.n. 3399.

Chapter 1

Introduction

1.1 Myelin

Myelin is a fundamental structure of the central (CNS) and peripheral (PNS) nervous systems. It is mainly a lipid-protein structure (proportions are roughly $\sim$80% lipid and $\sim$20% proteins, and may vary slightly according to the location in the body), and wraps around neuronal axons in a concentric fashion forming an electrically insulating layer.

At a microscopic level (at the scale of nm), myelin is composed of tightly packed glial cell membranes (oligodendrocytes or Schwann cells), that are arranged in a bilayer configuration (figure 1.1).

The myelin bilayer envelops axons in such a way that it appears as a lamellar structure, where repetitions of glial cell membrane produce a periodic alternations of cytoplasmic space and extracellular space layers of around 3-4 nm thickness (figure 1.1), filled with water that accounts for approximately $\sim$40 % of myelin weight [1]. Within those spaces, myelin proteins can be found, mainly myelin basic protein (MBP), and proteolipid protein (PLP).

At a more macroscopic level (at the scale of mm), myelin is found predominantly in white matter (WM), representing around $\sim$50 % of its dry weight, but it is also present in smaller quantities in grey matter (GM).

The main function of myelin is to ensure efficient action potential transmission along axons. It therefore plays a fundamental role in allowing complex motor, sensory and behavioural functions to occur. Myelin is also involved in the regulation of the axonal environment, resulting in an intimate link between the myelin sheaths and the inner axon. In fact, in many pathologies myelin damage and axonal damage occur simultaneously and are difficult to disentangle.

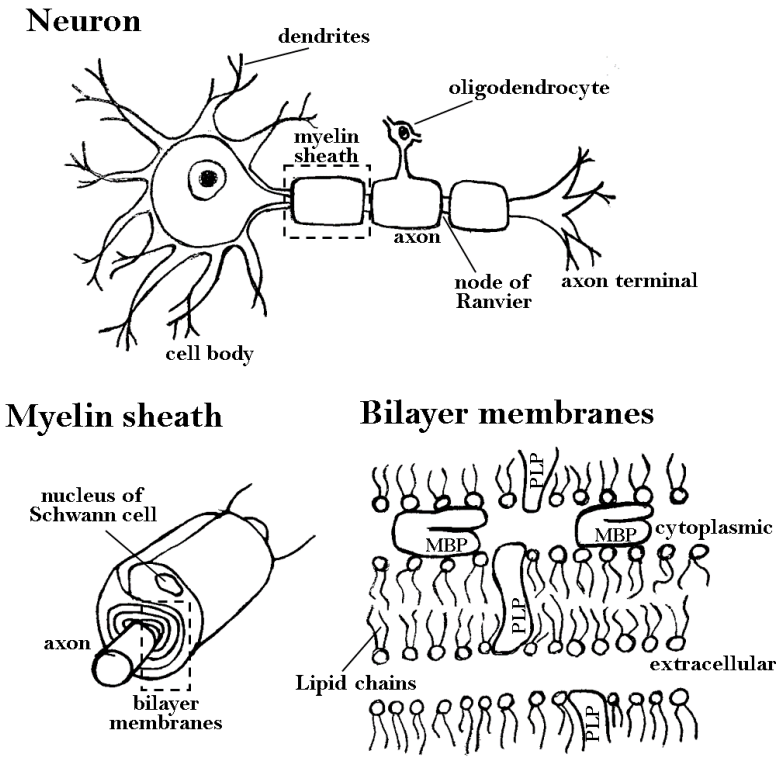

Figure 1.1: Illustration of a myelinated axon with details of the myelin sheaths and bilayer membrane structure. The myelin sheath does not fully cover the axon, but there are intermittent gaps, known as nodes of Ranvier. Myelin is an outgrowth of glial cells, such as oligodendrocytes in the CNS and Schwann cells in the PNS. Myelin sheaths wrap around axons many times in a concentric fashions. At a microscopic level, myelin is composed by a bilayer membrane with alternating extracellular and cytoplasmic spaces. In the latter myelin proteins, such as PLP and MBP, can be found.

Myelin alterations are key in brain development and in a number of neurological disorders. Therefore the ability to measure myelin in vivo has great consequences for furthering the knowledge of both normal physiology and disease mechanisms.

In this thesis the focus is on the quantitative measurement of myelin using Magnetic Resonance Imaging (MRI).

1.2 Multiple Sclerosis

Among the major diseases causing myelin disruption is Multiple Sclerosis (MS).

MS is an autoimmune disease of the CNS which manifests with inflammatation, edema, demyelination and axonal loss [2]. Such processes can take place as focal damage, i.e. lesions or plaques, or as diffuse and lesion-free abnormalities in the so called normal appearing tissue.

MS is predominantly a WM disease, although involvement of the GM has also been demonstrated [3].

MS is considered as one of the leading causes of disability in young adults, who suffer from physical disability, cognitive and sensory impairments. Disease onset can occur in the early 30s, and average disease duration is of a few decades. Most commonly, it appears firstly with periodic cycles of disability and recovery, the *relapsing-remitting* phase, and translates with time into permanent and progressive disabilities, the *secondary progressive* form. Sometimes, MS can present with progressive and irreversible disabilities from onset, the *primary progressive* form.

A site of particular interest for MS is the spinal cord: (*i*) MS abnormalities can be seen in the spinal cord with MRI in the vast majority of patients, around 90%, and damage to the spinal cord is in fact included in the criteria for diagnosing MS [4], (*ii*) the amount of spinal cord abnormalities is thought to reflect physical disabilities and to convey prognostic value [4, 5]. The inclusion of damage to the spinal cord in clinical trials, and the use of spinal cord derived MRI metrics (such as atrophy) as trial outcome measures is indeed suggested for the evaluation of neuprotective therapies in MS [4].

1.3 Spinal Cord

The spinal cord connects the brain with the periphery of the body. It extends from the medulla oblongata (in the brain stem), to the lumbar level (with the caudal termination varying among individuals), and it is usually divided into different segments according to the corresponding vertebral level (cervical, thoracic and lumbar).

The spinal cord has a cylindrical shape, elongated in the foot-head direction with a length of approximately $\sim$45 cm, and restricted cross-sectional extension, with a diameter of 15 mm at its widest and an area of approximately $\sim$ 80 mm^2 (with two enlargements, at the cervical and lumbar levels, in correspondence with the connection innervating the limbs).

The spinal cord is protected by the vertebral bodies, enclosed in the spinal canal filled by cerebrospinal fluid (CSF) and surrounded by a meningeal layer, the pia matter. An illustration of the spinal cord and its surrounding anatomy is shown in figure 1.2. The CSF also fills two tight fissures, the anterior and posterior fissure, and a tiny foramen in the center of the cord, the central canal.

The internal organization of the spinal cord is reversed compared to that of the brain, with WM surrounding GM, which occupies the inner part of the cord and assumes the charac-

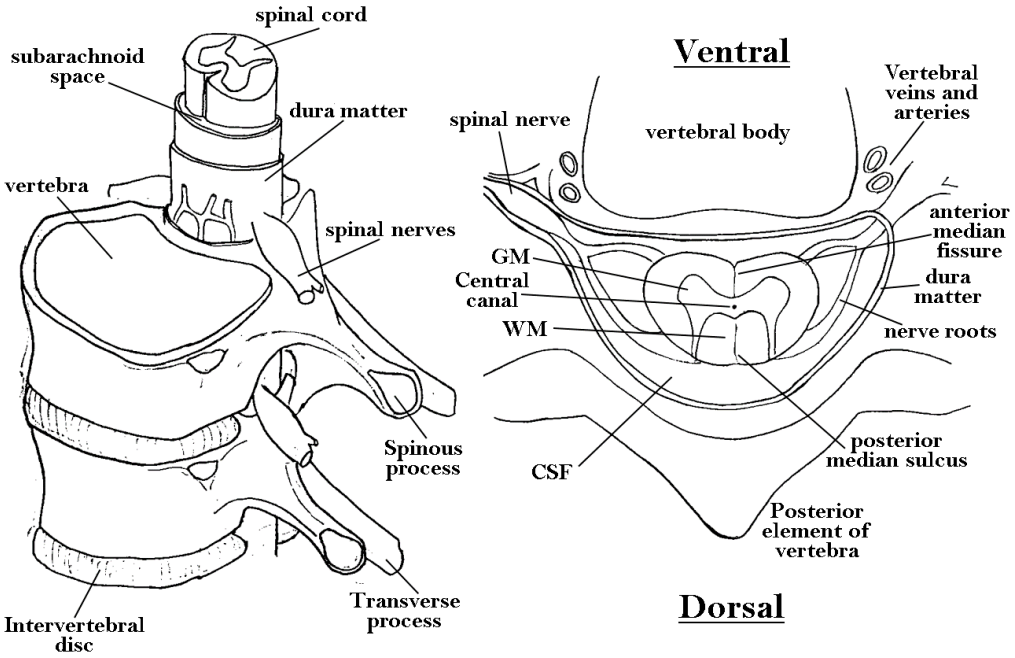

Figure 1.2: The spinal cord and surrounding anatomy. Location of the spinal cord inside the body is shown on the **left**. A horizontal section through a vertebra and the spinal cord is drawn on the **right**, with details of spinal cord anatomy.

teristic *butterfly* shape. WM is composed mostly of axons and glial cells, and organized hierarchically in groups of fibre bundles that run predominantly along the foot-head direction. The spinal cord WM can be divided into three main regions, the dorsal column, and the left and right lateral columns, containing different WM tracts, both ascending (e.g. spinothalamic and spinocerebellar tracts) and descending (e.g. corticospinal tract).

The GM is composed mostly of cell bodies, dendrites and the connection with the nerves that branch off to the periphery.

The spinal cord has a key role in controlling voluntary movements and coordination, as it serves as a link between the brain and the limbs. It also receives sensory information from the periphery of the body and regulates internal organ functions at the different levels of the vertebral column, e.g. thorax, abdomen and pelvis.

1.4 Putting the pieces together: aim of the thesis

Tissue damage occurring in MS can be detected using conventional MRI examinations, such as T_1-weighted (also with contrast enhancement) and T_2-weighted imaging. MRI has also proven useful for imaging spinal cord damage, improving the diagnostic process and providing a better understanding of the disability seen in patients. However, the correla-

tion between clinical disability and evidence from spinal cord MRI, such as lesions counts, remains modest [4]. The cause of the poor agreement has been identified in the lack of sensitivity and specificity of conventional MRI methods to the underlying complexity and dynamics of the tissue changes taking place in MS: inflammation, demyelination, axonal loss, and remyelination.

Quantitative MRI methods have been proposed to overcome the limitations of conventional MRI investigations. Quantitative MRI combines advanced magnetic resonance pulse sequences with mathematical models of the tissue of interest to extract quantitative and biologically meaningful parameters. Such parameters have a more direct interpretation in terms of tissue microstructure features (e.g. axonal density, myelin volume fraction, axon diameter, and many others) compared to visual evaluation of image contrast. Robust measurements of quantitative parameters have an improved clinical relevance, and may help to further the understanding of disease mechanisms, to identify early pathological changes in the tissue, and provide a better explanation of patient disability.

In the context of MS, methods able to quantitatively map myelin content are of great interest, especially in the spinal cord given its primary involvement in the development of the irreversible disability.

However, quantitative MRI in the spinal cord suffers from technical challenges and lack of critical mass that have hampered its robust and systematic development. While quantitative MRI methods are well characterized in the brain, their translation to the spinal cord is slow and partial [6, 7]. As a result, quantitative MRI in the spinal cord is not yet mature enough to be used with clinical relevance. Only small pieces of the full picture that quantitative MRI methods can provide are at the moment exploited in a clinical setting, such as measurements of spinal cord cross-sectional area, and rate of atrophy. This fact represents a substantial restriction in the potential of using MRI to investigate complex and varying diseases such as MS.

The aim of this thesis is to progress the state-of-the art of quantitative MRI in the human spinal cord, with particular focus on methods sensitive to myelin content.

We develop novel methods for the spinal cord to measure quantitative parameters that have been shown to correlate, in the brain to different extents, with myelin content, namely the longitudinal relaxation time (T_1) and quantitative Magnetization Transfer (qMT) parameters, and we compare them with a large set of myelin sensitive MRI indices in the post

mortem MS spinal cord.

In doing so, we contribute to the field of quantitative MRI in the spinal cord by: (*i*) providing new unexplored ways to map myelin-sensitive parameters with an approach usually previously only considered for diffusion-weighted imaging, therefore expanding the field, allowing comparisons between methods and fostering the implementation of multi-contrast (i.e. multi-modal) studies; (*ii*) evaluating the different levels of sensitivity to MS alterations in the spinal cord of a wide set of quantitative myelin-sensitive techniques.

The thesis is structured as follows:

Chapter 2 reviews some of the basic principles of MRI and introduces the theory behind the measurement of surrogate indices of myelin content with MRI, to provide sufficient background information for understanding the work developed in this thesis;

Chapter 3 reviews an existing imaging sequence for the spinal cord, namely Zonally Magnified Oblique Multislice Echo Planar Imaging (ZOOM-EPI), extends its use to allow the measurement of myelin sensitive parameters, and discusses potential improvements for in vivo applications;

Chapter 4 proposes, validates, and applies in healthy individuals an efficient method to measure the T_1 in the cervical spinal cord in vivo;

Chapter 5 develops a novel framework to perform quantitative Magnetization Transfer studies in the spinal cord, combining a dedicated acquisition sequence, signal modelling and protocol optimization;

Chapter 6 evaluates the performance of the methods developed in the previous chapter, together with other prospective myelin mapping methods, in the healthy and MS post mortem human spinal cord, and investigates correlations between them.

Chapter 2

Background: MRI principles & quantitative measurements of myelin

This chapter aims to provide a theoretical background for the notions and the methodologies that are used or further developed in this thesis. Two main areas are covered in the following, in two separate sections.

The first section focuses on the theory behind MRI. An exhaustive and comprehensive explanation of magnetic resonance physics is far beyond the scope of this chapter. The aim of the section is rather to provide sufficient information regarding the principles that will be invoked in the experimental chapters, and to provide readers seeking deeper and more rigorous explanations with the correct literature references.

The second section of the chapter instead gives an overview of the main quantitative MRI techniques currently available for measurements of surrogate indices of myelin content in vivo. Particular attention is given to the Magnetization Transfer effect and its quantitative description, given the main role played by this technique in this thesis. Other myelin-sensitive techniques, some still exploiting the Magnetization Transfer phenomenon and others employing different types of contrast (T_2 relaxation, diffusion, etc.), are also described. As the aim of the section is to provide the reader with adequate background information on quantitative MRI techniques sensitive to myelin content, the description will focus on the rationale behind each particular technique and the general analysis methods to be employed in the quantification stage, leaving the details of each particular implementation to the relevant references. The state-of-the-art of each technique for spinal cord applications will also be reported.

We are aware of the unavoidable limitations of this chapter, in terms of completeness and

detail. However we hope readers can find it helpful to better understand and appreciate the work developed in the subsequent chapters of this thesis.

2.1 MRI prinicples

A full account of MRI theory is beyond the scope of this section, and can be found elsewhere [8, 9, 10, 11], whose consultation has been essential for writing this chapter.

This section should be intended more as a walk-through of some of the main concepts of MRI, with some more detailed descriptions for the theory that will be used extensively in this thesis, e.g. Bloch equations, spin echo sequence and echo-planar imaging.

2.1.1 The basic NMR experiment and the fundamental NMR parameters

In this section we describe the basic Nuclear Magnetic Resonance (NMR) experiment and we introduce the concepts of resonance frequency, excitation, precession, relaxation and the fundamental NMR parameters involved, such as spin density ρ, longitudinal relaxation time T_1 and transverse relaxation time T_2.

Nuclei are characterized by an intrinsic angular momentum, or *spin*. In NMR, the interest is in nuclei with an odd number of both protons and neutrons as they have a net angular momentum, and hence a magnetic dipole moment μ. Hydrogen nuclei ^{1}H, given their abundance and key localization in the human body, as a constituent of water molecules, are the nuclei of interest in (conventional) MRI.

In this thesis, the words *spin*, *proton* or *water proton*, without any further specification, will be used interchangeably.

We now consider the behaviour of protons when placed in a large static magnetic field $\mathbf{B}_0$ as in the basic NMR experiment, depicted in figure 2.1. For this purpose we define a system of reference, called the *laboratory* frame of reference, where the z axis points along the direction of $\mathbf{B}_0$ and the x and y axes define a plane orthogonal to it, i.e the *transverse* plane. A sample containing protons (e.g. a sample of water) is placed in the magnetic field $\mathbf{B}_0$, and a coil of wire is placed near the sample with its axes perpendicular to $\mathbf{B}_0$. The magnetic dipoles will align *along* or *against* the magnetic field, producing a small excess (roughly $\sim$1 in 10^6 at room temperature, described by quantum mechanics) along the direction of $\mathbf{B}_0$, that can be viewed, macroscopically, as a single net magnetization vector $\mathbf{M}$=$[0\ 0\ M_0]^{\mathrm{T}}$ resulting from the net sum of all the local magnetic dipoles. The magnitude of $\mathbf{M}$, the equilibrium magnetization indicated by M_0, is again accurately characterized by quantum

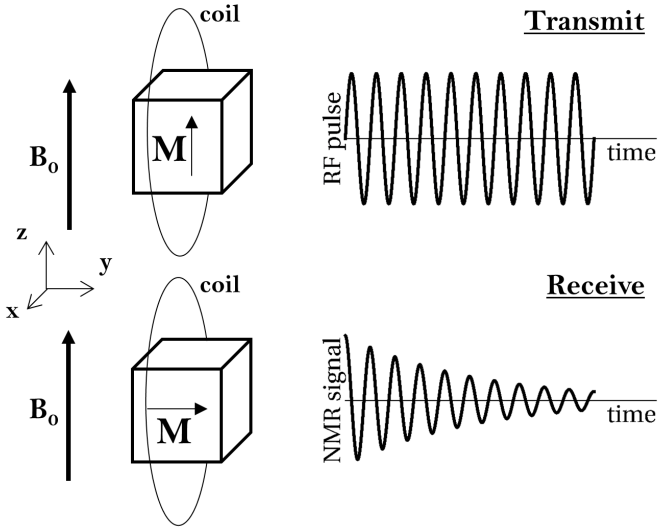

Figure 2.1: Illustration of the basic NMR experiment. During the **transmit** phase, the spins in the sample are excited by a RF magnetic field oscillating at the Larmor frequency. Through the magnetic resonance effect, spins will be tipped in to the transverse plane where their precession will induce an oscillating current in the coil, which can be measured in the **receive** phase. This figure qualitatively reproduces figure 4.2 of [11]

.

mechanics, but as a first approximation can be thought of as proportional to the spin density ρ.

While **M** is static along z, the single nuclei, due to their angular momentum, precess around the main magnetic field, with a frequency ω_0 governed by the equation:

$$\omega_0 = \gamma B_0 \tag{2.1}$$

where B_0 is the magnetic field strength, γ is the gyromagnetic ratio, whose value depends on the nucleus considered (for ^{1}H, $\gamma = 267.54 \times 10^6 \frac{rad}{T}$), and ω_0 is the *Larmor* frequency or resonance frequency of the nuclei in question.

The system is perturbed during the *transmit* phase: an oscillating current, at frequency ω_0, is applied to the coil for a few ms, generating a small oscillating magnetic field $\mathbf{B}_1(t)$ oriented along the axes of the coil, i.e. perpendicular to $\mathbf{B}_0$. $\mathbf{B}_1(t)$ is called a radio-frequency (RF) pulse or *excitation* pulse.

During the *receive* phase, the coil is used to detect small oscillating currents in the wire loop. While there is little effect if the RF pulse oscillates at frequencies far from ω_0, in the proximity of the Larmor frequency the spins in the sample absorb RF energy and depart from their equilibrium (low energy state) configuration, with **M** tipping away from the z

axis. At the end of the RF pulse **M** has been tilted by a particular angle (the excitation angle or *flip angle*, dependent on the duration of the RF pulse and its amplitude B_1), and there will be a component of **M** in the transverse plane, i.e. the transverse magnetization $\mathbf{M}_{x,y}$. The precession of **M** around $\mathbf{B}_0$ is now *visible* on the transverse plane, as a rotating magnetic field at the Larmor frequency. The oscillating magnetic field produced by $\mathbf{M}_{x,y}$ will induce a current in the coil loop, and produce a measurable signal (figure 2.1).

The oscillating magnetic field in the transverse plane is *transient* due to the relaxation phenomenon.

The transverse magnetization decays over time, with a characteristic time constant T_2 known as the transverse (or spin-spin) relaxation time. The longitudinal component of the magnetization instead slowly regrows over time, with a time constant T_1, the longitudinal (or spin-lattice) relaxation time. At 3 T, typical values for T_1 and T_2 values are around 900 ms and 80 ms for WM, and 1300 ms and 100 ms for GM [12, 13].

In the following we describe some basic concepts regarding the physical and molecular basis of the NMR relaxation phenomenon. The original theory and rigorous modelling of relaxation times can be found in [14, 15].

Relaxation processes are linked to the tumbling of water molecules due to their thermal motions. Water molecules are in constant motion, colliding with other molecules, rotating and tumbling randomly. As a result, protons experience a fluctuating magnetic field resulting from the change in relative position between protons in the same molecule or with other molecules. The z component of this fluctuating field adds to or subtracts from to B_0 causing slightly different precession rates between spins. This produces dispersion in the distribution of spin phases, which builds up over time as the pattern of random fields felt by each proton is different. The net signal, given by the sum of the many local dipole vectors with their phase distribution, is therefore attenuated compared to when all dipoles are added coherently. The rate of this phase dispersion links to the T_2, that according to a simplified model [11] can be seen as:

$$\frac{1}{T_2} \sim B_{fluct}^2 \tau_c \tag{2.2}$$

where B_{fluct} is the magnitude of the fluctuating field, and τ_c is the *correlation time*, qualitatively defined as the time for a water molecule to significantly modify its orientation.

The T_1 can be described in a similar way. The key difference is that to produce longitudinal relaxation, the magnetic field fluctuations must occur at the Larmor frequency along one of

the transverse plane axes. This will cause the magnetization to precess slightly around this field in the transverse plane, changing the z component.

The take home message of the simplified explanation given above is that relaxation times are determined by the magnitude and the correlation time of the local fluctuating magnetic fields, which ultimately depend on the local environment of the water molecules. For example, in highly organized structures such as myelin sheaths around axons, τ_c is very long producing a drastic shortening of the T_2, i.e. myelin has a T_2 on the order of μs (see section 2.2).

The transverse component of the magnetization always decays faster than is predicted by the T_2. A simple model for the transverse relaxation rate is:

$$\frac{1}{T_2^*} = \frac{1}{T_2} + \frac{1}{T_2'} \tag{2.3}$$

Equation 2.3 shows that transverse magnetization decays with a time constant $T_2{}^*$, enhanced by an additional component ($\frac{1}{T_2'}$). Such a component accounts for the effect of static local field inhomogeneities, which adds to the random fluctuating fields causing T_2 relaxation.

Starting from the NMR signal as described in this section, we discuss how to encode in the transverse magnetization generating the detected signal: (*i*) information on tissue properties by manipulating the weight that fundamental NMR parameters have in the measured signal through dedicated magnetic resonance sequences; and (*ii*) information regarding the spatial localization of the signal source so that an image can be created from a set of NMR signals. In the following two sections (2.1.2 and 2.1.3) we will focus on these two aspects, introducing: (*i*) the Bloch equations as a tool to describe the measured signal as a function of tissue and sequence parameters; and (*ii*) the spatial encoding process, and its generalization through k-space, as a tool to understand image formation.

2.1.2 The Bloch equations and contrast manipulation

The Bloch equations [16] relate the time evolution of $\mathbf{M}$ to the external magnetic fields ($\mathbf{B}_0$ and $\mathbf{B}_1$(t)), relaxation times (T_1 and T_2) and, in their expanded version also to the molecular self-diffusion coefficient $\mathbf{D}$ [17], and other parameters through adequate modifications (an example is given in section 2.2.1.3 in the context of the quantitative description of the magnetization transfer effect).

The general form for the Bloch equations is [16]:

$$\frac{d\mathbf{M}(t)}{dt} = \gamma\mathbf{M}(t) \times \mathbf{B}(t) - \mathbf{R}\big(\mathbf{M}(t) - \mathbf{M}_0\big) \tag{2.4}$$

where $\mathbf{M}(t)=[M_x\ M_y\ M_z]^T$ is the magnetization vector, $\mathbf{B}(t)=\mathbf{B}_0+\mathbf{B}_1(t)$ is the sum of static field $\mathbf{B}_0 = \mathbf{z}B_0$, and RF field $\mathbf{B}_1(t) = \mathbf{x}B_1(t)\cos\omega_{rf}t - \mathbf{y}B_1(t)\sin\omega_{rf}t$, $\mathbf{R}=diag[\frac{1}{T_2}\ \frac{1}{T_2}\ \frac{1}{T_1}]^T$ is the relaxation matrix, which implicitly (and empirically) models the relaxation process in the form of exponential functions.

The analysis of the evolution of $\mathbf{M}(t)$ is simplified through a change of system of reference, via the adoption of the so called *rotating* frame of reference. In this new reference frame the transverse plane rotates around the z axis of the laboratory frame of reference at an angular frequency ω_0, such that the effect of the precession around $\mathbf{B}_0$ is cancelled out in the equations. The change of coordinates between the two systems is given by:

$$\begin{aligned} x' &= x\cos(\omega_0 t) - y\sin(\omega_0 t) \\ y' &= x\sin(\omega_0 t) + y\cos(\omega_0 t) \\ z' &= z \end{aligned} \tag{2.5}$$

where $[x'\ y'\ z']^T$ are the coordinates of the rotating frame of reference. The Bloch equations in the new reference frame become:

$$\frac{d\mathbf{M}'(t)}{dt} = \gamma\mathbf{M}'(t) \times \big[B_1(t)\big(\mathbf{x}'\cos(\omega_r f - \omega_0)t - \mathbf{y}'\sin(\omega_r f - \omega_0)t\big) + \mathbf{z}'\big(B_0 - \frac{\omega_0}{\gamma}\big)\big] \tag{2.6}$$

where the relaxation term has been neglected for simplicity. From equation 2.6 in the rotating frame of reference, it can be shown that: (*i*) in the absence of a $\mathbf{B}_1$ field, $\mathbf{M}$ is stationary along the z axis, as $\frac{d\mathbf{M}'(t)}{dt} = 0$; and (*ii*) when an RF field is applied perpendicularly to the main field, $\mathbf{B}_1$ is demodulated and appears stationary in the transverse plane (it can be thought of as being applied arbitrarily along the x' axis) and $\mathbf{M}$ precesses about $\mathbf{B}_1$, as $\frac{d\mathbf{M}'(t)}{dt} = \gamma\mathbf{M}(t) \times \mathbf{B}_1(t)$.

The Bloch equations in the rotating frame of reference can be used to derive the signal expression for a given magnetic resonance sequence. Here we provide an example for the spin echo (SE) sequence which is used extensively throughout this thesis.

2.1.2.1 A signal equation for the SE sequence

A schematic of the basic SE sequence is shown is figure 2.2. We neglect for the moment the imaging gradients, as those will be discussed in the next section (2.1.3), and we will focus on the sequence parameters: echo time *TE*, repetition time *TR*, and flip angles θ_1 and θ_2. The calculation of the signal equation follows what is shown in section 14.3.1 of [10]. It

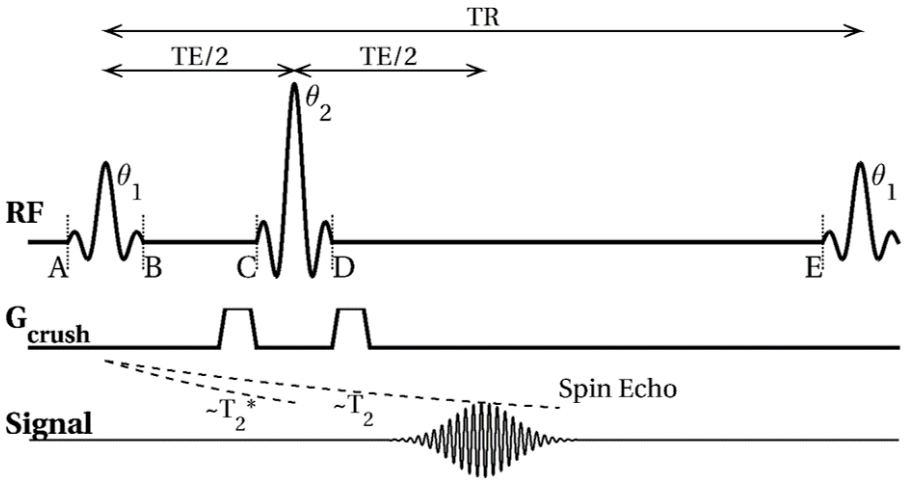

Figure 2.2: The standard SE sequence consists of two RF pulses, the *excitation* pulse and the *refocusing* pulse, separated by a time $\tau = \frac{TE}{2}$ that will produce a signal known as the *spin echo* after a time $2\tau = TE$ from the excitation pulse. The refocusing pulse compensates for part of the dephasing occurring in the first $\frac{TE}{2}$ interval, by flipping the magnetization configuration in the transverse plane, so that the sources of field inhomogeneities that are static now have a reverse effect on spin dephasing. This results in a signal maximum at the time *TE*, showing a pure T_2 attenuation. Usually the SE sequence has $\theta_2 = 2\theta_1 = 180°$. A pair of gradients of equal total area, called *crusher* gradients, are placed on both sides of the refocusing pulse so that for $\theta_2 \neq 180°$the component of the magnetization flipped in the transverse plane is dephased and will not contribute to the later spin echo.

is assumed that: (*i*) transverse magnetization is null at the end of the sequence (point E in figure 2.2), (*ii*) flip angles are those typically used in a SE sequence: θ_1=90°and θ_2=180°, and (*iii*) the magnetization is in a *steady-state*, a condition meaning that the sequence has been repeated a certain number of times such that **M** behaves periodically between *TR*s, i.e. the magnetization at point *E* is equal to the magnetization at point A in figure 2.2 ($\mathbf{M}_E$=$\mathbf{M}_A$). The longitudinal magnetization at the point B is given by:

$$M_{z,B} = M_{z,A} \cos\theta_1 = 0 \tag{2.7}$$

which is equivalent to solving the Bloch equations neglecting relaxation during the RF excitation pulse. Longitudinal relaxation occurs between B and C. According to the Bloch equations $M_{z,C}$ is:

$$M_{z,C} = M_0\left(1 - e^{-\frac{TE}{2T_1}}\right) \tag{2.8}$$

where M_0 is the equilibrium magnetization. After the refocusing pulse, neglecting again relaxation during the the pulse, the magnetization at D is given by:

$$M_{z,D} = M_{z,C}\cos\theta_1 = -M_0\left(1 - e^{-\frac{TE}{2T_1}}\right) \tag{2.9}$$

and accounting for T_1 relaxation after the refocusing pulse:

$$\begin{aligned} M_{z,E} &= M_{z,D} + \left(M_0 - M_{z,D}\right)\left(1 - e^{-\frac{TR-\frac{TE}{2}}{T_1}}\right) \\ &= M_0\left(1 - 2e^{\frac{TR-\frac{TE}{2}}{T_1}} + e^{-\frac{TR}{T_1}}\right) \end{aligned} \tag{2.10}$$

The Bloch equations show that the transverse magnetization at the time of the measurement TE, proportional to the measured signal, is given by:

$$M_{x,y} = M_{z,A}\left(\sin\theta_1\right)e^{-\frac{TE}{T_2}} = M_{z,A}e^{-\frac{TE}{T_2}} \tag{2.11}$$

Exploiting the steady-state condition, i.e. $M_{z,A}$ is equal to $M_{z,E}$ in equation 2.11, an equation for the SE signal as function of T_1, T_2 and M_0 can be obtained:

$$M_{x,y}(TE) = M_0\left(1 - 2e^{\frac{TR-\frac{TE}{2}}{T_1}} + e^{-\frac{TR}{T_1}}\right)e^{-\frac{TE}{T_2}} \tag{2.12}$$

An important property of the SE sequence is that the refocusing pulse will reverse the magnetization in the transverse plane, cancelling the dephasing produced by static sources of field inhomogeneities at a time $\frac{TE}{2}$ following its application (i.e. cancelling the contribution $\frac{1}{T_2'}$ in equation 2.3), therefore resulting in higher signal at a time TE from the excitation pulse, which will then exhibit a pure T_2 decay.

2.1.3 Image formation and the signal sampling

Magnetic resonance pulse sequences allow the manipulation of the magnetization to obtain different contrasts, according to the interplay between tissue parameters and sequence parameters. This can be quantitatively described by the phenomenological Bloch equations,

as shown for the basic SE sequence in the example provided in section 2.1.2.1. In order to produce an image of the magnetization distribution, spatial information must also be encoded in the recorded signals.

Spatial information is encoded in the transient signal measured in the transverse plane using a system of magnetic field gradients applied along three orthogonal directions.

For the purpose of signal localization, it is useful to introduce a new system of reference, the *image* reference system (*gradient* reference system), which defines the three directions along which the magnetic field gradients are applied. The *image* frame of reference consists of: slice encoding (S) direction, phase encoding (P) direction and frequency encoding or measurement (M) direction. The [$S\ P\ M$] system has no fixed relationship with the [$x\ y\ z$] system used to described magnetization evolution. It should also be noted that the convention used for the image reference system is purely arbitrary, other conventions for referring to the gradient axes may be found elsewhere.

Magnetic field gradients $\mathbf{G}$ are small spatially variant magnetic fields (on the order of $\frac{mT}{m}$) that, superimposed on the main field $\mathbf{B}_0$, alter the precession frequency of the spins as a function of the position $\mathbf{r}$=[$s\ p\ m$], as follows:

$$\begin{aligned}\omega(\mathbf{r}) &= \omega_0 + \mathbf{G}(\mathbf{r}) \\ &= \gamma\left(B_0 + G_S s + G_P p + G_M m\right)\end{aligned} \tag{2.13}$$

where $\mathbf{G}$=[$G_\mathrm{S}\ G_\mathrm{P}\ G_\mathrm{M}$]$^\mathrm{T}$ indicates the magnetic field gradient along the three orthogonal directions.

The process of spatial encoding through imaging gradients can be more easily understood through the example provided by figure 2.3.

Through the *slice selection* mechanism only spins within a limited region along the S direction are tipped into the transverse plane. This is achieved by switching on G_S during the time the RF excitation pulse is applied. The RF pulse is designed to contain a narrow and selective range of frequencies which translates into a segment of locations along S, through the concomitant application of G_s.

The *frequency encoding* is achieved by switching on a gradient along the M direction during the data acquisition window. The precession frequency of the local magnetization is therefore linearly dependent on the spatial position of spins along M, resulting in a detected

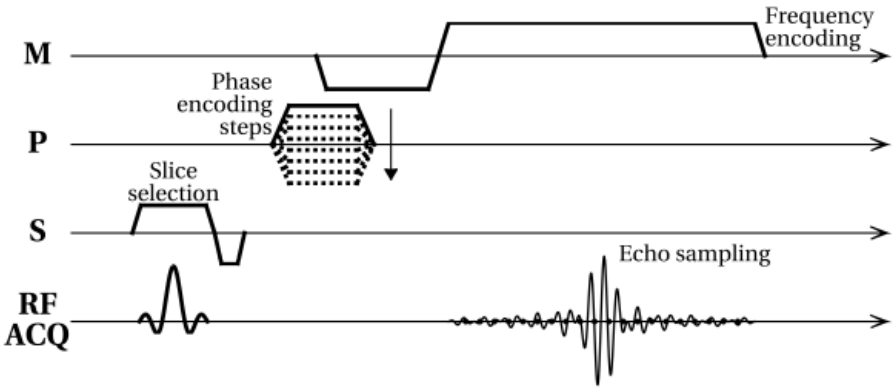

Figure 2.3: A basic GE sequence is shown with imaging gradients along 3 orthogonal axes *S*, *P* and *M*. A signal, known as a *gradient echo*, is obtained by compensating the effect of the pre-phasing gradient (first gradient lobe along *M*) with a *readout* gradient creating an echo, with maximum amplitude in its center, showing T_2* dependent attenuation. As the signal is sampled during the readout gradient, different precession frequencies can be related to different locations along *M*. During slice selection, a gradient, applied along *S*, makes the RF selective only for a range of locations. Repetition of the sequence with different phase-encoding steps, i.e. different amplitudes of the gradients along *P*, enables the acquisition of sufficient information to reconstruct an image.

signal in the time domain containing a range of frequencies, each corresponding to a specific spatial location. Frequency content can be easily be separated by an inverse Fourier transform of the acquired NMR signal.

The *phase encoding* is accomplished by switching on for a short interval a gradient along the *P* direction, between the RF pulse and data readout. During the application of G_{p} spins at different positions along *P* precess at different rates, producing a phase difference between signal from two locations that increases linearly with time. The phase difference is locked, once the G_{p} is switched off, resulting in magnetization precessing with a different phase offset, dependent on the position along *P*. Different phase offsets can be induced by increasing G_{P} between different sequence repetitions, i.e phase-encoding steps.

To summarize, the image formation can be seen as the process of creating an image of the magnitude of the local transverse magnetization by encoding the spatial location of the signal in the phase of the magnetization: the position along *M* is encoded as a rate of change of the phase during the acquisition window, while the position along *P* is encoded as a rate of change of the local phase between phase-encoding steps.

The general expression of the acquired signal formalizes this concept. The time domain signal created by the transverse magnetization and measured in the receive coil, after de-

modulation to remove rapid oscillation at ω_0, is [9]:

$$S(t) = \int_V \rho'(\mathbf{r}) e^{-i\phi(\mathbf{r},t)} d^3V \tag{2.14}$$

where ρ' is the effective spin density, dependent on the magnitude of the transverse magnetization (and hence ρ, T_1, T_2 and sequence parameters), the receiver coil properties, and other factors, e.g. temperature; and $\phi(t,\mathbf{r})$ is the accumulated phase, given by:

$$\begin{aligned} \phi(t,\mathbf{r}) &= \gamma \int_0^t \left[\mathbf{G}(t')\right]^T \mathbf{r} dt' \\ &= \gamma \Big[\int_0^t \mathbf{G}(t') dt' \Big]^T \mathbf{r} \end{aligned} \tag{2.15}$$

Defining the following quantity:

$$\mathbf{k}(t) = \frac{\gamma}{2\pi} \int_0^t \mathbf{G}(t') dt' \tag{2.16}$$

equation 2.14, by using equation 2.15, becomes:

$$S(t) = \int_V \rho'(\mathbf{r}) e^{-i2\pi\mathbf{k}(t)\mathbf{r}} d^3V \tag{2.17}$$

The measured signal can be seen as the Fourier transform of the effective spin density $\rho'(\mathbf{r})$. The quantity $\mathbf{k}$(t) is a vector, whose element has the units of inverse distance, and is the defined in a space called *k*-space. The definition of the *k*-space, via equations 2.16 and 2.17, allows us to interpret the image formation as the sampling of the spatial frequencies of the image, which is subsequently obtained via the inverse Fourier transform of the acquired signal in the reconstruction stage.

Properties of *k*-space, such as extension and sampling interval, can thus be related to properties of the image, such as resolution and field-of-view (FOV). The sampling of the *k*-space is subject to the Nyquist criterion, requiring a FOV larger than the size of the encoded object. The way the *k*-space is sampled, the *k*-space trajectory, is determined by imaging gradients through equation 2.16. Useful reviews on *k*-space can be found in [18, 19, 20, 21].

In the following section we introduce one of the most common signal sampling techniques, the echo-planar trajectory, which will be used extensively in this thesis.

2.1.3.1 The Echo-Planar-Imaging readout

Echo-planar imaging (EPI) is a fast method for sampling *k*-space following a few (*multi-shot*), or just one (*single-shot*), excitation pulses [22, 23]. EPI is capable of producing an image in a few tens of milliseconds.

EPI samples the *k*-space by going back and forth in the *M* direction on a Cartesian grid. This is achieved using a train of *readout* gradients (the EPI echo train) with alternating signs in the *M* direction to travel along the lines of the grid, interleaved by small *blip* gradients in the *P* direction to jump between adjacent lines of the grid, as shown in figure 2.4.

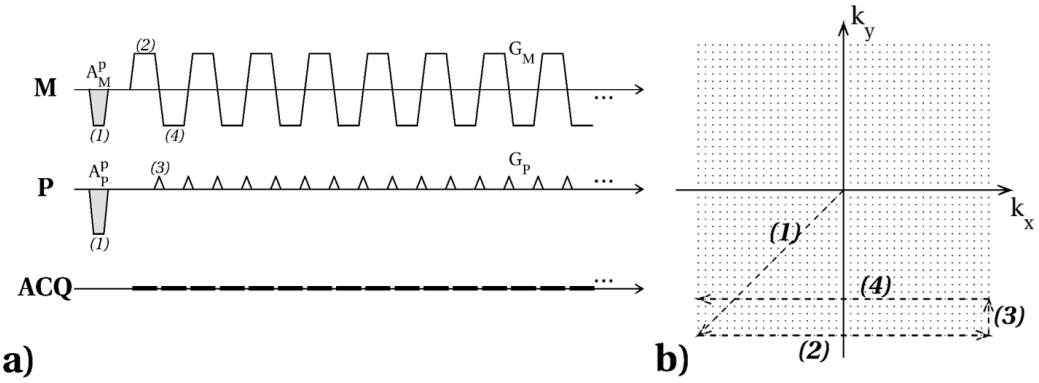

Figure 2.4: Example of a 2D EPI readout (**a**), and the associated trajectory in 2D *k*-space (**b**). The train of *readout* gradients corresponds to a Cartesian trajectory in *k*-space, with positive lobes and negative lobes moving in opposite directions along the k_x axis (*M* direction in image space). The gradient amplitude G_M determines the speed of the Cartesian trajectory. Similarly, the *blip* gradients in the *P* direction produce jumps along the k_y axes (*P* direction in the image space). The area of the *blip* gradient (controlled by their amplitude G_P, as the duration is kept fixed to the minimal value) determines the distance between *k*-space lines in the k_y direction. Prior to the readout gradients, *pre-phasing* gradients in both the *M* and *P* directions are used to move the starting point of the trajectory. The initial position is determined by their areas $A_M{}^p$ and $A_P{}^p$.

EPI has played, and still plays, a fundamental role in the development of a number of challenging MRI applications, especially regarding quantitative MRI. The 2D single-shot EPI (ssh-EPI), where the entire two-dimensional *k*-space is sampled after a single excitation, has been used extensively for example in diffusion (section 2.2.4) and perfusion imaging, and represents the workhorse for functional MRI, due to the high temporal resolution achievable. In general EPI sequences offer fast imaging (single-shot images are usually referred to as *snapshot*, as they are taken in a fraction of a second, and thus able to *freeze* motion within data readout) in combination with the ability to adapt to a number of preparation pulses (e.g. inversion pulses, tagging pulses) and imaging sequences (e.g. SE, GE). These

features make EPI particularly advantageous for quantitative studies.

As the measured signal is decaying while the EPI readout is performed, it is fundamental for EPI readouts to travel across the *k*-space as quickly as possible, to avoid substantial signal decay. This condition requires high performances of the gradient system. The speed with which the *k*-space is covered is, in fact, heavily dependent on readout gradient amplitude and slew rate.

EPI readouts are also prone to a variety of artefacts. First of all, EPI images are heavily affected by distortions arising from local field inhomogeneities, such as those encountered at the interfaces between tissues with significantly different magnetic susceptibilities. Magnetic susceptibility differences create off-resonance effects, $\Delta\omega$, that lead to displacement of voxels along a specific direction, as quantified by:

$$d(\mathbf{r}) = \Delta\omega(\mathbf{r})\frac{Lt_{esp}}{N_{sh}R_{PI}} \tag{2.18}$$

where L is the size of the FOV along the considered direction, and t_{esp} is the time interval between the sampling of two adjacent locations in the *k*-space along the considered dimension, N_{sh} is the number of shots required to sample the *k*-space, and R_{PI} is the acceleration factor introduced by parallel imaging techniques, if used, which are described in section 2.1.4.

Equation 2.18 implicitly shows that for EPI acquisitions distortions are predominant in the *P* direction, given the slower sampling in that direction, i.e. lower effective bandwidth in the *P* direction compared to the *M* direction, as well as the benefits of performing multi-shot acquisitions, i.e. $N_{\mathrm{sh}}>1$, to mitigate distortions.

Moreover EPI is affected by ghosting along the *P* direction (Nyquist ghost) [24], chemical shift artefacts, and image blurring due to T_2* decay during the signal acquisition [25].

2.1.4 Accelerating MRI with Parallel Imaging

Parallel imaging refers to a group of techniques that allow the acceleration of MRI acquisition by skipping lines in *k*-space, and retrieving the missing information at the reconstruction stage exploiting additional spatial encoding information available when the signal is acquired using an array of receive coils. Modern receive coils comprise a set of independent elements geometrically arranged to cover the specific anatomy they are designed for. Each coil is characterized by a different sensitivity to the imaged object (i.e. the *coil sensi-*

tivity maps or *coil sensitivity profiles*), which provide additional encoding information that complements the signal encoding with RF pulse and gradients.

Parallel imaging is nowadays an established techniques and is regularly used in clinical practice.

All parallel imaging methods allow a reduction in the scan time, which is proportional to the number of lines skipped at the acquisition stage, but in turn introduce a signal-to-noise (*SNR*) penalty, which is dependent on how the reconstruction of the undersampled *k*-space is performed (and hence method-dependent), as well as the quality of the additional spatial encoding information (i.e. the coil sensitivities) available in the reconstruction (hence site- and application-dependent).

The most common parallel imaging methods are: sensitivity encoding (SENSE) [26], and generalized auto-calibrating partially parallel acquisition (GRAPPA) [27]. In the following the SENSE approach will be briefly explained. For the other methods readers should refer to the respective references.

2.1.4.1 Sensitivity Encoding (SENSE)

In the SENSE reconstruction, the density of line sampling along P is reduced at a fixed maximum *k*-space value along that direction. By doing so, data readout is sped up by a factor R_{PI}, the acceleration factor of the parallel imaging method, but in turn will produce a set of aliased images, one for each coil.

In the aliased images, each pixel contributes to R_{PI} different positions in the final full-FOV image. The signal superimposition is resolved when combining the aliased coil images, exploiting different coil sensitivities which act as weighting factors in the signal summation (figure 2.5).

For a single pixel I, the following equations can be given for the N receive coils available:

$$\begin{aligned} I_1 &= S_{1,1}\rho_1 + S_{1,2}\rho_2 + \ldots + S_{1,R}\rho_{R_{PI}} \\ I_2 &= S_{2,1}\rho_1 + S_{2,2}\rho_2 + \ldots + S_{2,R}\rho_{R_{PI}} \\ &\ldots \\ I_N &= S_{N,1}\rho_1 + S_{N,2}\rho_2 + \ldots + S_{N,R}\rho_{R_{PI}} \end{aligned} \tag{2.19}$$

where I_{j} is the intensity of the folded pixel in the aliased image from coil j, ρ_{i} is the intensity of the pixel i in the full FOV image, and $S_{\mathrm{j,i}}$ refers to the sensitivity of the coil j for the pixel i in the full FOV image.

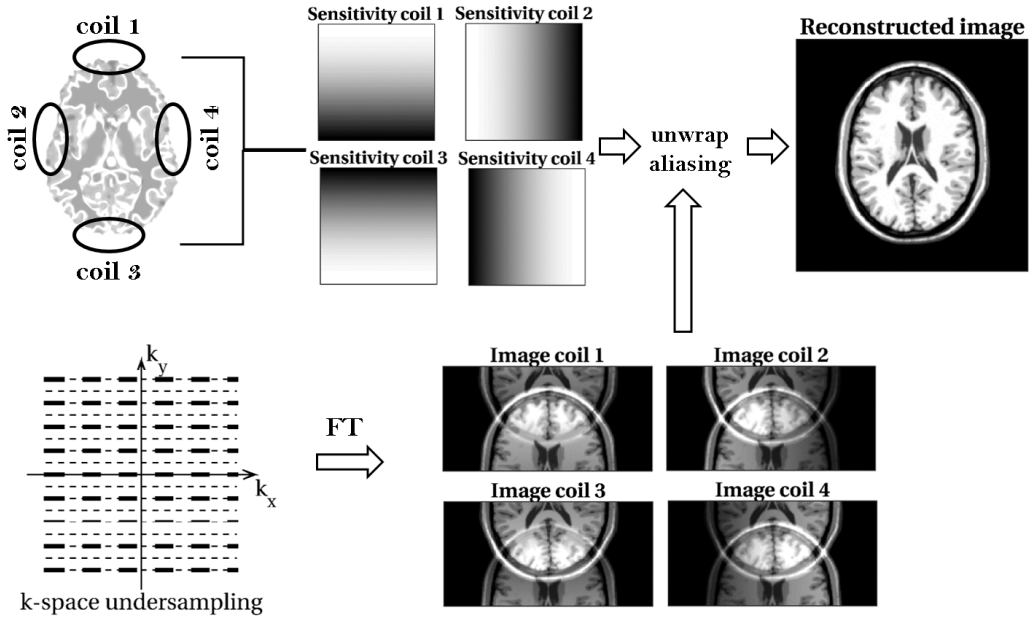

Figure 2.5: Schematic representation of the main steps of SENSE reconstruction. An example for acceleration factor R_{PI}=2 is illustrated, with one acquired line (**dashed bold** lines) every other *k*-space line.The undersampling of *k*-space produces a set of aliased images, one per coil. The missing spatial encoding information, due to the skipped lines in *k*-space, is retrieved via the coil sensitivity images that act as weighting factors to different pixel contributions in the aliased images, and enable the unwrapping of the aliasing by solving equation 2.19 for each pixel.

Equation 2.19 is solved for every pixel j in the aliased image, to produce a set of pixel intensities ρ_1,ρ_2,...,$\rho_{\mathrm{R_{PI}}}$ from a single pixel in the N aliased coil images, via the unfolding matrix **U**. The matrix **U** contains the effects of the coil sensitivities S and the receiver noise matrix, that describes the level and the correlation of noise in the receiver coils.

It can be shown [26] that the *SNR* in SENSE reconstructed images relates to the *SNR* of images acquired without parallel imaging, through the equation:

$$SNR(\mathbf{r})^{SENSE} = \frac{SNR(\mathbf{r})^{FULL}}{g(\mathbf{r})\sqrt{R_{PI}}} \tag{2.20}$$

where g is called the *geometry factor* or g-factor, it depends on the coil geometry, and denotes the noise amplification due to the SENSE reconstruction, at each position **r**, producing a spatially varying noise level.

The combination of SENSE, and in general parallel imaging techniques, with EPI has the great benefit of reducing the length of the EPI echo train, which translates into: (*i*) a substantial improvement of the geometrical distortions; (*ii*) a shortening of the *TE*, that helps

to counteract the *SNR* penalty associated with the acceleration (as shown in equation 2.20).

2.1.5 Accelerating MRI with Simultaneous Multislice Imaging

In simultaneous multislice imaging (SMS), two or more slices are excited simultaneously by a RF pulse with a *multiband* spectral content, and *ad hoc* reconstruction techniques are employed to separate the simultaneously acquired slices. Similarly to the parallel imaging techniques introduced in section 2.1.4, additional encoding information must be exploited to compensate for the shared spatial encoding information along the *S* direction of the slices that are acquired simultaneously.

The main features of the SMS approach are therefore special RF pulses (the *multiband* pulses) and specific signal sampling and reconstruction techniques. These two aspects are briefly introduced in the following. Excellent reviews on the topic can be found in [29, 30].

An RF excitation pulse $\mathbf{B}_1$(t) can be seen as a product of two complex functions:

$$\begin{aligned} \mathbf{B}_1(t) &= B_1(t)P(t) \\ &= B_1(t)e^{i\Delta\omega t+\phi} \end{aligned} \tag{2.21}$$

where B_1(t) is the complex RF waveform that determines the slice profile and P(t) is an additional phase modulation that determines the slice position ($\Delta\omega$) and phase (ϕ) of the excited magnetization. The simplest way to obtain a multiband pulse is to sum multiple B_1(t), each one with a different P(t), so that different slices will be excited when a common slice selection gradient is applied:

$$\mathbf{B}_{1,MB}(t) = B_1(t)\sum_N e^{i\Delta\omega_n t+\phi_n} \tag{2.22}$$

Multiband pulses suffer from two major issues: both peak amplitude and RF power are prone to exceeding their respective limits, dictated by RF amplifier performance and SAR restrictions. These aspects can be shown to be dependent on the number of simultaneous slices acquired *N*. Specific RF design solutions are available to mitigate these issues [30].

Spatial encoding for simultaneous slices can be achieved via a number of mechanisms. The first in vivo SMS images [31] were obtained with the same coil encoding mechanism used for parallel imaging, with the additional challenges given by the facts that: (*i*) coil sensitivities are similar among simultaneous excited slices, and (*ii*) common receiver coils are not designed to provide encoding power along the *S* axis. SMS reconstruction is in practice al-

ways achieved by combining coil encoding with additional encoding information, obtained via additional gradient encoding or RF encoding.

The main objective of both approaches is to introduce a controlled slice shifting in the P direction within the FOV for slices acquired simultaneously, so that the overlap between slices is reduced and the different degrees of in-plane coil sensitivity can also be exploited. This method was implemented in the original SMS application with EPI [32], and has led to an explosion of the use of SMS acceleration in combination with EPI, for diffusion-weighted imaging (DWI) [33], functional MRI (fMRI) [34] and perfusion studies [35].

SMS has proven particularly advantageous for multislice acquisition using EPI readout, complementing the advantages introduced by parallel imaging techniques. Parallel imaging for EPI allows acceleration of the readout duration, leading to substantial mitigation of distortions in the P direction, but limited scan time reduction. SMS accelerates EPI acquisition by reducing the overall scan time by a factor R_{SMS} equal to the number of simultaneous acquired slices N. Moreover, SMS has no *SNR* penalty associated with the acceleration factor, other than that introduced by the g-factor noise in the reconstruction, as no undersampling is involved in the acceleration of the acquisition.

2.2 Quantitative MRI for myelin imaging

In this section we provide an overview of the most common methods used to quantitatively measure myelin in vivo using MRI.

It is important to note that, with the technology currently available in a clinical setting, it is not possible to image myelin protons directly, as there is not enough time available to play out imaging gradients before myelin signal has decayed away. Considering a myelin proton T_2 of $\sim$10 μs, the lifetime of myelin signal is $\sim$50-60 μs. This would be only possible with techniques that achieve very short echo time, e.g. ultra-short (UTE) and zero (ZTE) echo time imaging, where the additional challenge of removing the non myelin signal contamination also exists.

All the quantitative MRI methods presented here are instead inherently indirect, in the sense that they provide measures of myelin content through surrogate indices thought to reflect myelin content. In this thesis the expression *quantitative myelin measure* is intended with the meaning elucidated above: a quantitative index indirectly reflecting myelin content. Such methods are all sensitive to myelin content, but their specificity is partial and still under debate.

In this section we introduce the following techniques: magnetization transfer imaging (MTI), multi-component T_2 relaxation, and diffusion-weighted imaging (DWI). These techniques, together with conventional relaxometry (e.g. quantitative T_1 and T_2 relaxation times), represents the core of quantitative MRI measurements of myelin currently available.

2.2.1 Magnetization Transfer Imaging

2.2.1.1 MT effect

Magnetization Transfer (MT) is a contrast mechanism based on the exchange of magnetization occurring between groups of spins characterized by different molecular environments, first demonstrated in vivo almost 30 years ago [36]. Traditionally MT is associated with the exchange between *mobile* protons, such as those belonging to water molecules, and *restricted* protons, such as those residing in macromolecules (proteins and lipids).

Protons attached to macromolecules exhibit an extremely short T_2, on the order of μs, and are therefore invisible to conventional MRI techniques, as the minimum achievable *TE* is on the order of ms. However, protons in water molecules are in constant contact with macromolecules due to their mobility, allowing the exchange of magnetization either via direct chemical exchange or spin-spin interactions.

It is possible to interact with this coupled system of mobile and restricted protons due to their different resonance lineshapes (see figure 2.6), since: (*i*) mobile water protons have a narrow resonance line width (of a few tens of Hz) around the Larmor frequency, (*ii*) macromolecular protons have a broader resonance line (of a few kHz), which makes them sensitive to RF pulses applied off-resonance, i.e. oscillating at frequency $\omega = \omega_0 + \Delta\omega$. Such pulses are usually referred to as RF saturation pulses, MT pulses, or simply off-resonance pulses.

If sufficient RF power is applied (through the use of high peak amplitude or long duration pulses), macromolecular spins are saturated and the net longitudinal magnetization is heavily reduced. Part of this saturation is then transferred to the mobile water protons via the exchange mechanism described above, resulting in a loss of longitudinal magnetization in the MR *visible* pool of spins (the water protons), and hence a signal attenuation in the acquired images, that will show the so called MT contrast.

2.2.1.2 Magnetization Transfer Ratio: strengths and pitfalls

MT provides an indirect probe to access the macromolecular compartment of biological tissues, and assumes great interest for potential applications in the CNS, as myelin accounts for $\sim$50% of the dry weight of human WM in the CNS [37].

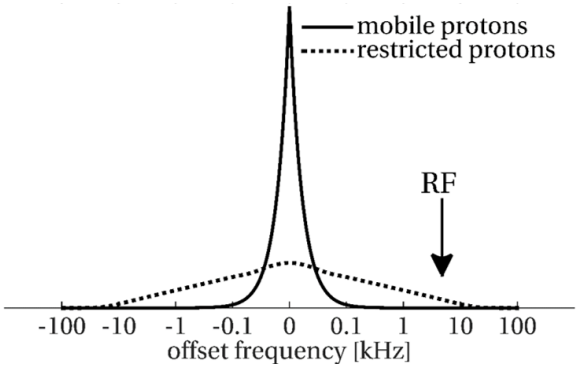

Figure 2.6: Schematic of different magnetic resonance lines for free protons in mobile water molecules, shown with a **solid** line, and restricted protons in macromolecules, shown with a **dashed** line. RF saturation applied off-resonance (e.g. 1-10 kHz) affects predominantly macromolecular protons providing the basis for detecting the magnetization transfer contrast with MRI.

The most widely used method to quantify the MT effect is through the Magnetization Transfer Ratio (*MTR*) [38], defined as:

$$MTR = \frac{MT_{off} - MT_{on}}{MT_{off}} \times 100 \tag{2.23}$$

where MT_{off} and MT_{on} are images acquired without and with off-resonance saturation pulses, i.e. MT_{on} is the MT-weighted image, and MT_{off} the so called M_0 image.

The *MTR* has found widespread applications in clinical studies for its *simple* implementation and its high *sensitivity* to demyelination in MS [39], and tissue integrity more generally. Although the *MTR* is reproducible and comparable among healthy subjects for the same acquisition sequence and centre, the resulting absolute *MTR* value reflects a complex combination of *sequence* and *relaxation* parameters in addition to the basic MT effect. Moreover, characterizing the MT phenomenon by a single *MTR* value hampers the physical interpretation of such a metric, and overlooks potentially useful diagnostic information that could be gained by adopting a model-based approach, where quantitative biologically meaningful parameters describing the MT effect are extracted.

2.2.1.3 Theoretical description of the MT effect: the two-pool model

The first quantitative description of the MT effect in biological tissue was devised in 1993 by Henkelman *et al.* [40], and it is still considered as the reference model for interpreting the MT effect. The MT model, known as the two-pool model, is depicted in figure 2.7, and briefly explained hereafter.

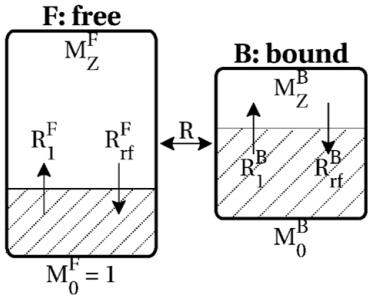

Figure 2.7: Two-pool model for MT effect. Dashed areas of compartments represent portion of spins that are saturated. Saturation growth is described by the rates $R_{\mathrm{rf}}{}^{\mathrm{F,B}}$, opposed by longitudinal relaxation described by rates $R_1{}^{\mathrm{F,B}}$. Free pool R_{rf} is governed by a Lorentzian absorption lineshape, that is implicitly imposed by the Bloch equations formalism, while bound pool R_{rf} is defined empirically (usually via a super Lorentzian absorption lineshape). Magnetization can be transferred between the two pools with rates $k_{FB} = RM_0^B$ and $k_{BF} = RM_0^F$, with R being the fundamental exchange rate. In the analysis, data are usually normalized with an M_0 (or MT_{off}) image, which is equivalent to set $M_0{}^{\mathrm{F}}$=1.

The two-pool model divides spins into two compartments: (*i*) the *free* pool composed of protons in mobile water molecules (superscript F), and (*ii*) the *bound* pool composed of water protons attached to macromolecules, such as proteins, lipids and cell membranes (superscript B). Each pool is characterised by its own relaxation times: longitudinal ($T_1{}^{\mathrm{F}}$=$\frac{1}{R_1^F}$, $T_1{}^{\mathrm{B}}$=$\frac{1}{R_1^B}$), and transverse ($T_2{}^{\mathrm{F}}$, $T_2{}^{\mathrm{B}}$); and spin density ($M_0{}^{\mathrm{F}}$, $M_0{}^{\mathrm{B}}$), representing the equilibrium value of the longitudinal magnetization of the two pools, $Mz^{\mathrm{F,B}}$. The two pools are allowed to exchange magnetization, a process modelled with an exchange rate R including cross-relaxation and chemical exchange, and made symmetrical, with forward exchange F $\rightarrow$B equal to $k_{FB} = RM_0^B$, and backward exchange B $\rightarrow$F equal to $k_{BF} = RM_0^F$, so that R represents a pseudo-first order exchange rate, as $M_0{}^{\mathrm{F}} >> M_0{}^{\mathrm{B}}$. The mathematical representation of the two-pool model is given by the Bloch equations (given in 2.6), modified to include the exchange terms between the two pools, (i.e. the *coupled Bloch equations*):

$$\begin{aligned}
\frac{dM_x^F(t)}{dt} &= -\frac{M_x^F(t)}{T_2^F} - 2\pi\Delta M_y^F(t) \\
\frac{dM_y^F(t)}{dt} &= 2\pi\Delta M_x^F(t) - \frac{M_x^F(t)}{T_2^F} - \omega_1(t)M_z^F(t) \\
\frac{dM_z^F(t)}{dt} &= \omega_1(t)M_y^F(t) - \frac{M_0^F - M_z^F(t)}{T_1^F} - k_{FB}M_z^F(t) + k_{BF}M_z^B(t) \\
\frac{dM_z^B(t)}{dt} &= k_{FB}M_z^F(t) - k_{BF}M_z^B(t) - \frac{M_0^B - M_z^B(t)}{T_1^B} - R_{rf}^B(t)M_z^B(t)
\end{aligned} \tag{2.24}$$

In equation 2.24, magnetization of either pool is described by its longitudinal component ($M_z{}^{F,B}$) and its transverse components ($M_x{}^{F,B}$ and $M_y{}^{F,B}$). However, the exchange associated with the transverse components can be considered negligible due to the extremely short $T_2{}^B$, therefore equations for $M_{x,y}{}^B$ are discarded. The off-resonance saturation is described by the offset frequency Δ (in Hz), and the time course profile of the RF pulse $\omega_1(t) = \gamma B_1(t)$ (in Hz).

The effect of the off-resonance saturation on the bound pool is entirely described by the saturation rate, $R_{rf}{}^B$(t), defined as:

$$R_{rf}^B(t) = \pi\omega_1(t) g_B\left(T_2^B, \Delta\right) \tag{2.25}$$

where g_B is the bound pool RF absorption lineshape, dependent on $T_2{}^B$ and Δ. The selection of the g_B is done empirically, often guided by data-driven approaches (i.e. the lineshape providing the best fit to the experimental data is chosen) [41]. For in vivo studies in the CNS the super-Lorentzian lineshape is commonly considered:

$$g_B = \int_0^{\frac{\pi}{2}} \sin\theta \sqrt{\frac{2}{\pi}} \frac{T_2^B}{|3\cos^2\theta - 1|} e^{-2\left(\frac{2\pi\Delta T_2^B}{3\cos^2\theta - 1}\right)^2} d\theta \tag{2.26}$$

although a more advanced lineshape, taking into account WM fibre directionality, has recently been proposed [42].

The model was initially developed for acquisition carried out with long duration continuous wave (CW) off-resonance pulses, i.e. $\omega_1(t) = \gamma B_1$, driving the system into a steady-state, i.e. $\frac{d\mathbf{M}}{dt} = 0$, for which an analytical solution with respect to $M_z{}^F$ (proportional to the measured signal) could be derived [43].

2.2.1.4 Measuring and quantifying MT: the qMT approach

The two-pool model described above represents the foundation of the quantitative Magnetization Transfer (qMT) approach. From equations 2.24, an expression relating $M_z{}^F$, which is proportional to measured signal intensity, to the two-pool model parameters and the off-resonance saturation parameters can be derived. Such a relation, the qMT model, is used to fit a set of MT-weighted images (produced by varying sequence parameters defining the off-resonance saturation, which are in the simplest model pulse amplitude B_1 and frequency offset Δ) to obtain the tissue parameters of the two-pool model. These parameters are quan-

titative in nature, sequence independent, and reflect biological tissue properties, overcoming the limitations intrinsic in the *MTR*.

The CW qMT model devised in the Henkelman *et al.* paper [43] can not be employed for in vivo MT studies, as clinical scanners do not have continuous RF capabilities and SAR limitations are more stringent for human studies.

For in vivo studies, CW saturation is replaced by multiple, short (10-50 ms duration) shaped off-resonance pulses that are are distributed throughout the sequence. This poses two interconnected challenges: (*i*) how to design pulse sequences to produce MT weighting in an effective manner, i.e *measuring* MT; (*ii*) how to obtain a qMT model from equations 2.24 containing time dependent terms ($\omega_1(t)$ and $R_{\mathrm{rf}}{}^{\mathrm{B}}(\mathrm{t})$), i.e. *quantifying* MT.

A range of sequences have been proposed for MT-weighted acquisitions, with the MT-weighted spoiled GE sequence being the workhorse for qMT studies in vivo [44]. Similarly various approximations for the time varying terms have been developed and validated in order to obtain analytical qMT models [45, 46, 47]. A review of such methods is beyond the scope of this section. Excellent overviews on the topic can be found in [48, 49].

In this section we want to highlight that to define a qMT approach, both the acquisition protocol and the signal model have to be specified. These two elements are closely related to each other. Figure 2.8 provides a unified view of the sequences available to acquire MT-weighted images, with the sequence parameters that directly impact on the qMT model highlighted.

Any MT sequence can be viewed as a repetition of a basic unit consisting of: (*i*) a preparation pulse (or a train of), interleaved with (*ii*) an imaging pulse (or series of), such as excitation or refocusing pulses. Preparation pulses are usually off-resonance pulses, but can be also inversion pulses (as in [50] and following developments), or be entirely neglected leaving to only the imaging pulses the task of inherently producing MT weighting [51].

A qMT model, based on the two-pool model description, has to predict $M_z{}^{\mathrm{F}}$ at the time the center of the k-space is excited (which could be, for example, after a certain number N of sequence repetitions, or at the time of excitation in single-shot EPI acquisitions where N=1). From a general point of view, this is done by solving equations 2.24 according to the particular realization of the MT-weighted sequence considered, by in turn combining solutions for the different building block of the sequence (similarly to what has been shown in section 2.1.2.1 for the simple SE sequence). The solution can be achieved by adopting

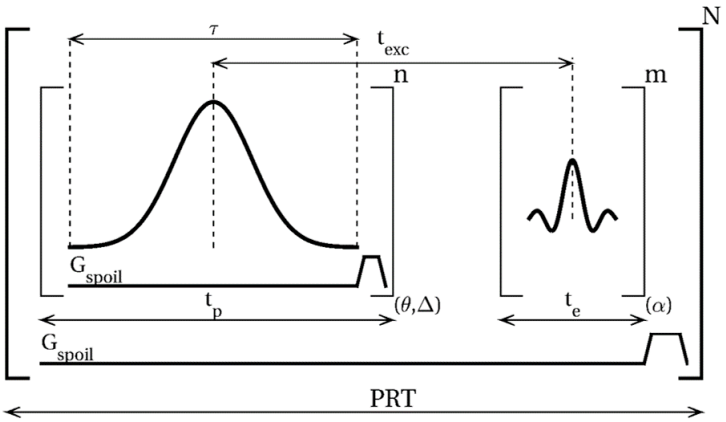

Figure 2.8: Unified representation of the MT-weighted sequence, with highlighted sequence parameters that affect the overall MT weighting: pulse effective flip angle θ, pulse offset frequency Δ, pulse duration τ, inter-pulse time t_p, number of pulses per repetition n, excitation delay t_{exc}, excitation flip angle α, imaging pulses repetition time t_e, excitation pulses per repetition m, sequence repetition time PRT and sequence repetition N. Spoiler gradients to null transverse magnetization can be placed between off-resonance pulses and/or between sequence repetitions.

different types of approximations for dealing with the time dependency in equations 2.24, hence the number of different models.

The most general qMT model is obtained by recursively solving the set of Bloch equations describing the two-pool model [48, 52], with a fixed integration step η=10-100 μs. This approach has been termed as Minimal Approximation Magnetization Transfer (MAMT) as it allows us to model magnetization behaviour and estimate MT parameters avoiding unwarranted simplifications, such as assuming steady-state or neglecting imaging pulses, and can be straightforwardly adapted to arbitrary sequences generated as in figure 2.8. Such models allow us to explicitly account for pulse shapes, timing between pulses, effects of on-resonance excitation and transient behaviour of magnetization towards steady state. Example of different model predictions at varying sequence parameters are given in figure 2.9.

Depending on the actual model used, different model parameters or combinations of model parameters can be extracted. In general, those regarding the macromolecular pool are of major interest: the bound pool transverse relaxation time ($T_2{}^{\mathrm{B}}$), the exchange rate between free pool to bound pool (k_{FB}), and the relative size of the bound pool. This parameter is known in literature with different names and symbols (e.g. macromolecular proton fraction *MPF*, pool size ratio *PSR*, F, f, amongst others). In the context of this thesis, we will refer

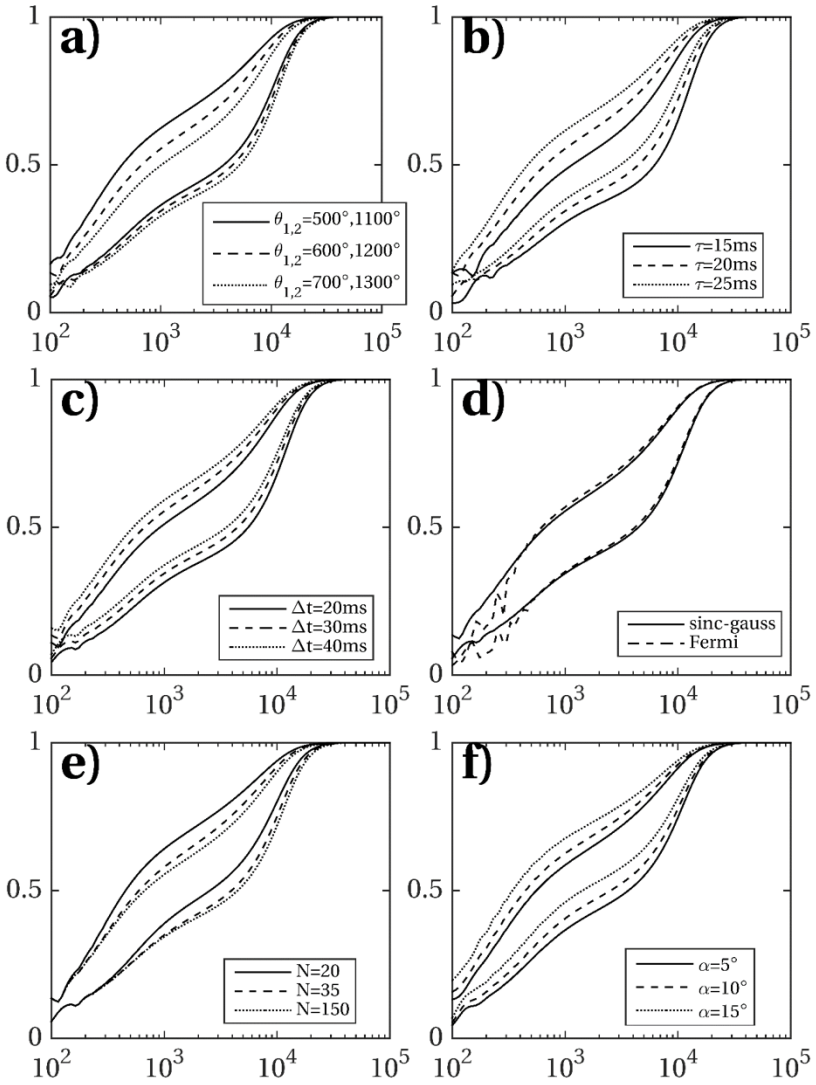

Figure 2.9: MAMT model predictions for different acquisition sequence parameter values. The panels show the predicted normalized Mz^{F} in the y axis, over frequency offset (from 100 Hz to 100 kHz) in the x axis, at two different saturation powers (effective flip angles θ_1=600°and θ_2=1200°). In each panel a particular sequence parameter is modified in turn from a standard setting: pulse shape sinc-Gaussian, pulse duration 20 ms, inter pulse gap 30 ms, number of pulses 150. The MAMT model allows us to account for any variation of the sequence parameters: (**a**) different pulse flip angle at fixed pulse duration, (**b**) different pulse duration at fixed flip angles, (**c**) different inter-pulse gap, (**d**) different pulse shape, (**e**) different number of pulses for non steady-state acquisition; and (**f**) the presence at imaging pulses at different flip angles. Model predictions are calculated using a single tissue model parameter configuration: BPF=0.13, ${T_2}^{\mathrm{F}}$=35 ms, ${T_2}^{\mathrm{B}}$=12 μs, k_{FB}=2.5 s^{-1}, ${R_1}^{\mathrm{B}}$=1 s^{-1}, ${R_1}^{\mathrm{F}}$=0.9 s^{-1}.

to it as the bound pool fraction (BPF), defined as:

$$BPF = \frac{M_0^B}{M_0^F + M_0^B} \tag{2.27}$$

The *BPF* is the parameter of main interest in qMT applications for its direct biological interpretation as macromolecular volume fraction (or macromolecular density). Ex-vivo studies in human tissue as well as animal models have suggested the use of *BPF* as a potential marker for myelin content in healthy and pathological condition [53, 54, 55, 56]. More on this parameter, with an updated account of qMT applications in the spinal cord, will be discussed in chapters 5 and 6.

2.2.1.5 MT_{sat} and the multi-parameter mapping technique

The multi-parameter mapping method [57, 58] takes one step towards the quantification of the two-pool model parameters while maintaining the simplicity characterizing *MTR* data acquisition and analysis.

It employs a three-point acquisition scheme to quantify, together with the apparent proton density (PD_{app}), and the longitudinal relaxation time (T_1), a parameter called MT_{sat}, which shows improved contrast between differently myelinated structures compared to the conventional *MTR*. [59]

The quantification is based on the linearised equation for the spoiled GE signal:

$$S = PD_{app}\alpha \frac{\frac{TR}{T_1}}{\frac{TR}{T_1} + \frac{\alpha^2}{2}} \tag{2.28}$$

where α is the excitation flip angle, and *TR* the sequence repetition time, and a phenomenological signal equation for the MT-weighted spoiled GE, where a GE readout module is prepared with an off-resonance saturation pulse. Similarly to equation 2.28, a linearised signal equation can be obtained for such a sequence [57]:

$$S = PD_{app}\alpha \frac{\frac{TR}{T_1}}{\frac{TR}{T_1} + \frac{\alpha^2}{2} + MT_{sat}} \tag{2.29}$$

The MT_{sat} parameter incorporates the effects of macromolecular pool saturation, direct (free water pool) saturation, and MT exchange produced by a single MT pulse during a *TR* period. Similarly to the *MTR*, MT_{sat} still represents a semi-quantitative parameter, meaning that it lacks a direct biological meaning and is dependent on sequence parameters, but compared to the *MTR* it provides corrections for T_1 relaxation and on resonance excitation, and appears to be inherently insensitive to RF inhomogeneity [57].

Applications of such techniques in the spinal cord can be found in [60, 61].

2.2.1.6 inhomogeneous Magnetization Transfer (ihMT)

Inhomogeneous Magnetization Transfer (ihMT) is a recently discovered contrast mechanism based on MT thought to provide an improved specificity towards myelin content compared to conventional MT [62].

In this thesis, applications of ihMT in the spinal cord have not been explored. However, to provide a complete overview of the available and emerging myelin mapping techniques using MRI, here below we describe the main features of ihMT for imaging myelinated tissue. ihMT uses a dedicated MT preparation to specifically select myelin, exploiting a unique feature of myelin among tissues in the CNS: an inhomogeneously broadened spectral line [62].

The broad line that characterises the bound pool in conventional MT (as depicted in figure 2.6) can be seen as a result of efficient mechanisms, as translational and rotational motion, chemical exchange and spin diffusion, between multiple lines centred at different offset frequency, such that different lines cannot be separated. The hypothesis of homogeneous broadening is modelled by assuming that the off-resonance pulses saturate the entire line equally, according to the applied power and the absorption spectrum of the line g_B, as in equation 2.25.

Non-homogeneous broadening has been proposed as a unique property of myelin. The densely packed sheaths of lipid bilayer composing myelin allow rotation of lipid chains around an axis perpendicular to the surface [63], and results in restricted or inefficient spin diffusion and molecular motion mechanisms [64], producing a significant residual dipolar coupling.

An appropriate acquisition scheme is employed to isolate such an effect. It requires: (*i*) an MT-weighted signal obtained at a positive offset frequency $+\Delta$, (*ii*) an MT-weighted signal obtained at a negative offset frequency $-\Delta$ at the same RF power, and (*iii*) an MT-weighted signal acquired saturating simultaneously (or quasi-simultaneously) both frequencies $+\Delta$ and -Δ at same total RF power used for (*i* and *ii*). Under the condition of symmetry for the NMR line, homogeneously broadened tissues are saturated equally by both the single and dual offset frequency experiments, showing no difference between the two signals, while a non zero difference signal is an indicator of magnetization transfer from inhomogeneous lines.

The ihMT ratio (*ihMTR*) can be defined in an analogous way to the *MTR* from the above

acquisition scheme:

$$ihMTR = \frac{S(+\Delta) + S(-\Delta) - 2S(\pm\Delta)}{S_0} \tag{2.30}$$

where S_0 represents the signal in a non-MT-weighted image (i.e. MT_{off} in equation 2.23). The use of both $S(\Delta)$ and $S(-\Delta)$ in equation 2.30 provides a first order correction for the known slight asymmetry of the MT spectrum [65].

A quantitative model, based on the two-pool MT model augmented by an additional pool to describe the dipolar coupling when dual frequency saturation is applied, has also been devised and preliminary results have been shown in phantoms and human data [66].

ihMT imaging has been successfully applied to in vivo human brain and spinal cord [67], ex-vivo animal tissues, and at different field strengths, showing consistency in selectively highlighting tissue with elevated myelin content, and providing higher contrast between GM and WM compared to the conventional *MTR* [62].

Despite its recent discovery and yet incomplete characterization (the original explanation of the ihMT effect has been challenged by other authors [68]), ihMT appears to be a promising mechanism to generate contrast specific to myelin in the CNS. Further developments in terms of quantitative description and histological validation are warranted in order to promote its widespread use as myelin biomarker.

2.2.2 Myelin Water Imaging

Myelin water imaging (MWI) refers to a quantitative MRI technique that aims to quantify the amount of tissue water that resides within myelin bilayer structures in the CNS, known as the myelin water fraction (*MWF*) [69].

In contrast to MTI methods (described in section 2.2.1) that attempt to measure myelin via the effect of the bound protons on the water protons, MWI tries to access myelin via the analysis of the free water signal (where $T_2 > 10$ ms). In the CNS, water can be visualized in three different compartments: (*i*) within the axons; (*ii*) in the extra-cellular space between axons, and (*iii*) trapped within bilayer myelin sheaths, as shown in figure 2.10.

This microscopic heterogeneity results in different relaxation behaviour of water protons in different compartments: water trapped in myelin has frequent and pronounced interactions with macromolecular and membrane protons due to the restricted space within myelin bilayers, which produces a shortened $T_2 \sim$10-20 ms; while intra- and extra-cellualar water is not in close contact with bound protons, resulting in a longer (and similar between the two compartments) $T_2 \sim$70-90 ms.

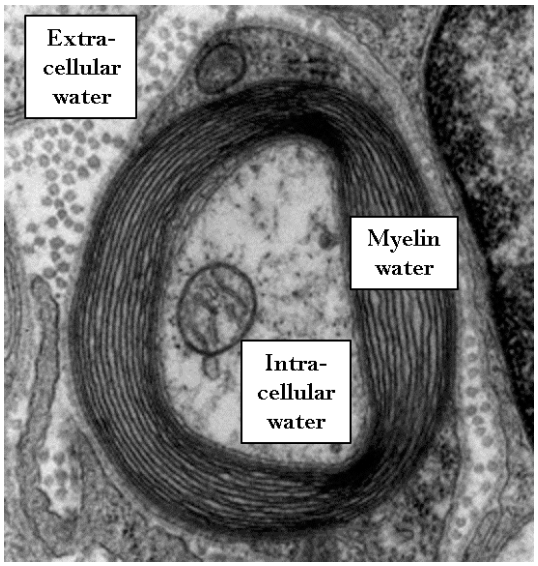

Figure 2.10: Transmission electron micrograph of a cross-section of an axon and its surrounding environment. The three compartments considered in MWI can be readily observed: (*i*) intra-cellular water, (*ii*) extra-cellular water, and (*iii*) water trapped within myelin bilayers. Intra- and extra-celluar water show similar T_2 relaxation times and therefore can not be separated in the multi-component T_2 used in MWI. The image is modified from `https://upload.wikimedia.org/wikipedia/commons/c/c1/Myelinated_neuron.jpg`, generated and deposited into the public domain by the Electron Microscopy Facility at Trinity College.

MWI aims to separate the myelin water signal from the intra and extra-cellular signal, and hence to quantify the *MWF*, via a quantitative multi-component analysis of T_2.

T_2 relaxation curves are usually acquired with a multi-echo sequence. The most common approach is the Carr-Purcell-Meiboom-Gill (CPGM) sequence [70], consisting of a 90°excitation pulse followed by a train of 180°refocusing pulses. A typical sampling scheme consists of 32 echoes spaced every 10 ms, from 10 ms to 320 ms, at 3 T.

The acquired signal is modelled as a multi-component T_2 decay signal:

$$S(TE_k) = \sum_{i}^{N_c} A_i e^{-\frac{TE}{T_{2,i}}} \tag{2.31}$$

where S_i and $T_{2,\mathrm{i}}$ are the relative amplitude and relaxation time for the various N_c components.

The estimation of S_i and $T_{2,\mathrm{i}}$ is commonly obtained by minimization of the least squares (LS) criterion, which in the case of sum of exponentials is hampered by the presence of local minima and ill conditioning [71]. The most common solution is the use of non-negative least square (NNLS) approach, which circumvents some of the problems by providing a fit

grid of T_2 times to which amplitudes S_i are fit, subject to constraints $S_\mathrm{i}>0$. This produces a sparse vector of amplitudes S_i, with most elements equal to zero. Often a regularized solution is pursued, by adding in the cost function a term penalizing a metric related to the smoothness of the distribution (e.g. first order differences of the estimated amplitude vector, or an energy constraint), as follows:

$$A_i = \arg\min_{A_i} \Big[\sum_{k}^{N_{TE}} \Big(S(TE_k) - \big(\sum_{i}^{N_c} A_i e^{-\frac{TE_k}{T_{2,i}}} \big) \Big) + \mu \sum_{i}^{N_c} |A_i^2| \Big] \tag{2.32}$$

where μ is the regularization term that determines the weight of the smoothness constraints in the minimization problem.

From the estimated spectrum, *MWF* is defined as the area under the shortest T_2 peak compared to the total signal distribution:

$$MWF = \frac{\sum_{T_{2,min}^{mw}}^{T_{2,max}^{mw}} S(T_{2,j})}{\sum_{i}^{N_c} S(T_{2,i})} \tag{2.33}$$

where $T_{2,min}^{mw}$ and $T_{2,max}^{mw}$ are the lower and upper bounds for myelin water signal, usually 10 ms and 40 ms at 3 T.

Due to magnetic field inhomogeneities, refocusing pulses in the multi-echo train are not necessarily 180°, producing spurious oscillations of the decay curve in equation 2.31, and bias in the multi-component estimation. Such artefacts are consequences of stimulated echoes due to imperfect refocusing pulses that move fraction of the magnetization into the longitudinal axis. The correction for stimulated echoes can be modelled using the extended phase graphs algorithm [72] and incorporated in the T_2 spectrum estimation [73].

For in vivo application, the 2D sequence of the original MWI implementation [69], requiring $\sim$20 min per slice, has to be modified to achieve sufficient coverage . Most of the in vivo studies published so far have exploited the 3D gradient and spin echo (GRASE) sequence which enables the avoidance of potential MT effect in multislice imaging and provides an acceleration factor over standard multi-echo SE, as a number of *k*-space lines are acquired with a GE train played within consecutive refocusing pulses [74]. Such sequence has also enabled the investigation of *MWF* in the human spinal cord in vivo in a recent publication [75], achieving improvement in tissue type separation as well as substantial acceleration

over a previous work [76].

2.2.3 Macromolecular Tissue Volume Imaging

Here we describe a technique aiming to estimate the fraction of macromolecular protons, called macromolecular tissue volume (*MTV*), via the quantitative mapping of the tissue proton density (*PD*).

When a quantitative *PD* map is normalized with a pure water signal reference (e.g. the signal from a voxel containing only CSF), so that it ranges between 0 and 1, the *MTV* is simply:

$$MTV = 1 - \frac{PD}{S_{ref}} \tag{2.34}$$

where S_{ref} is the reference signal used for normalization.

Many quantitative MRI techniques, especially those aiming to measure fundamental relaxation times, provide also a first approximation of the quantitative *PD*, via a parameter known as the apparent proton density PD_{app} (sometimes also called M_0). From a general point of view PD_{app} can be seen as:

$$PD_{app} = G\,PD\,R\left(T_1, T_2, T_2^*\right) \tag{2.35}$$

where G is the spatial *receiver profile* (or *receiver sensitivity* or *receiver gain*), and R models the residual effect of relaxation on PD_{app}, whose actual expression depends on the particular approach deployed. Usually R accounts for the transverse magnetization relaxation taking place between the excitation and the echo time, i.e. $R(T_1, T_2, T_2^*) = e^{-\frac{TE}{T_2}}$ or $e^{-\frac{TE}{T_2^*}}$, depending on whether the encoded signal is spin or gradient echo. The calculation of *PD*, and hence *MTV*, requires the inversion of equation 2.35, and therefore the measurements of relaxation times (T_2 or $T_2{}^*$), receiver coil profile and, subsequently, the selection of a tissue reference S_{ref}.

The main difficulty in extracting *PD* from equation 2.35 regards the separation from the receiver profile G, which is an ill posed problem [77]. Many methods are available for solving this problem, by exploiting different assumptions or a combination of them. These assumptions are: (*i*) the receiver sensitivity is smooth over the volume of interest, (*ii*) the biophysical relationship between *PD* and T_1, (*iii*) the additional information available by analysing coil channels separately. An evaluation of different approaches for *PD* estimation

is given in [77].

Here we briefly review a method that combines smoothness constraints and regularization of the solution through T_1 estimation [78].

The receiver sensitivity can be parametrized with a polynomial surface under the assumption that it is smooth in space. A 3D polynomial with order K can be used:

$$P(x,y,z) = p_0 + \sum_{i,j,k} p_{i,j,k} x^i y^j z^k \tag{2.36}$$

where i, j and k are non-negative and such that $i+j+k=K$. The smoothness constraint is not sufficient to solve for PD in equation 2.35, additional information is needed to regularize the solution. For example, an almost linear relationship between $\frac{1}{PD}$ and $\frac{1}{T_1}$ (as shown by [79, 80] amongs others) can be used to separate PD from G, through an iterative procedure [78]. This method in particular fits recursively the equations:

$$\begin{aligned} \frac{1}{PD_{app}} &= \frac{A}{T_1} + B \\ PD_{app} &= P(x,y,z)PD \end{aligned} \tag{2.37}$$

for voxels in selected regions of WM and GM (where the relationship has shown to be valid) until convergence of parameters A and B.

The applications of *MTV* in the spinal cord are to date very limited, with only a single study calculating and assessing the reproducibility of *MTV* in the spinal cord in vivo [81].

2.2.4 Diffusion-Weighted Imaging sensitive to myelin: radial diffusivity

Diffusion-weighted imaging (DWI) exploits the Brownian motion of water molecules due to their thermal agitation to produce contrast between tissues.

In a homogeneous medium in the absence of obstacles, water molecules diffuse in an isotropic manner with equal probability along any direction, resulting in an average displacement r over a period T_d given by:

$$< r >= \sqrt{6DT_d} \tag{2.38}$$

with D representing the diffusion coefficient (the intrinsic diffusivity of the medium).

However in biological tissues, the presence of different microstructural features, such as cell walls, membrane, myelin axon sheaths, etc., modifies the diffusion pattern of water

molecules impeding the pure isotropic behaviour described by equation 2.38. In the CNS diffusion is, indeed, rarely isotropic, with water molecules able to diffuse more preferentially along specific directions, such as along WM fibre tracts or perpendicularly to them in the extra-axonal space (*hindered* diffusion), or confined to move in closed spaces by physical barriers, such as inside impermeable cell walls (*restricted* diffusion). Such processes depend on the diffusivity of the medium as for Brownian motion, but also on the characteristics of the local environment on the scale of the mean displacement $<r>$. DWI hence represents a powerful MRI method to infer properties of tissue microstructure at a scale much smaller than imaging resolution.

The MRI signal can be made sensitive to the diffusion phenomenon within biological tissues. The most widely used sequence for diffusion MRI is the pulsed gradient SE (PGSE) sequence, introduced by Stejeskal *et al.* [82], shown in figure 2.11.

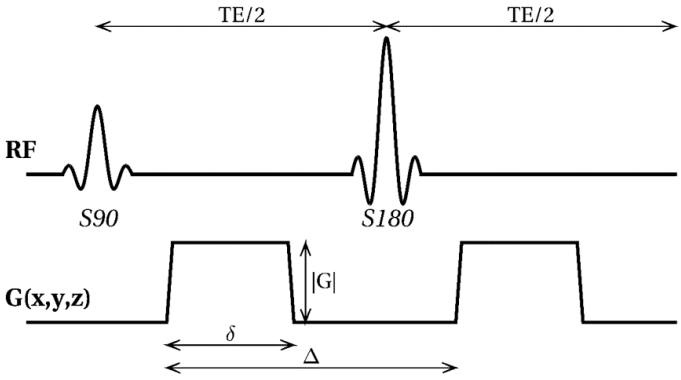

Figure 2.11: Basic pulse sequence for DWI. A pair of gradients are placed either side of the refocusing pulse of a *SE* sequence, to produce additional dephasing of the spins diffusing along the direction gradients are applied, while producing no net dephasing for static spins. The signal is usually acquired with ssh-EPI readout. Other than gradient direction, diffusion weighting is determined by gradient amplitude G, gradient duration δ and gradient interval Δ.

To obtain diffusion weighting, magnetic field gradients are applied along specific spatial directions **g**, causing a phase accrual at the time of sampling dependent on the applied gradient waveform **G**, and the displacement **r** exhibited by the spins over the time of the applied gradient. While for static spins, the phase accrual due to the second gradient would cancel out the one produced by the first one, in the case of diffusion spins experience different locations during the first and the second gradient lobes, which correspond to different phase accruals. The sum of the phase accruals over the whole spin ensemble in a voxel produces

a SE with reduced amplitude compared to when no diffusion gradients are applied. The diffusion time $T_d = \Delta - \frac{\delta}{3}$ is the time window during which the diffusion process is encoded by the pulse sequence, i.e. the time during which spins are allowed to explore and sense the surrounding before taking a measurement, and therefore defines scale of the microstructure environment probed by the DWI experiment.

The diffusion-weighted signal can be described by a variety of models. A broad classification can be made between the *phenomenological* models that capture the characteristics of the diffusion-weighted signal but do not parametrize the expression as a function of specific microstructural parameters, and the *biophysical* model where the diffusion-weighted signal is expressed as sum of contributions from different compartments described by a set of parameters that closely relate to microstructure tissue properties. In the following the theory behind the most famous phenomenological diffusion model, the diffusion tensor, is briefly described.

The simplest diffusion weighted model describes the diffusion-weighted signal as:

$$S\big(b, ADC\big) = S_0 e^{-bADC} \tag{2.39}$$

where $b = (\gamma\delta|G|)^2(\Delta - \frac{\delta}{3})$ is the b-value and measures the overall diffusion weighting strength, and ADC, the apparent diffusion coefficient, groups the effect of the diffusivity of the medium and the diffusion impedance caused by the interacting environment.

The model in equation 2.39 can be generalized to account for the spatial anisotropy of diffusion in ordered media such as WM in the CNS, where ADC is dependent on the direction $\mathbf{g}$ of the applied gradients, with the Diffusion Tensor Imaging (DTI) model [83].

In DTI, the description of ADC as a single scalar value is replaced with a full three-dimensional diffusion covariance matrix $\mathbf{D}$, the diffusion tensor:

$$\mathbf{D} = \begin{bmatrix} d_{xx} & d_{xy} & d_{xz} \\ d_{yx} & d_{yy} & d_{yz} \\ d_{zx} & d_{zy} & d_{zz} \end{bmatrix} \tag{2.40}$$

which is positive and symmetric by definition, i.e. d_{yx}=d_{xy}, d_{zx}=d_{xz} and d_{zy}=d_{yz}. Using the diffusion tensor, equation 2.39 becomes:

$$S\big(\mathbf{D}, b, \mathbf{g}\big) = S_0 e^{-b\mathbf{g}^T\mathbf{D}\mathbf{g}} \tag{2.41}$$

where **D** is defined in equation 2.40 and **g** is the gradient direction vector of dimension 3×1. As it can be seen straightforwardly for *ADC* in equation 2.39, also the elements of the diffusion tensor can be estimated using a log-transformation of equation 2.41, and acquiring a minimum of 6 diffusion weighted measurements with non-coplanar gradient directions. Usually more acquisitions are required to achieve a robust fit of the diffusion tensor elements [84, 85, 86].

The diffusion tensor can be decomposed into its 3 eigenvectors $\mathbf{v}_1$, $\mathbf{v}_2$ and $\mathbf{v}_3$, and related eigenvalues $\lambda_1 \geq \lambda_2 \geq \lambda_3$. From the eigenvalues and eigenvectors of the diffusion tensor a set of parameters can be extracted, which can be associated to tissue properties [87].

The eigenvector $\mathbf{v}_1$ that refers to the largest eigenvalues λ_1 is interpreted as the principal diffusion direction, with λ_1 know as the axial diffusivity (*AD*), as it corresponds to diffusivity parallel to WM axons.

Additional diffusion tensor metrics are:

$$MD = \frac{\lambda_1 + \lambda_2 + \lambda_3}{3} \tag{2.42}$$

$$FA = \sqrt{\frac{3}{2}\left[\frac{(\lambda_1 - MD)^2 + (\lambda_2 - MD)^2 + (\lambda_3 - MD)^2}{\lambda_1^2 + \lambda_2^2 + \lambda_3^2}\right]} \tag{2.43}$$

$$RD = \frac{\lambda_2 + \lambda_3}{2} \tag{2.44}$$

where *MD* is the mean diffusivity, *FA* is the fractional anisotropy, describing the degree of anisotropy diffusion in each voxel and therefore increasing when diffusion is highly directional, and *RD* is the radial diffusivity, describing the average diffusivity perpendicular to the principal diffusion direction. *RD* has gained particular interest as potential measure of myelin integrity in the CNS.

The interpretation of *AD* and *RD* in terms of radial and axial diffusivity is valid for a simplified microstructure scenario, where only a single fibre population is present within the image voxel, but becomes inaccurate in the case of more complex configurations such as crossing fibres or bending fibres. Moreover changes in pathology can produce significant changes in the shape of the diffusion tensor, making the interpretation of AD and RD as axonal and myelin integrity misleading, especially in the case of complex fibre configurations [88].

Nevertheless, in the spinal cord *AD* and *RD* have been used in a number of studies to in-

vestigate their association with pathological changes occurring in MS, such as axonal loss and demyelination. In particular *RD* has shown increases in demyelinating lesions in the ex-vivo multiple sclerosis spinal cord [89] and has been suggested as sensitive marker for demyelination, although the correlation was found to be less specific than previous studies on animal models [90].

It should be noted that the diffusion tensor model is based on the assumption of a Gaussian diffusion propagator (the diffusion propagator is the probability distribution of displacement of spins due to diffusion [91, 92]), which is not sufficient to describe the diffusion-weighted signal in the CNS when high b-values are used, necessitating the use of higher order terms proportional to powers of b. An example of such a non-Gaussian diffusion model is diffusion kurtosis imaging (DKI) [93].

2.2.5 Correction for magnetic field inhomogeneities

MRI heavily relies on the homogeneity of the both static and RF magnetic fields used. Inhomogeneities in the $\mathbf{B}_0$ and $\mathbf{B}_1(t)$ fields affect both signal localization and signal contrast. In quantitative MRI, field inhomogeneities have the additional detrimental effect of introducing errors in the calculated metrics.

Therefore, while for improving image quality it is essential to mitigate such inhomogeneities at the acquisition stage, in quantitative MRI their absolute measurement is also needed in order to allow correction terms to be introduced in the respective quantitative models.

The measurement of field inhomogeneity, in general indicated with the expression B_0 and B_1 mapping, represents a huge topic, for which we provide here below only a summary introduction.

2.2.5.1 B_0 mapping

B_0 mapping methods aim to measure the spatial distribution of the static magnetic field $\mathbf{B}_0(\mathbf{r})$. The observed B_0 inhomogeneities are mainly due to susceptibility-induced gradients arising from interfaces between different tissue types, or between tissues and air cavities, in combination with poor shimming procedures.

One of the most commonly used methods to calculate B_0 inhomogeneity consists of acquiring two gradient echo signals with slightly different *TE* values and relating their phase

difference to offsets in the main magnetic field ΔB_0, as follows [94, 95]:

$$\begin{aligned}\Delta\phi(\mathbf{r}) &= \phi(\mathbf{r})\Delta TE \\ &= 2\pi\gamma\Delta B_0(\mathbf{r})\big(TE_1 - TE_2\big)\end{aligned} \tag{2.45}$$

from which B_0 is simply obtained by inversion:

$$\Delta B_0(\mathbf{r}) = \frac{\Delta\phi(\mathbf{r})}{2\pi\gamma\big(TE_1 - TE_2\big)} \tag{2.46}$$

One of the main challenges of this technique is regarding the accuracy of the phase difference map $\Delta\phi(\mathbf{r})$ that needs to be pre-processed for phase unwrapping, in order to map phase variation from the $\big[-\pi,\pi\big]$ range, that would produce abrupt changes due to phase periodicity, to a linear space.

2.2.5.2 B_1 mapping

B_1 mapping methods aim to measure the spatial distribution of the active component of the RF field $\mathbf{B}_1(\mathbf{r})$. Such a field can be decomposed into a longitudinal component ($B_{1,z}$), and two counter rotating components in the transverse place ($B_{1,-}$ and $B_{1,+}$), among which the one rotating in the same direction as spin precess is responsible for the excitation of magnetization, and is therefore called the *active* field [96]. This component, referred to simply as the B_1 field in this thesis, relates to the excitation flip angle α through the known integral equation $\alpha = \gamma\int_0^\tau B_1(t')dt'$, and is the target of the mapping techniques briefly introduced in this section.

The B_1 varies according to several factors: size and shape of the object, its electric properties (tissue dieletric constant), the resonance frequency (for the RF wavelength effect), and the distance from the RF transmit coil.

There are several techniques available to measure the B_1 distribution in vivo, exploiting either the magnitude or the phase signal dependency on B_1 variations. There has been increasing interest on such applications in the recent years, in conjunction with the advent of ultra-high field systems (e.g. 7T), where field inhomogeneities are exacerbated. In the following, two of the most common methods to map the $\mathbf{B}_1$ field are briefly outlined. For a complete overview of different B_1 mapping approaches, with particular focus on challenges at ultra-high fields, the reference [97] is suggested.

Double Angle Method (DAM) The Double Angle Method (DAM), originally described in [96], is based on the ratio of the signal intensities of two SE images, I_1 and I_2, acquired with identical scan parameters but different nominal excitation angles, α_1 and α_2. By assuming $TR>5T_{1,\max}$ (where $T_{1,\max}$ is the longest T_1 of the object being imaged), and the proportionality between nominal flip angles, $\alpha_2=2\alpha_1$, then the flip angle distribution $\alpha_1(\mathbf{r})$ can be calculated as:

$$\alpha_1(\mathbf{r}) = \arccos \frac{I_2(\mathbf{r})}{2I_1(\mathbf{r})} \tag{2.47}$$

which inherently allows for the elimination of coil sensitivity through the signal intensities ratio.

The main disadvantage of the technique is regarding the prolonged scan time due to the condition $TR>5T_{1,\max}$. However, given the coarse resolution at which B_1 maps are typically acquired and its successful combination with multislice single-shot EPI readout [98], the DAM represents a common choice for in vivo B_1 mapping.

Actual Flip Angle Imaging (AFI) The Actual Flip Angle (AFI) Imaging technique [99] is based on differences of signal intensities of two images acquired with an interleaved scan. In particular, the method exploits the steady-state signal equation of a dual TR gradient echo sequence, where two excitations, with the same flip angle α, are interleaved by two different repetition times, TR_1 and TR_2. It can be shown (see the original paper [99] for the full derivation) that, when taking the first-order approximation of such an equation, the flip angle distribution $\alpha(\mathbf{r})$ can be calculated as:

$$\alpha(\mathbf{r}) = \arccos \frac{rn-1}{n-r} \tag{2.48}$$

where $r = \frac{I_2}{I_1}$ is the ratio of the two acquired signal intensities I_1 and I_2, and $n = \frac{TR_2}{TR_1}$ is the ratio of the two respective time intervals.

The accuracy of flip angle mapping using AFI depends on the ratio n, recommended to be such that $TR_2>5TR_1$, and the quality of the transverse magnetization spoiling at the end of each TR, suggested to be achieved via strong gradient spoiling (large spoiling gradients area) and appropriate phase increments of the RF excitations [100].

Chapter 3

Quantitative MRI of the spinal cord using reduced FOV imaging

As described in chapter 1, the spinal cord is key in the connection between the brain and the periphery of the body. Spinal cord damage or degeneration can have devastating consequences on cognitive and motor functions. It is therefore of high importance to be able to probe spinal cord microstructure, and quantitative MRI offers a highly powerful non invasive means of doing so.

At the same time, given spinal cord anatomical dimensions, reaching a diameter of 15 mm at its widest, and spinal cord location within the body, surrounded by CSF and in proximity to moving organs (e.g. lungs, heart), the development of robust quantitative MRI methods in the spinal cord is extremely challenging. Such challenges are well described in [6], and briefly reviewed here in the following.

The small spinal cord physical dimensions require the use of high resolution protocols to reliably depict spinal cord anatomical details (white matter and gray matter) in the transverse plane, resulting in long acquisitions. Therefore, most quantitative MRI techniques become excessively time-consuming or suffer from poor *SNR*.

The location of the spinal cord within the body makes it particularly susceptible to physiological noise deriving from respiratory motion and pulsatile flow, as well as to subject movements associated with breathing and swallowing, deteriorating quality and consistency over time of images used for quantification.

Finally, the proximity to lungs and the alternating interfaces between vertebral discs and bones produce an inhomogeneous B_0 field, with both static and dynamic variations reported [101, 102], resulting in space- and time- varying image artefacts (e.g. geometrical distor-

tions, apparent motion, signal dropouts a signal intensity variations).

As a result, development of quantitative MRI in the spinal cord lags heavily behind the brain, with a fairly limited number of studies in both healthy conditions and pathology, and poor standardization between approaches.

A great number of the studies that have attempted to quantitatively investigate spinal cord microstructure have used diffusion as contrast mechanism, leading to the use of various reduced FOV (rFOV) methods, necessary to acquire ssh-EPI images (which DWI relies upon) in the spinal cord (the next section 3.1 will quickly touch upon some of the most used rFOV methods).

In this chapter, we lay the foundation for a wider and more comprehensive investigation of spinal cord microstrucure in vivo using quantitative MRI. In particular, one of the imaging approaches previously used for DWI studies in the spinal cord, namely ZOOM-EPI, is revisited and further expanded to accommodate different types of MR contrasts to be acquired.

Although far from being complete and exhaustive, this chapter aims to delineate a framework to perform, in vivo, quantitative MRI in the spinal cord using the same base sequence. Similarly to EPI, often referred to as an *engine* to produce multiple contrasts in a time-efficient manner in the human brain, we propose ZOOM-EPI, a combination of EPI readout with an Inner Volume Imaging (IVI) strategy, as analogous in the spinal cord, underlining the importance of utilizing a unified imaging method to better understand and address spinal cord imaging challenges.

The chapter begins with a brief introduction to the most common rFOV methods. It then focuses on ZOOM-EPI, which is used extensively throughout this thesis, by reviewing its main characteristics and providing details of its implementation. The use of ZOOM-EPI to perform qMRI in the spinal cord in vivo is then introduced. In depth investigation of such techniques will be object of chapter 4 and chapter 5. Finally, the chapter concludes with some considerations to further improve the applicability of ZOOM-EPI in vivo, and potential future developments.

3.1 Overview of reduced FOV imaging methods

Reduced FOV imaging allows the acquisition of a small region within an object avoiding artefacts in the final reconstructed images.

Acquisition of small structures is often highly inefficient with normal *large* FOV methods, as the time effectively used to acquire the region of interest is only a small fraction of the time needed to complete the sampling of the remaining prescribed FOV. Longer acquisition times limit the temporal resolution of the MRI experiment, and increases the potential for physiological and motion related artefacts, as well as degradation from signal blurring and distortions induced by susceptibility effects (particularly when EPI readouts are used).

As pointed out before, magnetic susceptibility artefacts are accentuated in the spinal cord, and become unacceptable when sequences like ssh-EPI for DWI are used. Therefore, the use of rFOV methods, for a faster sampling of k-space, would greatly improve the image acquisition in the spinal cord.

However, when the structure of interest is embedded within other MR-visible tissue simply imaging a region smaller than the actual size of the object results in aliasing (or *foldover*, or *wraparound*) artefacts as the Nyquist criterion is not satisfied. rFOV methods alleviate this problem by exciting only the specific region of interest, i.e. the Inner Volume Imaging (IVI) methods [103], or by suppressing the signal arising from outside the FOV of interest with spatially selective saturation pulses before excitation [104, 105].

The main challenges involved with the use of rFOV methods are the intrinsic *SNR* reduction (due to smaller matrix and/or voxel size), and the ability to avoid aliasing without introducing too many constraints on the sequence, e.g. in terms of power deposition, coverage, and acquisition time. An exhaustive comparison between multislice rFOV methods, implemented on a 7T scanner, can be found in [106] (although it should be noted that the specific implementation of rFOV methods can vary considerably among scanners and vendors).

Given the anatomy of the spinal cord, which enables significant FOV reductions cross-sectionally, rFOV methods are particularly well suited for spinal cord imaging, and have indeed been exploited for developing quantitative MRI protocols in the spinal cord, especially for DWI.

In the rest of this section, two of the most widespread rFOV modalities used in the spinal cord are described. The core of the chapter instead is dedicated to the rFOV technique used in this thesis, namely ZOOM-EPI, and its use to carry out quantitative MRI experiments in the spinal cord.

3.1.1 Reduced FOV imaging with outer volume suppression pulses

Outer Volume Suppression (OVS) based rFOV methods utilize a set of spatially selective pulses followed by dephasing gradients to null the signal arising from outside the FOV of interest. Effective OVS methods require complete dephasing of transverse magnetization and complete nulling of longitudinal magnetization by the time excitation is performed. The OVS pulses are therefore placed before each slice excitation (see figure 3.1b) and target both sides of the FOV in *P* direction, to suppress signal from unwanted regions.

The design of the OVS pulses can be optimized to achieve simultaneous B_1 and B_0 insensitivity, in order to produce the desired tipping angle in well-defined spatial locations, even in the presence of inhomogeneous B_0 field, as well as robustness over a range of different T_1 values. Optimization of OVS pulses for rFOV DWI of the spinal cord in vivo using ssh-SE-EPI (including a fat suppression module) can be found in [107, 108], amongst others.

As it will be further described later in this chapter, one of the main limitations of the approach regards the lack of flexibility in the design of quantitative protocols, other than those based on diffusion. OVS pulses, in fact, introduce constraints on the minimal time interval between consecutive slices (e.g. in [107] the minimum slice spacing achievable was 750 ms), and are demanding in terms of SAR, thus reducing the possibility of using additional magnetization preparation pulses, e.g. off-resonance saturation pulses to generate MT weighting.

3.1.2 Reduced FOV imaging with 2D RF excitation pulses

rFOV imaging can be accomplished also through the use of two-dimensional spatially selective RF excitation pulses which excite the magnetization along the slice direction in addition to selecting a limited region in the phase encoding direction.

The 2D excitation volume of such pulses can be designed using the excitation *k*-space formalism, devised in [109], where the RF excitation profile results from the Fourier transform of a function dependent on the B_1 profile and a *k*-space trajectory (the most common are echo-planar and spiral) defined by gradient waveforms in the *S* and *P* directions played out during the excitation pulse (see figure 3.1c).

Using the excitation *k*-space formalism it can be shown, for instance, that long RF excitation pulses ($\sim$20-30 ms) are needed to obtain selection profiles with sharp edges, and that the excitation profile is periodic in space, i.e. it produces side excitation lobes.

The main advantages of a 2D RF excitation to perform rFOV imaging are the reduced

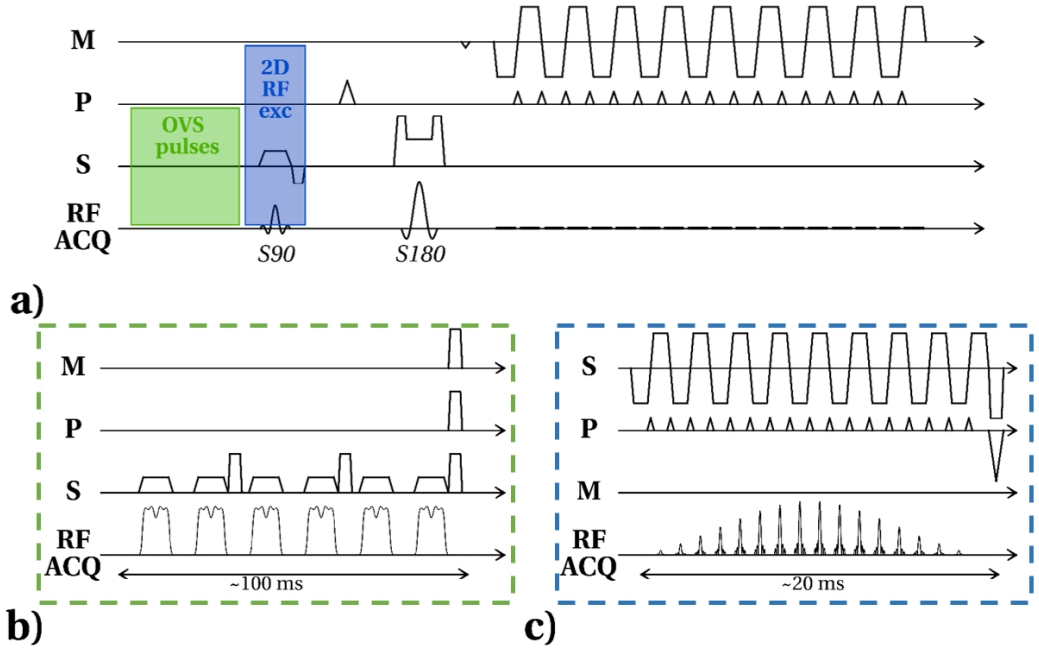

Figure 3.1: (**a**) The majority of the rFOV methods adopted for in vivo imaging of the spinal cord are based on the ssh-SE-EPI sequence used in DWI. (**b**) OVS based methods modify ssh-SE-EPI by using a set of spatially selective satuaration pulses prior to each slice excitation. Number of pulses, pulse amplitude, time intervals and bandwidth are optimized in order to null outer volume signal at the time of slice excitation. OVS preparation length is around 100 ms. (**c**) 2D RF excitation method replaces normal 1D excitation with spatially selective pulses in 2 orthogonal dimensions, while the refocusing pulse remains a standard 1D pulse. A 2D echo-planar RF pulse is shown in the figure. Pulse duration is dependent on the number of blips in the *P* direction. Usually these type of pulses last around 20-30 ms.

energy deposition, their flexibility to be incorporated into a wide range of sequences compared to other approaches (e.g. OVS based methods), and the reduced acquisition time, as multislice imaging can be performed without requiring interleaved schemes (which is instead needed with ZOOM-EPI described in the next section). Additionally, when using 2D echo-planar RF pulses, the excitation profile of the fat can be shifted in such a way that it is completely outside the excited water profile [110]. Such advantages are however subject to compromises at the RF design stage. For the case of 2D echo-planar RF pulses, both displacement between periodic lobes in the *S* direction and displacement between water and fat excitation profiles depends on the number of blip gradients along the *P* direction (i.e. the RF pulse duration), with longer pulses improving both separations. The obvious drawback of long RF excitation pulses is an increase in *TE*. Theoretical considerations regarding compromises in designing 2D RF pulses for inner volume excitations, together

with a solution to improve their applicability for large coverage in vivo applications can be found in [111].

3.2 Zonally Magnified Oblique Multislice Echo Planar Imaging: ZOOM-EPI

Zonally-magnified oblique multislice (ZOOM-) EPI [112, 113, 114] is a rFOV method based on a multislice ssh-SE-EPI sequence, in which slice excitation (*S90*) and slice refocusing (*S180*) pulses are not collinear but tilted by an angle ϑ in the plane defined by the *S* and *P* directions.

For the following chapters in this thesis (chapter 4 and chapter 5), the ZOOM-EPI sequence used is implemented with *S90* tilted with respect to *S180*, which is normally applied along the prescribed *S* direction, although the reverse implementation (oblique *S180*) is equally valid.

Oblique slice excitation is achieved by switching gradients in both the *P* and *S* directions simultaneously with *S90*. Beyond this feature, ZOOM-EPI is identical to a ssh-SE-EPI sequence (see figure 3.2).

By doing so, the extension of the area effectively refocused in the *P* direction is reduced,

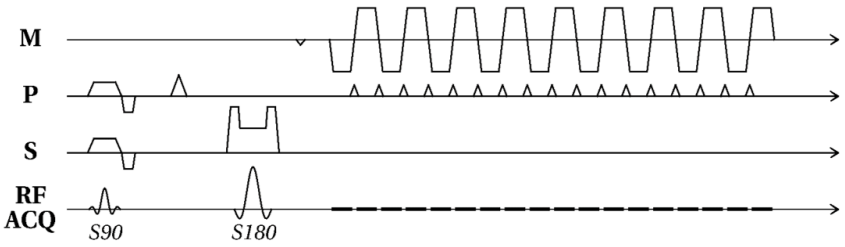

Figure 3.2: Pulse sequence diagram of ZOOM-EPI. The sequence is identical to a ssh-SE-EPI where a single EPI echo train is used to sample the k-space after a slice selective excitation/refocus pulse pair. Oblique slice excitation (*S90*) is achieved by simultaneous gradient waveforms along the *P* and *S* directions. As a result the extension of the fully-refocused area along *P* direction is reduced, allowing a shorter EPI echo train (for the same resolution).

and consequently is the minimum size of the FOV to sample to avoid aliasing artefacts.

In particular, the non-collinear excitation/refocusing results in a fully refocused rectangle, the inner volume (*IV*), straddled by two partially refocused regions, the transition bands (*TB*s). To avoid signal from the *TB*s folding over within the *IV*, the *TBs* also need to be

encoded in the *P* direction. As these are discarded after reconstruction to produce images of only the *IV*, the minimal (and hence optimal) FOV in *P* direction includes half of the *TB* on both sides of the *IV*, to allow wraparound of the reconstructed image only on the remaining half *TBs*, while keeping the *IV* clean.

The tilted *S90* affects the magnetization of the neighbouring locations, but leaves slices sufficiently far away unaffected, depending on the tilting angle ϑ and the extension of the *IV* in the *P* direction. Therefore multislice imaging can be performed by arranging the slice order in such a way that slices far apart in space are acquired sequentially, while contiguous (in space) slices are sampled with a time interval long enough to allow magnetization to recover to its equilibrium value following *S90*. The stack of slices is thus divided into *packages* (i.e. group of maximally spaced locations in the *S* direction), with each package acquired within a sequence repetition time. The *TR* is therefore subject to a constraint on longitudinal magnetization recovery, i.e. $TR > 5T_1$, where T_1 refers to the longitudinal relaxation time of the tissue of interest.

From this point of view, ZOOM-EPI can be seen as an inner volume SE sequence [103] with multislice capabilities, where an acceleration factor along the *S* direction is gained at the expense of a longer EPI echo train for the same resolution and *IV*, as part of the *TB*s need to be sampled (see figure 3.3).

In practice, the sequence is fully defined once the *IV* (extension of the FOV of interest along the *P* direction) and the number of packages N_{pkg} are chosen. This represents the most straightforward way to plan such a sequence as the user can directly control the geometry (FOV of interest and number of slices N_{s}) and the protocol duration (N_{pkg} is the number of packages or, equivalently, the number of *TR* periods needed to cover the prescribed stack of slices, see also equation 3.8), without knowing the details of the sequence implementation: the tilting angle ϑ and the extension of *TB*.

Using figure 3.4 as guidance, once the user defines the size of the *IV* (L_{y} in figure 3.4), slice thickness Δz, slice gap Δs, and N_{pkg}, then ϑ follows the relation:

$$\tan\vartheta = \frac{L_y}{\Delta z\left(N_{pkg}-1\right)+\Delta s N_{pkg}} \tag{3.1}$$

producing *TB*s whose extension is:

$$TB = \Delta z \tan\vartheta = \frac{L_y}{\left(N_{pkg}-1\right)+\frac{\Delta s}{\Delta z}N_{pkg}} \tag{3.2}$$

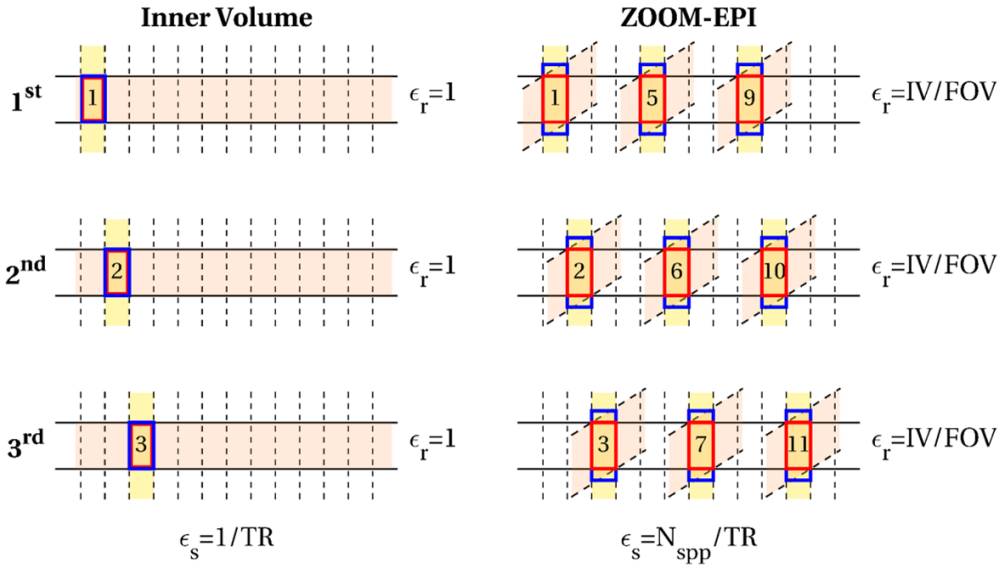

Figure 3.3: Inner volume imaging (on the **left**) where S90 and *S180* are played out on perpendicular axes, and ZOOM-EPI (on the **right**) where *S90* is oblique compared to *S180*. IVI is efficient in terms of readout (readout efficiency ϵ_r=1) as the encoded *FOV* in the *P* direction (**blue** box) equals the *IV* (**red** box), i.e no oversampling is needed. However, only a single slice per sequence repetition can be acquired, resulting in poor overall sequence efficiency $\epsilon_s=\frac{1}{TR}$. On the other hand, ZOOM-EPI has a less efficient readout as *TB*s need to be encoded for imaging the *IV* (resulting in $\epsilon_r=\frac{IV}{FOV}$), but allows more efficient multislice imaging as an entire package can be acquired per sequence repetition, giving $\epsilon_s=\frac{N_{spp}}{TR}$, where N_{spp} indicates the number of slices per package.

Once *TB* is known, the amount of oversampling K_y needed in the *P* direction is readly given by:

$$K_y = \frac{N_y^{ext}}{N_y} = \frac{\frac{L_y^{ext}}{\Delta y}}{\frac{L_y}{\Delta y}} = \frac{L_y^{ext}}{L_y} = \frac{IV + \frac{TB}{2} + \frac{TB}{2}}{IV} = 1 + \frac{TB}{L_y} \tag{3.3}$$

where Δy is the voxel size along the *P* direction, N_y is the number of phase encoding steps (acquired matrix size in the *P* direction) for the *IV* (L_y defined by the user), and N_y^{ext} is the number of phase encoding steps necessary to sample the extended FOV comprising the half *TB*s on both sides (i.e. the minimum extension for the sampled FOV in the *P* direction). Combining equations 3.1 and 3.3, the oversampling factor K_y becomes:

$$K_y = 1 + \frac{1}{\left(N_{pkg} - 1\right) + N_{pkg}\frac{\Delta s}{\Delta z}} \tag{3.4}$$

If no gap is set between slices, equations 3.2 and 3.4 simplify to the following:

$$TB = \frac{L_y}{N_{pkg} - 1} \tag{3.5}$$

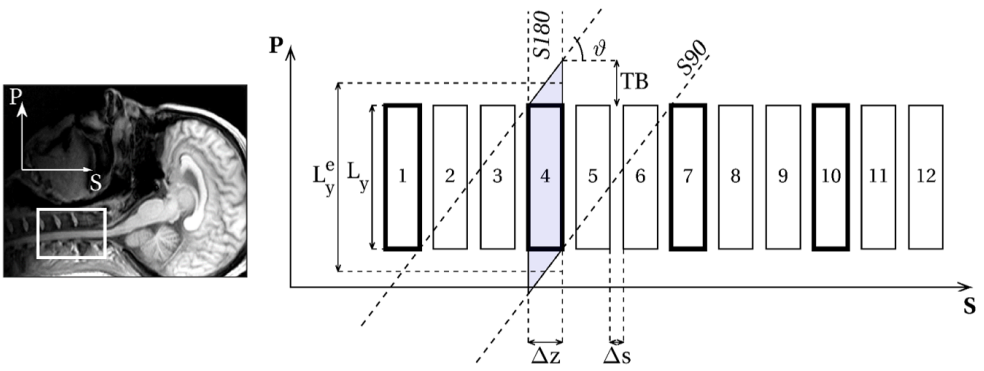

Figure 3.4: ZOOM-EPI for rFOV imaging of the spinal cord. The *P* direction is usually associated with the Anterior-Posterior direction, while the *M* direction is associated with the Left-Right direction. Slices belonging to the first package (1,4,7,10) are shown in **bold**. Once N_{pkg}, Δz, Δs, and L_{y} (the *FOV* along the *P* direction) are known, the tilting angle ϑ can be calculated and, hence, the size of the *FOV* that needs to be sampled along the *P* direction, L_{y}^{e}. Acquisition of subsequent packages must allow for magnetization recovery of partially excited contiguous slices, e.g. slices 2,3,5,7 in the figure. This is controlled by the *TR*, constrained to be $TR > 5T_1$.

$$K_y = 1 + \frac{1}{N_{pkg} - 1} \tag{3.6}$$

where K_{y} is only dependent on N_{pkg}. For example, if the stack of slices is split into 3 packages, fold-over artefacts are avoided by sampling 50% more than the FOV of interest in the *P* direction.

Figure 3.5 shows some examples of ZOOM-EPI images acquired in the spinal cord with N_{pkg}=3 and 4, together with a structural T_2^*-weighted GE scan and the *SNR* distribution, calculated within the cord, for both ZOOM-EPI scans.

It can be appreciated from visual inspection of figure 3.5, that typical geometrical distortions affecting ssh-EPI readout are kept within acceptable levels despite the use of high in-plane resolution, thanks to the use of ZOOM-EPI. N_{pkg} becomes a crucial parameter affecting: (*i*) EPI train length (see equations 3.6 and 3.4), and hence entity of geometrical distortions, quantified by equation 2.18; (*ii*) image *SNR* via the acquired matrix size and the *TE*, and (*iii*) total acquisition time, given by $TR \times N_{pkg}$. While the optimal N_{pkg} should be identified for each specific application, as a rule of thumb N_{pkg}=3 appears to be the best compromise between resolution, distortions and total scan time, for axial resolutions up to 0.75×0.75 mm^2 and $FOV \sim 5$ cm in the *P* direction.

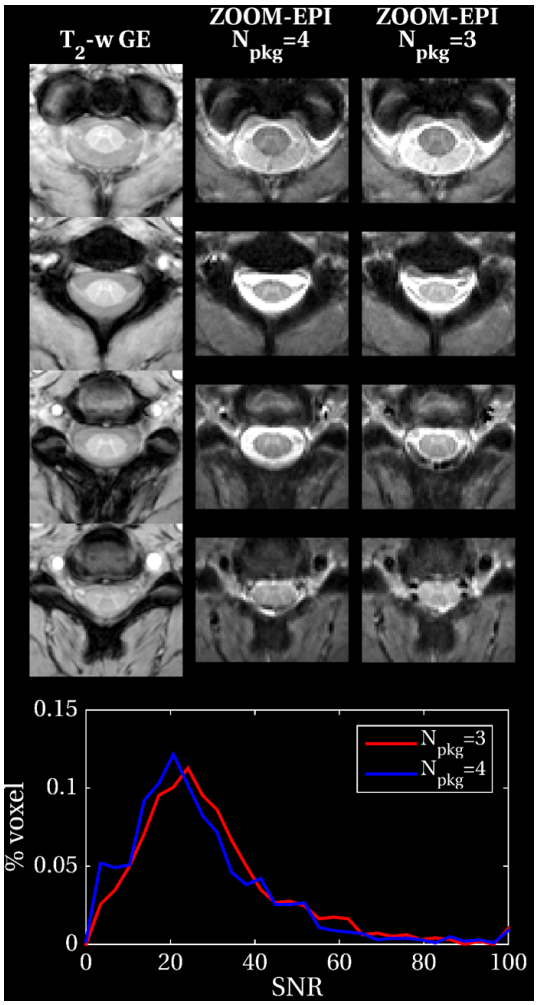

Figure 3.5: Examples of ZOOM-EPI images acquired in vivo in the cervical spinal cord, at different levels. From **left** to **right**: high resolution ($0.58\times0.58\times5$ mm^3 resolution) $T_2{}^*$-weighted scan, ZOOM-EPI with N_{pkg}=3 (EPI train length=77, total acquisition time=39 sec) and ZOOM-EPI with N_{pkg}=4 (EPI train length=69, total acquisition time=52 sec). ZOOM-EPI acquisition parameters are: *TR*=6500 ms, *TE*=27 ms, Partial Fourier factor=0.6, *FOV*=64×51 mm^2 at $0.8\times0.8\times5$ mm^3 resolution,N_s=12, receiver bandwidth=216 kHz, signal averages=2. The **bottom** panel shows the *SNR* distribution calculated voxelwise inside the cord from 5 repetitions of the same acquisition for ZOOM-EPI with N_{pkg}=3 (in **red**) and N_{pkg}=4 (in **blue**).

3.3 Using ZOOM-EPI for quantitative MRI in the spinal cord

The ZOOM-EPI sequence described in the previous section provides a means to perform ssh-EPI imaging in the spinal cord. In particular, it enables relatively high in plane resolution (data to be acquired with sub-millimetre voxel size, as required by spinal cord anatomical size) while keeping geometrical distortions, typical of EPI readout, limited as the EPI echo train is shortened following the non-collinear *S90*/*S180* pulse pair (see figure 3.5 for some examples).

Single-shot imaging may represent a preferable approach for the spinal cord, given its intrinsic sensitivity to physiological noise (e.g. cardiac pulsation, breathing and subject motion). However, as for a conventional EPI readout, ZOOM-EPI is subject to the same compromises between highest achievable resolution, geometrical distortions and resulting *SNR* to perform quantitative analysis.

The anatomy of the spinal cord, fairly uniform along the foot-head direction, allows the use of relatively large slice thickness to counteract the loss of *SNR* due to using high axial resolution. Typical protocols use Δz from 3 to 5 mm (or even more [115]), with in plane resolution ranging between Δx=Δy=0.7-1 mm.

The main differences compared to the conventional ssh-SE-EPI sequence is with regard to the slice coverage. In particular, the same temporal resolution (time to acquire the whole set of slices, in other words the conventional *TR*) can not be achieved. In ZOOM-EPI, the whole set of slices is acquired over a number (N_{pkg}) of *TR* periods, as contiguous slices are affected by non collinear SE pulses (see figure 3.3). As mentioned in the previous section, the choice of N_{pkg}=3 is common in quantitative protocols using ZOOM-EPI as readout and is dictated by the need to limit scan time, which is linearly dependent on N_{pkg}, while effectively reducing the FOV, and hence distortions, in the *P* direction (oversampling of 50% compared to a 100% oversampling with N_{pkg}=2). The choice of N_{pkg} as well as resolution and coverage is however dependent on the particular application, as suggested hereafter.

Due to the the package grouping of the slice stack with ZOOM-EPI, quantitative protocols utilizing this sequence will in general have a rather limited coverage in the-foot head direction, in part overcome by the use of relatively thick slices. An alternative solution to improve the slice coverage is presented in section 3.4.3.

EPI, in particular ssh-EPI, has found widespread applications for quantitative MRI, as it allows to take *snapshot* of the anatomy of interest, with high temporal resolution and with different contrasts (a variety of preparation pulses can be placed in front of the readout). Similarly, we suggest the use of ZOOM-EPI as a unified signal readout to perform quantitative MRI in the spinal cord. The ZOOM-EPI sequence reviewed in this chapter allows the translation, to the more challenging imaging environment of the spinal cord, of the quantitative MRI approaches based on EPI that have been extensively used in the brain.

Here, the use of ZOOM-EPI to obtain different MRI contrasts for quantitative applications in the spinal cord is briefly introduced. Figure 3.6 provides an overview of the use of the

same base readout, ZOOM-EPI, to obtain: (*i*) diffusion-weighted data, (*ii*) inversion recovery data, and (*iii*) MT-weighted data. Details of the full development of inversion recovery and quantitative MT protocols in the spinal cord are given in chapters 4 and 5 respectively.

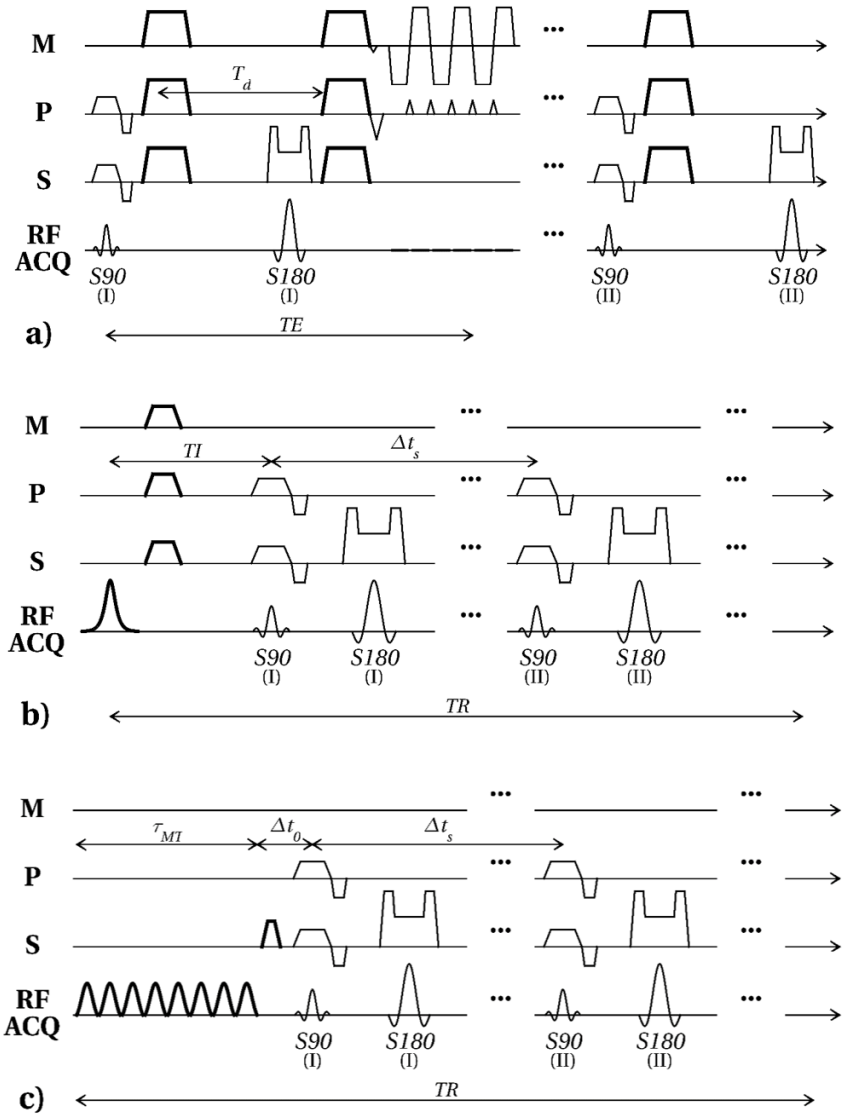

Figure 3.6: quantitative MRI with ZOOM-EPI. (**a**) Diffusion-weighted imaging. Diffusion gradients are placed on both sides of the *S180* pulse as for standard diffusion-weighted SE-EPI. (**b**) Inversion Recovery with ZOOM-EPI. An inversion pulse is played out every *TR* to perform global inversion at the beginning of every package acquisition. Slices within the same package (*I*, *II*, ...) are acquired sequentially following inversion producing a range of different inversion times (depending on *TI* and Δt_s). (**c**) MT-weighted ZOOM-EPI sequence. A train of off-resonance pulses is played out every *TR* prior to the acquisition of each package. The overall MT weighting is dependent on the off-resonance saturation period τ_{MT}, its RF power and frequency offset, and slice time intervals Δt_0 and Δt_s. For both IR and MT-weighted sequences, the *TR* is prolonged by a *recovery* time to allow longitudinal magnetization to recover before the subsequent global inversion or off-resonance saturation.

3.3.1 Diffusion weighted imaging

The main previous application of ZOOM-EPI is for DWI.

Currently, DWI still heavily relies on ssh-SE-EPI. ZOOM-EPI therefore represents one of the most natural and preferable approaches for performing DWI in the spinal cord [116].

Diffusion sensitization is obtained by inserting diffusion weighting gradients on both sides of *S180* as for a standard SE-EPI (figure 3.6a).

Such applications will not be covered in this thesis. Interested readers should refer to [113] for pioneering work on diffusion tensor imaging (DTI) in the spinal cord, [117] for application to more advanced diffusion models, in particular neurite orientation dispersion and density imaging (NODDI), and [118] for a recent application of the sequence for DTI at the lumbar level of the spinal cord.

3.3.2 Inversion Recovery

T_1 mapping of the spinal cord can be accomplished using ZOOM-EPI as readout of an IR protocol (figure 3.6b).

A non-spatially selective inversion pulse can be placed at the beginning of each package, exploiting the inherent constraint $TR >> T_1$, and the sequence repeated at different delays, *TI*, to sample the recovery of longitudinal magnetization towards equilibrium following the inversion. Full recovery must be ensured between global inversions. This is achieved by extending the *TR* by an adequate recovery time, T_{rec}, defined as the time interval between the last slice excitation in the package and the subsequent inversion pulse.

An efficient use of the sequence shown in figure 3.6b is presented in chapter 4 where the IR-ZOOM-EPI sequence is described in detail, validated and applied to the healthy spinal cord.

3.3.3 Magnetization Transfer weighted imaging

Similarly to the IR protocol, MT-weighted acquisition can be performed by combining trains of off-resonance pulses with multislice ZOOM-EPI readouts (figure 3.6c). For more time-efficient protocols, a train of pulses should be placed in front of each package in order to exploit the inherently long *TR* of the ZOOM-EPI sequence and introduce MT weighting without substantially increasing the protocol duration.

MT-weighted acquisitions with EPI readouts have not been thoroughly investigated so far. Only a few studies are available in the literature [119, 120], as MT experiments are usually performed with 3D readouts. The use of a shared preparation train with a multislice readout

in fact poses additional challenges compared to a more standard solution (i.e. MT-weighted spoiled GE). These challenges include: (*i*) a variable amount of MT weighting in different locations according to the order in which slices are acquired with following the train of pulses, (*ii*) potential contamination from on-resonance excitation (*S90*/*S180* pulse pairs) which is, in turn, an additional source of off-resonance saturation for the other slices, (*iii*) the lack of steady-state for the MT weighting, when the duration of the train of pulses is shortened to limit protocol duration. How these challenges are accounted for is specific to the particular application being considered.

In this thesis, a qMT protocol using ZOOM-EPI is devised and applied to the healthy spinal cord. This is fully described in chapter 5, which comprises sections detailing the sequence development, signal modeling, protocol optimization, simulations and in vivo acquisition. An application for *MTR* measurements in the spinal cord is instead described later on this chapter, in section 3.4.2.1. Potentially the same sequence as shown in figure 3.6c could be employed to perform chemical exchange saturation transfer (CEST) studies in the spinal cord, although such an application will not be covered in this thesis.

3.4 Potential and limitations of ZOOM-EPI

In this section we discuss the combination of the ZOOM-EPI sequence with some of the most widely used solutions to accelerate data acquisition or improve data consistency in quantitative MRI, namely parallel imaging, cardiac triggering and simultaneous multislice imaging.

While far from being exhaustive, this section aims, through a few examples of techniques that can already be incorporated into the ZOOM-EPI sequence or that need further development or adaptation, to provide a better understanding of the potential and the current limitations of ZOOM-EPI to carry out quantitative MRI examinations in the spinal cord in vivo.

3.4.1 Parallel imaging

From a data acquisition point of view, rFOV methods and parallel imaging methods (see section 2.1.4) work in the same way: they reduce the density of the k-space sampling for a given resolution. The main difference lies in how they deal with the aliasing that arises when data are undersampled: rFOV methods suppress or avoid effectively exciting the signal in portions of the object that would cause aliasing; parallel imaging methods apply dedicated

reconstruction pipelines to resolve the aliasing in the acquired data.

The combination of parallel imaging with rFOV could allow a further reduction in the read-out duration, to produce even higher resolution images (provided that the resulting *SNR* supports subsequent quantitative analysis). The advantages and the feasibility of such combinations must be evaluated on a case specific basis. Here, we briefly discuss the combination of ZOOM-EPI introduced above with the SENSE parallel imaging method described in section 2.1.4.1.

In ZOOM-EPI, foldover artefacts are allowed to occur in portions of the *TB*s (which are subsequently discarded after reconstruction). Full FOV images, therefore, contain already aliased pixels. As pointed out in [121], in these cases the SENSE reconstruction fails to unfold the acquired images, if additional aliasing is introduced by the parallel imaging approach. This can be better appreciated by taking equation 2.19 and adapting it for the case of ZOOM-EPI where some pixels (belonging to the *TB*s) are folded into the full FOV image, as follows:

$$\begin{aligned} I_1 &= S_{1,1}\rho_1 + S_{1,2}\rho_2 + S_{1,3}\rho_3 \\ I_2 &= S_{2,1}\rho_1 + S_{2,2}\rho_2 + S_{2,3}\rho_3 \\ &\dots \\ I_N &= S_{N,1}\rho_1 + S_{N,2}\rho_2 + S_{N,3}\rho_3 \end{aligned} \tag{3.7}$$

which describes the particular case of the folding equations of a pixel in the *TB*, when SENSE with acceleration factor R_{PI}=2 is used in conjunction with ZOOM-EPI.

Reconstruction will produce artefacts as the additional folding is not recognized, meaning that the unfolding matrix used to solve the system will not have the correct dimensions. This results in a residual aliasing artefact occurring predominantly in the middle of the image.

An example is given in figure 3.7, where ZOOM-EPI data on a phantom acquired without and with increasing SENSE acceleration factor are shown.

In this thesis, methods to allow the combination of ZOOM-EPI with SENSE parallel imaging have not been explored. However, potentially viable solutions are: (*i*) the encoding of the entire *TB*s to avoid aliasing in the full FOV images; (*ii*) the use of a fictitious higher acceleration factor R_{PI} in the reconstruction for those pixels belonging to the *TB*, which need to be recognized at the reconstruction stage, (*iii*) the use of *apparent* coil sensitivity, to build the unfolding matrix (i.e. the pseudo-inverse of $[\mathrm{S_{i,j}}]$ in equation 3.7), that provides

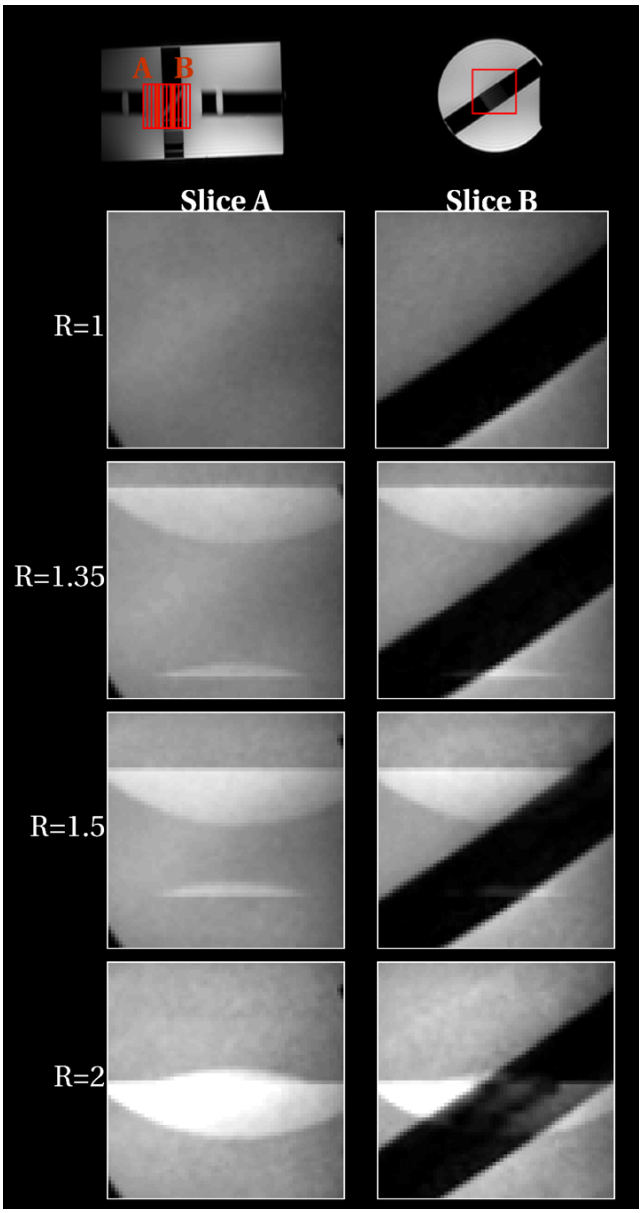

Figure 3.7: Residual aliasing artefact in reconstructed images when SENSE is used in conjunction with ZOOM-EPI. Two example slices of a multislice ZOOM-EPI acquisition on a structural phantoms are shown. Data are acquired at increasing SENSE acceleration factor R_{PI}. From **top** to **bottom**, R_{PI}=1 (no SENSE), 1.35, 1.5 and 2. The SENSE artefact can be appreciated when $R_{PI}>1$, with unaliased pixel intensities *moving* towards the center of the image as R_{PI} increases.

spatial encoding information for aliased pixel values in the full FOV images. These could be obtained by dividing aliased coil images with an aliased image from the body coil, which is assumed to have uniform sensitivity [121].

While the combination of ZOOM-EPI and SENSE could be useful to achieve higher in-plane resolution without worsening geometrical distortions, from a practical point of view

it is essential to consider the *SNR* penalty associated with a further readout acceleration (through the SENSE *g*-factor). Given the already limited *SNR* of ZOOM-EPI data (e.g. *SNR*$\sim$10-15 for a b_0 image at *TE*=71 ms, to accommodate *b* values up to 2800 mm s^{-1}, with $1\times1\times5$ mm^3 voxel size at 3T [117]), and the limited development of dedicated receiver coils for spinal cord applications, only a low acceleration factor (e.g. $R_{PI}<2$) may be feasible in quantitative studies, at least at 3T.

3.4.2 Cardiac gating

As the spinal cord is surrounded by slow-moving CSF, spinal cord protocols may benefit from triggered acquisition schemes. CSF flow in the foot-head direction corresponding with the cardiac cycle and dynamic B_0 field fluctuations with the respiratory cycles represent the two main sources of physiological noise corrupting image quality in the spinal cord. For a complete characterization of the dynamic B_0 changes induced by the respiration at various level of the cervical spinal cord, the reader is directed to the following references [101, 102]. In this section instead, we will only investigate solutions to synchronize the ZOOM-EPI readout with the cardiac cycle for quantitative MRI in the spinal cord.

DWI is particularly sensitive to artefacts arising from CSF flow, which are exacerbated in the spinal cord [122]. Cardiac triggering for DWI in the spinal cord has been proposed as a standard approach since the earliest works [113]. Diffusion-weighted ZOOM-EPI is fully compatible with cardiac triggering, as shown in figure 3.8. Each *shot* of diffusion-weighted ZOOM-EPI is triggered by the detection of a QRS complex, for example by a peripheral device. A *shot*, comprising of fat suppression module, diffusion weighting gradients and EPI readout, can easily fit within the R-R interval for a wide range of physiological heart rates, given the relatively short duration of the *active* part of the diffusion weighted ZOOM-EPI sequence (e.g. *shot* duration for *b*=2800, with 1×1 mm^2 in plane resolution with fat suppression module is $\sim$140 ms). This results in more robust triggering compared to other approaches, such as OVS sequences where the *shot* duration can be up to 750 ms [107], allowing image slices to be acquired in the same period of the cardiac cycle, which can be tuned (empirically) to match the quiescent part of the CSF flow pattern, by adjusting the trigger delay window. The inevitable consequences of gated acquisitions are variable protocol duration (dependent on the subject heart rate), and proneness to protocol lengthening due to skipped signal detection.

The adjustment of the IR and the MT-weighted sequences to cardiac gated acquisition is

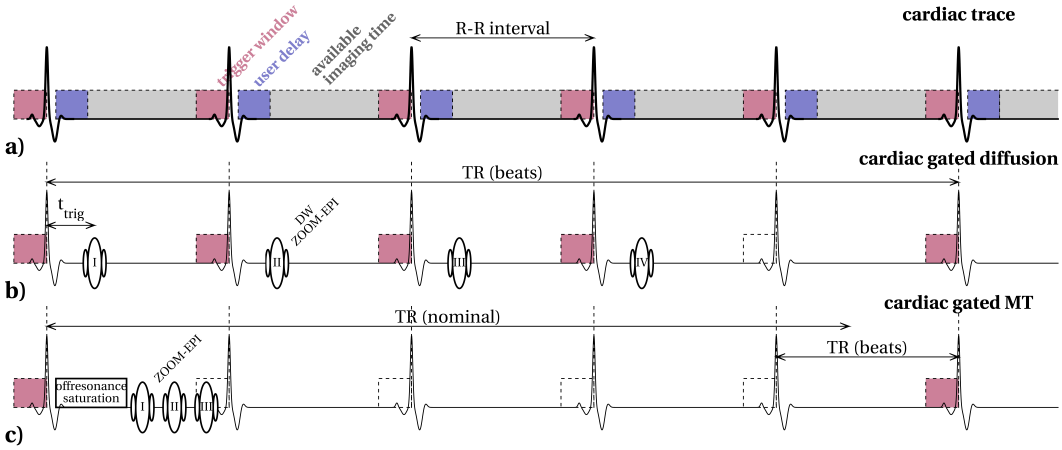

Figure 3.8: Strategies to trigger ZOOM-EPI with cardiac cycle for quantitative MRI in the spinal cord. (**a**) The cardiac trace is acquired by a peripheral device. The detection window, shown in **red**, is open for a percentage of the R-R interval to allow the detection of a valid QRS complex. Once an R wave is detected, imaging can be performed (available imaging time is shown in **grey**). The start of the MRI sequence can be adjusted by inserting an adequate trigger delay time (shown in **blue**), to ensure imaging is performed in the quiescent part of the cardiac cycle. (**b**) cardiac triggered ZOOM-EPI for DWI. By selecting a *TR* (in number of cardiac cycles) long enough ($TR > N_{spp}$, a ZOOM-EPI *shot* can be performed per each cardiac cycle, ensuring robust gating of diffusion-weighted images. (**c**) MT-weighted ZOOM-EPI can be cardiac-gated by forcing a *shot* to last over multiple cardiac cycles. However, the *active* part of the sequence (off-resonance train and slice acquisition) is designed to fit within a single R-R cycle (calculated on the worst case scenario) so that imaging is empirically constrained within the quiet segment of the cycle.

less straightforward than DWI, due to the use of *shared* preparation pulses that act over a set of slices (the package), for which it is important to maintain the precise timing for quantification purposes (see figures 3.6b and 3.6c).

In general IR protocols are rarely combined with a triggered acquisition. The need to sample *TI*s of the order of hundreds of milliseconds to accurately estimate the T_1 complicates the design of efficient triggered schemes (such applications are mostly considered in cardiac MRI where the needs for gated acquisitions are obvious). In this thesis, a triggered version of the IR-ZOOM-EPI sequence will not be considered.

For similar reasons, MT-weighted acquisitions have rarely been combined with cardiac gating, as a variable *TR* resulting from an acquisition triggered with the cardiac cycle will produce variable contrast and will make the correct interpretation of the resulting MT effect in a quantitative setting non trivial. Retrospective data gating has been explored in a pioneering work on ihMT in the spinal cord [67], however such an application suffers from limited spatial coverage in order to collect enough data to robustly correct for the *TR* varia-

tions during the acquisition.

The MT-weighted sequence proposed in figure 3.6c, where the MT preparation is separated from data readout, allows a more flexible implementation of a triggered acquisition, which could be helpful for spinal cord applications. As the timing between off-resonance train of pulses and slice excitation, and timing among slice excitations within the package have to be fully controlled (either for a qMT experiment or for ensuring reproducible MT weighting in different locations), the whole *active* part of the sequence has to be fit within an R-R cycle, as shown in figure 3.8c. This can be achieved by shortening the train of off-resonance pulses, and splitting the stack of N_s slices into more packages. In general, this approach will translate into reduced MT weighting (as shorter trains of pulses are be used), and longer acquisition times (as more packages are used), but in turn could substantially improve the consistency of data against CSF flow related artefacts.

A potential alternative solution, diametrically opposed to the one proposed here, is to force a steady-state MT regardless of the cardiac cycle, and trigger only the package acquisition. The MT train of pulses can be designed to ensure steady-state MT saturation under a variety of biological configurations (i.e. tissue model parameter values), generally by increasing its duration. Once the steady-state is established, the off-resonance saturation can continue until the first peak detection that will trigger the package acquisition. The implementation of such a solution, however, requires a dynamic update of the MT train duration, and makes the sequence more prone to exceeding SAR limits.

In the following section, we describe and show preliminary results of a cardiac-gated *MTR* protocol using the MT-weighted ZOOM-EPI sequence shown in figure 3.8.

3.4.2.1 A cardiac-gated *MTR* protocol for the cervical spinal cord

The MT-weighted ZOOM-EPI sequence presented in section 3.3.3 can be used for *MTR* protocols in the spinal cord, in conjunction with the cardiac-gating approach described in the previous section. The definition of *MTR* and the rationale for its application in the CNS have been given in section 2.2.1.2.

As can be appreciated from figure 3.8, to trigger the MT-weighted ZOOM-EPI sequence with the cardiac cycle, the MT preparation train and the set of ZOOM-EPI *shots* (i.e. a package) have to fit within the R-R interval. This can be achieved by adequately selecting (*i*) the length of the train of off-resonance pulses (τ_{MT}), and (*ii*) the number of slices to be acquired after each preparation (N_{spp}).

While conditions (*i*) and (*ii*) alone do not ensure the correct triggering with the cardiac cycle, as it is dependent on the subject-specific cardiac rate, a robust approach can be developed by designing τ_{MT} and N_{spp} based on the *worst case*, i.e. the minimum R-R interval allowed. In appendix A, a strategy to optimize the MT weighting when a short τ_{MT} has to be used is presented.

Ideally, a cardiac-gated sequence would excite and acquire slices during the quiescent part of the cardiac cycle, the diastole. However, for the MT weighted sequence considered, a train of off-resonance pulses has to be fit in between the R wave detection and the ideal window for slice acquisition. The length of such a train, τ_{MT}, is subject to a compromise: shorter trains have to be used in order to allow enough time for imaging within the R-R interval, while longer trains would produce higher MT weighting and hence would result in higher *SNR* on the final *MTR* maps, as shown by equation A.6.

We empirically select τ_{MT} = 300 ms, and set the trigger delay t_{trig} (and the interval Δt_0) to the minimum allowed, resulting in the first slice excitation after 330 ms from the trigger signal. Therefore, considering a minimum R-R interval of approximately 600 ms (for a *worst case* heart rate of ∼95 beats/minute), this would leave approximately 300 ms for acquiring a package of ZOOM-EPI. Depending on the duration of the ZOOM-EPI readout, mostly driven by $N_y{}^e$ (hence resolution, FOV and N_{pkg}), we seek to maximize N_{spp} within the time available.

In the implementation we propose, for a *FOV*=60×42 mm^2 at 0.75×0.75 mm^2 in plane resolution, we split N_s=12 slices into N_{pkg}=4 packages, resulting in a train of N_{spp}=3 slices acquired after each MT preparation of duration 300 ms, with Δt_s set to the minimum value allowed.

The MT-weighted ZOOM-EPI sequence proposed produces variable MT weighting according to the slice position within the package, as different delays occur between the end of the train of pulses and each *S90* pulse. While this could be accounted for in a qMT experiment, to produce unbiased model indices (see chapter 5), in the context of *MTR* it introduces another source of variability that makes the resulting *MTR* unusable. To homogenize the *MTR* across slices, multiple signal acquisitions are performed while cycling the slice acquisition order within the package, prior to performing signal averaging. If a number of repetitions equal to a multiple of N_{spp} is chosen, each slice will experience the same position pattern within the package during sequence repetition, resulting in an average signal where the

position-dependent factor is cancelled out.

In table 3.1 a summary of *MTR* sequence parameters is given.

Parameter	Value
MT weighting	
N	30
$\tau/\Delta t$	15 ms/1 ms
ϑ	1500 °
Δ	2100 Hz
T_{rec}	6000 ms
Δt_0	18 ms
Δt_{s}	93 ms (*minimal*)
trigger delay	*minimal*
ZOOM-EPI	
$N_{\text{s}}/N_{\text{pkg}}/N_{\text{spp}}$	12/4/3
$\Delta x\Delta y\Delta z$	$0.75\times0.75\times5$ mm^3
FOV	60×40 mm^2
matrix size	80×75
TE	28 ms
Partial Fourier factor	0.6
receiver bandwidth	254 kHz
signal averages	6

Table 3.1: Summary of *MTR* sequence acquisition parameters used in to carry out in vivo acquisition. For the MT weighting parameters: N is the number of pulses in the train, Δt is the pulse gap, τ is the pulse duration, ϑ is the pulse flip angle, Δ is the offset frequency, T_{rec} is the recovery time between train of pulses, Δt_0 is the delay between train of pulses and first slice excitation in the package, Δt_{s} is the delay between slice excitations. The nominal sequence acquisition time is 5:40 sec.

Parameters relating to the MT weighting are selected according to the strategy presented in appendix A, where the MT weighting for *MTR* is optimized according to a sensitivity analysis while accounting for the constraints on the time available for off-resonance saturation, i.e. τ_{MT}=300 ms.

The effect of the triggering scheme implemented on acquired data is shown in figure 3.9 for the MT_{off} and MT_{on} images used in the *MTR* calculation. Cardiac pulsation causes CSF to flow in the spinal canal with a pulsatile pattern, producing strong signal dephasing in the area surrounding the spinal cord, evident as zero intensity pixels in the resulting images. While these artefacts can not be eliminated entirely, the use of the triggered MT-weighted ZOOM-EPI sequence proposed ensures that slices are acquired within the same phase of the cardiac cycle, resulting in a more reproducible appearance of flow artefact in the MT_{off} and MT_{on} images. On the other hand, in the non-triggered version flow artefacts show varying patterns and locations (sometimes extending close to the edge with of spinal cord) between

the two images, which could hamper the efficacy of motion correction schemes and therefore affect the calculated *MTR*.

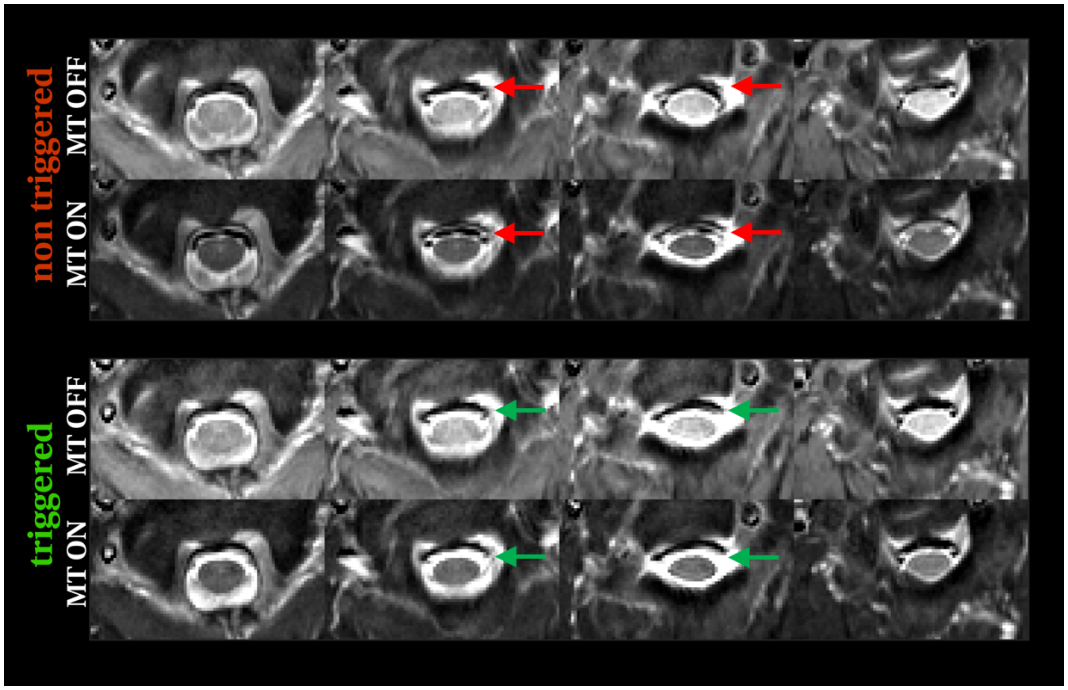

Figure 3.9: MT-weighted ZOOM-EPI acquisitions for *MTR* calculation in a few example locations, without cardiac triggering (**top** panel), and with the triggering strategy presented in this section (**bottom** panel). The same slices are shown for the two conditions. The lack of any triggering scheme in the top panel is apparent as different flow-related artefacts pattern in the CSF between the MT_{off} and MT_{on} images, as indicated by the **red** arrows. The triggered acquisition proposed improved the robustness against flow-related artefacts: MT_{off} and MT_{on} images are similarly affected by flow artefacts (highlighted by the **green** arrows) and their conspicuity appears greatly reduced compared to the non-triggered acquisition.

Preliminary results on a healthy subject of the cardiac-gated *MTR* protocol proposed are shown in figure 3.10. The mean *MTR* over the portion of spinal cord imaged is 41.7(6.0) percentage unit (p.u.), and no clear variation is appreciable across slices (mean *MTR* per slices ranges between 39.5(8.3) p.u. and 44.3(3.0) p.u.), suggesting that the averaging mechanism while shuffling slice position over sequence repetitions effectively homogenizes the MT weighting in the multislice sequence proposed.

The sequence nominal acquisition time is 5:40 sec, and preliminary tests have shown an increase of approximatively $\sim$10% when the triggering scheme proposed here is applied (although it remains a subject-dependent factor).

The *MTR* protocol proposed here has the advantage of allowing relatively fast *MTR* examinations in the cervical spinal cord, with the unique feature over conventional approaches,

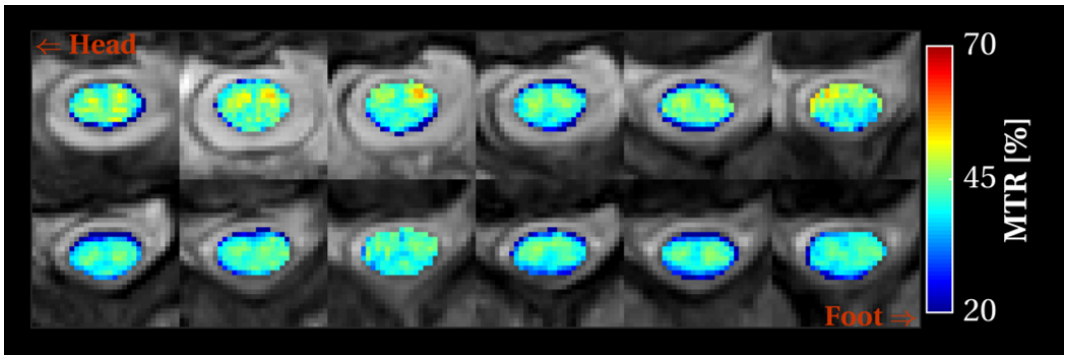

Figure 3.10: *MTR* maps spanning from level C1 to level C4 of the cervical spinal cord obtained with the cardiac-gated MT-weighted ZOOM-EPI sequence presented in this section. The slice-shuffling strategy while repeating signal acquisition allows the homogenization of the MT weighting over slices, resulting in no appreciable variation of the *MTR* along the slice direction

.

such as those adopting 3D spoiled GE readouts [123], of the possibility to introduce cardiac-triggering. This is obtained however at the cost of a reduction in the SNR_{MTR} due to the much reduced SNR_0 in the $\mathrm{MT_{off}}$ image (see equation A.6) as a consequence of the type of readout chosen, i.e 2D ssh-EPI versus 3D GE. For the data acquired in this preliminary study, in fact, *SNR* in the $\mathrm{MT_{off}}$ image is $\sim$30.

A systematic evaluation of the *MTR* protocol proposed through a comparison study with more standard approach is warranted to better understand the potential of this alternative way to carry out *MTR* measurements in the spinal cord.

3.4.3 Simultaneous Multislice Imaging

As introduced in section 2.1.5, the acceleration provided by the SMS technique has recently allowed the development of protocols based on EPI readouts with increased slice coverage, resolution and/or reduced overall duration that were otherwise unachievable [33].

The extension of SMS imaging to ZOOM-EPI is relatively straightforward, as the latter is essentially a ssh-SE-EPI sequence. There is however a conceptual difference in the use of ZOOM-EPI in conjunction with SMS compared to the standard counterpart ssh-SE-EPI.

Whilst for standard EPI readouts, SMS allows either a reduced *TR* for a given set of slices, or for a given *TR* to acquire more slices, the oblique excitation implemented in ZOOM-EPI does not allow a scan time reduction given a certain number of acquired slices N_s.

This can be better appreciated by looking at equation 3.8 defining the scan time (T_{vol}) necessary to acquire a volume, i.e. a *data point*, for the quantitative ZOOM-EPI sequences

(as shown in figure 3.6):

$$T_{vol} = TR \times N_{pkg} \tag{3.8}$$

T_{vol} is dependent on *TR* and N_{pkg}, which are both constrained by the tilted *S90*/*S180* pulse pair of ZOOM-EPI. SMS can not be used to shorten the *TR*, as the condition $TR{>}5T_1$ still has to be fulfilled, neither to reduce N_{pkg}, which is a mere consequence of the tilted *S90*/*S180* pulse pair. In fact, N_{pkg}=3 already represents an optimal compromise between the opposing requirements of: (*i*) limiting distortions (lower N_{pkg} will result in larger *TB* and hence a longer EPI train; see equations 3.2 and 3.5), and (*ii*) reducing scan time (higher N_{pkg} will result in longer protocol duration; see equation 3.8).

Whilst a scan time reduction, although limited, could be obtained by simultaneously acquiring the slices within a a package, the most powerful combination of ZOOM-EPI with SMS is to extend the slice coverage without increasing the scan time, as depicted in figure 3.11. In such a way the limitation of ZOOM-EPI for in vivo imaging the spinal cord in terms of coverage along the *S* direction can be elegantly overcome.

This could potentially allow quantitative studies to be performed in large sections of the spinal cord, covering the whole cervical level or extending to the thoracic level, or simultaneously including the brain, without additional time penalty.

The use of a high acceleration factor is hampered by the availability of specific coils with optimized design for spinal cord applications, however even the use of a mild acceleration factor, i.e. R_{SMS}=2, is sufficient to carry out whole cervical level acquisitions.

As a proof-of-concept study, we used SMS (R_{SMS}=2) to perform an *MTR* protocol in the whole cervical spinal cord in 6 minutes of scan time. Preliminary results are shown in figure 3.12

The combination of SMS with ZOOM-EPI should be evaluated and optimized specifically for the particular quantitative approach considered. In the case of MT-weighted sequences, for example, the on resonance pulses used for simultaneous excitation, due to their higher peak amplitude, could enhance the additional MT effect in neighbouring slices being off-resonace during on-resonance excitations (see also chapter 5).

To conclude, the use of SMS with ZOOM-EPI appears promising to substantially improve coverage, within clinical scan time, of quantitative MRI in the spinal cord. Currently these types of studies are limited to preliminary investigations [124], however we expect the interest in these approaches to grow quickly in the near future.

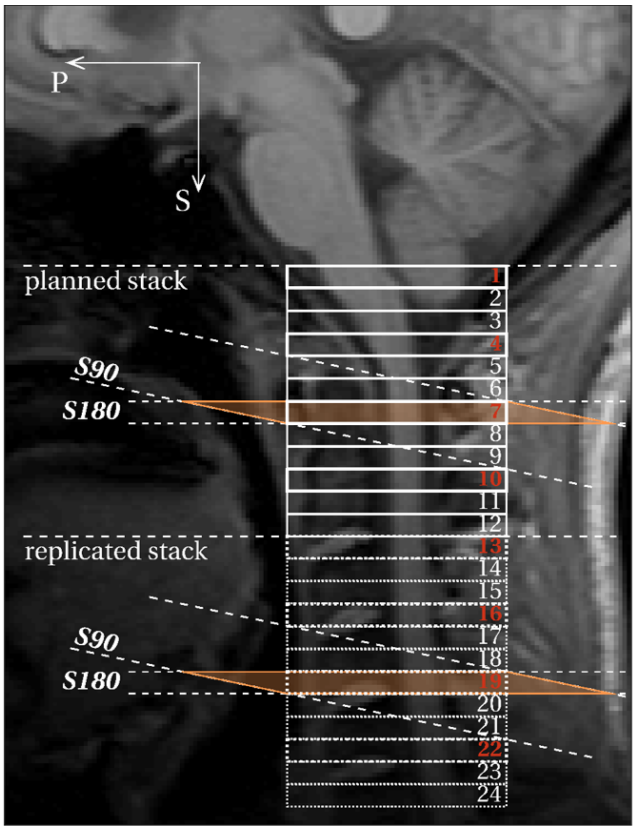

Figure 3.11: Example of ZOOM-EPI in combination with simultaneous multislice imaging. SMS can be used to increase the slice coverage for a fixed scan time. In the figure an acceleration factor R_{SMS}=2 is shown, producing a stack containing double the slices. SMS can be seen as a duplication of the planned stack (**solid** line), which is acquired simultaneously. Slices belonging to the same package (shown in **bold**) for the planned stack, e.g. 1,4,7 and 10, are excited and acquired simultaneously with their homologous slices in the replicated stack (**dashed** line), e.g. 13,16,19 and 22. The acquisition is still planned with the same N_{pkg}, but $R_{SMS} \times \frac{N_s}{N_{pkg}}$ slices are fit within each package (as those labelled in **red**), with simultaneous acquisitions performed per group of R_{SMS} slices (e.g. slices 7 and 19 shown in the figure).

3.5 Conclusion

rFOV methods have been available for years, and their applications for localized imaging are many and diverse. In the specific application of improving DWI of the spinal cord in vivo, rFOV methods have been used extensively.

Here, we have extended the use of ZOOM-EPI to other quantitative MRI approaches, such as T_1 mapping through IR and qMT, both known to be, to different extents, sensitive to myelin content in the CNS. These approaches will be fully investigated in the next chapters, showing that ZOOM-EPI can be effectively used for quantitative MRI methods in the spinal cord, other than those based on diffusion contrast.

We would like to remark upon the importance of characterizing tissue microstructure from

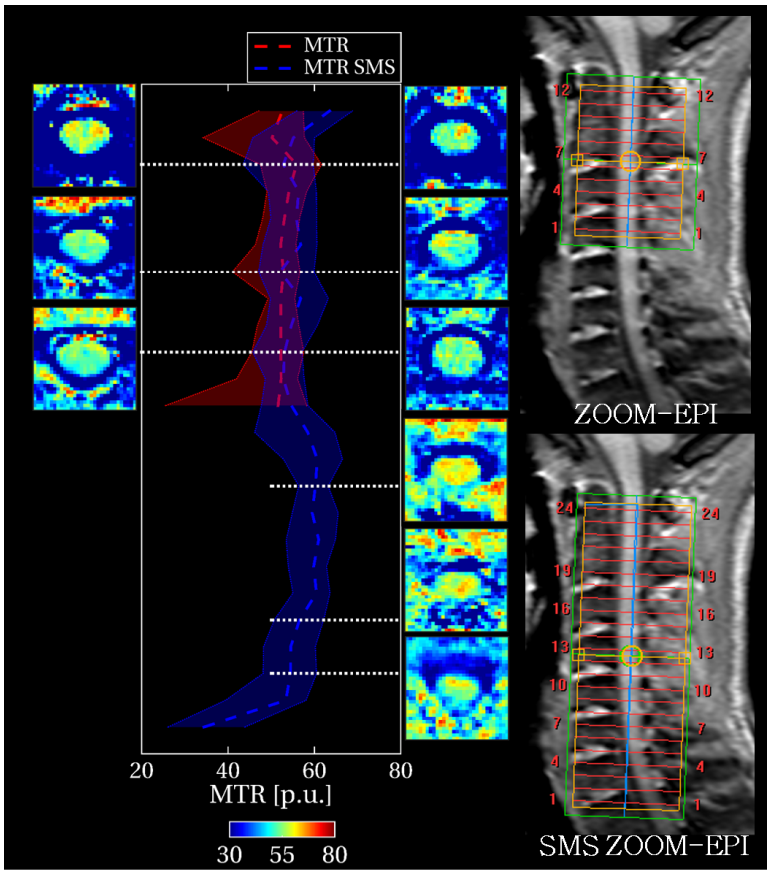

Figure 3.12: Example of ZOOM-EPI combined with SMS for a whole cervical spinal cord *MTR* protocol. A set of 12 slices is shown on the **left** for the *MTR* protocol without acceleration, while the extended stack with SMS is shown on the **right**. R_{SMS}=2 is used for a total of 24 slices covering the entire cervical spinal cord (from C1 to C7). Protocol duration is 6:02 sec for both versions. In the central panel the median *MTR* is plotted against the slice level for the protocol with (**blue**) and without (**red**) SMS, and shaded areas represent the 10^{th}-90^{th} range. *MTR* maps are shown at different levels for the two version of the protocol. Sequence parameters are: *FOV*=60×42 mm^2 at 0.75×0.75×5 mm^3 resolution, *TE*=30 ms, 8 signal averages, with MT-weighting optimized according to appendix A for a duration τ_{MT}=800 ms ($N/\Delta t/\tau$=40/5 ms/15 ms , Δ=2100 kHz, ϑ=1150 °).

different angles, i.e. using different contrasts within a multi-modality approach, to enhance the specificity of quantitative analyses to the underlying tissue features at a microscopic level, and their alteration in pathology. The g-ratio [125] is a representative case, where qMT-derived indices and diffusion-derived indices are combined to obtain a specific measure of demyelination in vivo. The use of a unified acquisition scheme to obtain combined metrics, such as the g-ratio, could improve the precision and reproducibility of those measurements [126].

We have pointed out the main features of ZOOM-EPI for quantitative MRI in the spinal

cord, highlighted some of the current limitations and suggested potential improvements. In particular, the advent of SMS imaging is extremely attractive for rFOV imaging based on EPI. In this chapter, we suggested a simple use of SMS to improve the slice coverage of ZOOM-EPI, although there are several potential solutions. For example, SMS could be used to perform simultaneous IVI, whereby a set of simultaneously excited slices are refocused by an orthogonal refocusing pulse. This solution would: (*i*) improve the readout efficiency, as the oversampling in the P direction would no longer be needed; (*ii*) allow SENSE acceleration; (*iii*) result in a faster protocol as N_{pkg}=2 can be used, provided that a sufficiently high acceleration factor is achievable (R_{SMS} should be at least comparable with N_{spp} used in a standard ZOOM-EPI acquisition).

Chapter 4

T_1 mapping of the spinal cord in vivo

In this chapter a method for quantitatively mapping the T_1 in the cervical spinal cord in vivo is presented. The sequence, termed IR-ZOOM-EPI, is based on the inversion-prepared ZOOM-EPI method described in chapter 3. The chapter provides: sequence description, validation against a gold standard T_1 mapping method in phantoms, and the first demonstration of the protocol in a small cohort of healthy subjects. The chapter concludes with future improvements and potential applications of the method herein developed.

The content of this chapter has been published in *Magnetic Resonance in Medicine* in July 2017 (*doi: 10.1002/mrm.26852*).

4.1 Introduction

The longitudinal relaxation time T_1 is one of the most fundamental quantitative parameters in MRI. Several studies have investigated the biological correlates of T_1. It is well-established that T_1 is dependent on myelin content [127]: relaxation of myelin water occurs faster than non-myelin water, therefore tissues with higher myelin content show a lower average T_1. A linear relationship has in fact been demonstrated between $\frac{1}{T_1}$ and $\frac{1}{(1-MTV)}$, where *MTV* is macromolecular tissue volume (introduced in section 2.2.3), thought to reflect myelin content in white matter. However, T_1 has been shown to depend also on additional microstructural features with a constant total myelin volume, such as water content [128], axonal size in white matter [129], and iron concentration in grey matter [130]. Histological studies on post mortem brain tissue have shown correlations between T_1 and both myelin content and axonal count [54, 39].

Despite the lack of specificity to a single particular biological feature, T_1 is sensitive to changes in tissue microstructure caused by pathologies and inflammatory events. It also provides a quantitative measure comparable across subjects and centres, which is more in-

formative than visual examination of conventional T_1-weighted images. Precise and robust characterization of T_1 in vivo is therefore of great importance. Moreover, the accurate knowledge of T_1 serves as the basis for other quantitative MR methods (e.g. perfusion and quantitative magnetization transfer imaging), and in the optimization of imaging sequence parameters.

Several techniques are available to estimate T_1 in vivo, especially in the brain. Considerable progress has been made in the development of fast mapping techniques: methods such as the Look-Locker Inversion Recovery (LL-IR) [131, 132], and the Variable Flip Angle (VFA) [133, 134] are particularly appealing for their ability to achieve T_1 estimates with large coverage within just a few minutes of scan time. However, great variability among T_1 estimates can be found in literature, which has been ascribed to the sensitivity of the various methods employed to site-specific factors such as RF field uniformity, RF pulse imperfections, and incomplete spoiling [135]. Thus, the time-consuming Inversion Recovery (IR) T_1 mapping approach, where the recovery of the longitudinal magnetization following an inversion is sampled at different delays (i.e. the inversion times), is still regarded as the reference (*gold standard*) method for in vivo T_1 measurements.

Development of quantitative MRI techniques for the spinal cord, including the characterization of T_1, generally lags behind the brain [7, 6], despite the crucial involvement of the spinal cord in several diseases, such as multiple sclerosis [136, 137, 138], amyotrophic lateral sclerosis [139], spinal cord injury [140], and neuromyelitis [141].

Current techniques for measuring T_1 in the spinal cord rely upon the mere application of brain protocols to the cervical level of the spinal cord, mostly employing the VFA method [142]. The T_1 is estimated from a series of GE images acquired at varying excitation flip angle. However, the VFA method makes use of 3D (or 2D) spoiled GE acquisitions which are inherently more sensitive to intra-scan motion artefacts, when compared to other approaches such as ssh-EPI. If not properly addressed, these artefacts could propagate into the T_1 maps, especially in spinal cord applications where effects of physiological noise and subject motion are exacerbated. Additionally, several volumes (with varied flip angle) should be acquired to avoid noise bias in the fitting [143], complete magnetization spoiling has to be ensured [144], and an accurate map of the transmitted RF field (the B_1 map) has to be obtained to correct for the actual flip angle at the voxel level [145]. These facts contribute to preventing the design of fast, accurate and robust protocols for T_1 mapping in the

spinal cord using the VFA method. On the other hand, methods based on the IR approach are less sensitive to the aforementioned limitations [135] and thus represent a more robust approach to for T_1 mapping in challenging environments such as the spinal cord, where multiple noise sources and field inhomogeneities coexist.

In this chapter, we introduce an IR-based T_1 mapping method for the spinal cord based on the sequence described in section 3.3.2, and making use of the slice-shuffling scheme initially developed for application to the brain [146, 147]. It is shown that the method allows for in vivo T_1 mapping of the whole cervical spinal cord in a clinically acceptable scan time. We validate the method against the *gold standard* IR approach in a phantom experiment, and we demonstrate its intra- and inter-subject reproducibility in vivo in a small cohort of healthy subjects.

4.2 Methods

4.2.1 Sequence description

The slice-shuffling mechanism consists of cycling the order in which different slices are acquired over sequence repetitions. Here, we employed the slice-shuffling mechanism in the context of T_1 mapping [146, 147].

An IR sequence was developed for T_1 measurements in the spinal cord, making use of ZOOM-EPI [112, 113, 114], which allows artefact-free multislice imaging of small structures using a ssh-EPI readout, as described in chapter 3. The inversion-prepared ZOOM-EPI sequence has been introduced in section 3.3.2, here we review its salient features in the context of T_1 mapping.

Slices are acquired with an interleaved order, allowing a time interval between contiguous slice excitation (TR) long enough for restoration of longitudinal magnetization after each oblique SE pulse pair, approximately $TR \sim 5T_1$. This results in N_{pkg} groups (i.e. *packages*) each including $N_{spp} = \frac{N_s}{N_{pkg}}$ maximally spaced out slices acquired every TR, where N_{s} is the total number of prescribed slices (figure 4.1a). An IR experiment is implemented using non-selective adiabatic inversion pulses, applied prior to the acquisition of each package. Hyperbolic secant adiabatic inversion is used to achieve robust inversion over the target volume against B_1 and B_0 inhomogeneities [148]. Multiple Inversion Time (TI) data are acquired by shuffling the slice acquisition order within the package for any of the M given delays between the inversion pulse and the first excited slice (TI_{app}), i.e. for a given TI_{app} a total of N_{spp} effective TIs are obtained. To avoid contamination between tilted slice excita-

tions and inversion pulses, the *TR* is extended by a recovery time T_{rec}=6 s (figure 4.1b).

The combination of IR preparation with a rapid ZOOM-EPI readout allows the exploitation

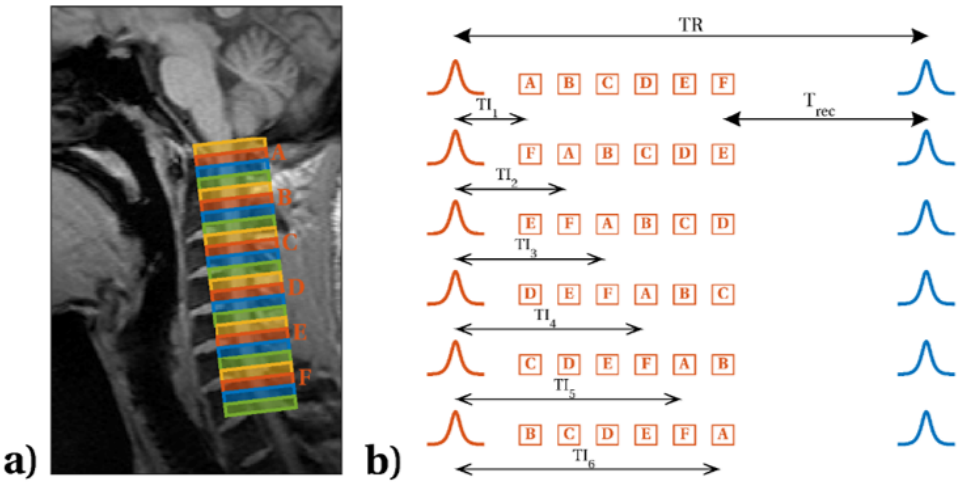

Figure 4.1: Schematic of ZOOM-EPI multislice acquisition in the whole cervical cord, from levels C1 to C7. Slices are grouped in packages (identified by colours); a package is acquired in each *TR* (**a**). IR-ZOOM-EPI is implemented adding a global inversion pulse prior to each package acquisition (i.e. in each *TR*). Between acquisitions of different packages, a recovery time (T_{rec}>5 s) is added to ensure full recovery of magnetization (**b**). Slice order is shuffled within packages to avoid *TR* lengthening in a multi-*TI* experiment, producing a number of effective *TI*s equal to the number of slices per package (N_{spp}).

of the slice shuffling mechanism to reduce dead time when large slice coverage is required. For a given stack of N_s slices grouped in N_{pkg} packages, and M different TI_{app}, resulting in $N_{spp} \times M$ different effective *TI*s (TI_{eff}), the total protocol time T_{prot} is:

$$T_{prot} = \sum_{i=1}^{M} N_{spp} N_{pkg} \left[TI_{app,i} + \Delta t_s \left(N_{spp} - 1 \right) + T_{rec} \right] \tag{4.1}$$

where uniform temporal slice spacing Δt_s is assumed. The sampled *TI*s (TI_{eff}) can be chosen by rearranging Δt_s, TI_{app}, and potentially M, according to the specific applications which dictate coverage, and available scan time T_{prot}. Although a theoretical investigation of protocol optimization is beyond the scope of this chapter, equation 4.1 shows how different settings of (N_{spp}, N_{pkg}, M) for the same N_s can be used to reduce T_{prot}, therefore providing the basis to exploit the interplay between sequence parameters N_s, N_{pkg}, N_{spp} and sampling scheme parameters M, TI_{app}, Δt_s in optimization procedures.

4.2.2 Phantom validation

The IR-ZOOM-EPI was validated against a more standard IR approach in a phantom experiment. Seven gel-filled test tubes (TO5 phantom, Eurospin II Test System, Diagnostic Sonar Ltd., Edinburgh, UK), with T_1 values ranging from approximately 0.2 s to 1.6 s, were used.

The IR sequence chosen as a reference makes use of a non-selective adiabatic inversion pulse (to avoid contamination from slice profile effects) and reads out a single slice (to avoid potential contamination from MT effects). TR=10 s was considered in order to ensure full recovery of longitudinal magnetization between inversions for all phantoms. The readout was a msh-EPI (EPI factor = 7), FOV=160x160 mm^2, voxel size 1x1x5 mm^3.

The IR-ZOOM-EPI was performed separately in each phantom (FOV=64x64 mm^2, voxel size 1x1x5 mm^3), acquiring N_s=6 slices (with N_{pkg}=1). The same TIs of the sequence proposed in vivo were reproduced (see section 4.2.3 on in vivo imaging), and matched for the standard IR. The acquisition with IR-ZOOM-EPI was performed three times on each phantom, with different recovery times: T_{rec}=10 s (to match the TR of the standard IR), T_{rec}=8 s, and T_{rec}=6 s (to match the in vivo application described in section 4.2.3).

The same quantification pipeline used for the in vivo application (see section 4.2.3) was followed to generate quantitative T_1 maps (no motion correction was performed). Paired t-tests were used to assess differences between T_1 estimates with the two approaches. All versions of IR-ZOOM-EPI (at different T_{rec}) were tested.

4.2.3 In vivo imaging

Five healthy volunteers (range age 27-37, 4 males 1 female) were enrolled in the study. Imaging was performed on a Philips Achieva 3T (Philips Healthcare, Best, The Netherlands) MRI system with a 16-channel neurovascular coil, using parallel transmission technology.

The whole cervical spinal cord (i.e. C1-C7) was imaged using the following sequence parameters: FOV=64x48 mm^2, in-plane voxel size=1x1 mm^2, EPI train length=63, TE=22 ms, partial Fourier factor=0.6, 24 slices with slice thickness of 5mm. Magnetization recovery was sampled using the IR-ZOOM-EPI sequence described above, at 12 TIs obtained by grouping slices in N_{pkg}=4 packages, and using M=2 different TI_{app} of 100 ms and 1300 ms, and slice temporal spacing Δt_s=200 ms, to produce the following TI_{eff} =100, 300, 500, 700, 900, 1100, 1300, 1500, 1700, 1900, 2100, 2300 ms. A noise only scan obtained without RF

and gradients, was added to characterize noise standard deviation (σ) in the quantification. Total protocol duration was 7:06 minutes (including noise scan).

A structural 3D gradient-echo (3D-GE) scan (flip angle=7°, *TR*=19 ms) was acquired for image registration and region-of-interest (ROI) definition.

The protocol was repeated in a separate session (different day, maximum interval 110 days) for each subject to assess the reproducibility of the T_1 mapping method.

Within-subject motion across time points was corrected slice-wise, by means of 2D linear transformations with 3 degrees of freedom (FLIRT [149, 150]), using a model-based image registration approach [151]. Straightening of spinal cords was performed on IR-ZOOM-EPI and 3D-GE data based on [152], enabling inherent co-registration between different modalities and facilitating registration of a spinal cord template to 3D-GE volumes in subsequent analysis.

A mono-exponential signal recovery model:

$$S(TI) = |M_0(1 - 2e^{-\frac{TI}{T_1}})| \tag{4.2}$$

was fitted to magnitude data using maximum likelihood estimation, assuming Rician distributed noise, to estimate the equilibrium magnetization M_0 and T_1. σ was obtained from the noise only scan, after smoothing image intensities with a moving average filter (3x3 voxel kernel size) and correcting for noise floor bias [153]:

$$\sigma = \eta\sqrt{\frac{2}{\pi}} \tag{4.3}$$

where η is the image intensity of the *noise only* scan, after smoothing.

Spinal cord ROIs were defined automatically via registration of a spinal cord template [154] to each individual 3D-GE scan, separately for each session. Template registration was performed using the spinal cord toolbox [155], and refined by supplying cord white (WM) and grey matter (GM) masks obtained using [156]. Four different ROIs were selected: GM obtained from segmentation, WM dorsal column (DC), obtained by merging the fasciculus cuneatus and fasciculus gracilis atlases from the template, WM left lateral column (LCL) and WM right lateral column (LCR), obtained by merging the respective spinothalamic, spinoreticular, rubrospinal and lateral corticospinal tracts atlases from the template.

The mean T_1 and standard deviation were measured in each ROI, and in the whole cord,

for both sessions. Inter-session coefficient-of-variation (*COV*) was calculated for each ROI using:

$$COV = \frac{1}{N}\sum_{i=1}^{N}\sqrt{2}\frac{|T_1^{i,1} - T_1^{i,2}|}{T_1^{i,1} + T_1^{i,2}} \tag{4.4}$$

where $T_1{}^{i,j}$ refers to the mean T_1 of subject i (with i=1,2,..,5) for session j (j=1,2) in a specific ROI. Reproducibility of T_1 estimates at regional level was assessed using Bland-Altman plots, linear regression and correlation analysis. The intra-class correlation coefficient (ICC(2,1)) was calculated for ROIs pooled among subjects using a two-way random effects model [157, 158]. The ICC measures the fraction of the total variability attributable to differences among subject-specific ROIs.

4.3 Results

4.3.1 Phantom validation

Results from the phantom validation experiment are given in figures 4.2, 4.3 and table 4.1. Figure 4.2 shows a comparison between T_1 estimates from single slice standard IR and the central slice of IR-ZOOM-EPI with matching T_{rec}=10 s. Figure 4.3 shows correlations be-

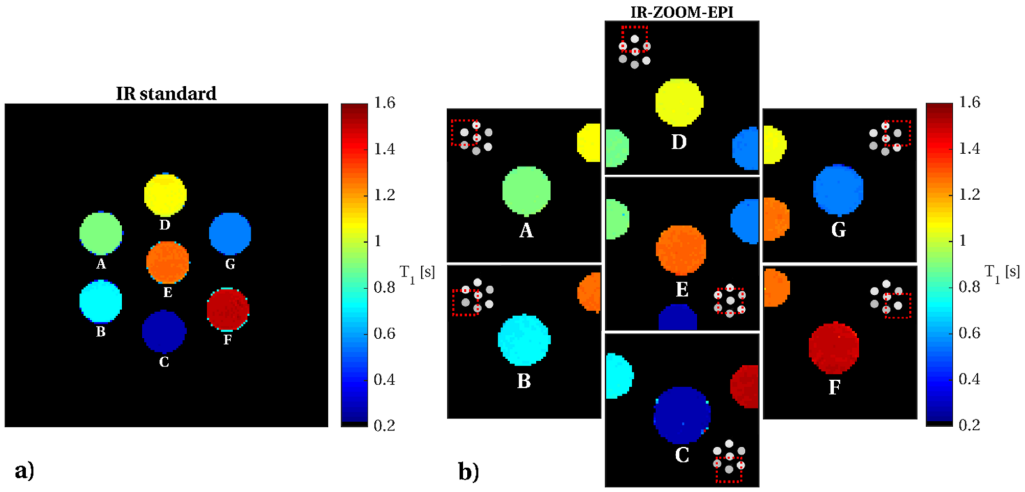

Figure 4.2: Comparison of T_1 estimates in phantoms between standard IR (**a**), and IR-ZOOM-EPI (**b**). IR-ZOOM-EPI is repeated separately on each phantom (with the respective *FOV* highlighted in the corner of each map). N_s=6 slices were acquired. The central slice is shown here for the purpose of comparison.

tween T_1 estimates from standard IR and IR-ZOOM-EPI at varying T_{rec}=10, 8, 6 s (figures 4.3a, 4.3b and 4.3c respectively). Quantitative comparison between approaches is shown in figure 4.3d.

Visually there is a strong agreement between the gold standard and IR-ZOOM-EPI. T_1

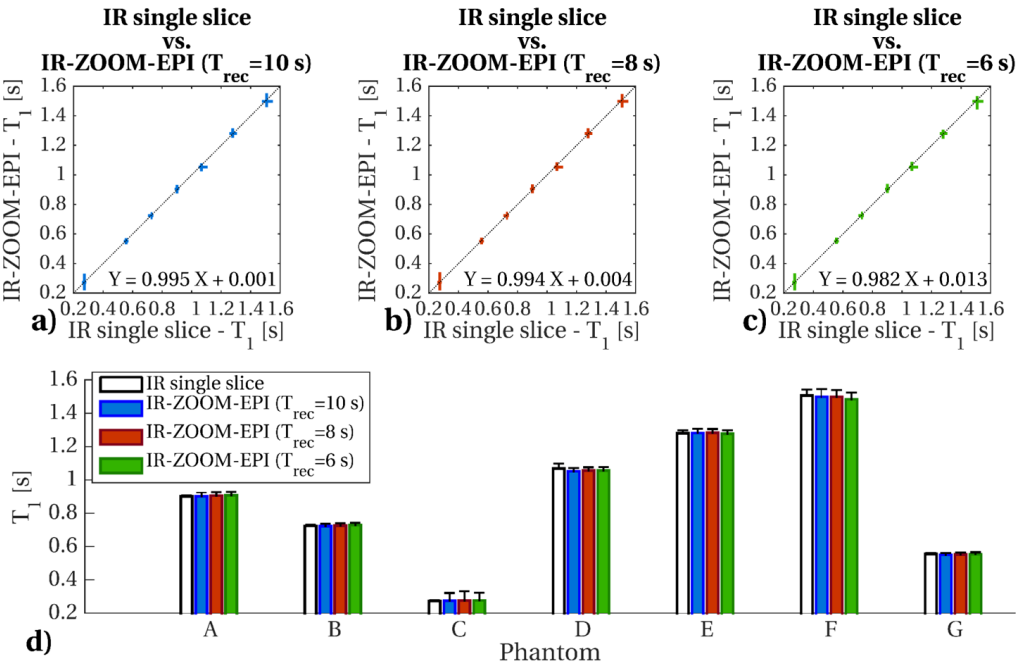

Figure 4.3: Correlation plots between T_1 estimates from standard IR and IR-ZOOM-EPI with T_{rec}=10 s (**a**), T_{rec}=8 s (**b**) and T_{rec}=6 s (**c**). In each plot, the widths of the marker in each direction (horizontal and vertical) correspond to the width of the relative distribution (standard IR and IR-ZOOM-EPI) within the 1st and 99th percentile. The identity line (indicating an ideal linear relationship), together with parameters for the linear fit of T_1 from IR-ZOOM-EPI against T_1 from IR single slice are shown. The bar graph (**d**) shows a quantitative comparison between T_1 estimates in all the phantoms. Bar height represents mean T_1 value, while error bars indicate the 99th percentile of the distribution. No differences between standard IR and all versions of IR-ZOOM-EPI were detected by a paired t-test.

mean and standard deviation are reported in table 4.1. Linear regression demonstrates an almost perfect linear relationship between standard IR and IR-ZOOM-EPI (linear coefficient=0.99, 0.99 and 0.98 for IR-ZOOM-EPI at T_{rec}=10, 8 and 6 s respectively), and negligible bias (intercept=1, 4, 13 ms for IR-ZOOM-EPI at T_{rec}=10, 8 and 6 s respectively). No differences were detected by paired t-tests (P value=0.16, 0.5 and 0.43 when standard IR mean T_1 values were compared to IR-ZOOM-EPI T_1 estimates with T_{rec}=10, 8 and 6 s respectively).

4.3.2 In vivo imaging

An example of the data acquired with IR-ZOOM-EPI at different cervical levels is given in figure 4.4. T_1 maps at different vertebral levels of the cervical spinal cord (from C1 to C7) are shown in figure 4.5, for two example subjects. T_1 values appear very homogeneous across all the cord levels and show very little variability between scan and rescan maps.

	T_1 [ms]			
	IR single slice TR=10 s	**IR-ZOOM-EPI** T_{rec}=10 s	**IR-ZOOM-EPI** T_{rec}=8 s	**IR-ZOOM-EPI** T_{rec}=6 s
A	902(2)	902(8)	906(9)	908(9)
B	725(3)	723(7)	726(7)	729(7)
C	274(2)	275(16)	276(18)	277(16)
D	1068(8)	1052(9)	1056(10)	1056(10)
E	1280(7)	1282(9)	1282(10)	1277(9)
F	1508(10)	1498(14)	1499(15)	1484(15)
G	556(2)	551(5)	553(5)	554(5)

Table 4.1: Mean and standard deviation (in brackets) of T_1 estimates in the phantoms for standard IR single slice, IR-ZOOM-EPI with T_{rec}=10 s, IR-ZOOM-EPI with T_{rec}=8 s and IR-ZOOM-EPI with T_{rec}=6 s.

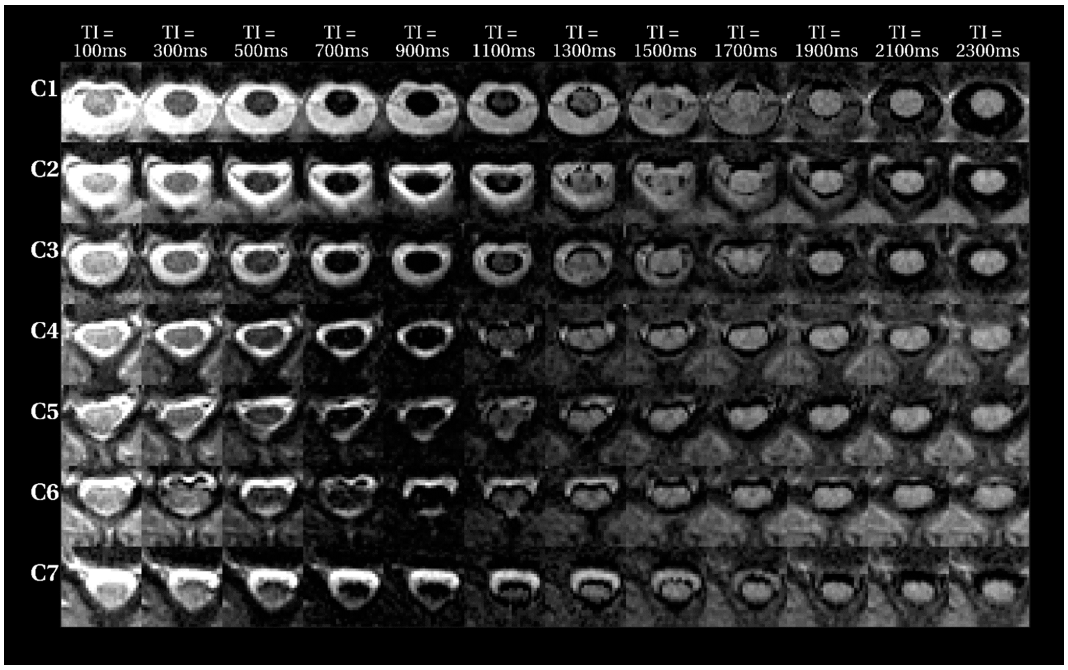

Figure 4.4: Example of IR data acquired with IR-ZOOM-EPI at varying *TI*s (from 100 ms to 2300 ms) in different cervical levels from a single subject.

Whole cord T_1 mean, averaged across sessions and subjects, was 1142.3(±148.2) ms. Regional T_1 values across subjects and sessions are given in table 4.2. Average T_1 was 1108.5(±77.2) ms for LCL, 1110.1(±83.2) ms for LCR, 1150.4(±102.6) ms for DC, and 1136.4(±90.8) ms for GM.

Inter-session *COV* for different ROIs was: 0.93% for LCL, 0.89% for LCR, 0.74% for DC and 1.02% for GM. *COV* for the whole cord ROI was 0.95%. Regional T_1 estimates showed good scan-rescan correlation, as demonstrated in figure 4.6a. The Pearson correlation co-

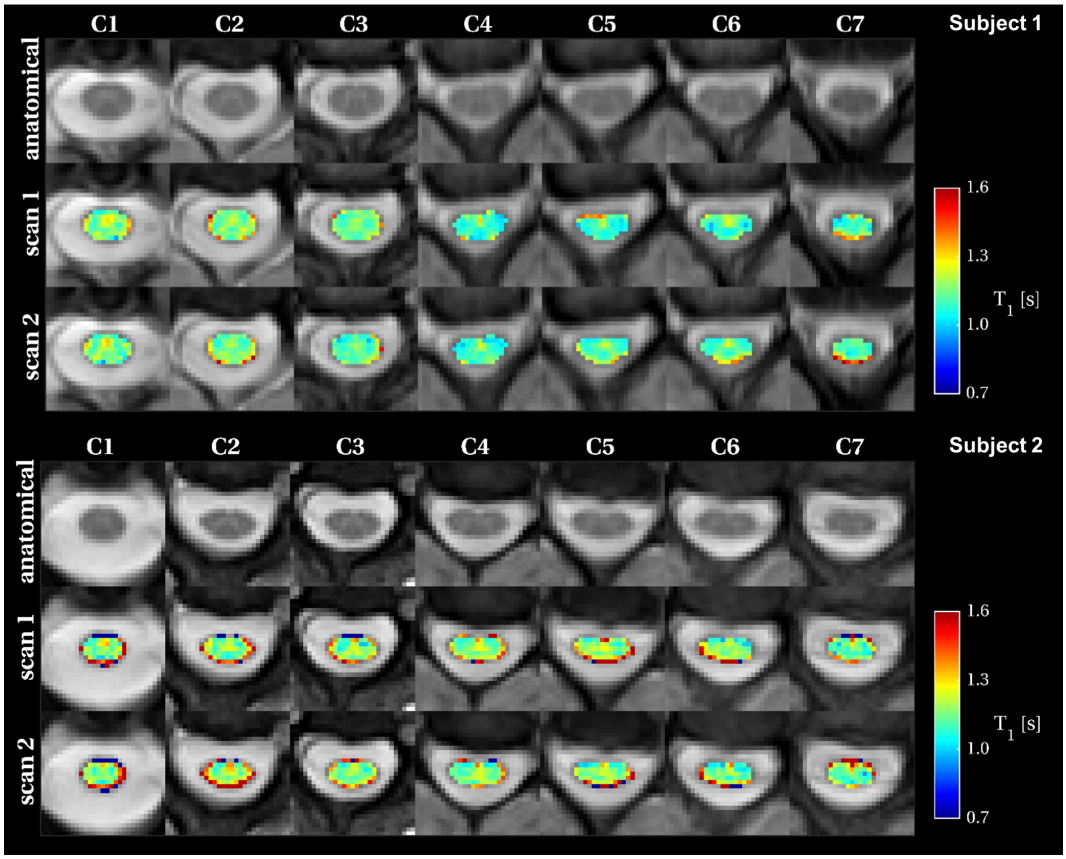

Figure 4.5: Example of T_1 maps for scan and rescan in two subjects. An example slice is shown for each cervical level, together with the corresponding anatomical images in the top row, for each subject.

efficient was 0.89 (P value <0.01), and the slope of linear regression was 0.73 (confidence interval 0.54-0.92). The Bland-Altman plot in figure 4.6b shows a negligible bias between T_1 estimates (2 ms), and very narrow 95% limits of agreement (approximatively ±20 ms). Intra-class correlation coefficient for regional T_1 was 0.88 (P value<0.01, confidence interval 0.71-0.95).

4.4 Discussion

In this study, we have demonstrated a new, simple, fast and reproducible method for mapping T_1 in the whole cervical spinal cord in vivo without deviating from the standard IR approach. Quantitative characterization of spinal cord microstructure is important in a variety of neurological disorders. More effort is required in developing robust methods to assess it, as many aspects of spinal cord microstructure are as yet not characterized in vivo with the current state-of-the-art of quantitative MRI.

The proposed sequence, IR-ZOOM-EPI, combines advantageous solutions for T_1 mapping

		ROI				
	scan	**LCR**	**LCL**	**DC**	**GM**	**whole cord**
S1	*i*	1080.0(61.3)	1088.7(80.3)	1134.0(61.6)	1103.3(55.3)	1113.9(80.4)
	ii	1054.2(103.0)	1074.1(51.5)	1130.1(118.3)	1098.8(75.4)	1113.5(129.7)
S2	*i*	1097.3(52.1)	1113.3(85. 0)	1134.4(95.3)	1135.9(57.2)	1135.9(131.0)
	ii	1097.5(66.1)	1117.7(75.7)	1138.7(47.6)	1141.9(64.9)	1129.8(97.1)
S3	*i*	1187.4(89.8)	1151.6(93.8)	1196.6(97.2)	1188.0(64.4)	1185.7(105.8)
	ii	1168.5(99.1)	1155.3(98.1)	1179.9(74.1)	1166.6(66.1)	1173.3(132.7)
S4	*i*	1113.9(69.5)	1100.1(70.6)	1183.5(151.4)	1191.0(246.9)	1187.3(241.2)
	ii	1120.1(67.4)	1113.0(77.8)	1181.8(168.9)	1142.6(119.1)	1168.0(217.4)
S5	*i*	1072.7(81.0)	1077.0(84.6)	1095.7(124.4)	1099.3(91.3)	1088.6(137.1)
	ii	1093.5(82.7)	1110.6(115.0)	1128.9(87.0)	1096.3(67.1)	1127.0(210.3)
Mean(sd)		1108.5(77.2)	1110.1(83.2)	1150.4(102.6)	1136.4(90.8)	1142.3(148.3)
COV		0.93%	0.89%	0.74%	1.02%	0.95%

Table 4.2: Mean and standard deviation for T_1 estimates in different ROIs and whole cord in the cohort of subjects, and inter-session *COV* for each ROI type.

in the spinal cord. The use of a ZOOM-EPI readout to perform reduced FOV single-shot acquisition, while limiting distortions and freezing intra-scan motion, is essential to achieve clinically feasible protocol durations. In fact, a previous in vivo T_1 mapping study in the spinal cord using IR required 20 minutes per slice and used a large FOV [142]. In addition, the ZOOM-EPI readout is compatible with the magnetization preparation of an ideal

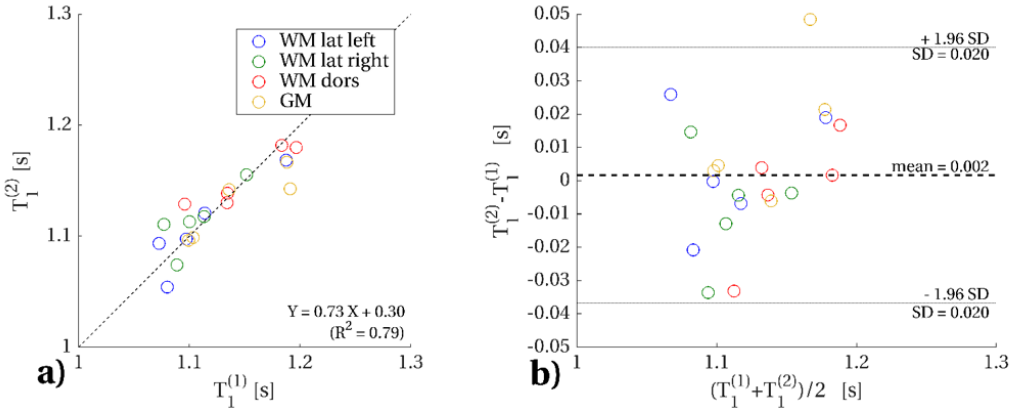

Figure 4.6: Correlation between T_1 estimates from the first scan ${T_1}^{(1)}$ and second scan ${T_1}^{(2)}$ (**a**). A total of 20 different mean T_1 values are obtained in a scan-rescan study from four different ROIs of five healthy subjects. Different ROI types are visualized with different colours: left lateral column (LCL) in **blue**; right lateral column (LCR), in **green**; dorsal column (DC) in **red**; and grey matter (GM) in **yellow**. The dashed line shows ideal identity between ${T_1}^{(1)}$ and ${T_2}^{(2)}$ mean estimates. Linear fit between mean T_1 estimates, and coefficient of determination (R^2) are also reported. Bland-Altman plot for absolute agreement between T_1 estimates from first scan and second scan (**b**). Mean bias and 95% limits of agreement are shown with the dashed line and dotted lines respectively.

IR experiment, where inversion is performed by a non-spatially selective pulse. Since a *TR* constraint ($TR>>T_1$) is inherently in place with ZOOM-EPI to avoid cross-contamination from the oblique excitation pulse, the use of such an inversion pulse has a limited time penalty compared to the normal SE sequence (the maximum *TR* increment is always lower than the maximum TI_{eff} chosen). The adiabatic inversion is also robust against magnetic field inhomogeneities, which are exacerbated in the spinal cord [6], and effects of the imperfect slice profile of the inversion pulse, thought to contribute to the variability of T_1 measurements [135]. Together with the adiabatic inversion, slice shuffling enables the optimal use of scan time [147, 146, 159], as a range of effective *TI*s can be produced for the same nominal *TR*.

The combination of these factors into a single sequence allows the design of time-efficient T_1 mapping IR protocols for the spinal cord, of comparable duration to those using the VFA method with linear approximation fitting (usually under 10 minutes).

In phantoms, paired t-tests show that there is no evidence to reject the null hypothesis that IR-ZOOM-EPI provides the same T_1 estimates than a more standard single slice IR. While small differences could still exist between the two approaches, they do not appear to noticeably impact the accurate characterization of T_1. From the validation experiment in phantoms, it can be concluded that no systematic bias is introduced in the T_1 estimation when using IR-ZOOM-EPI.

In vivo, quantitative T_1 values measured here lie within the expected range for tissues in the central nervous system at 3T [160, 161], with WM values being on the upper side of the reported values. This could be explained by the presence of larger white matter axons [162], which leads to higher T_1 values for constant myelin volume fraction [129], or the presence of myelinated grey matter, as shown by histological findings [163, 136]. Other spinal cord studies, where the T_1 was not the primary parameter of investigation, have indeed reported even higher values than those obtained here [164, 165, 60].

From scan-rescan experiments we obtained excellent measures of reproducibility. Inter-session *COV* was $\sim$1% for all the ROIs considered. This suggests that the T_1 can be measured precisely in the spinal cord using a relatively short protocol. Moreover the high ICC values suggest that most of the variabilities in the T_1 estimates among subjects and ROIs derive from biological differences rather than measurement errors.

4.4.1 Limitations

Contrary to brain T_1 studies, we did not observe consistent contrast between WM and GM. As previously reported [142], this may be due to the axial resolution used in this study (1×1 mm^2), which may not allow for clear delineation of the GM/WM boundaries, as well as contamination from CSF flow. The use of higher resolution is warranted for pursuing detailed tissue specific analysis. The choice of 5 mm as slice thickness is common in axial spinal cord imaging, and justified by the smooth variation of spinal cord anatomy in the cranial-caudal direction. However, the use of thinner slices could be beneficial for improving the accuracy of the tissue specific characterization, as well as for the efficacy of motion correction techniques. Residual misalignments can in fact further confound the resultant WM/GM separation in parametric maps.

The periodic alternation of vertebrae and intervertebral disks along the spinal cord produces signal intensities variations in the slice encoding direction (as can be seen along columns of figure 4.4). The trend is evident also on the M_0, estimated from the mono-exponential model given by equation 4.2, while it is greatly attenuated on the T_1 maps displayed in figure 4.5, showing only a slight decrease of T_1 with the cervical level, which is consistent with recent findings at ultra-high field [166]. However, the implementation of techniques to mitigate signal intensity variation along the S direction, such as slice-wise z-shimming [167], should be considered in future studies to precisely assess the impact of this effect on T_1 estimation.

4.4.2 Future improvements

The approach proposed here can be used in multimodal studies to better characterize spinal cord microstructure. IR-ZOOM-EPI has the potential to be extended to other spinal cord levels, as ZOOM-EPI has proven successful in diffusion studies at the lumbar level [118]. Improvement in the analysis pipeline, such the use of complex images in a five-parameter model fitting as described in [168], can be readily incorporated in the protocol, and could be beneficial for T_1 estimation in the low *SNR* regime characterizing IR-ZOOM-EPI data. Additionally, more room for optimization is available in terms of: (*i*) parameter precision, via accurate selection of *TI*s with protocol optimization techniques [169, 170], and (*ii*) acquisition time through combination with ultra-fast imaging techniques (e.g. SMS imaging [32]). The singular interplay between sequence parameters already allows scan time to be gained without needing to use acceleration techniques, i.e. N_{spp} and M can be arranged to

provide a time efficient protocol even when higher N_s are used. For example, by rearranging the N_s=24 slices acquired in this study in N_{pkg}=3 packages, an IR protocol consisting of 8 TI_{eff} (using M=1), spanning a similar range of the 12 *TI*s adopted in this study, would take only 4:10 min.

Moreover, the sequence efficiency could be further optimized by adopting a saturation recovery approach instead of the inversion recovery method used here. In this type of approach, a non-spatially selective saturation pulse forces the longitudinal magnetization to 0, avoiding the requirement to wait for the recovery of magnetisation to equilibrium necessary when using an inversion pulse. For the same TI_{eff}, N_s, N_p, Δts used in this study, a saturation recovery approach would result in a reduction of approximately 60% of T_{prot}, as T_{rec} could be very close to 0 (see equation 4.1). A possible drawback of such a solution is related to the diminished signal dynamic range associated with a saturation recovery compared to an Inversion recovery method. We plan to investigate the advantages of such an implementation in a future comparison study with the proposed IR-ZOOM-EPI.

In general, formal optimization accounting for protocol duration and *TI*s selection could be devised starting from equation 4.1, to produce an optimal T_1 protocol in the spinal cord simultaneously addressing the issues of spatial coverage, *SNR*, protocol time, and T_1 estimatez precision. Additional time gains could, in turn, be used to increase *SNR* through signal averaging for higher resolution imaging. Alternative emerging approaches for T_1 mapping, such as MR fingerprinting (MRF)[171], could allow further scan time reduction, although its implementation to the spinal cord has not yet been proposed, and only applications to the brain are currently available.

4.5 Conclusion

In conclusion, the evidence reported here in this chapter strongly supports the use of IR-ZOOM-EPI to perform unbiased T_1 mapping using a multislice rFOV sequence (ZOOM-EPI) in combination with the slice-shuffling mechanism to greatly improve the time efficiency over conventional approaches. T_1 estimates in the cervical spinal cord are reproducible using IR-ZOOM-EPI. The short acquisition time and large slice coverage of this method paves the way for accurate T_1 mapping for various spinal cord pathologies.

Moreover, quantitative T_1 estimation is often part of more complex quantitative MRI methods aiming at measuring myelin, such as the macromolecular tissue volume (*MTV*) method, or quantitative Magnetization Transfer imaging, and T_1 is itself, to some extent, an indicator

of myelin content. Therefore a fast and robust way of measuring it opens new possibilities for developing the aforementioned techniques in the spinal cord and to gain insights into spinal cord microstructure in healthy and pathological conditions.

Chapter 5

Quantitative Magnetization Transfer Imaging of the spinal cord in vivo

In this chapter a method to quantitatively map parameters of the two-pool model for the MT effect in biological tissue is developed and applied to the human cervical spinal cord in vivo.

The MT-weighted ZOOM-EPI sequence, introduced in chapter 3, is described in depth and its utilization within a quantitative MT framework explained. The theory of quantitative MT analysis, outlined in section 2.2.1.3, is adapted to the particular imaging sequence developed herein. Additionally, protocol optimization techniques are used to guide the definition of the acquisition parameters. Evaluation of the framework proposed is carried out through extensive simulations, and in vivo experiment in a small cohort of healthy subjects.

The following chapter demonstrates an example of the potential of using a unified readout for peforming quantitative MRI. Namely, ZOOM-EPI can be used as an engine to efficiently produce different image contrasts for quantification of spinal cord microstructural parameters. Here, the estimation of two-pool model parameters is shown. A natural extension of the methods described in this chapter would be the incorporation of a DWI protocol, for in vivo g-ratio measurement in the spinal cord.

The content of this chapter has been published in *Magnetic Resonance in Medicine* in September 2017 (*doi:10.1002/mrm.26909*).

5.1 Introduction

The physical basis of MT effect, the theory behind quantitative MT methods, and the rationale for its application in the CNS have been described extensively in section 2.2.1.

The spinal cord is a primary location of demyelination and axonal loss in a variety of

diseases, such as multiple sclerosis [136, 137, 138], amyotrophic lateral sclerosis [172], spinal cord injury [173], and neuromyelitis optica [174]. Post mortem studies have demonstrated focal and diffuse abnormalities in cord WM and GM in these conditions [136, 138, 175, 176, 177]. The development of MRI methods to sensitively, and ideally specifically, look at myelin in the spinal cord are therefore an urgent need, to provide better explanation of clinical symptoms, to improve the accuracy of current prognosis and to enable the assessment of emerging neuroprotective or reparative treatments.

As described in section 2.2.1.4, qMT methods enable quantitative inferences on the macromolecular component of tissues which have been shown to correlate with myelin content [54, 178, 55]. Therefore, qMT is of particular interest for spinal cord imaging, although so far the technique has mainly been applied in the brain [179, 44, 180, 181, 182].

The translation of qMT to the spinal cord has proven challenging for several reasons: the demands of high-resolution (to depict spinal cord structure) and, at the same time, adequate SNR images to robustly perform quantitative model fitting result in prohibitive qMT protocol lengths, not feasible in clinical practice. Furthermore, quantitative MRI of the spinal cord is hindered by high susceptibility to motion artefacts and physiological noise [7, 6].

There are only a few studies that have carried out qMT examinations in the spinal cord in vivo. qMT has been used to detect differences between healthy subjects and patients affected by adrenomyeloneuropathy, a neurological disorder characterised by demyelination without an inflammatory component [183]. However, parameter estimation was performed at a region-of-interest (ROI) level, and a single RF irradiation power was used to limit protocol length to 32 minutes at 1.5T.

A simplified version of the full qMT approach in the spinal cord has also been proposed [184]. In that study, high-resolution *BPF* maps were obtained within 10 minutes following a single MT-weighted acquisition by exploiting model approximations believed to hold in a variety of cases [185]. Although high WM/GM contrast and good sensitivity to pathology were shown, the large number of assumptions made to perform a single-point fit can have an impact on the accuracy of the *BPF* estimation, due to unmet conditions in other fixed model parameters, especially when applied to disease.

Preliminary results were also presented using a selective inversion recovery sequence at 7T [186], where again, despite the use of ultra-high field, data had to be averaged within ROIs prior model fitting to allow robust parameters estimation.

The above approaches are very diverse in nature, rely on several assumptions, or have as yet only been conducted in the form of preliminary feasibility studies. As a result, qMT model parameter characterization in the spinal cord is fragmentary and the agreement between results in literature is only partial.

In this work we propose a novel framework to foster the implementation of qMT in the spinal cord in vivo, tackling the whole chain, from pulse sequence design, to signal modelling, and optimization of sampling scheme, in order to enable robust assessment of qMT model parameters in acceptable scan times. In particular, the MT-weighted ZOOM-EPI sequence described in section 3.3.3 is combined with a dedicated model for unbiased parameter estimation. The sampling scheme is optimized via Cramer-Rao-Lower-Bound (CRLB) minimization, and the reproducibility of qMT metrics is demonstrated in a cohort of healthy volunteers at the cervical level.

This framework will easily adapt to other situations where rFOV imaging may be beneficial for assessing indices sensitive to macromolecular components of tissues.

5.2 Methods

The novel framework, consisting of pulse sequence and signal model developments, and protocol optimization, is described below and tested through simulations and in vivo experiments.

5.2.1 Pulse sequence

As described in section 3.3.3, MT sensitization is achieved via a train of off-resonance RF pulses preceding acquisition of each package of ZOOM-EPI (figure 5.1a-c). In this configuration, N_{spp} slices experience the same MT pulse train as they are acquired sequentially following a MT preparation. As a consequence, the delay t_{d} between the end of the off-resonance saturation and each slice excitation is dependent on the slice order of the package, and will contribute to create different MT weighting between slices. To homogenize the MT weighting across slices, the acquisition is repeated N_{spp} times, reshuffling the slice order within each package and averaging the slice signal obtained from each sequence repetition (Figure 5.1c). By doing so, slices are reconstructed with homogeneous MT weighting and benefit from increased *SNR* following signal averaging (theoretically by a factor $\sqrt{N_{spp}}$).

The same shuffling mechanism is employed for the acquisition of the non-MT-weighted im-

ages (commonly referred to as M_0 images, in analogy with b_0 images in diffusion-weighted protocols) used for signal normalization prior to model fitting. Such a mechanism allows, through image normalization, compensation for any potential slice-dependent off-resonance effect induced by the excitation/refocusing of neighbouring slices, as quantified through simulations shown in figure 5.10.

Acquisition parameters are given in section 5.2.5.

5.2.2 Signal model

Traditional MT acquisitions in the steady-state regime would require the use of long trains of MT pulses (>2 s) [43, 45, 46, 47]. To exploit the separation of MT preparation from image acquisition for time efficient protocols, trains of pulses have to be shortened. As a consequence, a steady-state MT saturation cannot be established.

The numerical model based on the coupled Bloch equations [48] can be adapted to predict the signal acquired with the sequence described above and estimate fundamental model parameters, accounting for the non-steady state condition. The model integrates the two-pool Bloch equations describing the evolution of the three components (x, y and z) of the magnetization of both pools undergoing exchange and saturation (see equations 2.24). Given the extremely short $T_2{}^{\mathrm{B}}$, the transverse components of bound pool magnetization can be discarded. Using the same formalism adopted in [52], two-pool Bloch equations can be given in the form of homogeneous differential equations, with the following matrix representation:

$$\frac{d\mathbf{M}(t)}{dt} = \mathbf{L}(t)\mathbf{M}(t) \tag{5.1}$$

with $\mathbf{M}(t) = \left[\frac{1}{2}, M_x^F, M_y^F, M_z^F, M_z^B\right]^T$, and:

$$\mathbf{M}(t) = \begin{bmatrix} 0 & 0 & 0 & 0 & 0 \\ 0 & -\frac{1}{T_2^F} & 2\pi\Delta & 0 & 0 \\ 0 & -2\pi\Delta & -\frac{1}{T_2^F} & \omega_1(t) & 0 \\ R_1^F & 0 & -\omega_1(t) & -\left(R_1^F + k_{FB}\right) & k_{FB}\frac{1-BPF}{BPF} \\ R_1^B\frac{BPF}{1-BPF} & 0 & 0 & k_{FB} & -\left(R_1^B + k_{FB}\frac{1-BPF}{BPF} + R_{rf}^B\right) \end{bmatrix} \tag{5.2}$$

Above, Δ is the frequency offset of the MT pulse (in Hz); ω_1=γ B_1(t) the time dependent amplitude of the MT pulse expressed (in rad/s), characterized by peak amplitude B_1 (in T) and shape function s(t), i.e. B_1(t)=$B_1 s$(t); $R_1{}^{\mathrm{F}}$ and $R_1{}^{\mathrm{B}}$ the longitudinal relaxation rates

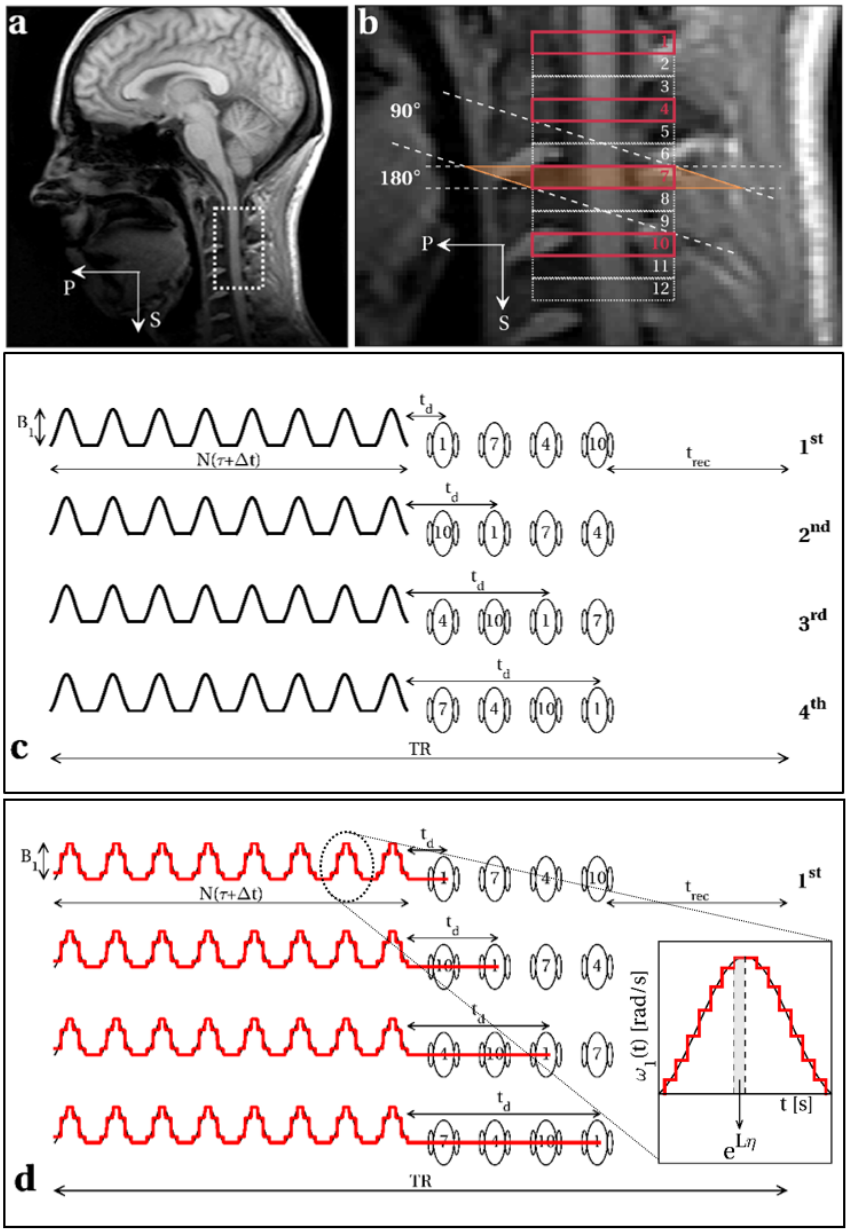

Figure 5.1: Portion of spinal cord imaged in the sagittal view (**a**), with details of the prescribed slices with ZOOM-EPI (**b**). Outlined in bold (1, 4, 7, 10) are slices belonging to the same package, that are acquired within the same *TR*. Slice order within a package is shuffled over different sequence repetitions (**c**), resulting in different delays t_d between train of pulses and slice excitation. If a number of sequence repetitions which is a multiple of N_{spp} (N_{spp}=N_s/N_{pkg}; N_s=number of slices, N_{pkg}=number of packages) is prescribed, images can be reconstructed from the average of all slice order configurations, resulting in a homogeneous weighting among different slices. Sequence parameters (N, B_1, τ, Δt, t_d and offset frequency Δ) are accounted for in a quantitative setting by an adequate modelling procedure that iteratively solves the two-pool model Bloch equation (equation 5.1), through the exponential matrix formalism, using a constant piecewise approximation (discretization step η=100μs) for the time dependent function ω_1(t) describing the off-resonance saturation (**d**).

of the two pools; $T_2{}^{\mathrm{F}}$ the transverse relaxation time of F; $R_{\mathrm{rf}}{}^{\mathrm{B}}$ the rate of saturation of B (proportional to the super-Lorentzian absorption line shape [187], dependent on $T_2{}^{\mathrm{B}}$); k_{FB} the forward exchange rate; and *BPF* is:

$$BPF = \frac{M_0^B}{M_0^B + M_0^F} \tag{5.3}$$

where $M_0{}^{\mathrm{F}}$ and $M_0{}^{\mathrm{B}}$ are the equilibrium magnetizations of the two pools.

The model assumes full relaxation between shots of MT-weighted ZOOM-EPI. Within each package magnetization evolution is predicted by iteratively solving Equation 5.1, after replacing the time continuous function $\omega_1(\mathrm{t})$ with an appropriate piecewise approximation. Such a function contains the discretized version of the train of MT pulses used (discretization step η=100 μs) and free precession periods (i.e. when $\omega_1(\mathrm{t})$=0) of length t_{d} according to the position in the package of the slice currently being acquired, as outlined in figure 5.1d.

In addition to the frequency offset Δ, the model explicitly accounts for pulse duration τ, pulse peak amplitude B_1 (instead of coupling them into the effective flip angle θ), pulse shape $s(\mathrm{t})$, inter-pulse gap Δt, and number of pulses in the train N, which define $\omega_1(\mathrm{t})$ over the time period considered in the numerical integration. It also accounts for different delays t_{d} resulting from signal averaging while shuffling slices over sequence repetitions (figure 5.1d).

The model can be fitted to a set of MT-weighted images to estimate *BPF*, $T_2{}^{\mathrm{F}}$, $T_2{}^{\mathrm{B}}$ and k_{FB}, in combination with a separate measurement of the longitudinal relaxation time $T_1{}^{\mathrm{obs}}$.

5.2.3 Protocol optimization

CRLBs are theoretical lower limits for the variance of parameter estimates [188], and are often used in MRI protocol optimization (see [189, 190, 191, 192] amongst others).

Here CRLB theory is applied to derive combinations of sequence parameters $\mathbf{p}_s = \left[B_1\ \Delta\ \tau\ \Delta t\ N\right]$ that maximize the precision of estimated model parameters $\mathbf{p}_m = \left[BPF\ T_2^F\ T_2^B\ k_{FB}\right]$.

The search is framed in terms of an optimization problem: combinations of $\mathbf{p}_{\mathrm{s}}$ that minimize the mean weighted sum of $\mathbf{p}_{\mathrm{m}}$ CRLBs, for a set of K measurements, are defined as an

optimized sampling scheme. The cost function V to minimize is:

$$V\left(\mathbf{p}_{s,1},\mathbf{p}_{s,2},...\mathbf{p}_{s,K},\mathbf{p}_m\right)=\sum_{i=1}^{M} w_i \frac{\left[F^{-1}\right]_{ii}}{\left(p_i\right)^2}=\sum_{i=1}^{M} w_i CV_i^2 \tag{5.4}$$

where $\left[F^{-1}\right]_{ii}$ represents the i^{th} diagonal element of the inverse of the Fisher matrix F, p_{i} is the i^{th} element of the vector $\mathbf{p}_{\text{m}}$, and M the total number of model parameters. Equation 5.4 states that V is the sum of the squared ideal coefficients of variation (CV) of model parameters $\mathbf{p}_{\text{m}}$. The weights w_{i} are used to select which model parameter to include in V, and therefore assume values w_{i}=[0,1].

Knowledge of $\mathbf{p}_{\text{m}}$ is needed in equation 5.4 to solve for optimal $\mathbf{p}_{\text{s}}$. To account for heterogeneity in biological tissue, in practice V in equation 5.4 is averaged over N_{T} different plausible tissue configurations $\mathbf{p}_{\text{m,n}}$ (with n=1,...,N_{T}), taken from previous published studies and summarized in table 5.1.

		BPF *[n.u.]*	$\boldsymbol{T_2}^{\mathbf{F}}$ *[ms]*	$\boldsymbol{T_2}^{\mathbf{B}}$ *[μs]*	$\boldsymbol{k}_{\mathbf{FB}}$ *[s^{-1}]*
i	**WM**	0.17	23	13	2.3
	GM	0.07	41	12	1.08
ii	**WM**	0.15	37	12.3	4
	GM	0.07	51	10.6	1.8
iii	**WM**	0.14	37	12	4.3
iv	**whole cord**	0.09	40.6	9.7	1.1

Table 5.1: Set of tissue configurations $\mathbf{p}_{\text{m}}$ used in the optimization of the qMT sampling scheme. Values are taken from various qMT studies performed in the brain and spinal cord: (*i*) [52]; (*ii*) [193]; (*iii*) [44]; (*iv*) [194]. Combinations are chosen to span variability of tissue parameters shown both in white matter (**WM**) and grey matter (**GM**), and spinal cord (**whole cord**).

Optimal sequence parameters are obtained via minimization of the quantity V, performed using a self-organizing migratory algorithm (SOMA) [195], as in Alexander *et al.* [196].

To reduce the risk of incurring local minima, $T_2{}^{\text{F}}$ is excluded from equation 5.4, by setting $\mathbf{w}=\left[1,0,1,1\right]$. Previous studies have shown that this parameter is characterized by larger variability compared to other qMT parameters [48, 49]. However, it does not directly reflect properties of the macromolecular pool and it can be estimated separately with approaches other than qMT, therefore it can be regarded as being of minor importance compared to *BPF*, $T_2{}^{\text{B}}$ and k_{FB}.

Simultaneous optimization of all $\mathbf{p}_{\text{s}}$ could be impaired by the presence of local minima, given the model used (which requires numerical computation). We opted for optimizing

only for (Δ, B_1) pairs, similarly to other studies [189, 197, 198]. The remaining sequence parameters (τ, Δt, N) are selected with a heuristic approach by comparing a posteriori values of V for optimizations at several combinations of (τ, Δt, N). We adopted the following approach: (*i*) the effect of train length is investigated by optimizing for (Δ, B_1) at different N=10, 20, 30, 40, 50, 60 with fixed $\tau\backslash\Delta t$=20 ms\20 ms; (*ii*) once an optimal train length N_{opt} is determined, the effects of τ and Δt are separately tested by running optimization of (Δ, B_1) at different values of τ, with fixed Δt=20 ms, and vice versa (fix τ=20 ms), to select τ_{opt} and Δt_{opt}. The following values were tested: τ=10, 15, 20, 30, 40 ms, Δt=1, 10, 20, 40, 100 ms; (*iii*) final optimization of (Δ, B_1) is performed with (τ, Δt, N)=(τ_{opt}, Δt_{opt}, N_{opt}).
All optimizations were performed with K=14 sampling points, to produce a protocol consisting of 15 image acquisitions (including one M_0 image), similar to protocols used in the brain. However, the approach can be generalized to a smaller/larger value of K to allow for shorter/longer scan times. During optimization B_1 was constrained to be below the maximum peak amplitude achievable (13 μT), and simultaneously to avoid SAR deposition above 75% of the maximum allowed value. Δ was allowed to vary between 1 kHz and 100 kHz. All optimizations were performed assuming *SNR*=25 in the M_0 image, which is plausible for the *TE* and resolution used here, given previously reported *SNR* values with the same readout and instrumentation [117] (see also figure 3.5).
To provide a comparison, a non-optimized protocol, referred to throughout this chapter as the *uniform protocol*, was also devised. The uniform protocol is designed to resemble standard qMT protocols [179, 193]. MT-weighted data points (a total of K as for the optimized protocol) are equally split in two different RF power levels (identified with two distinct B_1) defined as 80% and 30% of the maximum SAR level allowed in the optimization. At each B_1 level, Δ are logarithmically spaced between 400 Hz and 20 kHz [179]. The same (τ_{opt}, Δt_{opt}) pair was used for the uniform protocol, whilst in order to ensure that the system approach the steady-state condition, which is met in standard qMT experiments, a train of N=50 pulses was chosen, as the maximum length available for the $B_{1,\text{max}}$, τ and Δt selected. Details of the uniform and optimized protocols are given in table 5.2.

5.2.4 Simulations

The efficacy of optimization was tested using Monte Carlo simulations.
Synthetic qMT datasets were computed using the optimized and uniform schemes of table 5.2. N_{MC}=1000 realizations were generated by adding Rician-distributed noise at different

uniform		optimized	
θ	Δ	θ	Δ
[°]	*[Hz]*	*[°]*	*[Hz]*
601	400	378	1018
601	768	383	1031
601	1474	385	1029
601	2828	393	1311
601	5429	426	1706
601	10420	456	2102
601	20000	1427	13710
1100	400	1464	1000
1100	768	1466	3250
1100	1474	1467	3517
1100	2828	1470	3348
1100	5429	1471	3283
1100	10420	1471	3420
1100	20000	1471	13985

Table 5.2: MT-weighted sampling points (flip angle (θ) and offset frequency (Δ)) for the uniform (**left**) and optimal (**right**) protocols. MT-weighted data points are given as effective flip angle (in °) and offset frequency (in Hz) pairs. Pulse duration and pulse gap are the same for the two protocols (15ms/15ms), while pulse train lengths are different (N=50 for the uniform protocol in order to achieve steady-state conditions as in previous qMT studies, N=25 for the optimal protocol). The MT pulse shape is sinc-Gaussian with no lobes.

SNR levels (100, 50, 25, 18, 12). For each signal realization, one of the tissue parameter configurations of table 5.1 was randomly chosen, and perturbed. Random perturbations were sampled from normal distributions with standard deviation of 0.02, 0.01 ms, 1 μs and 0.4 s^{-1} for BPF, ${T_2}^F$, ${T_2}^F$ and k_{FB} respectively.

Simulated signals were fitted with the model described in the section 5.2.2 and percentage errors on model parameters calculated. All model parameters were fitted, and the same ${T_1}^{obs}$ used for generating the signal was used in the fitting.

Additional simulations were performed to investigate the effect of: (*i*) including the model parameter ${T_2}^F$ in the protocol optimization; (*ii*) errors in pulse amplitude B_1 and frequency offsets Δ (i.e. B_1 and B_0 errors) on parameter estimates, for both the optimized and uniform protocols.

5.2.5 In vivo imaging

Five healthy volunteers (3M/2F, 27-40 years old) were scanned. One volunteer underwent repeated scans (3 times) in separate sessions, within 5 days. All volunteers gave informed consent and the study was approved by the local research ethics committee.

Imaging was performed on a 3T Philips Achieva system (Philips Healthcare, Best, The

Netherlands). The full protocol consists of both optimized and uniform qMT acquisitions, and an IR acquisition for ${T_1}^{obs}$ estimation, shared between qMT protocols.

MT data acquisition was performed with the MT-ZOOM-EPI sequence (see section 5.2.1) with: *FOV*=48x39 mm^2, in-plane resolution 0.75×0.75 mm^2, N_s=12 axial 5-mm thick slices centred at the C2/3 disk level, *TE*=28 ms, partial Fourier imaging factor=0.6. N_{spp}=4 slices were acquired after every off-resonance pulse train (t_d=18, 112, 206, 300 ms) resulting in a *TR* of 7786 ms and 7037 ms, and a total duration of 23:44 minutes and 21:27 minutes for the uniform and optimized protocols, respectively.

T_1 estimation was performed using the IR-ZOOM-EPI sequence presented in chapter 4. Magnetization recovery was sampled at 8 effective inversion times (TI_{min}/Δt=100 ms/350 ms), same *FOV*, *TE*, and signal averages as the MT-weighted acquisition, *TR*=10550 ms, for a total duration of 15:06 min.

Prior to fitting, motion within modalities was corrected slice-wise using FLIRT from FSL [149], and the spinal cord was straightened [152], to co-register the IR and qMT datasets to each other.

To evaluate protocol optimization in vivo, pooled histograms of model parameters were created for uniform and optimized protocols, and inter-subject *CV*s calculated. Additionally, from the repeated dataset a reproducibility figure for each parameter was calculated voxelwise. The reproducibility index I of a model parameter p_i was defined as [199]:

$$I\left(p_i\right) = 1 - \frac{1}{2}\left(\frac{\max\left(p_i\right) - \min\left(p_i\right)}{\frac{1}{3}\sum_{r=1}^{3} p_{i,r}}\right) \tag{5.5}$$

where *max()* and *min()* are evaluated over the 3 experiment repetitions. $I(p_i)$ spans from 0 to 1, where 1 indicates ideal reproducibility. Differences between optimized and uniform samplings were explored using a Kolmogorov-Smirnov (K-S) test for differences between distributions of $I(p_i)$ over the whole cord (significance level $P<0.05$).

5.3 Results

The optimization framework enables the use of non-steady-state sequences for accurate fitting of qMT model parameters, as shown in figure 5.2. For a given configuration (τ, Δt), errors on fitted parameters can be made almost independent of the length of MT saturation pulse train (figure 5.2b) through adequate selection of sampling points, achieved via CRLB optimization. The example given in figure 5.2b shows that a train of N=20 MT pulses (pro-

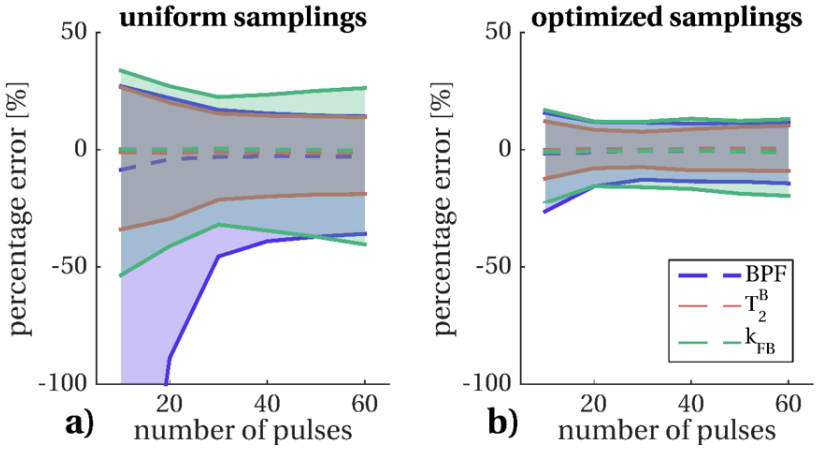

Figure 5.2: Percentage errors on fitted parameters obtained from Monte Carlo simulations (N_{MC}=1000 repetitions) for uniform sampling (**a**) and optimized sampling (**b**) for a varying number of pulses N and fixed $\tau\backslash\Delta t$=20 ms\20 ms combination. Dashed lines represent the median of error distributions, shaded areas span from the 25th to the 75th percentiles of the distributions. Model parameters considered in the optimization are shown: *BPF* (**blue**), $T_2{}^B$ (**orange**) and k_{FB} (**green**). Optimized selection of (Δ, B_1) pairs reduces parameter errors compared to uniform sampling, and greatly mitigates the dependency of the error on the length of the train N, allowing the use of shorter, more time-efficient saturation schemes.

ducing a saturation of 800 ms duration) is comparable in terms of estimation errors to a train of N=60 MT pulses (of 2400 ms duration). This is in contrast to uniform sampling (figure 5.2a), showing instead a strong dependency on N. As expected, errors on fitted parameters are reduced in the optimized protocol compared to the uniform protocol.

The length N=25 was identified as the threshold at which parameter errors cease to display dependency on pulse train duration, for the given configuration (τ, Δt), and was therefore used as the optimal length N_{opt} in the subsequent experiments.

Results of the heuristic search for optimal parameters τ_{opt} and Δt_{opt} are shown in figures 5.3a and 5.3b respectively. Individual parameter contributions and the total cost function V show similar trends in both tests (varying τ at fixed Δt, and varying Δt at fixed τ). Evidence from the combinations tested (τ, Δt) shows that optimal values for both τ and Δt at N_{opt}=25 are between 15 ms and 20 ms. We therefore chose (τ_{opt}, Δt_{opt}) = (15 ms, 15 ms) as it produces a train of pulses of shorter duration.

Table 5.2 reports the K=14 optimized pairs (Δ, B_1) selected by CRLB minimization with τ_{opt}, Δt_{opt}, N_{opt}=15 ms, 15 ms, 25; together with those defined through uniform sampling with τ_{uni}, Δt_{uni}, N_{uni}=15 ms, 15 ms, 50. Optimized sampling included points at high B_1 values, close to the maximum allowed ($\sim$12 μT producing an effective flip angle θ_{max}=1480°),

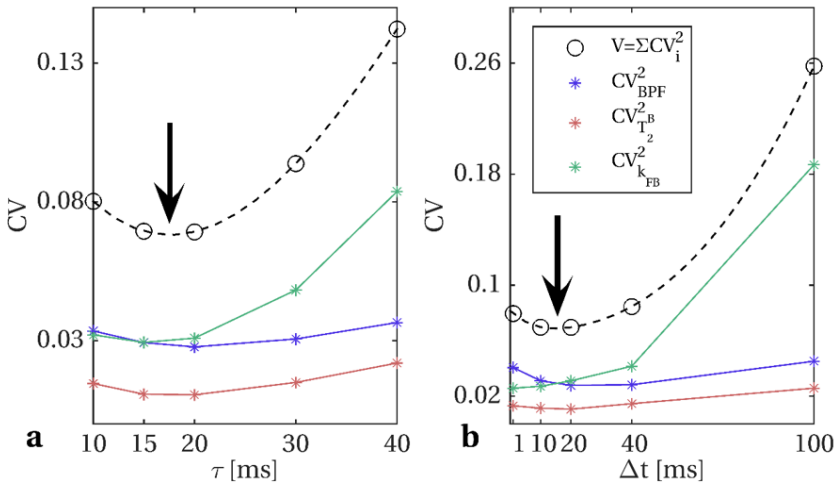

Figure 5.3: Heuristic search for optimal pulse duration (τ) and pulse gap (Δt), at optimal train length N_{opt}=25. Optimal cost function V values for different τ at fixed Δt=20 ms, and different Δt at fixed τ=20 ms are shown in **a** and **b** respectively. Spline interpolation between tested configurations is added to the graph (**dashed** lines), to guide the choice of τ_{opt} and Δt_{opt}. The individual contribution of each parameter to the cost function, given by the square of the theoretical *CV* (obtained from CRLB), is also shown for *BPF* (**blue**), $T_2{}^B$ (**orange**) and k_{FB} (**green**). Arrows indicate approximate location of minimal value of V as a function of the inspected parameters.

and low B_1 values. Various frequency offsets are selected, between 1 kHz and ∼2 kHz, as well as at higher values (i.e. 13-14 kHz).

Results from Monte Carlo simulations are shown in figure 5.4 for optimized and uniform protocols. CRLB minimization is reflected by a reduction in the variance of parameter errors in simulations, which is consistent at different *SNR* levels, and becomes more pronounced at lower *SNR*. Simulations show that improvements are expected for all the model

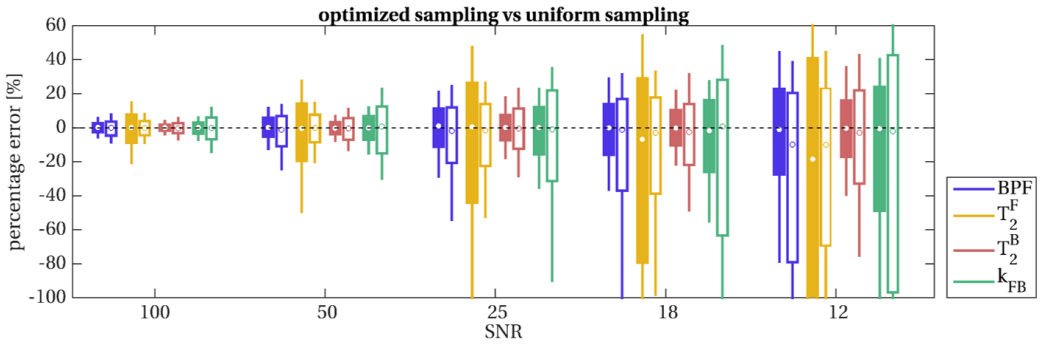

Figure 5.4: Percentage errors on fitted parameters obtained from Monte Carlo simulations for uniform (**unfilled** boxplots) and optimal (**filled** boxplots) protocols at different *SNR* levels. The optimal protocol produces unbiased and more precise estimates for all the parameters considered: *BPF* (**blue**), $T_2{}^B$ (**orange**) and k_{FB} (**green**). Improvements are consistent at every *SNR* level, including realistic scenarios for spinal cord imaging (*SNR*<25). Estimation of $T_2{}^F$, on the other hand, is more precise for the uniform protocol.

parameters included in the optimisation (*BPF*, $T_2{}^B$ and k_{FB}), with a stronger effect on the exchange rate k_{FB}. $T_2{}^F$ is found more precisely estimated in the uniform protocol than the optimized protocol. However, its inclusion in a further optimization does not improve estimation of the remaining model parameters when compared with the optimized protocol proposed here, as shown in figure 5.5.

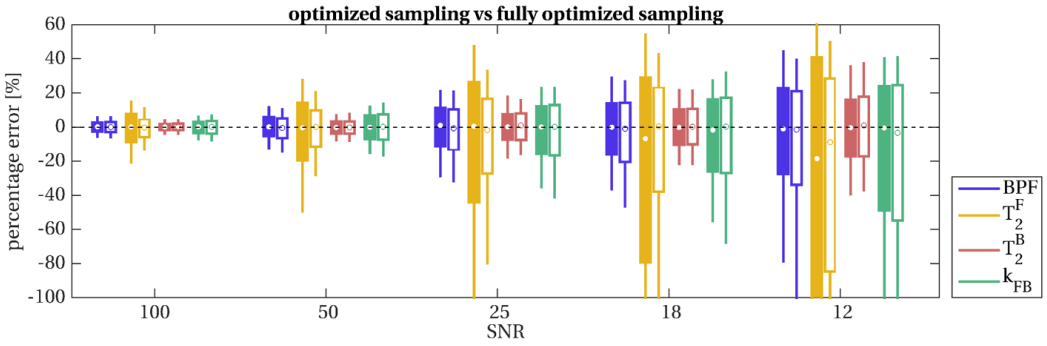

Figure 5.5: Percentage errors on fitted parameters obtained from Monte Carlo simulations for optimized protocol without including $T_2{}^F$ (**filled** boxplots) and full optimized protocol including $T_2{}^F$ (**unfilled** boxplots) at different *SNR* levels. The effect of a noisier estimation of $T_2{}^F$ does not affect other parameter estimates when sampling schemes are optimized, even at low *SNR*. Variance of errors on the remaining model parameters is in fact comparable in the two cases, with precision of k_{FB} being more effectively improved when optimization does not include $T_2{}^F$.

Optimized and uniform protocols show a similar dependency on B_1 errors (figure 5.6b). On the other hand, the optimized protocol appears more robust to B_0 errors compared to the uniform one, with distributions of parameters errors within the range [-10%, +10%] for *BPF*, $T_2{}^B$ and k_{FB}, for B_0 variations up to 50 Hz (figure 5.6a).

Figure 5.7 shows parametric maps for both the uniform and optimized protocols for all model parameters, from a few example slices in different subjects.

Improved spatial homogeneity is visible in k_{FB} and $T_2{}^B$ maps estimated from the optimized protocol. On the contrary, $T_2{}^F$ appears smoother when estimated from uniform sampling. Furthermore, systematic differences can be noticed between uniform and optimized protocol maps. $T_2{}^B$ seems to be underestimated in the uniform protocol, confirming the trend seen in simulations shown in figure 5.4 at decreasing *SNR*.

Table 5.3 shows mean and standard deviation for qMT model parameters and $T_1{}^{obs}$ for each subject, the inter-subject *CV* of means, and reproducibility indices calculated voxelwise for the repeated scan, over the whole upper cervical cord (levels C1-C4).The effect of the protocol optimization procedure can be straightforwardly appreciated by comparing the standard

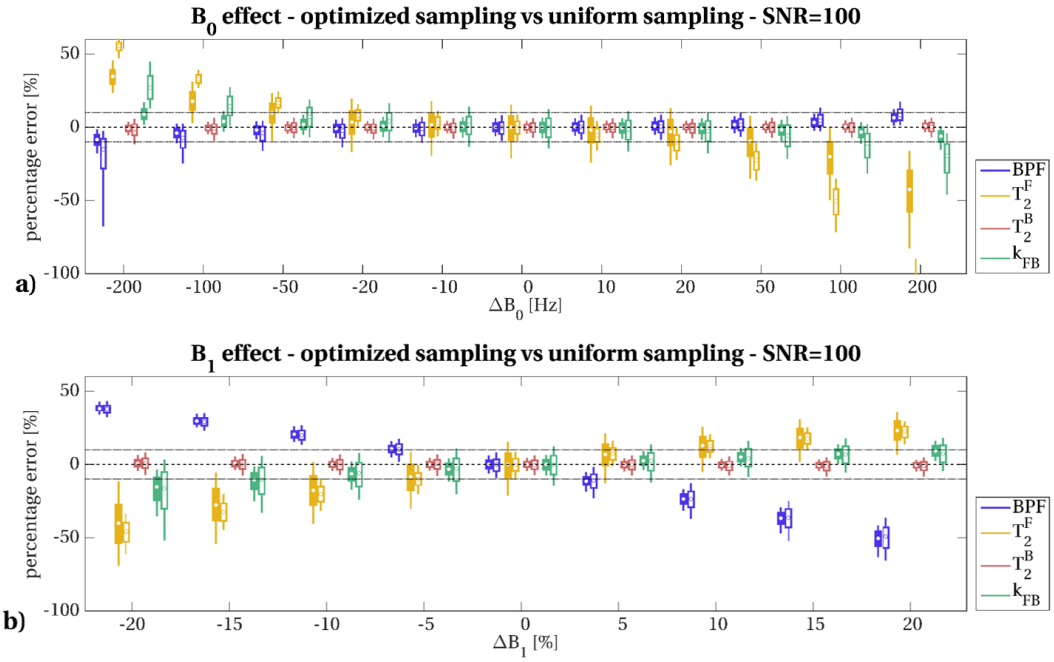

Figure 5.6: Effect on qMT model parameter estimates of simulated errors on MT pulse offset frequency (Δ) in panel **a**, and MT pulse amplitude (B_1) in panel **b**, for both optimized and uniform protocols (**filled** and **unfilled** boxplots, respectively). Errors were introduced by adding a shift in the offset frequency (ΔB_0= -200, -100, -50, -20, -10, 10, 20, 50, 100, 200 Hz) or a scaling factor (ΔB_1=0.8, 0.85, 0.9, 0.95, 1.05, 1.1, 1.15, 1.2), to the pulse amplitude respectively while generating synthetic signals (at *SNR*=100). Nominal values for Δ and B_1 were instead used in the fitting. The optimized protocol appears more robust than the uniform protocol to B_0 errors, with *BPF*, ${T_2}^B$ and k_{FB} error distributions within the [-10%; 10%] error range for the B_0 variations expected in the spinal cord (up to 70 Hz). Both protocols appear to be similarly affected by B_1 errors, with trends replicating previous findings on the effects of B_1 errors on qMT model parameters [200].

deviation over the whole cord of parameter estimates, which are substantially reduced for ${T_2}^B$ and k_{FB} in each subject, as shown by table 5.3.

Reproducibility indices are shown as parametric maps in figure 5.8. The Kolmogorov-Smirnov test confirmed that ${T_2}^B$ and k_{FB} were significantly more reproducible for the optimized protocol compared to the uniform protocol (P value $<<0.05$). No difference was detected for *BPF* reproducibility. ${T_2}^F$, although not included in the optimization, showed a statistically significant higher reproducibility (P $<<0.05$) when using the uniform sampling.

Figure 5.9 shows distributions of model parameters for uniform and optimized protocols, pooled among subjects, confirming findings provided by the single subject reproducibility test.

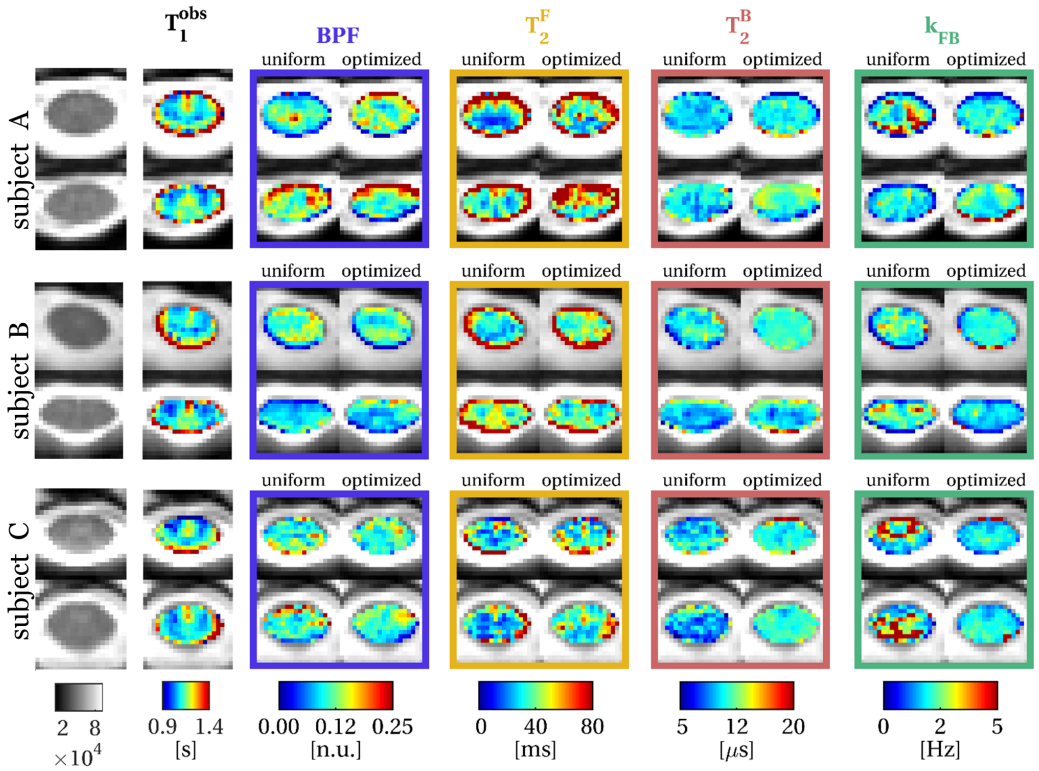

Figure 5.7: Spinal cord $T_1{}^{\text{obs}}$ (**black**), *BPF* (**blue** box), $T_2{}^{\text{F}}$ (*yellow* box), $T_2{}^{\text{B}}$ (**orange** box) and k_{FB} (**green** box) maps in 2 example slices from different subjects. For qMT parameters, maps obtained from both uniform and optimal protocol are shown. Greater spatial homogeneity is appreciable in k_{FB} maps obtained from the optimal protocol.

5.4 Discussion

This chapter describes a novel framework for qMT experiments in vivo in the cervical spinal cord that minimizes the number of assumptions in the analysis. The major challenges limiting the application of qMT in the spinal cord to date are: (*i*) the need for high-resolution data to depict the spinal cord in detail; (*ii*) the acquisition of enough data-points to accurately and reproducibly estimate all the model parameters (*BPF*, $T_2{}^{\text{F}}$, $T_2{}^{\text{B}}$ and k_{FB}) and $T_1{}^{\text{obs}}$; and at the same time (*iii*) the need to keep the overall protocol duration within clinically acceptable limits. The framework we propose allows these challenges to be tackled with higher flexibility than solutions that have been investigated so far.

5.4.1 Sequence and signal modelling

Spinal cord coverage and in-plane resolution needs are addressed by the use of the ZOOM-EPI readout, as described in section 3.2. Time-efficient generation of MT-weighting is

		Parameters				
subj	prot	***BPF***	T_2^F	T_2^B	k_{FB}	T_1^{obs}
		[n.u.]	[ms]	[μs]	[s-1]	[s]
i	*unif*	0.12(0.04)	38.7(26.9)	11.5(3.0)	2.71(1.54)	1.11(0.10)
	opt	0.12(0.04)	45.1(27.0)	11.1(1.6)	1.88(0.48)	
	I_{unif}	**0.74(0.17)**	**0.66(0.23)***	**0.83(0.11)**	**0.57(0.27)**	**0.94(0.05)**
	I_{opt}	**0.74(0.16)**	**0.62(0.23)**	**0.87(0.13)***	**0.81(0.20)***	
ii	*unif*	0.11(0.03)	38.3(22.0)	10.7(2.5)	2.41(1.25)	1.13(0.12)
	opt	0.11(0.04)	46.7(21.3)	11.3(1.9)	1.95(0.66)	
iii	*unif*	0.13(0.05)	36.7(21.0)	11.1(2.5)	2.20(1.30)	1.15(0.10)
	opt	0.12(0.05)	44.6(27.2)	10.6(1.4)	2.04(0.75)	
iv	*unif*	0.10(0.03)	46.6(26.0)	9.9(2.3)	2.50(1.17)	1.14(0.10)
	opt	0.10(0.03)	49.1(21.9)	11.0(1.0)	1.90(0.52)	
v	*unif*	0.12(0.04)	43.0(28.8)	10.4(2.6)	2.56(1.38)	1.14(0.16)
	opt	0.11(0.03)	46.9(25.9)	11.1(1.7)	1.99(0.53)	
Mean	*unif*	**0.12(0.01)**	**40.7(3.6)**	**10.7(0.6)**	**2.47(0.17)**	**1.13(0.01)**
sd	*opt*	**0.11(0.01)**	**46.5(1.6)**	**11.0(0.2)**	**1.95(0.06)**	
CV_{inter}	*unif*	**7.37%**	**8.93%**	**5.27%**	**6.78%**	**1.03%**
	opt	**7.31%**	**3.36%**	**2.14%**	**2.87%**	

(*) statistically significant (P value <0.05)

Table 5.3: qMT model parameters estimated in the cohort of five subjects for uniform (**first** row) and optimized (**second** row) protocols. Whole cord mean and standard deviation (in brackets) are reported. Means and standard deviations of the reproducibility index, calculated using equation 5.5, are also shown for subject *i*. (*) refers to significantly improved reproducibility as measured by the Kolmogorov-Smirnov test (P value <0.05) on distributions of I over the whole cord for either the uniform or optimized protocol when compared to one another. Inter-subject mean and CV are given at the bottom.

achieved by adding a train of off-resonance pulses prior to the acquisition of a package, exploiting the intrinsic constraints $TR >> T_1$ of the ZOOM-EPI sequence. Such a scheme allows the acquisition of a single MT-weighted data-point in $\sim$ 20 s, for the typical cervical cord coverage and resolution used in quantitative studies (i.e. 6-8 cm as coverage in the foot-head direction, using 5 mm as slice thickness).

Two main features, specific to this approach, are introduced regarding the MT-weighting: (*i*) a time dependency (i.e. the length of the off-resonance saturation); (*ii*) a spatial dependency (i.e. the slice position within a package).

When using MT-ZOOM-EPI, generating the steady-state MT effect (by applying trains of pulses with duration of the order of seconds) would compromise the claimed time efficiency of the sequence. CRLB optimizations, though, clearly demonstrate that even if MT weighting depends on pulse train length, the effect the latter has on model parameter estimates is greatly reduced when MT-weighted sampling points are optimized, resulting in similar

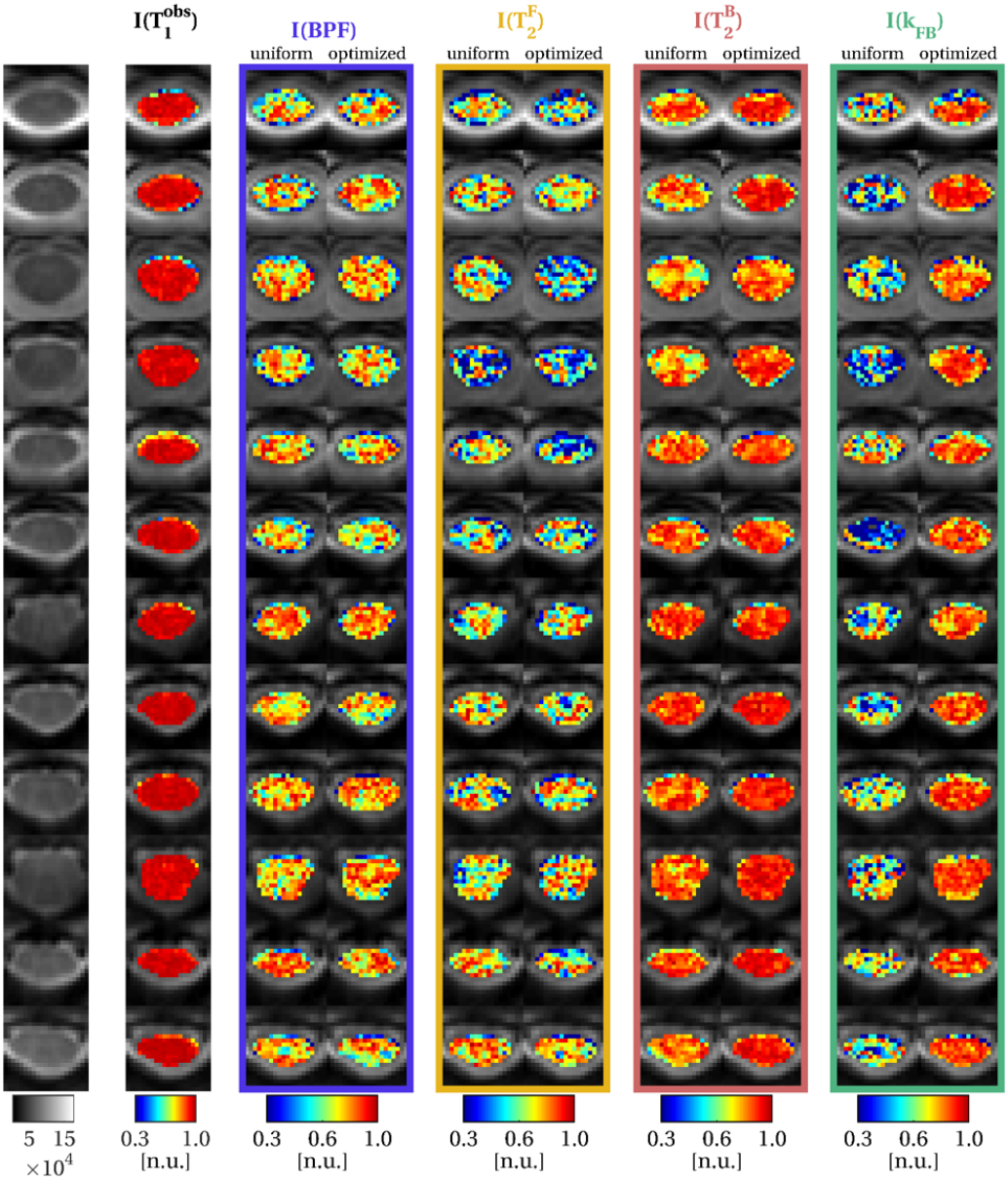

Figure 5.8: Reproducibility index maps for $T_1{}^{obs}$ (**black**), *BPF* (**blue** box), $T_2{}^{F}$ (**yellow** box), $T_2{}^{B}$ (**red** box) and k_{FB} (**green** box) in all the slices acquired (from C1 at the top to C4 at the bottom) for uniform and optimized protocols. Reproducibility index I for a given parameter p is calculated from the three repeated acquisitions using equation 5.5, and ranges between [0,1] (the higher, the more reproducible the metric is). Improved reproducibility of parameters with the optimized scheme are found for $T_2{}^{B}$ and k_{FB} . No differences are detected for *BPF*, while $T_2{}^{B}$ shows higher reproducibility in the uniform protocol. Note also the exquisite reproducibility of the $T_1{}^{obs}$ estimates obtained with the matched readout IR sequence used in this study.

performances between pulse trains of different N. Figure 5.2 is representative of such an effect.

In the proposed sequence, the MT weighting varies among slices belonging to the same

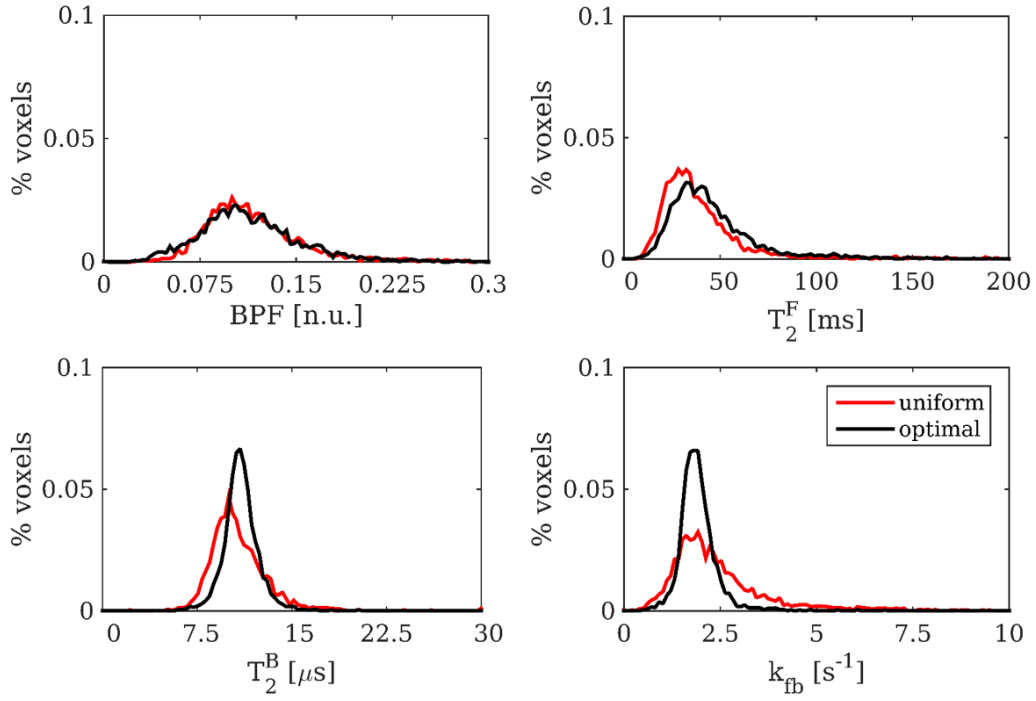

Figure 5.9: Pooled histograms of model parameters over the cohort of 5 subjects for uniform (**red** distributions) and optimized (**black** distributions). Protocol optimization produces narrower distributions for ${T_2}^B$ and k_{FB}, confirming evidence from the single subject reproducibility study.

package, as these are collected sequentially following the same preparation train: an increasing effect of T_1 relaxation is expected to reduce MT weighting for slices acquired later on. This fact will introduce bias in the quantitative analysis, if not properly addressed. However, the slice order can be shuffled in each sequence repetition to homogenize the MT weighting across different data-points [147, 120]. Shuffling can also be performed within signal averaging repetitions, provided that the number of averages is a multiple of N_{spp}, resulting in homogeneous MT weighting across slices for each MT-weighted data-point. This latter solution has been considered when designing the qMT protocol developed in this chapter for spinal cord imaging.

Furthermore, normalizing the MT-weighted signal by an M_0 image obtained with the same slice-shuffling mechanism provides an inherent correction for the additional MT weighting arising from the multislice acquisition module employed after the MT preparation, which could be up to 8% of the full signal for the particular sequence used in this study, as shown by simulation results summarized in figure 5.10. When such a normalization is used, the difference between model predictions and the simulated signal, accounting for inter-slice

on-resonance MT effect, was always below 0.6% over a wide range of sampling points and tissue parameter configurations in simulations, as shown in figure 5.11.

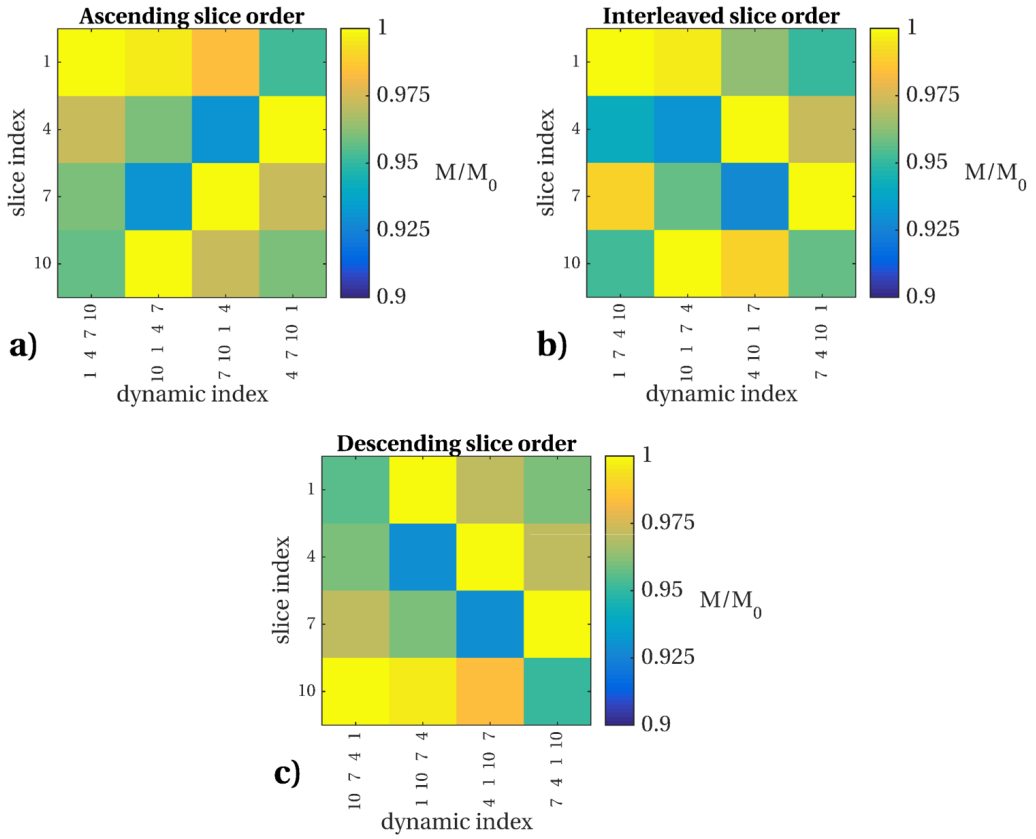

Figure 5.10: Effect of off-resonance saturation due to a train of on-resonance SE modules in a multislice acquisition, simulated within a package of ZOOM-EPI acquired with ascending (**a**), interleaved (**b**) and descending (**c**) order. Signal intensity for each slice in the package (numbers 1, 4, 7, 10) is plotted along the rows, whereas each column represents a different sequence repetition, where the slice order is shuffled. The actual slice acquisition order of each repetition is reported at the bottom of each column. The MT effect was simulated using the two-pool model and results were averaged over 100 combinations of model parameters (randomly sampled from distributions of $BPF \sim$N(0.13, 0.02), $T_2{}^F \sim$N(46.5 ms, 5 ms), $T_2{}^B \sim$N(11 μs, 1 μs), $k_{FB} \sim$N(1.95 s^{-1}, 0.2 s-1), and $T_1 \sim$N(1.1 s, 0.1 s). The effect of other slices in the package being off-resonance during on-resonance SE can be visualized for the MT-ZOOM-EPI sequence used in this study. However, given the limited number of slices per package (N_{spp}=4), and the relatively long interval between on resonance excitations (Δt_s=91 ms), this additional saturation was found not to exceed 8% of the unsaturated signal in all the simulated cases.

The additional degrees of freedom in the acquisition (N and t_d) are accounted for by implementing an appropriate model, first described by Portnoy et al. [48] and further developed for in vivo qMT in the brain [52]. This model was essential to achieve unbiased parameter estimates for images acquired before a steady-state is established (e.g. when using short

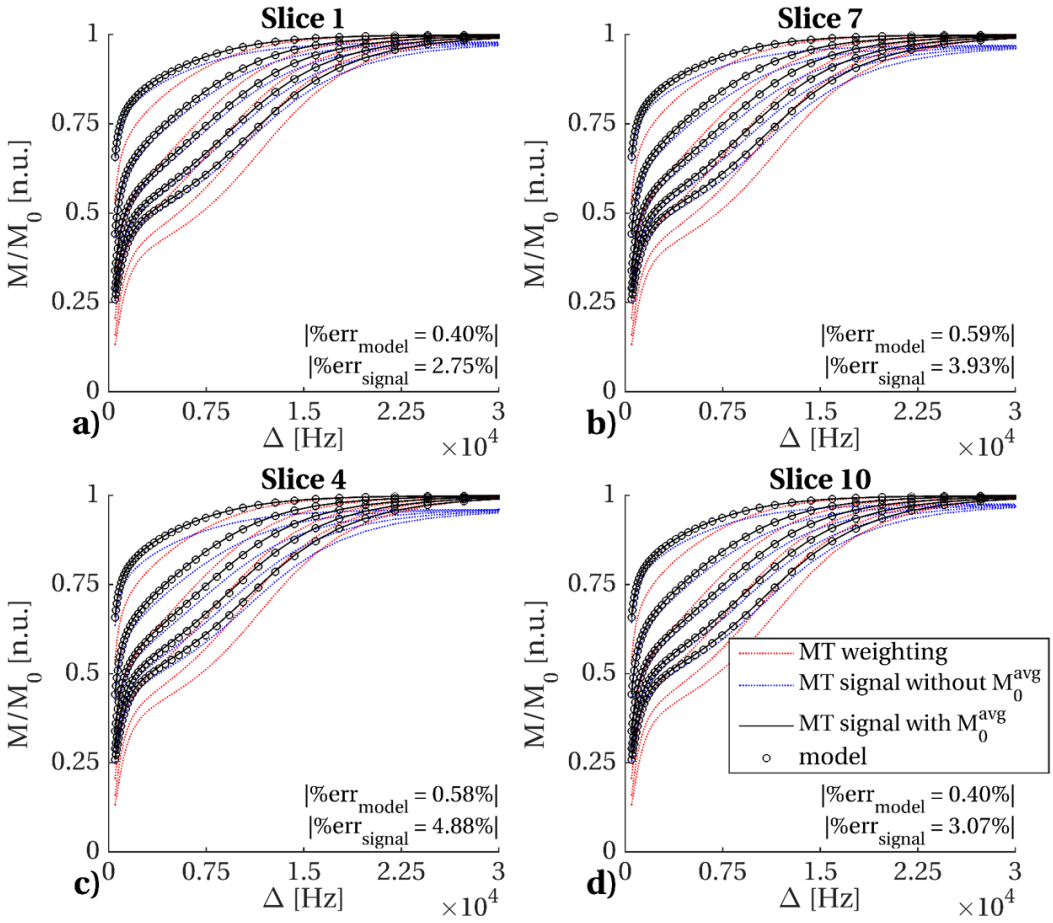

Figure 5.11: Simulations of the effect of off resonance saturation due to on resonance SE multislice acquisition on quantitative modelling. MT weighting produced by a train of N=25 pulses at 5 different flip angles (370°, 650°, 930°, 1205°, 1485°) for 50 offset frequencies, logarithmically spaced between 500 Hz and 100 kHz, is shown in **red**. The acquired signal undergoes longitudinal relaxation due to the varying distance between the end of the pulse train and on-resonance excitation, averaged among different delays t_d, and concomitant off-resonance saturation due to on-resonance SE, dependent on the current slice position within the package. The full MT signal is shown in **blue**. Prior to model fitting, MT-weighted images are normalized to a reference image, M_0, acquired with the same shuffling strategy. Normalized MT-weighted signal is shown in **black**. For quantitative parameters estimation, on-resonance induced saturation is neglected and only the effect of averaging between different t_d is taken in to account. Model predictions are shown by the **black** dots. It can be appreciated how the normalization with an averaged M_0 provides a correction for the inter-slice MT effect (which is inherently present in the normalization term), resulting in only minor discrepancies between the acquired signal and model predictions (average errors over all data points and 50 different tissue configurations is below 0.6%). The normalization corrects for most of the difference between model predictions (**black** dots) and MT signal (**blue** lines) as shown by the greatly reduced average errors (from ∼4% to ∼0.6%). All slices in a ZOOM-EPI package are shown in different panels (interleaved order in the acquisition is assumed).

trains of pulses) and during transient evolution of the magnetization (producing different t_d), as shown in figure 5.4 where width of error distributions is minimal at high *SNR*, independently from the type of protocol used.

The framework is integrated with a separate T_1 measurement obtained from the IR-ZOOM-EPI sequence described in chapter 4, therefore adopting the same readout used for MT-weighted acquisition. In this way, the co-registration step is greatly improved, given similarities between the two datasets (also in terms of EPI-like distortions). This is essential to minimize error propagation into qMT parameters due to potential registration errors with the estimated T_1 maps. In general, the choice of ZOOM-EPI to carry out qMT examination enables images with additional contrast, such as diffusion-weighted images, to be acquired in the spinal cord in the same fashion for further multi-parametric analysis. Furthermore, the development of qMT with a rFOV approach could prove beneficial in other challenging imaging environments, such as cardiac, prostate, optic nerve and musculoskeletal imaging.

5.4.2 Protocol optimization and model parameters estimation

The numerical model used here, whilst introducing a considerable computational burden, gives full control on sequence parameters, which we try to exploit through protocol optimization techniques. qMT protocol optimisation has already been investigated in previous studies [189, 197, 198, 191] where sampling schemes were optimized by selecting Δ and θ using standard analytical models. Here, we considered a more general MT model and used CRLB theory to optimize Δ and B_1, while the remaining sequence parameters (N, τ_{opt}, Δt_{opt}) were selected by searching for their best combinations. We cannot disregard the possibility that the heuristic approach followed to determine (τ_{opt}, Δt_{opt}, N_{opt}), could lead to suboptimal protocols. Ideally, a simultaneous optimisation of all sequence parameters would be preferable, but this would require substantial modifications to the SOMA algorithm, in order to account for the interdependencies between different sequence parameters to be optimized.

An intermediate approach between the heuristic search implemented here and a full optimization of $\mathbf{p}_s$ would be to optimise sampling points split among more configurations of (τ, Δt, N). As shown in figures 5.3a and 5.3b, expected *CV*s for individual parameters follow different trends at varying τ and Δt: optimisation of *BPF* tends to favour slightly longer τ and Δt, while k_{FB} benefits from shorter pulse repetition time (τ+Δt). Similarly, from figure

5.2, *BPF* errors seem to stabilize at higher N compared to k_{FB}. The single configuration for (τ_{opt}, Δt_{opt}, N_{opt}) chosen in this study, based on the trend of the overall cost function value V, could have contributed to the lack of clear improvement that we observed in the *BPF* in vivo.

Alternatively, protocol optimization could be used to target only a specific parameter [197], by nulling other entries in the weights vector $\mathbf{w}$. This could allow the definition of reduced protocols to robustly estimate *BPF*, while still performing a full qMT model fitting, without introducing any limiting assumptions on other model parameters.

The pattern of optimized sampling points reported in table 5.2 shows interesting similarities with previous qMT protocol optimizations using CRLB with analytical models [189, 197]. Common features are the presence of repeated points (we counted 8 approximately unique points), the sampling at very high Δ values (that are likely to produce very little MT saturation), as well as points at the lowest offset allowed (Δ=1 kHz). The presence of nearly repeated sampling points could be an indicator of the possibility of reducing K, and hence the scan time, without sensibly affecting parameter estimates.

The definition of an optimal protocol requires the use of a specific combination of $\mathbf{p}_m$ to compute V, suggesting a dependence of the optimal sampling scheme on the set of $\mathbf{p}_m$ used. We cannot exclude such a dependency in the proposed optimized protocol, however results from Monte Carlo simulations in figures 5.2, 5.4 and 5.6 show that optimization is robust to perturbations on the combinations used, as the optimized protocol consistently outperforms the uniform protocol in terms of parameter errors.

Protocol optimization was validated in vivo by computing an index of reproducibility (I). This index can be used as a metric to compare optimized and uniform sampling and gain insight into the intrinsic reliability of parameter estimates when using the numerical model. The uniform sampling can be taken as an example of a standard qMT protocol, adapted for the sequence developed in this study. Reproducibility indices of qMT model parameters confirm considerations originally shown by Portnoy *et al.* [48]: ${T_2}^B$ is the best constrained parameter in the two-pool model, followed by *BPF*, ${T_2}^F$ and k_{FB}. Difficulties in estimating the latter two parameters have already been reported [189].

The protocol optimisation procedure implemented in this study shows beneficial effects on ${T_2}^B$ and k_{FB} calculated from in vivo data. Estimation of the latter parameter is particularly improved (I increases from 0.57 to 0.81), and its reproducibility is comparable to ${T_2}^B$ and is

higher than *BPF*. While the biological meaning of the parameter is not yet fully known, k_{FB} has recently received more attention following findings that relate it to inflammation [201] and metabolism [182]. Surprisingly, *BPF* was found to be insensitive to protocol optimization in the in vivo experiment (I(*BPF*)=0.74 for both uniform and optimized sampling), in contrast to the other model parameters whose reproducibility was significantly affected (I is increased for ${T_2}^B$ and k_{FB}, or decreased for ${T_2}^F$).

As it can be qualitatively appreciated in figure 5.7, and more quantitatively in figure 5.9, the optimization procedure also produced systematic differences in parameter estimates, especially in ${T_2}^B$ and ${T_2}^F$. This has already been observed in a previous study on optimization of qMT parameters [189], and is predicted by simulations reported in figure 5.4 which shows an improvement in the accuracy of parameter estimation (included in the optimization) at low *SNR*. This underlines the importance of implementing protocol optimization techniques when operating at low *SNR* levels (e.g. for spinal cord imaging).

The reduced reproducibility of ${T_2}^F$ in the optimized protocol is a direct consequence of its exclusion from the optimization. However, estimates of *BPF*, ${T_2}^B$ and k_{FB} are not affected by a less effective estimation of ${T_2}^F$ as shown via simulations in figure 5.4, and do not improve when the parameter is included in the protocol optimization, as reported in figure 5.5. While estimates of ${T_2}^F$ should be considered with caution, especially at low *SNR*, this approach appears more robust than fixing ${T_2}^F$ via constraints, as instead performed in some previous studies [165, 185].

When compared with previous findings in the spinal cord, which are summarized in table 5.4, qMT parameters estimates lie within the range expected for healthy subjects, with a slightly lower *BPF* range, and slightly higher ${T_2}^F$ than previously reported values.

The spinal cord *BPF* maps produced here do not provide the typical WM/GM contrast found in the brain, as reproduced in figure 5.12 where the optimized qMT framework was used for zoomed imaging of the brain. The exacerbated physiological noise characterizing the spinal cord environment, the achievable spatial resolution, which is quite coarse considering the much smaller, detailed anatomy of the spinal cord (with GM extending for only a limited number of voxels), as well as potential spatial inaccuracies arising from B_0 and B_1 errors surely play a major role in blurring *BPF* contrast. Aside from technical considerations, assuming that the *BPF* is mainly associated with myelin, such differences may also be inherently less pronounced compared to the brain, as shown by histological

	BPF *[n.u.]*		T_2^F *[ms]*		T_2^B *[μs]*		k_{FB} *[s^{-1}]*	
	WM	**GM**	**WM**	**GM**	**WM**	**GM**	**WM**	**GM**
1.5 T								
[183]	0.12	0.07	not estimated		9	9	7.84	5.36
3 T								
[202]	0.18	0.09	24**	35.4**	11*	11*	1.71	1.1
[165]	0.16	0.14	29.9***	32.6***	10.8	10.8	1.7	1.46
[165]	0.16	0.13	not estimated		not estimated		not estimated	
this study	**0.11**		**46.5**		**11**		**1.95**	
7 T								
[186]	0.12	0.11	not estimated		10(*)	10(*)	2.59	1.85

(*) fixed

(**) estimated from constraint $T_2^F R_1^F$=0.024, where R_1^F is fixed to 1 s^{-1} and 0.7 s^{-1} for white matter and grey matter respectively (from literature).

(***) estimated from constraint $T_2^F R_1^F$=0.0232, where R_1^F is derived from measured R_1^{obs} equal to 0.806 s^{-1} and 0.752 s^{-1} in white matter and grey matter respectively.

Table 5.4: qMT parameter estimates in the spinal cord obtained from the current study using the optimized framework, and from previous studies (single values refer to whole cord, instead of white matter and grey matter ROIs).

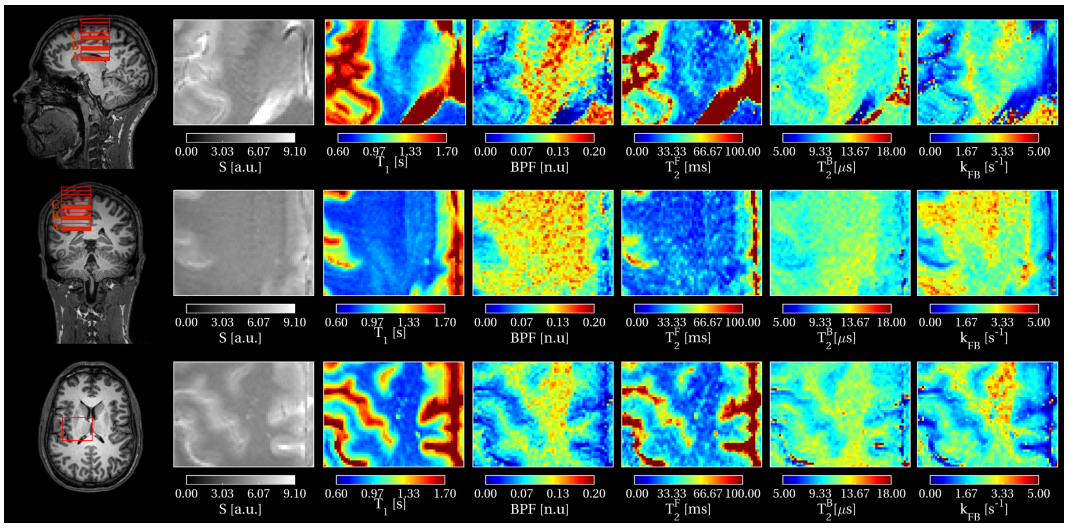

Figure 5.12: Reduced FOV image of the brain displaying WM/GM interfaces, T_1 maps from Inversion Recovery and qMT parameter maps. The identical optimized protocol as that developed for the spinal cord was applied on a localized region of the brain, showing the ability of the framework to differentiate tissue types producing the expected contrast for brain qMT parameters. Specifically, clear contrast in the *BPF* map between GM and WM can be observed. Three example slices **a**, **b**, and **c** (see **left** for slice positions) are shown along figure rows.

studies [203, 204], where rather uniform intensity maps were observed following staining for myelin. We aim to further the understanding of spinal cord myelination through a post mortem study of the human spinal cord, presented in chapter 6.

5.4.3 Limitations and future improvements

Through CRLB optimization we aimed to provide a guide in the definition of sequence parameters for the proposed framework, where additional degrees of freedom in the sampling scheme are available. More work is needed to refine the definition of the acquisition protocol through a more rigorous protocol optimization, both to achieve substantial improvement in the estimation of *BPF*, and to reduce the number of the data points K without degrading precision of estimates.

The use of an EPI-based readout enables the combination with further imaging acceleration techniques, such as simultaneous multislice imaging, that has been shown to be compatible with the ZOOM-EPI sequence [124] (see also preliminary data in section 3.4.3).

We remark that we did not address in vivo issues related to field inhomogeneities (B_0 and B_1 errors). While these inhomogeneities translate into discrepancies between nominal and actual B_1 and Δ, and hence inaccuracies in model parameters, especially *BPF*, ${T_2}^F$ and, to a lesser extent, k_{FB} (see figure 5.6), precise characterization of these variations is not straightforward in the spinal cord, and previous studies have reported difficulties in mapping them accurately at the spinal level [60]. Additionally, these factors are known to vary smoothly in space and therefore are usually acquired with sequences at coarser resolution ($\sim 3\times 3$ mm^2 in the axial plane), resulting in a limited number of pixels available for their characterization within the cord. These variations are expected to be of a similar size in both the optimized and uniform protocols, since both protocols were acquired within the same scanning session. Different sampling patterns can result in different sensitivities of qMT parameters estimates to such errors. The optimized protocol was in fact found to be more robust to errors in Δ than the uniform protocol, most likely due to the non-systematic sampling of the offset frequencies. However, improvements in the acquisition strategy to minimize (e.g. via dynamic shimming, or slice-wise shimming), or robustly map these field inhomogeneities are warranted towards an absolute quantification of qMT model parameter in the spinal cord.

Future work will necessarily focus on the addition of adequate B_0 and B_1 mapping techniques to the framework.

In the framework presented in this chapter, signal average was performed without any preprocessing step to correct for potential motion between repetitions. Future improvements

will seek to incorporate a motion correction step within the signal averaging mechanism. The advantage of performing signal averaging in the *image* domain instead of in the *k*-space domain will also be tested. Similarly, the adaptation of the quantitative framework developed here to a cardiac-gated acquisition, as the one described in section 3.4.2, should be investigated to minimize artefacts from physiological noise that could potentially propagate to parameter estimates.

5.5 Conclusion

The framework proposed allows robust assessment of qMT model parameters in the cervical spinal cord. The framework includes a dedicated sequence to measure longitudinal relaxation time, is suitable for multi-modal studies to fully characterize spinal cord microstructure, and is applicable to other anatomical environments where rFOV imaging is advantageous. For the first time parametric maps of qMT model parameters have been shown in vivo in the spinal cord, and their reproducibility assessed. Protocol optimization techniques have been used to guide the definition of sampling schemes with the aim of reducing protocol length while improving parameter precision.

While the specific framework developed here relies on a specific custom sequence, i.e. MT-ZOOM-EPI, the overall combination of sequence, signal model and protocol optimization can be reproduced for any qMT approach proposed in literature.

Correlative studies with histology are, in general, essential for any quantitative MRI methods, and even more so for the framework developed here given the substantial novelty introduced by the proposed approach and the lack of extensive literature results for a comparative study. This will be covered in the next chapter, where the qMT method presented here together with other supposedly myelin-sensitive quantitative MRI techniques, are compared in post mortem spinal cord tissue, as an initial stage toward a full comparison with quantitative histology-derived indexes.

Chapter 6

Comparison of prospective myelin biomarkers in the post mortem healthy and Multiple Sclerosis spinal cord

In this chapter, results from a quantitative MRI examination on post mortem MS spinal cord tissues are presented. Most of the techniques introduced in section 2.2 are here applied to the MS post mortem spinal cord. The results shown in this chapter are part of a larger comparison study among myelin mapping MRI techniques, to be completed through correlation with quantitative histology. The final aim of the study is to assess the sensitivity and specificity of some of the most promising MRI methods for measuring myelin to the underlying tissue microstructure changes taking place during MS in the human spinal cord.

6.1 Introduction

The spinal cord is a common site of involvement in MS. The majority of patients with MS have, in fact, spinal cord lesions that are observable in T_2-weighted and T_1-weighted images. More importantly, spinal cord abnormalities are of high interest in a clinical setting because: (*i*) cord lesions without overt clinical outcomes are rare in other neurological diseases [205]; and (*ii*) spinal cord pathology is an important determinant of permanent neurological disability. The assessment of damage to the spinal cord in MS has therefore both diagnostic and prognostic value [4].

Although the sensitivity of MRI to spinal cord abnormalities is high, the association between MRI evidence and clinical findings remains poor. This fact has been ascribed to the lack of radiological changes to specifically correlate with different underlying pathological changes occurring in MS, such as demyelination, axonal loss, gliosis and inflammation

[206]. More advanced quantitative MRI methods able to assess non invasively several features of tissue microstructure have been applied to try to unmask different pathological processes. Their robust development for a widespread use in clinic is therefore urgently needed.

Quantitative MRI has the potential to provide higher specificity and sensitivity to the changes taking place at a microscopic level. In particular, quantitative MRI methods for investigating MS disease could help to: (*i*) improve the correlation between clinical findings and the extent of radiological involvement; and (*ii*) enhance sensitivity to early and diffuse microscopic damage.

In this context, post mortem studies offer a unique window of opportunity to evaluate the gain of adopting quantitative MRI methods to study MS. MRI findings can be validated against metrics calculated from histological images, where tissue properties can be isolated through dedicated staining at a resolution and precision that may exceed that of MRI by several orders of magnitude, therefore providing a *ground truth* for quantitative MRI metrics. MRI-histology correlative studies can be used to assess specificity and sensitivity of each quantitative MRI metric to particular microstructure features, such as myelin content, axonal density, axonal size, water content, etc.; in healthy tissue and, more importantly, in pathology. These types of investigation are needed even more in the spinal cord as the performance of different MRI indices to assess tissue microstructure is still largely uncertain, given the challenges associated with performing reliable and robust measurements of quantitative metrics in the spinal cord in vivo [7, 6].

So far, post mortem studies of the human spinal cord in MS involving quantitative MRI have been limited to relaxation times T_1, T_2 and $T_2{}^*$, magnetization transfer via the *MTR*, and diffusion weighted imaging using metrics derived from DTI [207, 208, 209]. Recently, a more advanced diffusion model, namely NODDI [210], has been validated in the MS spinal cord, where the degree of variability of axon orientations in white matter was suggested as a new biomarker for axonal pathology in MS [204]. Preliminary results on a single case were also reported for *MWF* [211].

In this study we focus on a specific aspect of MS disease: demyelination. The ability to quantitatively assess myelin content may have important repercussions, both for gaining insights into disease processes, and potentially for monitoring clinical therapy (where slowing down myelin loss, or promoting remyelination are among the main targets).

We consider a comprehensive battery of quantitative MRI metrics that have been reported to be sensitive to myelin content. We aim to elucidate, for each of the considered metrics, the degree of correlation with myelin content and the effect of additional microstructural features via histological validation, in the MS human spinal cord. Along with already investigated T_1, T_2 and T_2*, *MTR* and radial diffusivity (*RD*), we also included more advanced techniques, proposed as myelin biomarkers, namely: *BPF* from qMT model fitting (introduced in section 2.2.1.4, and developed for the spinal cord in vivo in chapter 5), *MWF* from myelin water imaging (introduced in section 2.2.2), *MTV* from quantitative proton density mapping (introduced in section 2.2.3), and MT_{sat} from the multi-parameter mapping method (described in section 2.2.1.5). These putative myelin biomarkers have as yet found limited application in the spinal cord in vivo, in healthy controls and/or MS population, and have either rarely or not yet been investigated in a validation study with histology. The dataset of this study thus represents a novel opportunity to further the understanding of how quantitative myelin sensitive MRI metrics relate to each other and to underlying tissue changes in MS, for the particular case of the human spinal cord. For the first time, in fact, a complete set of quantitative myelin mapping techniques is acquired and assessed against histology, simultaneously in the same study.

The following chapter covers only the first part of the aforementioned full validation study for MRI myelin biomarkers in the MS spinal cord. In particular, here we describe MRI data acquisition and analysis, we show several examples of quantitative maps for a variety of cases, and we investigate correlations between different quantitative MRI metrics. The last section of the chapter (section 6.5) instead outlines briefly how we plan to complete the validation with histology, and how we intend to investigate correlations between quantitative MRI metrics and measurements derived from histological images.

6.2 Methods

6.2.1 Specimens

Formalin fixed post mortem tissue from spinal cord of three non-demented controls and four MS tissue donors was used. Samples were obtained from the Netherlands Brain Bank (Amsterdam, the Netherlands). Samples were washed from fixative and stored in 10 $\frac{mmol}{L}$ phosphate buffered saline (PBS) solution for subsequent imaging at room temperature. Table 6.1 provides a summary of the details of all samples.

Samples details					
	age [*years*]	**sex**	**diagnosis**	**PM delay** [*hr:min*]	**pH**
i	72	f	healthy	6:50	7.22
ii	78	f	healthy	7:10	6.32
iii	60	f	healthy	8:10	6.58
iv	35	f	MS	10:20	6.37
v	61	f	MS	10:00	6.88
vi	70	m	MS	6:55	6.51
vii	56	f	MS	10.30	6.42

Table 6.1: Summary of the salient details for the post mortem samples scanned with the MRI protocol. Healthy controls (samples *i*, *ii* and *iii*) and MS cases (samples *iv*, *v*, *vi* and *vii*) were placed in two separate holders.

In order to allow the use of a small FOV, and hence improve the MRI protocol time efficiency, samples were placed in a four-compartment plastic holder: two separate holders were used: sample *i*, *ii* and *iii* in one holder; sample *iv*, *v*, *vi*, *vii* in another holder. Sample positioning for MRI is described in appendix B. MR-visible glue markers were placed on two sides of the plastic compartments (see appendix B) in order to ease the identification of different samples in the MR images.

6.2.2 MRI protocol

All specimens were scanned on a 3T Philips Achieva system (Philips Healthcare, Best, The Netherlands) with a 32-channel head coil, in two separate sessions (one for the healthy controls, one for the MS cases). Preliminary tests showed that the *SNR* was maximized if samples were laid on the lower surface of the coil instead of positioned in the center. Additionally, magnitude image reconstruction from a subset of selected coil images (with detectable amount of signal) did not introduce any visible improvements in terms of *SNR* compared to routine online magnitude reconstruction (data not shown).

A series of structural images were acquired sagittally and coronally using a multislice turbo SE sequence to facilitate the positioning of the stack of slices used for the quantitative MRI protocol, and to allow offline mapping of slice positions for subsequent histological procedures (see appendix B). Slices were as close to perpendicular as possible to the main sample direction (which could vary slightly between different samples), and placed to ensure coverage of interesting features, such as lesions.

The quantitative MRI protocol, with respective quantitative MRI metrics that can be derived, is summarized in table 6.2. All quantitative sequences shared the same imaging geometry.

Scan	Sequence	TE [ms]	TR [ms]	Resolution [mm^2]	Slices	Acceleration factor	NSA	Quantitative imaging	Duration	Parameters estimated
quantitative MT	multi-shot SE-EPI	22	3755	0.3×0.3	8 slices, 3mm thickness, 1mm gap, 2 packages	EPI factor 13, Partial Fourier factor 0.6	4	5 M_0 and 25 MT-w images (60 pulses saturating train, 5ms/1ms pulse duration/gap) at various offset frequency/pulse amplitude pairs[1]	2hr 30mins	**BPF** **T_2^B** **k_{FB}**
Inversion Recovery	multi-shot SE-EPI	22	3905	0.3×0.3	8 slices, 3mm thickness, 1mm gap, 2 packages	EPI factor 13, Partial Fourier factor 0.6	4	12 Inversion Times, from 20ms to 900ms, every 80ms	1hr 05mins	**T_1**
Diffusion	multi-shot SE-EPI	86	3500	0.45×0.45[2]	8 slices, 3mm thickness, 1mm gap	EPI factor 13, Partial Fourier factor 0.6	1[3]	12 b=0, b={1000, 2200, 3500, 4700, 6000}s mm^{-2} with {10, 16, 24, 29, 41} gradient directions	1hr 35mins	**RD**
Variable *TE*	multi-shot SE-EPI	24	3200	0.3×0.3	8 slices, 3mm thickness, 1mm gap, 2 packages	EPI factor 13, Partial Fourier factor 0.6	4	10 different TE, from 24ms to 114ms, every 10 ms	44min	**T_2**
Multi-parameter Mapping	2D spoiled GE	4	16	0.3×0.3	8 slices, 3mm thickness, 1mm gap	no	20	4 volumes acquired: PD_1-w (flip angle=9°), T_1-w (flig angle=25°), MT-w (flip angle=9°, TR=36ms) with off-resonance saturation (offset=1kHz, pulse angle=250°), and PD_2-w (flip angle=9°, TR=36ms)	35min	**R_1** **MT_{sat}** **MTR** **MTV** [4]
Multi-TE	2D spoiled GE	6	68	0.3×0.3	8 slices, 3mm thickness, 1mm gap	no	20	8 different TE, from 6ms to 62ms, every 8ms	23min	**T_2*** **MTV**[5]
Myelin water imaging	2D multi-echo SE	8	2500	0.3×0.3	8 slices, 3mm thickness, 1mm gap	Partial Fourier factor 0.75	2	32 different TE, from 8ms to 256ms, every 8ms	1hr 05min	**MWF**

[1] protocol optimized as described in chapter 5; [2]voxels reconstructed at 0.3×0.3mm^2; [3]diffusion protocols is repeated twice; [4]calculated using T_2^* from Multi-TE protocol; [5]calculated using R_1 from Multi-parameter mapping protocol

Table 6.2: Summary of the sequence parameters for the quantitative MRI protocol developed in this study, with the respective quantitative calculated metrics. Where not specified, a single package was used (meaning that all the prescribed slices are acquired within the same *TR*). Structural T_1-weighted and T_2-weighted scans, and B_1 and B_0 field mapping sequences were also performed in addition to the quantitative protocols listed in the table.

In addition to the quantitative sequences detailed in table 6.2, structural 3D isotropic T_1-weighted and T_2-weighted scans were also acquired. For the T_1-weighted acquisition the following parameters were used: 3D spoiled GE at $0.3\times0.3\times0.3$ mm^3 resolution, *FOV*=$38\times38\times90$ mm^3, *TR*=20 ms, *TE*=5.3 ms, flip angle=60°, *NSA*=8. For the T_2-weighted acquisition instead the sequence parameters were: 3D turbo SE with turbo factor=16, at $0.3\times0.3\times0.3$ mm^3 resolution, *FOV*=$38\times38\times90$ mm^3, *TR*=128 ms, *TE*=36 ms, flip angle=90°, refocusing angle=120°, Partial Fourier factor 0.6 (along one *P* direction), *NSA*=12.

B_0 and B_1 mapping were also performed to correct, when needed, quantitative MRI parameters for static and RF field inhomogeneities. In particular, the DAM (see section 2.2.5.2) (2D msh-SE-EPI, EPI factor=13, Partial Fourier factor=0.6, *TR*=4200 ms, *TE*=22 ms, *FOV*=38×38 mm^2, 0.3×0.3 mm^2 in-plane resolution, 8 slices at 3 mm thickness, 2 packages, *NSA*=4, repeated for flip angle=60°and 120°, total scan time: 11:50 minutes) was used for B_1 mapping, and the reversed EPI blip method [95] (multislice msh-SE-EPI, EPI factor=13, Partial Fourier factor=0.6, *TR*=3000 ms, *TE*=22 ms, *FOV*=38×38 mm^2, 0.3×0.3 mm^2 in plane resolution, 8 slices at 3 mm thickness, 2 packages, *NSA*=4 repeated for both polarity of blip gradients in the *P* direction of the EPI readout, total scan time: 8:25 minutes) was used for B_0 mapping.

6.2.3 Data Analysis

As indicated in table 6.2, a set of different quantitative MRI metrics can be calculated from each acquisition. Details of data analysis are briefly outlined in the following section. If not explicitly stated otherwise, data analyses are performed with custom-written software in Matlab 2015 (The Mathworks, Natick, MA).

6.2.3.1 Relaxation Times: T_1, T_2 and T_2^*

Relaxation times T_1, T_2 and T_2^* were estimated from their respective acquisitions (Inversion Recovery, variable *TE*, multi-*TE* acquisitions), using single relaxation time models:

$$S(TI) = |M_0^{(IR)}\left(1-2e^{-\frac{TI}{T_1}}\right)| \tag{6.1}$$

$$S(TE) = M_0^{(vTE)}e^{-\frac{TE}{T_2}} \tag{6.2}$$

$$S(TE) = M_0^{(mTE)}e^{-\frac{TE}{T_2^*}} \tag{6.3}$$

where $M_0{}^{(\mathrm{IR,mTE,vTE})}$ are the apparent proton densities estimated from the different acquisitions. Maximum likelihood estimation, with a Gaussian noise model, was used.

6.2.3.2 Bound proton pool parameters: BPF, $T_2{}^{\mathrm{B}}$ and k_{FB}

From the qMT acquisition, parameters characterizing the macromolecular pool (i.e.protons attached to macromolecules) are obtained: BPF, $T_2{}^{\mathrm{B}}$ and k_{FB}.

As reported in table 6.2, data were acquired with the same strategy outlined in chapter 5, but with ZOOM-EPI replaced by a msh-SE-EPI readout. The sampling of different offset frequencies and MT pulse amplitudes was optimized following the pipeline explained in section 5.2.3, accounting for the different tissue parameters values expected in the post mortem spinal cord following fixation. In particular the protocol optimization was found to be more effective when using longer trains of MT pulses, with shorter pulse durations and gaps, compared to in vivo (data not shown).

Parameter estimation was carried out using the numerical model described in section 5.2.2, with integration step η=100μs. A three-parameter fit approach was considered, where the free pool transverse relaxation time $T_2{}^{\mathrm{F}}$ was set to the T_2 estimated voxelwise from the variable TE acquisition, as previously performed in [119], and the T_1 obtained from the IR protocol was used as an external measurement for the observed relaxation time $T_1{}^{\mathrm{obs}}$, leaving the macromolecular pool parameters BPF, $T_2{}^{\mathrm{B}}$ and k_{FB} to be estimated from the data. A super-Lorentian lineshape for the bound pool was assumed. Pulse peak amplitude was corrected on a voxel-by-voxel basis during the fitting using the B_1 map estimated from the DAM acquisition. Maximum likelihood estimation, with a Gaussian noise model, was used.

6.2.3.3 Relaxation and Saturation: R_1, MT_{sat} and MTR

The standard multi-parameter mapping approach described in section 2.2.1.5 was applied to obtain estimates of the saturation rate MT_{sat}, the longitudinal relaxation rate R_1, together with the apparent proton density PD_{app}. The B_1 map output by the DAM acquisition was used to correct for inhomogeneities of the transmitted RF field on a voxel-by-voxel basis.

The additional PD-weighted acquisition, termed as PD_2-w in table 6.2, performed with the same TR, TE and excitation flip angle of the MT-weighted acquisition, was used as the $\mathrm{MT}_{\mathrm{off}}$ image together with the MT-weighted acquisition (i.e. the $\mathrm{MT}_{\mathrm{on}}$ image) in the calculation of the MTR (as defined in section 2.2.1.2).

6.2.3.4 Macromolecular Tissue Volume

The *MTV*, described in section 2.2.3, was computed by correcting the PD_{app} from the multi-parameter mapping protocol for the effects of: (*i*) transverse relaxation, using ${T_2}^*$ estimates from the multi-*TE* acquisition; and (*ii*) the receiver coil sensitivity profile, using the iterative method proposed in [78], which exploits the linear relationship between PD and T_1, and a reference signal from CSF, replaced here by the signal obtained form an ROI positioned in the PBS. The inverse of R_1 estimated from the multi-parameter mapping acquisition was used as a T_1 measurement.

Bias field correction parameters (number of iterations=10, degrees of polynomial surface=8, and size of smoothing kernel=$0.3 \times 0.3 \times 1$ mm^3) were tuned empirically to ensure convergence during iterative estimation of the receiver coil sensitivity profile.

6.2.3.5 Myelin Water Fraction

The *MWF* was obtained from multi-T_2 fitting of data acquired with the *MWI* protocol reported in table 6.2. *MWF* was calculated on a voxel-by-voxel basis from the estimated T_2 spectrum, as described in section 2.2.2. To separate myelin water peak from intra- and extra-cellular water peak, a threshold of 35ms was used, which is lower than what is normally used in vivo to account for reduction in T_2 following fixation [212].

Multi-T_2 fitting was performed via NNLS fit to a sum of 130 exponentials signals with T_2 values logarithmically spaced between 5 ms and 500 ms, implemented by the freely available Multi Exponential Relaxation analysis (MERA) toolbox [213]. The cost function was regularized with a minimum curvature constraint, whose weight was selected according to the generalized cross validation criteria implemented in the toolbox. The effect of stimulated echoes from non ideal refocusing pulses was accounted for in the fitting, similarly to [73], using as external input the B_1 estimated from the DAM acquisition.

6.2.3.6 Myelin sensitive metrics from DWI: radial diffusivity

The *RD* and the others DTI parameters, introduced in section 2.2.4, were calculated from the fitting of the diffusion tensor model to the diffusion data, using the *dtifit* routine from FSL (FMRIB, Oxford, UK). All the acquired *b*-values were considered in the fitting, and repeated data points were fitted separately.

6.2.3.7 B_0 and B_1 field maps

The B_1 map was calculated from the DAM acquisition as explained in section 2.2.5.2. The resulting map was post-processed with the same pipeline suggested in [98] (smoothing with

a Gaussian kernel of size 7×7 voxels and full-width-half-maximum of 10×10 mm^2), to remove effect of noisy estimation in the final map.
The B_0 was calculated using the *fsltopup* routine of FSL (FMRIB, Oxford, UK), applied to the msh–SE-EPI data acquired with reversed polarity of the *blip* gradients of the EPI read-out (i.e. anterior to posterior, and posterior to anterior).

ROIs were manually drawn for WM and GM in all slices in the healthy samples, and for normal appearing WM (NAWM), normal appearing GM (NAGM) and lesions (where visible) in all slices in the MS samples, on the echo-averaged image from the multi-*TE* protocol (showing a $T_2{}^*$-weighted contrast).
Metrics were qualitatively compared by examining their distributions within different tissue types.
Pearson's linear correlation coefficient r was used to evaluate the strength of the linear relationship between different myelin sensitive MRI metrics. In particular, correlations of putative MRI myelin biomarkers, namely *BPF*, *MTV* and *MWF*, with each other and with other quantitative measurements sensitive to myelin content (from relaxation, diffusion and magnetization transfer contrast) were explored.

6.3 Results

All the quantitative parameters calculated reproduced the expected contrast between tissue types in healthy and normal appearing tissue: R_1, *MTR*, MT_{sat}, *BPF*, *MTV* and *MWF* show higher values in WM compared to GM in control cases, as well as NAWM compared to NAGM in MS cases; while $T1$, T_2, $T_2{}^*$ and *RD* show lower values in WM/NAWM compared to GM/NAGM, as expected given their reported sensitivity to myelin content. Figure 6.1 gives a comprehensive overview of the calculated parameters, showing the variety of myelin sensitive metrics available in an example slice for each of the samples included in the study. Alterations of the aforementioned contrast are visible in lesion areas (examples highlighted by arrows in the anatomical images of figure 6.1), in all the calculated parameters, although with different intensity patterns.

This is more clearly depicted in figures 6.2, 6.3, 6.4 and 6.5 showing zoomed details in lesions for different quantitative metrics (T_1, T_2, MT_{sat}, *BPF*, *MTV* and *MWF*) together with

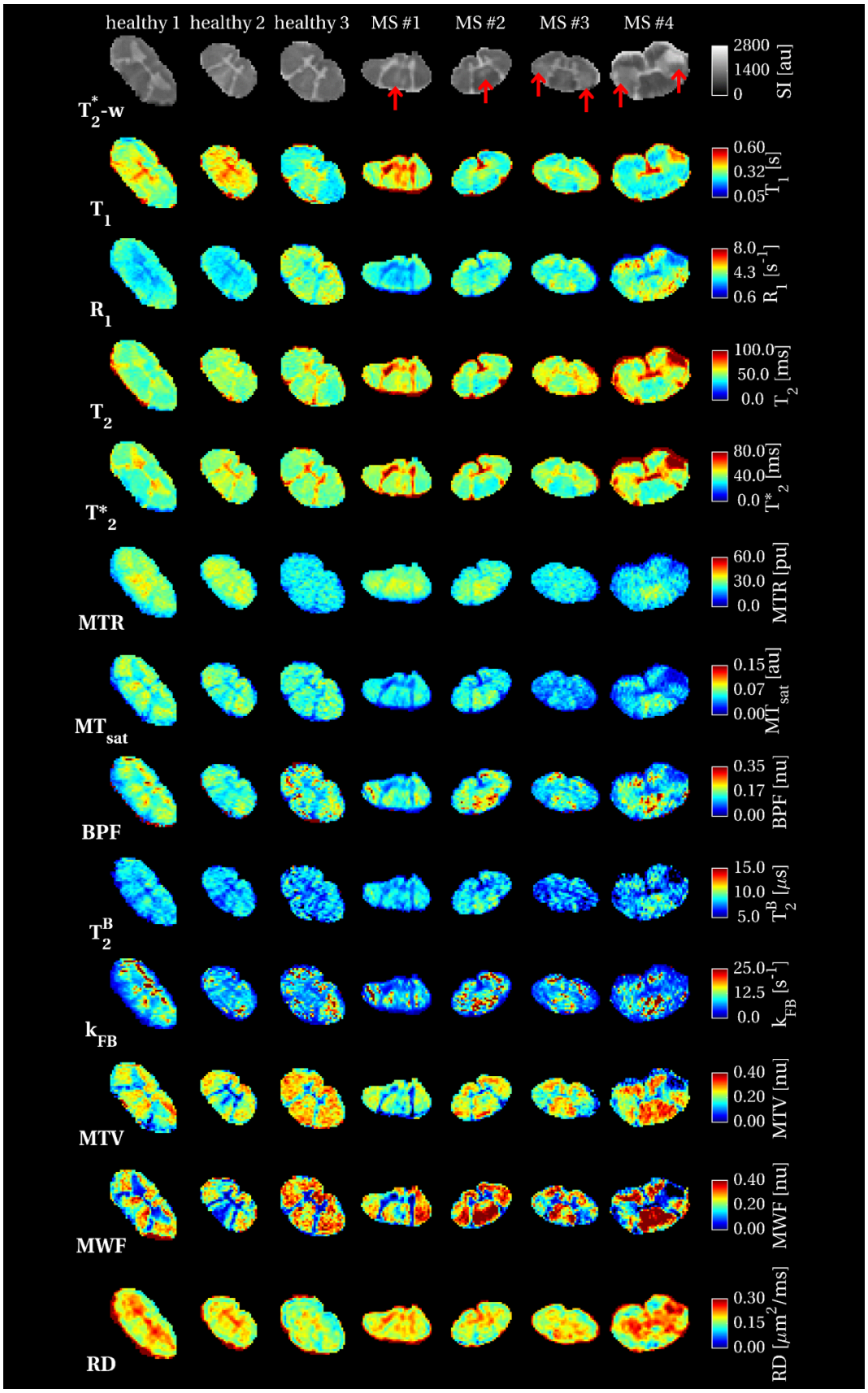

Figure 6.1: Quantitative MRI metrics estimated from the imaging protocol described in table 6.2, in all the post mortem samples available (3 healthy cases and 4 MS cases, from left to right). Typical MS lesions are highlighted by red arrows in the $T_2{}^*$-weighted image for the MS samples to ease their visualization in the respective quantitative maps.

their respective T_1-weighted and T_2-weighted images. MS abnormalities can show different appearances in T_1-weighted and T_2-weighted images: lesions can be visible in both types of contrast (figure 6.2), visible in just one modality and silent in the other (figures 6.3 and 6.4), or exhibit different spatial patterns (figure 6.5). Tissue abnormalities are always captured by quantitative MRI metrics, although with subtle qualitative differences. For example, *MWF* produces the highest contrast between lesions and the surrounding normal appearing tissue, and in some cases seems to display an intensity gradient within the lesion region as well, while other metrics, such as *BPF*, have a more uniform appearance within lesions and display less contrast with the surrounding normal appearing tissue.

Linear correlation tests showed strong linear positive correlations among candidate myelin biomarkers in all the controls and the MS samples (as shown in figure 6.6 for the MS cases). *BPF* correlated positively with *MWF* (r=0.89; $P<<0.01$) and *MTV* (r=0.74; $P<<0.01$), and *MTV* correlated positively with MWF (r=088; $P<<0.01$), when observations (mean ROI value per slice in each sample) from all cases were grouped together (figure 6.7).

Significant negative correlations ($P<<0.01$) were also found in the MS samples between all the candidate myelin biomarkers and *RD* estimates from DWI, which has been shown to be associated with myelin integrity in the human spinal cord. These correlations are shown in figure 6.8 separately for the MS samples, and in figures 6.9A, 6.9B and 6.9C grouped together with the healthy controls.

The lower panels of figure 6.9 show also overall correlations between candidate myelin biomarkers and MT_{sat} which has been suggested as a myelin sensitive technique with the potential for clinical feasibility.

Weaker correlations were found between candidate myelin biomarkers and MT-based measurements (*MTR* and MT_{sat}), which are both thought to be myelin-sensitive. Correlations with *MTR* were the weakest among all those investigated. In particular, the correlation between *MTR* and *MTV* was not significant (data not shown). However, *BPF* showed a strong correlation with MT_{sat}, a result which is qualitatively supported by the visual similarities between *BPF* and MT_{sat} maps in all the examples provided in this section. Overall correlations with the latter parameter are shown in figures 6.9D, 6.9E and 6.9F.

In general, myelin sensitive parameters are strongly correlated with each other, and with relaxation times, although with varying strengths, e.g. *BPF* is strongly correlated with T_2

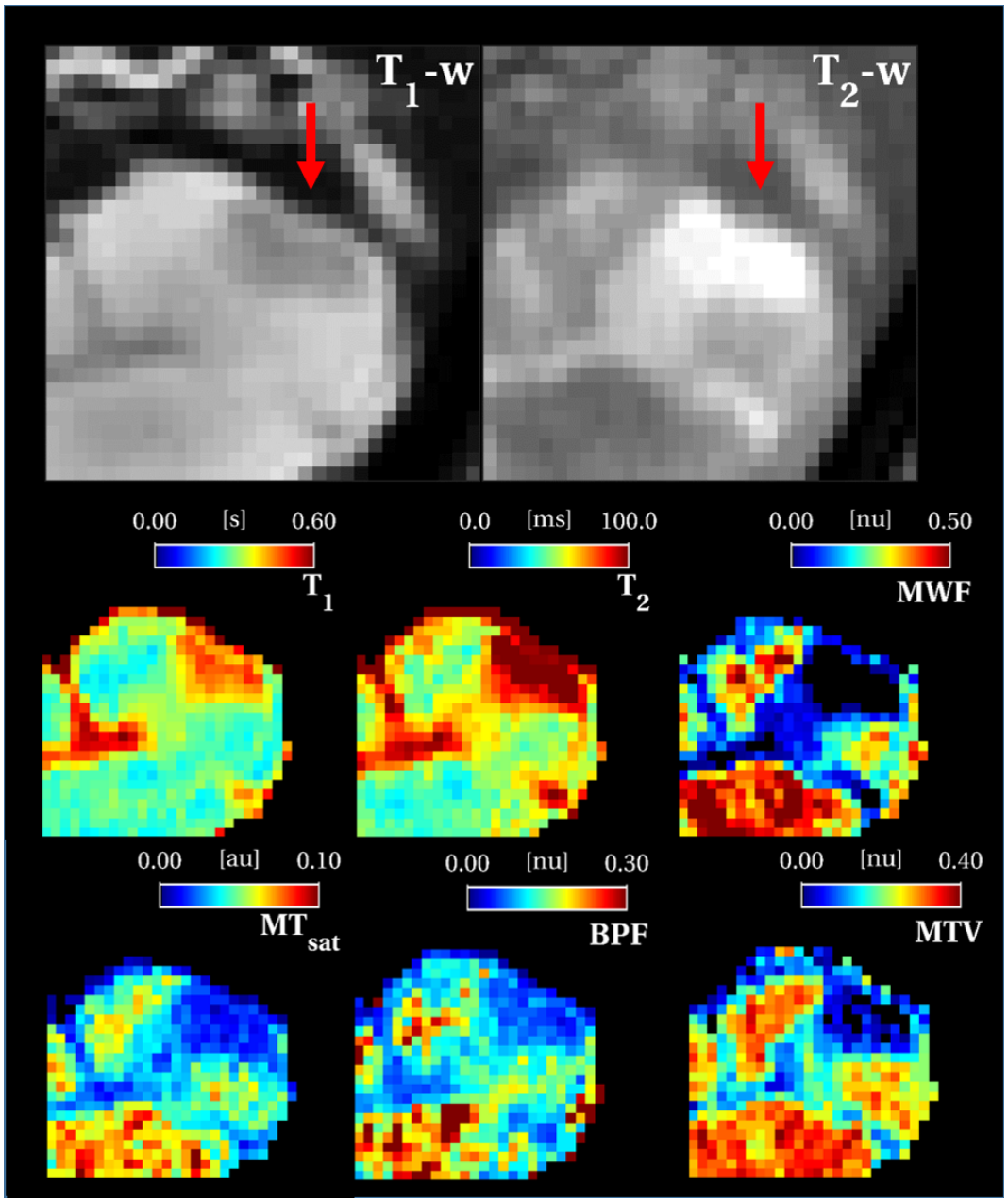

Figure 6.2: Zoomed detail for a spinal cord MS lesion (indicated by the arrow), visible in both T_1-weighted (**left**) and T_2-weighted (**right**) images. From the top left corner to the bottom right corner, quantitative MRI metrics are: T_1, T_2, *MWF*, MT_{sat}, *BPF* and *MTV*.

but less so with T_1. An overview of correlations with fundamental relaxation times is given in figure 6.10.

In lesion ROIs parameter distributions shifted towards higher or lower values (according to the metric considered) when compared to WM/NAWM distributions. Quantitative parameter distributions within different tissue type ROIs are shown in figure 6.11. Heterogeneity between samples, possibly due to different post mortem delays prior to excision and fixa-

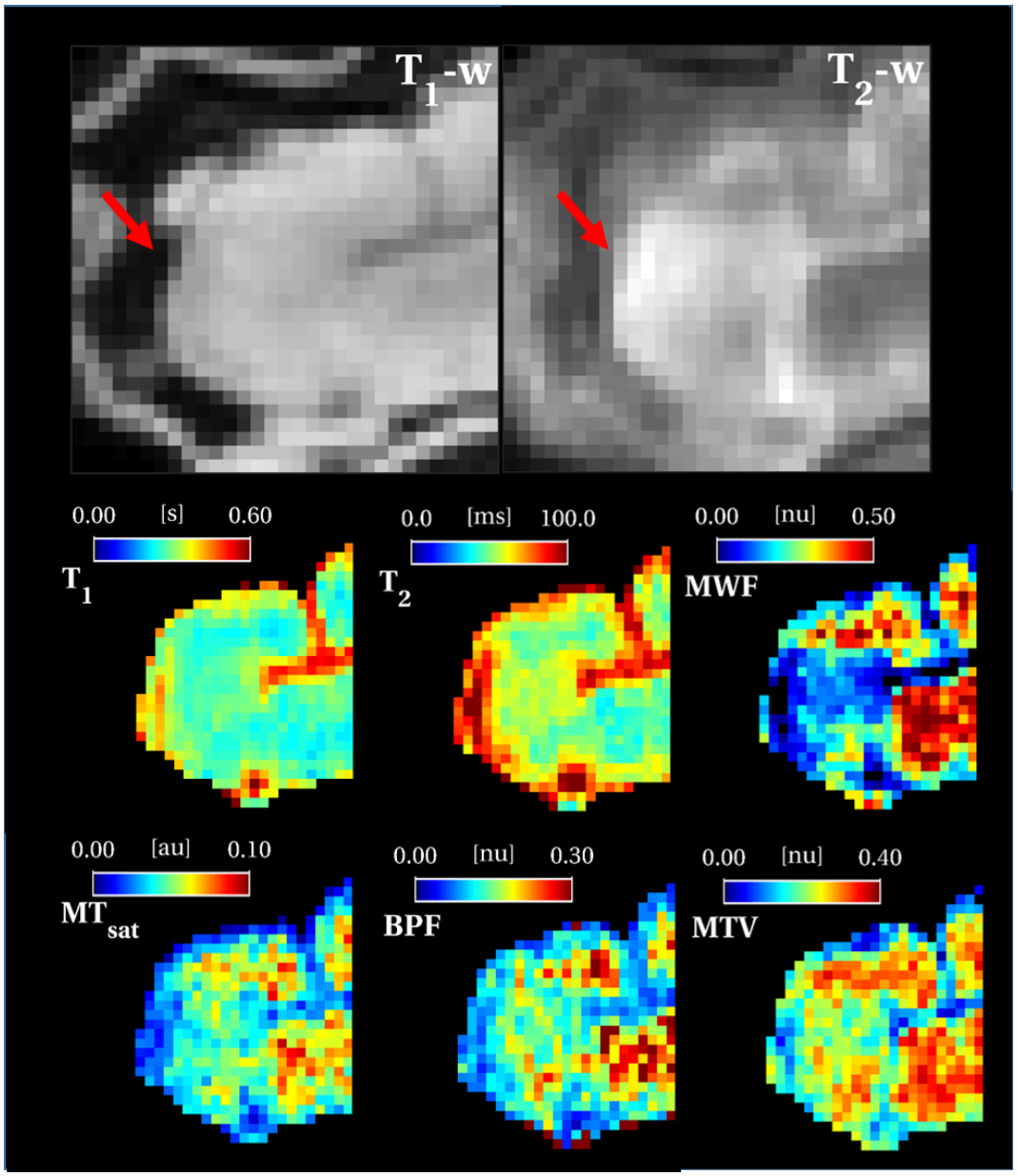

Figure 6.3: Zoomed detail for a spinal cord MS lesion (indicated by the arrow), visible only on the T_2-weighted image (**right**). From the top left corner to the bottom right corner, quantitative MRI metrics are: T_1, T_2, *MWF*, MT_{sat}, *BPF* and *MTV*. Different trends are appreciable for T_2 and *MWF* compared to the other quantitative metrics shown.

tion, different lengths of the fixation process, or variability in other factors (e.g. pH), are likely to blur the separation between different tissue type distributions for some of the metrics (e.g. T_1 and *MTR*). Distributions are quantitatively summarized in table 6.3.

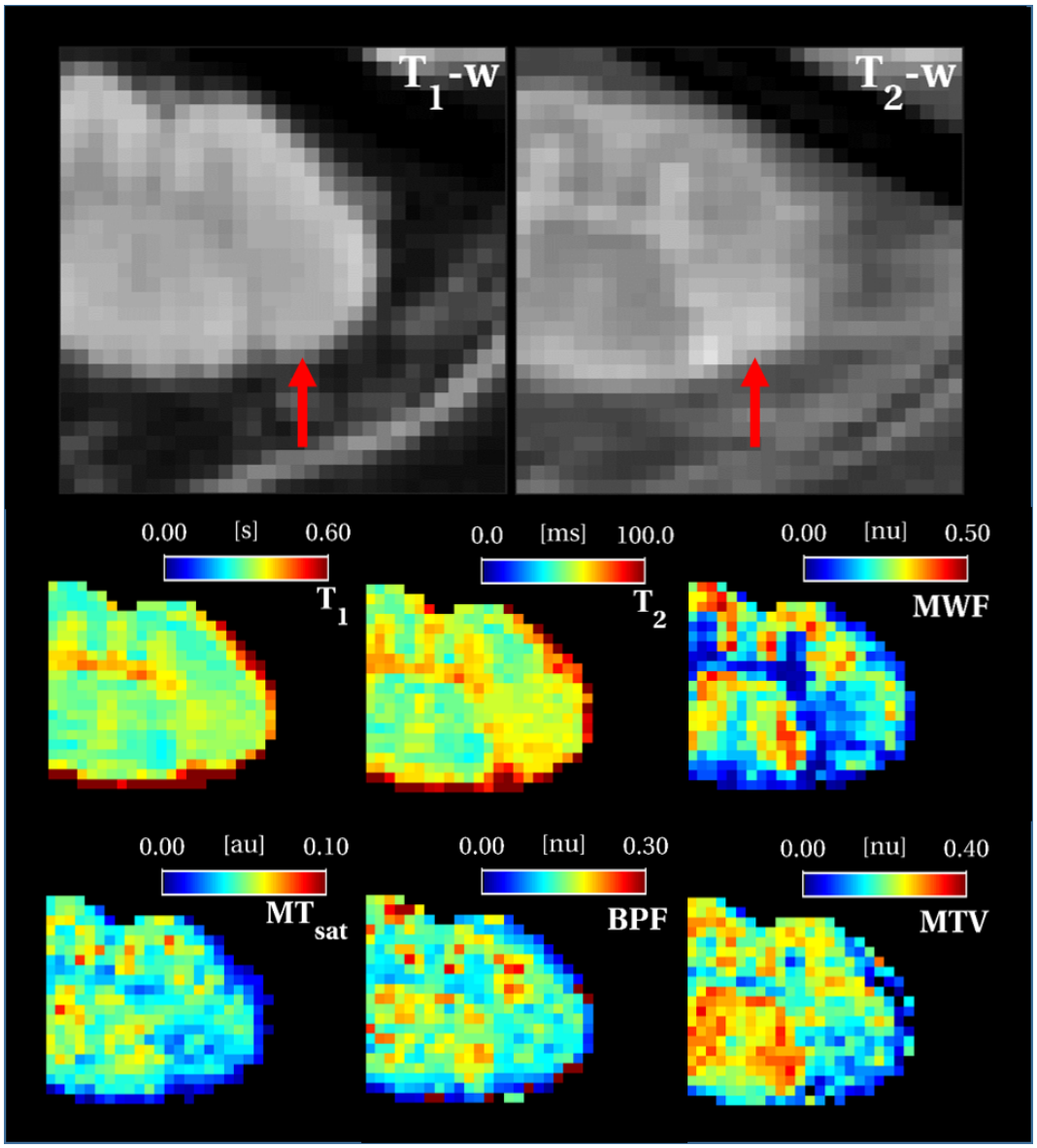

Figure 6.4: Zoomed detail for another spinal cord MS lesion (indicated by the arrow), visible only on the T_2-weighted image (**right**). From the top left corner to the bottom right corner, quantitative MRI metrics are: T_1, T_2, *MWF*, MT_{sat}, *BPF* and *MTV*. In this case, all the quantitative metrics show a more similar trend among each other, in contrast with the case shown in figure 6.3.

6.4 Discussion

In this chapter we have showed results of a comprehensive comparison between myelin sensitive MRI metrics in the post mortem MS spinal cord. The evidence showed here should be considered as preliminary, and hence partial, results of a larger study aiming to investigate the histological correlates of different myelin sensitive measures in the spinal cord. Results from MRI data alone allow only speculative considerations.

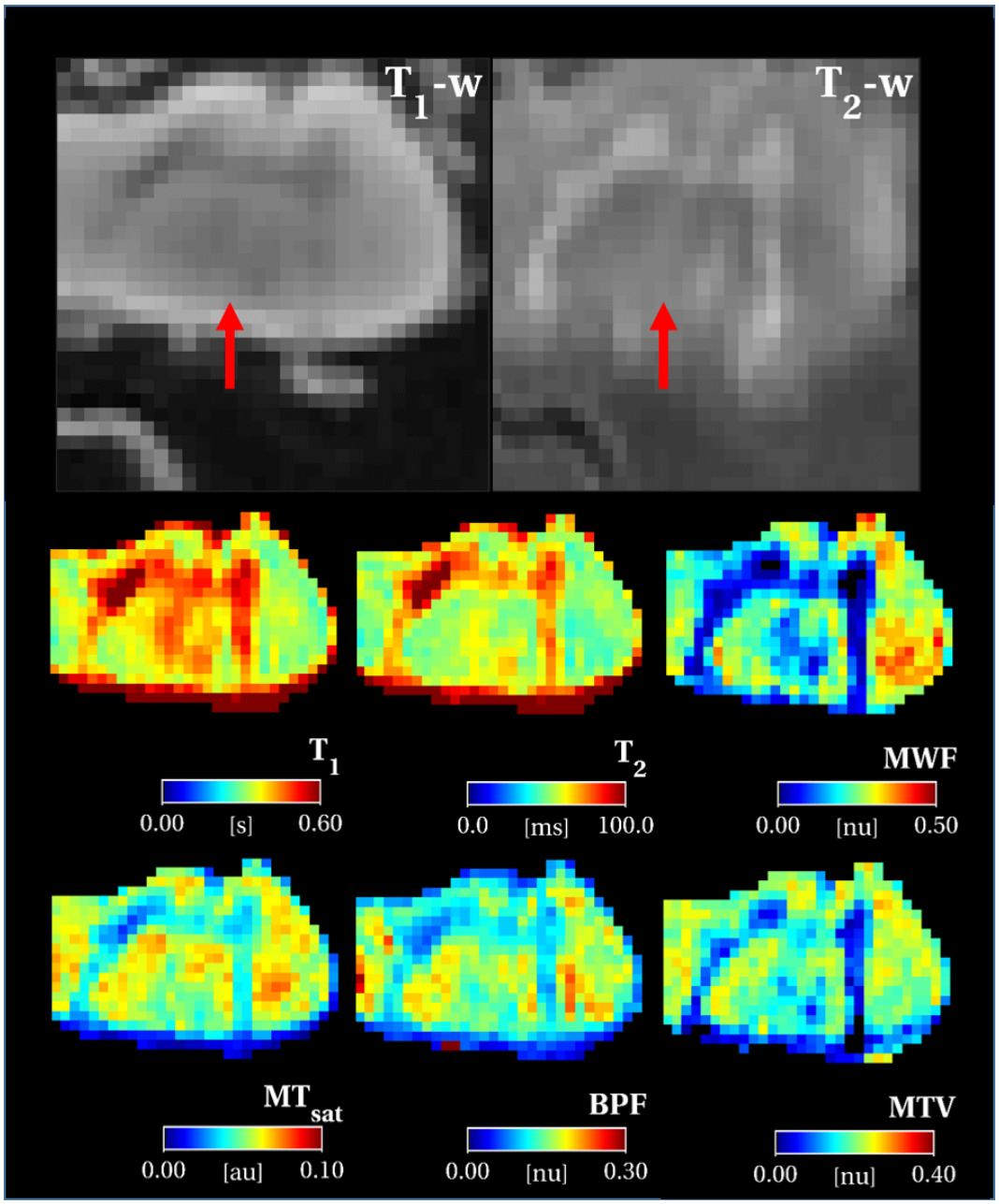

Figure 6.5: Zoomed detail for a spinal cord MS lesion (indicated by the arrow), producing abnormalities visible on both T_1-weighted (**left**) and T_2-weighted (**right**) images. Lesion appears as a diffuse subtle hypointensity in the T_1-weighted image and as a smaller focal hyperintensity in the T_2-weighted image. From the top left corner to the bottom right corner, quantitative MRI metrics are: T_1, T_2, *MWF*, MT_{sat}, *BPF* and *MTV*.

The overall goal is to determine sensitivity and specificity of quantitative myelin mapping techniques (with particular interest in *BPF*, *MWF* and *MTV*) to myelin content in the spinal cord, in order to better understand to which extent different metrics can be used as myelin biomarkers to improve MS therapeutics.

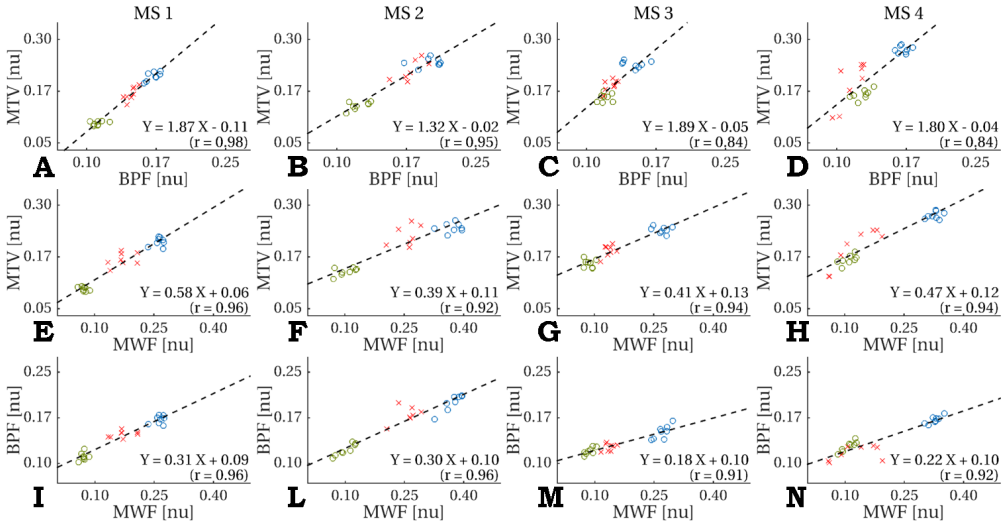

Figure 6.6: Correlations between putative MRI myelin biomarkers in MS spinal cord samples. Each column refers to a different MS spinal cord sample. Correlations between *MTV* and *BPF* are shown in the first row (graphs **A**, **B**, **C** and **D**); correlations between *MTV* and *MWF* are shown in the second row (graphs **E**, **F**, **G** and **H**); correlations between *BPF* and *MWF* are shown in the third row (graphs **I**, **L**, **M** and **N**). NAWM, NAGM and lesion values are displayed with in light blue circles, dark green circles and red crosses respectively. A single ROI per tissue type per slice is taken in each sample. All the correlations are significant ($P<<0.01$). Parameters of the linear fit between variables are also reported in each graphs.

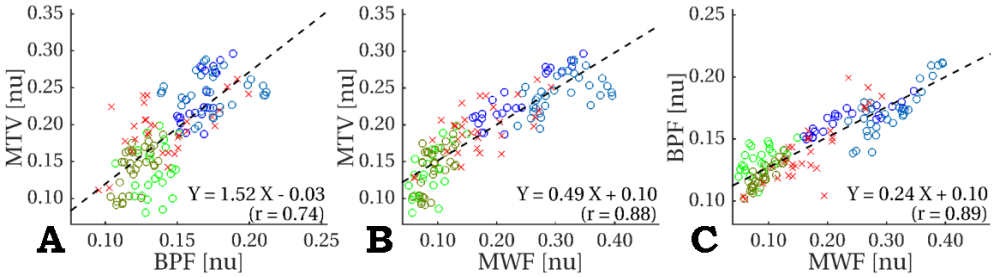

Figure 6.7: Correlations between putative MRI myelin biomarkers in all post mortem spinal cord samples studied here (3 controls and 4 MS cases). *BPF* vs. *MTV* in graph **A**, *MWF* vs. *MTV* in graph **B** and *MWF* vs *BPF* in graph **C**. In each slice of the samples the mean values in different tissue type ROIs are taken: WM and GM in control samples (shown in blue and green); NAWM, NAGM and lesions in MS samples (shown in light blue, dark green and red).

To our knowledge, this study represents the most complete, in terms of the number of MRI techniques simultaneously investigated, carried out (or being carried out) in the human post mortem spinal cord.

The implications of this study are, thus, potentially important and numerous, considering also the difficulty in implementing and interpreting results for in vivo quantitative MRI of

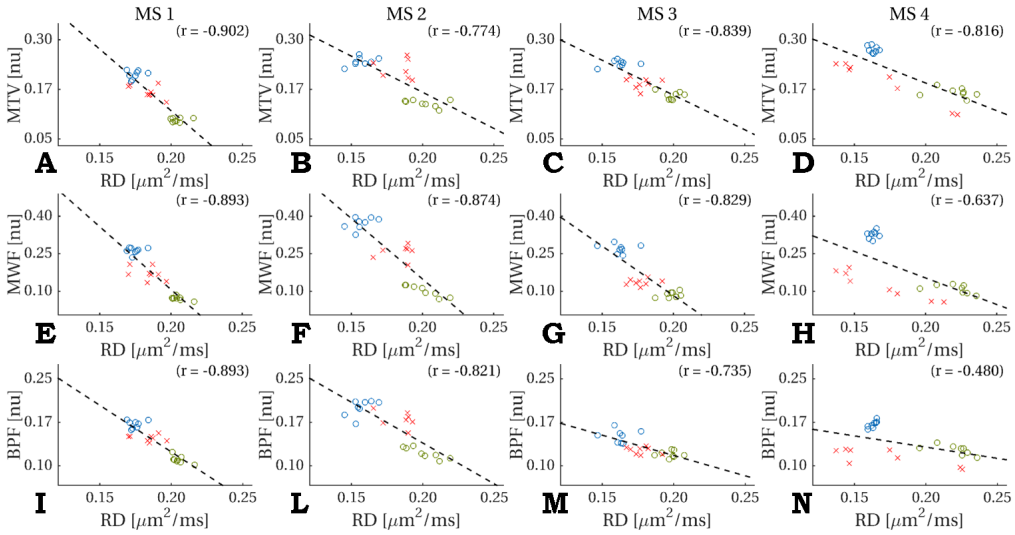

Figure 6.8: Correlations between *RD* from DWI and *MTV* (first row), *MWF* (second row) and *BPF* (third row) in MS spinal cord samples. Each column refers to a different MS sample. Correlations between *RD* and *MTV* are shown in the first row (graphs **A**, **B**, **C** and **D**); correlations between *RD* and *MWF* are shown in the second row (graphs **E**, **F**, **G** and **H**); correlations between *RD* and *BPF* are shown in the third row (graphs **I**, **L**, **M** and **N**). NAWM, NAGM and lesion values are displayed with in light blue circles, dark green circles and red crosses respectively. A single ROI per tissue type per slice is taken in each sample. All the correlations are significant ($P<<0.01$).

the spinal cord. In fact, some of these techniques have been poorly applied in the spinal cord in vivo. To our knowledge, there is only one study available in literature that has applied *MTV* in the spinal cord in vivo [164], while *MWF*, despite its widespread use in the brain, has been successfully translated to the spinal cord only recently [75], after an earlier initial attempt [214]. A literature review on *BPF* measurements in the spinal cord in vivo has been given instead in section 5.1. Additional knowledge from histological studies of the microstructural correlates of these metrics, and insights into their specificity to myelin content in MS, would promote a faster development of more effective in vivo MRI myelin biomarkers for the spinal cord.

Moreover, specific features of the spinal cord tissue microstructure (e.g. larger axons compared to the brain) require quantitative MRI metrics to be validated for the specific case of spinal cord tissue, as some of the relationships between quantitative MRI measurements and tissue properties may vary compared to the brain [215].

The MRI metrics considered were able to detect abnormalities in the tissue shown in anatomical T_1-weighted and T_2-weighted images, with quantitative values deviating from the distribution characterizing the surrounding normal appearing tissue. However, most of

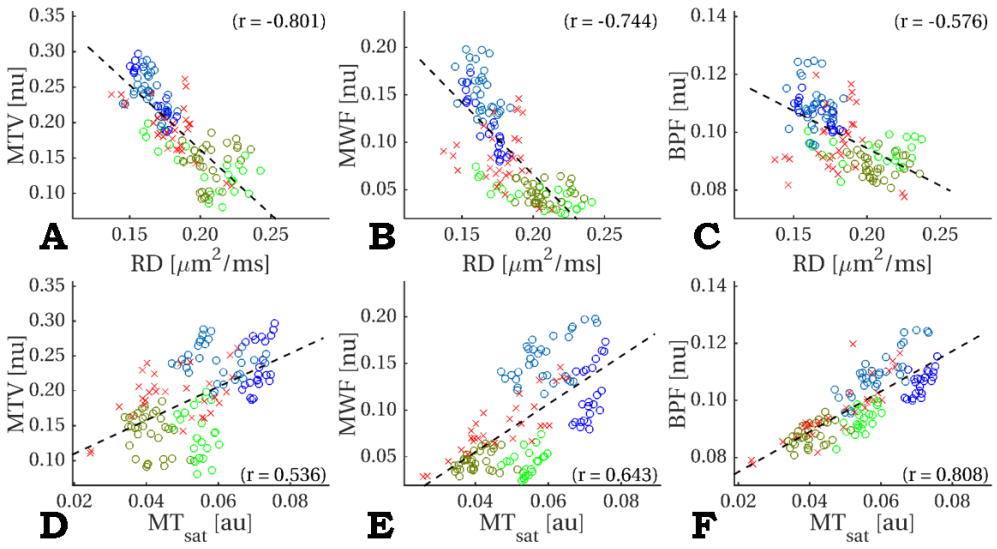

Figure 6.9: Correlations between putative MRI myelin biomarkers and metrics from DWI and MTI in the post mortem spinal cord (3 controls and 4 MS cases). Correlations with DWI-derived metric: *RD* vs. *MTV* in graph **A**, *RD* vs. *MWF* in graph **B** and *RD* vss *BPF* in graph **C**. Correlations with MTI-derived metric: MT_{sat} vs. *MTV* in graph **D**, MT_{sat} vs. *MWF* in graph **E** and MT_{sat} vs. *BPF* in graph **F**. In each slice of the samples the mean values in different tissue type ROI are taken: WM an GM in control samples (shown in blue and green); NAWM, NAGM and lesions in MS samples (shown in light blue, dark green and red).

the metrics are characterized by substantial variability in lesion ROIs, as shown by the width of lesion distributions in figure 6.11, as well as inter-quartile ranges reported in table 6.3, suggesting a complex relationship between alterations in tissue microstructure and variations displayed by quantitative MRI metrics. Data from histology will be essential to shed light on the underlying dependencies between quantitative MRI metrics and tissue properties at a microscopic level, e.g. myelin content, axonal density, axonal size, etc.

In a previous study, conducted on post mortem rat spinal cord, *BPF* and *MWF* were compared in term of specificity to myelin content, against properties of WM microanatomy, such as axon diameters, myelin thickness and intra-axonal density, that could interfere with the exchange rate between different water compartments and hence introduce dependencies on water exchange in the myelin sensitive metrics considered [215]. *MWF* was found to be sensitive to myelin content, as well as to the dimensions of tissue microstructure in the WM spinal cord: in tracts with smaller axons and thinner myelin *MWF* was lower than tracts characterized by bigger axons and thicker myelin but similar myelin content. On the other hand *BPF* was found to be relatively insensitive to microanatomical variations across tracts.

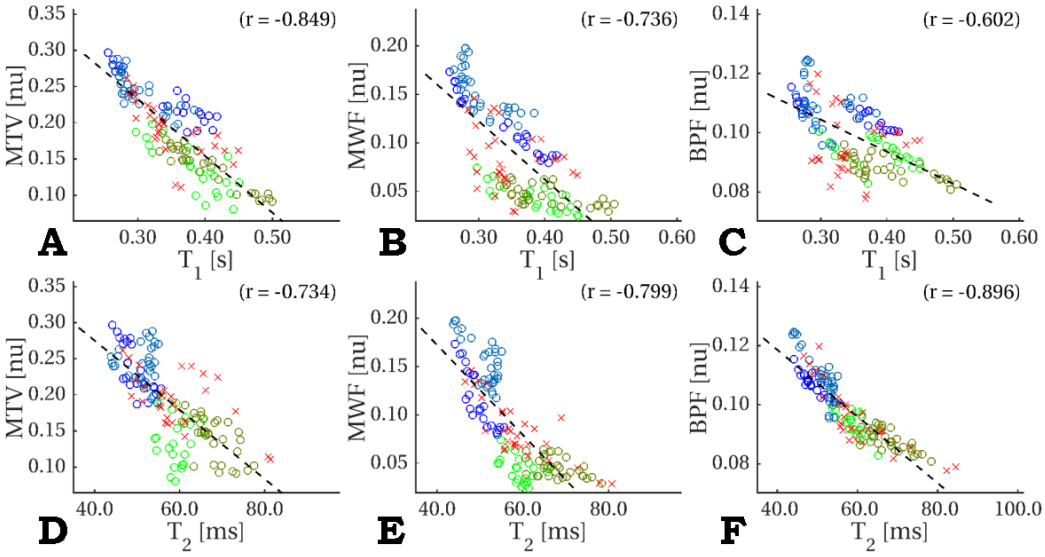

Figure 6.10: Correlations between putative MRI myelin biomarkers and fundamental relaxation times in the post mortem spinal cord (3 controls and 4 MS cases). T_1 vs. *MTV* in graph **A**, T_1 vs. *MWF* in graph **B**, T_1 vs. *BPF* in graph **C**, T_2 vs. *MTV* in graph **D**, T_2 vs. *MWF* in graph **E**, T_2 vs. *BPF* in graph **F**. In each slice of the samples the mean values in different tissue type ROI are taken: WM an GM in control samples (shown in blue and green); NAWM, NAGM and lesions in MS samples (shown in light blue, dark green and red).

In another study aiming to identify the best measure for an absolute (not only correlative) measure of myelin using MRI, performed in mice brains, *BPF* and *MWF* were found to be strongly correlated with each other and with myelin content from quantitative histology (using transmission electron microscopy) [216].

However, there are also studies that have failed to report consistent correlations between putative myelin biomarkers, as in [217] where *BPF* and *MWF* were found to be only partially correlated. The potential sensitivity in different proportions to other disease factors (e.g. inflammation and axonal loss) was hypothesized as the origin of the reported variability.

Correlations with histology data will also help to elucidate the potential for quantitative MRI metrics to detect subtle damage that extends beyond visible lesions, potentially occurring prior to focal lesion appearance. Sensitivity to such early abnormalities, non detectable with conventional examinations, is key for improving the diagnosis of MS. Without the availability of histological data is difficult to draw any conclusions regarding the potential power of each technique to detect damage in normal appearing tissue. Comparisons between quantitative metrics in healthy WM and GM with MS NAWM and NAGM may be

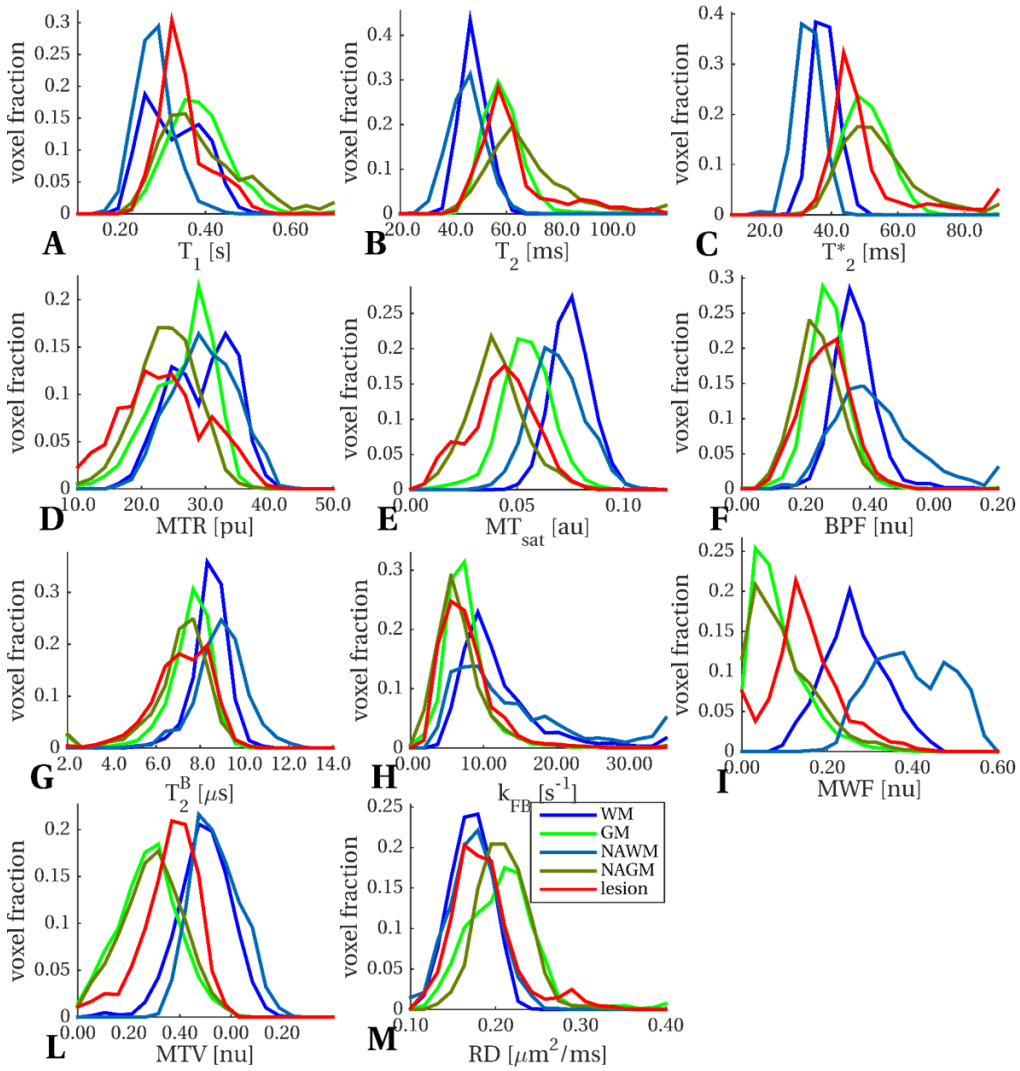

Figure 6.11: Distributions in different tissue type ROIs of quantitative MRI metrics estimated from the imaging protocol described in table 6.2, in all the post mortem samples available (3 healthy cases and 4 MS cases). Distributions are shown for WM (**blue**) and GM (**light green**) in healthy samples; and NAWM (**light blue**), NAGM (**dark green**) and lesion (**red**) for MS samples.

confounded by sample heterogeneity (e.g. different post mortem delays, fixation duration, pH, together with physiological between-sample variability). These processes are known to impact on measured MRI parameters, and could be the reason why parameter distributions in WM and NAWM are not well separated, with the exception of MT_{sat}.

Formalin fixation has been shown to greatly impact relaxation times [218, 219], with T_1 being the most affected parameter. The T_1 measured in our cohort is more than 3 times shorter than values expected in vivo (see chapter 4 for in vivo measurement of T_1 in the

	Region-of-Interest				
	WM	**GM**	**NAWM**	**NAGM**	**Lesions**
T_1	0.34	0.38	0.28	0.37	0.33
$[s]$	(0.25-0.67)	(0.3-048)	(0.24-0.35)	(0.28-0.53)	(0.28-0.44)
R_1	3.70	3.14	4.33	3.29	3.58
$[s^{-1}]$	(2.50-5.05)	(2.61-3.93)	(3.53-5.25)	(2.45-4.11)	(2.71-4.20)
T_2	49.89	57.84	50.23	64.07	58.58
$[ms]$	(42.46-105.5)	(49.93-68.19)	(40.70-62.85)	(50.74-87.83)	(49.25-87.13)
T_2^*	38.684	49.92	36.50	52.04	46.07
$[ms]$	(33.76-53.51)	(41.87-59.15)	(30.44-43.49)	(41.76-68.76)	(40.46-71.78)
MTR	27.1	27.47	26.62	24.06	23.27
$[p.u.]$	(16.39-34.73)	(19.47-32)	(19.32-34.10)	(17.82-29.87)	(14.97-32.88)
MT_{sat}	0.07	0.05	0.06	0.04	0.04
$[n.u.]$	(0.02-0.08)	(0.04-0.07)	(0.04-0.08)	(0.02-0.06)	(0.02-0.06)
BPF	0.16	0.13	0.17	0.12	0.13
$[n.u.]$	(0.03-0.21)	(0.10-0.17)	(0.11-0.25)	(0.08-0.17)	(0.08-0.18)
T_2^B	8.22	7.68	8.58	7.32	7.28
$[\mu s]$	(6.28-9.26)	(6.20-8.56)	(6.95-9.81)	(5.43-8.48)	(5.46-8.67)
k_{FB}	8.57	6.95	8.89	6.16	7.07
$[s^{-1}]$	(1.96-16.79)	(4.47-10.82)	(4.55-20.59)	(3.25-11.49)	(3.93-12.09)
MTV	0.24	0.14	0.25	0.15	0.19
$[n.u.]$	(0.14-0.30)	(0.06-0.21)	(0.19-0.32)	(0.06-0.22)	(0.10-0.24)
MWF	0.23	0.07	0.32	0.08	0.14
$[n.u.]$	(0.11-0.35)	(0.02-0.17)	(0.20-0.46)	(0.01-0.20)	(0.04-0.25)
RD	0.17	0.2107	0.16	0.21	0.18
$[n.u.]$	(0.14-0.27)	(0.16-0.25)	(0.13-0.20)	(0.17-0.25)	(0.15-0.23)

Table 6.3: Summary statistics for quantitative MRI parameters in different tissue types: healthy white (WM) and grey matter (GM), and MS normal appearing white (NAWM) and grey matter (NAGM) and lesions. Median values and the 10^{th}-90^{th} percentiles ranges are reported.

spinal cord), and fresh post mortem tissue [160], and characterized by a consistent between-sample variability. This fact could explain the highly varying *MTR* between samples (the *MTR* is known to be dependent on T_1), and in general a rather low *MTR* and poor contrast between tissue types, as a consequence of a much shortened T_1 which hampers the piling up of a substantial MT effect in a progressive saturation experiment. Interestingly, such differences, potentially driven by T_1 variability, vanish in the MT_{sat} and *BPF* maps (as shown in figure 6.1) which explicitly account for T_1. This suggests that MT_{sat} and *BPF* are better positioned than *MTR* to provide a quantitative biomarker for myelin, as it has previously been demonstrated in the post mortem MS brain for the case of the *BPF* [54].

Particularly interesting is the association with the MT_{sat} parameter, which has never been explored in the spinal cord. The strong correlation MT_{sat} showed with *BPF* makes it partic-

ularly appealing as a prospective myelin biomarker for clinical studies, given the substantial simplicity in terms of implementation and feasibility within a clinically accepted scan time compared to *BPF*. However, MT_{sat} (similarly to the *MTR*) is dependent on sequence parameter details which makes its interpretation as absolute measure of myelin content more complicated than *pure* quantitative (i.e. volume fraction) measures, such as *BPF*, *MWF* and *MTV*.

The histological correlates of *BPF* have already been shown in a post mortem study of the MS brain [54]. In that study *BPF* was found to be a predictor of myelin content in post mortem MS WM, and was therefore suggested as a useful tool to monitor the evolution of both demyelination and remyelination in MS WM. On the other hand, ${T_2}^B$ did not appear to be a useful marker in post mortem MS brain, and only a weak non-significant correlation was found with *BPF*. This is in contrast with our evidence, showing a strong and positive correlation between these two indices from qMT model fitting (r=0.92, $P<<0.01$). Histological examination will help to shed light on the utility of ${T_2}^B$ as an informative marker for MS pathology in the spinal cord, as well as for the other parameters estimated from the qMT model, i.e. the exchange rate k_{FB}.

There are, however, studies where simpler quantitative MRI metrics have provided the strongest predictors of myelin content. This is the case for the T_2 measured in a study carried out on the post mortem MS human spinal cord [207]. When proposing a quantitative measurement as a potential biomarker, it is in fact important to consider the complexity and the practical challenges associated with robust measurements of such a parameter in vivo. Given the substantial development of DWI in the spinal cord compared to other contrast mechanisms (such as relaxometry or MTI) [220], diffusion-derived myelin sensitive metrics, such as *RD*, could be found to be better candidates for the translation to in vivo imaging, and therefore have been included in the current investigation.

Finally, it is important to comment on the differences between MRI protocols used for quantitative MRI validation on post mortem tissue and those that could be run in prospective in vivo examinations. In contrast with many MRI-histology validation studies, here MRI acquisition was carried out on a clinical system at 3T. Alteration of tissue MR parameters, post mortem and following fixation, required the use of different sequence parameters (e.g. *TR*, flip angle, pulse duration and pulse gap for MTI experiment, *b*-values for diffusion experiment, etc.) to obtain the desired contrast. For some of the protocols, e.g. the qMT

protocol, sequence parameters were optimized *ad hoc*. However, MRI protocols reported in table 6.2 do not substantially differ from their in vivo counterparts. The increase in scan time is mostly a consequence of the increased resolution compared to a hypothetical in vivo acquisition. This represents the main difference between the two scenarios (together with the lack of motion and physiological noise), while the number of data points for model fitting and intrinsic data *SNR* resemble those achievable in vivo. We are therefore confident that the results of the histological validation study, whose initial MRI results have been presented in this chapter, can be extended to in vivo applications.

6.5 Future work

Optimized procedures will be followed for the derivation of the quantitative histological metrics to be correlated with the quantitative MRI metrics presented in this chapter. Samples will be dehydrated and embedded in paraffin, before slicing and staining for specific anatomical features. Sections for histological staining will be selected so that they will fall within the acquired MRI slices, as outlined in appendix B, in order to ensure that correlations can be made between matched ROIs.

We plan to stain for the following tissue properties: (*i*) myelin content (with both Luxol Fast Blue (LFB), and myelin proteolipid protein (PLP) immunohistochemistry), (*ii*) axonal density (with Bielschowsky silver staining), (*iii*) astrocytes density (with glial fibrillary acidic protein (GFAP) immunohistochemistry), (*iv*) microglia density (with immunohistochemical labeling of ionized calcium-binding adapter molecule 1 antigen (Iba1+)), and (*v*) inflammatory infiltrates (with haemotoxylion and eosin (H&E)). Optical histological images will be processed at original high resolution, subsequently downsampled to the MRI resolution and co-registered with the MRI slices using a landmark guided non linear approach, as in [208, 163].

Associations will be investigated between quantitative MRI metrics and quantitative histology metrics in different ROIs, identified in the $T_2{}^*$-weighted images, for controls and MS cases. Pearson's correlation coefficient will be used to test the strength of the linear associations, and univariate multivariable linear regression models will be fit to quantify the sensitivity of each myelin mapping technique towards each histological index.

Chapter 7

General Conclusions

The overall goal of this thesis was to advance the field of quantitative MRI in the human spinal cord with regards to methods sensitive to myelin content.
The above aim should be seen as part of the more general goal to improve the understanding of how MS affects neuronal tissue, the diagnosis process, prediction of the disease progression and the evaluation of potential treatment outcomes, for which the development of robust and reproducible quantitative MRI methods to examine spinal cord damage is an important factor.

The major contributions of this thesis are summarized here below:

- the ZOOM-EPI sequence, successfully used for DWI in the spinal cord for over 10 years, has been adapted to allow the efficient generation of contrasts other than diffusion weighting. In particular the sequence has been extended for use in Inversion Recovery and MT-weighted protocols. The integration with parallel imaging and simultaneous multislice imaging, to speed up acquisition, and incorporation of cardiac triggering, to improve data quality, has been discussed and shown via preliminary results in one healthy subject.

- an MT-weighted ZOOM-EPI protocol has been developed for fast *MTR* in the spinal cord. This approach allows the incorporation of: (*i*) a cardiac triggering scheme, (*ii*) an optimized set of sequence parameters according to particular sensitivity criteria.

- T_1 has been successfully measured in the cervical spinal cord adapting the *gold standard* method for T_1 mapping, the Inversion Recovery sequence, to the spinal cord by using ZOOM-EPI. The protocol proposed is clinically feasible (duration is approx-

imately $\sim$7 min for the usual cervical level coverage) and reproducible in a cohort of healthy subjects. The protocol can be further optimized and accelerated through sequence parameter optimization and the incorporation of fast imaging techniques;

- a full quantitative Magnetization Transfer imaging examination and assessment of model parameter reproducibility have been performed in the spinal cord for the first time in vivo. Model parameter estimation has been achieved using an EPI-based readout departing from the steady-state configuration, usually assumed in quantitative MT studies. Non-steady-state acquisitions have been shown to lead to precise parameter estimates by using protocol optimization techniques, that greatly improve reproducibility of model parameter estimates. Protocol optimization techniques have been shown to be beneficial at the low *SNR* regime characterizing spinal cord imaging.

- Despite the different physical mechanism they are based upon, and the different description of tissue they provide, myelin mapping techniques are all sensitive to alterations caused by MS disease in post mortem tissue. However, some variability can be appreciated between techniques, which may hint different patterns of sensitivities to microstructural features.

The research presented in this study can be extended and complemented in several ways, including:

- the comparison through metrics derived from histology is essential to shed light on the differences between myelin mapping techniques for the spinal cord, and their relative sensitivity and specificity to disruption of the myelin compartment in MS. The completion of the post mortem comparison will serve the double goal of: (*i*) improving the understanding of the spinal cord microstructure, and (*ii*) foster the design of a in vivo MRI biomarker for myelin degeneration in MS for the human spinal cord, accounting for the challenges associated with its implementation.

- the development of a battery of quantitative methods using the ZOOM-EPI readout promotes the design of multi-modal studies via the combination of different contrasts. A natural and interesting extension of the work shown in this thesis, particularly important in the context of myelin mapping, is the in vivo measurement of the spinal

cord g-ratio. To achieve this, a myelin volume fraction index (e.g. from the qMT protocol developed here) and fibre volume fraction index (e.g. from NODDI, or any other DWI techniques already validated in the spinal cord) are combined in a single index, the g-ratio, which has shown promise for specific assessments of demyelination and axonal loss.

- the feasibility of the quantitative techniques proposed here can be further improved through protocol optimization refinements. In particular the qMT protocol proposed shows large room for improvement in terms of accuracy (adding B_0 and B_1 mapping), protocol duration (optimizing for number of data points or reducing the model parameters to be estimated from data) and precision (through a more rigorous optimization, the inclusion of a cardiac triggering scheme or a data de-noising step).

- ZOOM-EPI may benefit from technical developments, such as a widespread use and establishment of SMS imaging and the development of dedicated receiver coils for the spinal cord. In particular the possibility to perform Inner Volume imaging in a time efficient manner (i.e. a high multiband factor) is a solution that we seek to explore.

The spinal cord is a crucial structure in a number of neurological conditions, such as MS, and as yet overlooked by the research community. The efforts described in this thesis aim to foster the development of robust and clinically feasible protocols to characterize the spinal cord in healthy and pathology conditions.

While the methods developed in this thesis have been designed to answer the specific challenges posed by quantitative MRI in the spinal cord, we do not claim their superiority over more traditional approaches that could be implemented. However, we do remark upon the importance of expanding the methods available to look at spinal cord microstructure, providing quantitative values for model parameters to be used in further subsequent optimization and development of quantitative MRI methods, and allowing the comparison among different approaches, that all contribute to advancing the quantitative measurement of myelin in the spinal cord. We hope that the work developed here may provide useful to further the attempt to answer this urgent need in the MS field.

Appendix A

Optimizing MTR sensitivity to macromolecular content

In this appendix we demonstrate a strategy to design the MT weighting when produced by means of a train of saturation pulses prior to imaging pulses.

Within the sequence described in Section 3.3.3, the MT saturation block stands as a separate and independent block from data acquisition, and can therefore be freely designed according to the specific application being considered.

In the context of *MTR* experiments, we decide to select the sequence parameters (defining the saturating train) in order to tune *MTR* sensitivity to changes in the underlying macromolecular content, and jointly reduce *MTR* sensitivity to changes unrelated to myelin content, such as water content and hence T_1 relaxation. In fact, the final *MTR* value can be considered as the result of the competing effects of: (*i*) magnetization transfer, *destroying* longitudinal magnetization, and (*ii*) T_1 relaxation, *creating* longitudinal magnetization.

The quantitative description of the MT effect, based on the two-pool model (described in section 2.2.1.3), can be used as a basis for performing optimization of *MTR* sensitivity. The MT effect can be described quantitatively by equations 2.24 of the two-pool model, or equivalently by the matrix form 5.1, where model parameter definitions, including the *BPF*, have been given in section 2.2.1.3.

The numerical solution of equation 5.1 offers a means of predicting the time evolution of $M_z^F(t)$ for any configuration of tissue parameters, $\mathbf{p}_t$=[*BPF* T_1^F T_1^B T_2^F T_2^B R], and as a function of sequence parameters, $\mathbf{p}_s$=[Δ B_1 τ Δt N], and given a pulse shape $s(t)$ of the off-resonance pulses. Sequence parameters enters in the definition of $\omega_1(t)$ that describes the time-course of the off-resonance saturation over the whole period of integration of equation

5.1. Sequence parameters have been defined in section 2.2.1.4.

It is straightforward to obtain the relationship between $\mathbf{p}_t$, $\mathbf{p}_s$, and the *MTR* via numerical solution of $M_z{}^F(t)$:

$$\begin{aligned} MTR(\mathbf{p}_t, \mathbf{p}_s) &= \frac{MT_{off} - MT_{on}}{MT_{off}} \\ &= 1 - M_z^F(\mathbf{p}_s, \mathbf{p}_t) \\ &= 1 - S(\mathbf{p}_s, \mathbf{p}_t) \end{aligned} \tag{A.1}$$

where the latter notation will be used later on, for the theoretical derivation of *SNR* and contras-to-noise ratio (*CNR*).

Sensitivity of the *MTR* to a tissue parameter p is defined as the rate of change of the *MTR* with respect to the given tissue parameter, i.e. the partial derivative of the *MTR* with respect to p. The parameter sensitivities of major interest when considering *MTR* as a putative index of myelination are: macromolecular tissue content, i.e. *BPF* defined by equation 2.27, $\frac{\partial MTR}{\partial BPF}$, and longitudinal relaxation time, which can be approximated by sensitivity to $T_1{}^F$, $\frac{\partial MTR}{\partial T_1^F}$.

As an analytical expression of *MTR* as a function of $\mathbf{p}_s$ and $\mathbf{p}_t$ is not available, sensitivities must be computed numerically as a ratio of finite differences. To take into account a broader range of physiological scenarios, average sensitivities among a set of R and Q values of *BPF* and $T_1{}^F$ are considered. Using equation A.1, $\frac{\partial MTR}{\partial BPF}$ and $\frac{\partial MTR}{\partial T_1^F}$ are given by:

$$\begin{aligned} \frac{\partial MTR}{\partial BPF} &= \frac{1}{R}\sum_{r=1}^{R} \frac{\partial MTR\big(BPF_r, \mathbf{p}_t^{-BPF}, \mathbf{p}_s\big)}{\partial BPF} \\ &= \frac{1}{R}\sum_{r=1}^{R} \frac{\partial}{\partial BPF}\Big(\frac{1}{Q}\sum_{q=1}^{Q} MTR\big(BPF_r, T_{1,q}^F, \mathbf{p}_t^{-BPF,-T_1^F}, \mathbf{p}_s\big)\Big) \\ &= \frac{1}{R}\sum_{r=1}^{R} \frac{\partial \overline{MTR}_r\big(BPF_r, \mathbf{p}_t^{-BPF,-T_1^F}, \mathbf{p}_s\big)}{\partial BPF} \\ &\approx \frac{1}{R-1}\sum_{r=2}^{R} \Big|\frac{\overline{MTR}_r\big(BPF_r, \mathbf{p}_t^{-BPF,-T_1^F}, \mathbf{p}_s\big) - \overline{MTR}_{r-1}\big(BPF_{r-1}, \mathbf{p}_t^{-BPF,-T_1^F}, \mathbf{p}_s\big)}{BPF_r - BPF_{r-1}}\Big| \end{aligned} \tag{A.2}$$

$$\begin{aligned}\frac{\partial MTR}{\partial T_1^F} &= \frac{1}{Q}\sum_{q=1}^{Q}\frac{\partial MTR\left(T_{1,q}^F, \mathbf{p}_t^{-T_1^F}, \mathbf{p}_s\right)}{\partial T_1^F} \\ &= \frac{1}{Q}\sum_{q=1}^{Q}\frac{\partial}{\partial T_1^F}\left(\frac{1}{R}\sum_{r=1}^{R} MTR\left(BPF_r, T_{1,q}^F, \mathbf{p}_t^{-BPF,-T_1^F}, \mathbf{p}_s\right)\right) \\ &= \frac{1}{Q}\sum_{q=1}^{Q}\frac{\partial \overline{MTR}_q\left(T_{1,q}^F, \mathbf{p}_t^{-BPF,-T_1^F}, \mathbf{p}_s\right)}{\partial T_1^F} \\ &\approx \frac{1}{Q-1}\sum_{q=2}^{R}\left|\frac{\overline{MTR}_q\left(T_{1,q}^F, \mathbf{p}_t^{-BPF,-T_1^F}, \mathbf{p}_s\right) - \overline{MTR}_{q-1}\left(T_{1,q-1}^F, \mathbf{p}_t^{-BPF,-T_1^F}, \mathbf{p}_s\right)}{T_{1,q}^F - T_{1,q-1}^F}\right|\end{aligned} \tag{A.3}$$

where the following definitions have been used:

$$\overline{MTR}_r = \frac{1}{Q}\sum_{q=1}^{Q} MTR\left(BPF_r, T_{1,q}^F, \mathbf{p}_t^{-BPF,-T_1^F}, \mathbf{p}_s\right) \tag{A.4}$$

$$\overline{MTR}_q = \frac{1}{R}\sum_{r=1}^{R} MTR\left(BPF_r, T_{1,q}^F, \mathbf{p}_t^{-BPF,-T_1^F}, \mathbf{p}_s\right) \tag{A.5}$$

and absolute values are considered for final sensitivities.

To compute sensitivities in equations A.2 and A.3, R=Q=10 different values for *BPF* and $T_1{}^{\mathrm{F}}$, linearly spaced over physiological ranges were used, both for WM and GM, for a total of 100 different configurations for each tissue type. All the other tissue parameters were kept fixed at the following values (taken from [221]). $\mathbf{p}_{\mathrm{t}}$ values are: *BPF* from 0.12 to 0.17 (in 10 steps), $T_1{}^{\mathrm{F}}$ from 0.7 s to 1.1 s (in 10 steps), $T_2{}^{\mathrm{F}}$=23 ms, $T_2{}^{\mathrm{B}}$=13 μs, R=11.2 s^{-1} for WM, and *BPF* from 0.5 to 0.11 (in 10 steps), $T1^{\mathrm{F}}$ from 0.9 s to 1.4 s (in 10 steps), $T_2{}^{\mathrm{F}}$=41 ms, $T_2{}^{\mathrm{B}}$=12 μs, R=14.3 s^{-1} for GM. For each tissue combination, the *MTR* value was simulated over all possible combinations of $\mathbf{p}_{\mathrm{s}}$, varied as follows: Δ from 1 kHz to 15 kHz (20 steps), B_1 from 2 μT to 9 μT (in 20 steps), τ from 5 ms to 50 ms (in 15 steps), Δt from 1 ms to 50 ms (in 15 steps), and N=5, 8, 10, 12, 15, 18, 20, 25, 30, 35, 40, 50, 60. A single MT pulse shape, the sinc-Gaussian shape with no lobes, was considered.

MTR sensitivities were investigated over the range of variabilities for $\mathbf{p}_{\mathrm{s}}$.

As shown in figure A.1, $\frac{\partial MTR}{\partial T_1^F}$ shows a similar pattern to *MTR* as a function of Δ and B_1. On the other hand, higher $\frac{\partial MTR}{\partial BPF}$ are shifted towards higher Δ, requiring higher B_1 to maintain the same sensitivity. The dependence of $\frac{\partial MTR}{\partial T_1^F}$ and $\frac{\partial MTR}{\partial BPF}$ on Δ and B_1 show a repetitive pattern when varying other sequence parameters (N, Δt, τ), which influence the absolute

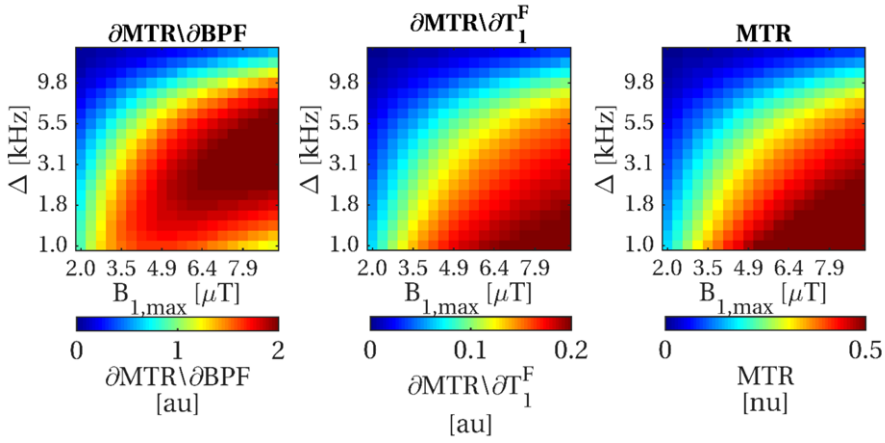

Figure A.1: Example of *MTR* sensitivity maps and simulated *MTR* as a function of pulse peak amplitude B_1 and offset frequency Δ for fixed τ=27 ms, Δt=33 ms and N=15, averaged over multiple tissue parameter combinations.

sensitivities values but not their trends (data not shown).

Visual inspection allowed the detection of different trends of $\frac{\partial MTR}{\partial BPF}$ and $\frac{\partial MTR}{\partial R_1^F}$ as a function of $\mathbf{p}_s$, with particular interest in those combinations that simultaneously led to increased $\frac{\partial MTR}{\partial BPF}$ and reduced $\frac{\partial MTR}{\partial R_1^F}$.

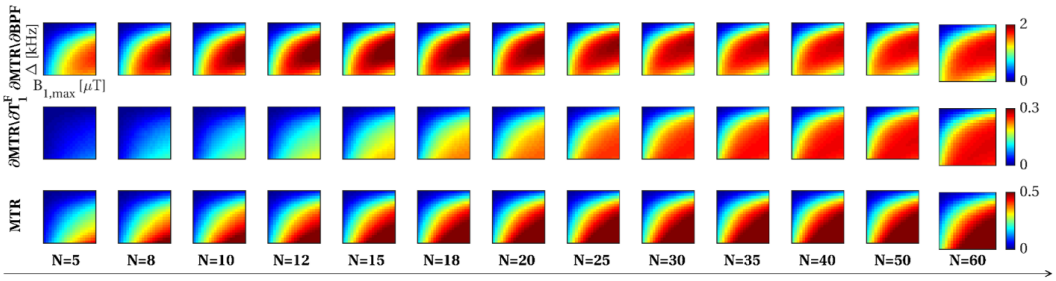

Figure A.2: *MTR* sensitivity trends as a function of number of pulses N in the saturation train, and simulated *MTR* value. A fixed combination of $\tau/\Delta t$=27 ms/33 ms is chosen. Sensitivities and *MTR* values are averaged over multiple tissue parameter combinations.

Figure A.2 shows the effect of varying N on the trends shown in figure A.1. $\frac{\partial MTR}{\partial T_1^F}$ increases with N, following the trend also observed for *MTR*. $\frac{\partial MTR}{\partial BPF}$ instead does not increase monotonically with N, but seems to reach a maximum value, then a plateau, before decreasing. Investigating the temporal evolution of the *MTR* is therefore essential to separate sensitivity trends.

For practical in vivo application, the effect of such sensitivities must be compared with random variation due to noise in the *MTR* maps. A theoretical prediction of the *SNR* in the

resulting *MTR* maps can be calculated using the error propagation law (similarly to [221]):

$$SNR_{MTR} = SNR_0 \frac{MTR}{\sqrt{(1-MTR)^2+1}} \tag{A.6}$$

where SNR_0 is the *SNR* in the M_0 image (i.e. the MT_{off} image). Similarly, also the *MTR* contrast-to-noise ratio (*CNR*) was simulated as a function of $\mathbf{p}_s$, using WM and GM $\mathbf{p}_t$ combinations. *CNR* can be obtained by applying the error propagation law (similarly to [221]):

$$\begin{aligned} CNR_{MTR} &= \frac{MTR_{WM} - MTR_{GM}}{\sqrt{\sigma^2_{MTR_{WM}} + \sigma^2_{MTR_{GM}}}} \\ &= \frac{S_{GM} - S_{WM}}{\sqrt{\frac{S^2_{WM}+1}{SNR^2_{WM}} + \frac{S^2_{GM}+1}{SNR^2_{GM}}}} \end{aligned} \tag{A.7}$$

where $S_{WM} = 1 - MTR_{WM}$ and $S_{GM} = 1 - MTR_{GM}$, and $\sigma_{MTR_{WM}}$ and $\sigma_{MTR_{GM}}$ are obtained via the propagation error law, such that $\sigma_{MTR} = \frac{\sigma_0}{M_0}\sqrt{S^2+1}$. As shown in the equation A.7, *CNR* in the *MTR* is dependent on the base *SNR* in the MT_{off} image in WM and GM, and the difference between MT-weighted signals (proportional to the sensitivity of the *MTR* to the specific parameter characterizing the regional variability in the tissue).

As an example, figure A.3 shows sensitivities for different configurations of (τ, Δt) at varying *N*, for a fixed pair of (Δ=3.6 kHz, B_1=5.3 μT). The combined effect of different parameter sensitivities can be visualized as *CNR* trends, computed as shown by equation A.7, between WM and GM averaged simulated signals. In the computation of the simulated CNR_{MTR}, the base image SNR_0 was set to SNR_{WM}=SNR_{GM}=25, which is plausible for *MTR* protocols using ZOOM-EPI. The weighting effect played by the *MTR* on the sensitivities can be appreciated in the *CNR* trends shown in figures A.3d and A.3h. To ease comparison among saturating trains with different timing configurations, the same trends of figures A.3a, A.3b, A.3c and A.3d, are also shown as a function of the total saturating time t_{sat}, figures A.3e, A.3f, A.3g and A.3h. A better separation between *BPF* sensitivity peak and ${T_1}^F$ sensitivity plateau can be achieved when short gap trains are used.

Protocols leading to different trends of sensitivities were selected for comparison in phantom study. Bovine-Serum-Albumin (BSA) phantoms at two different concentration levels (20% and 25% by weight) were used to mimic two tissue type types with differing macro-

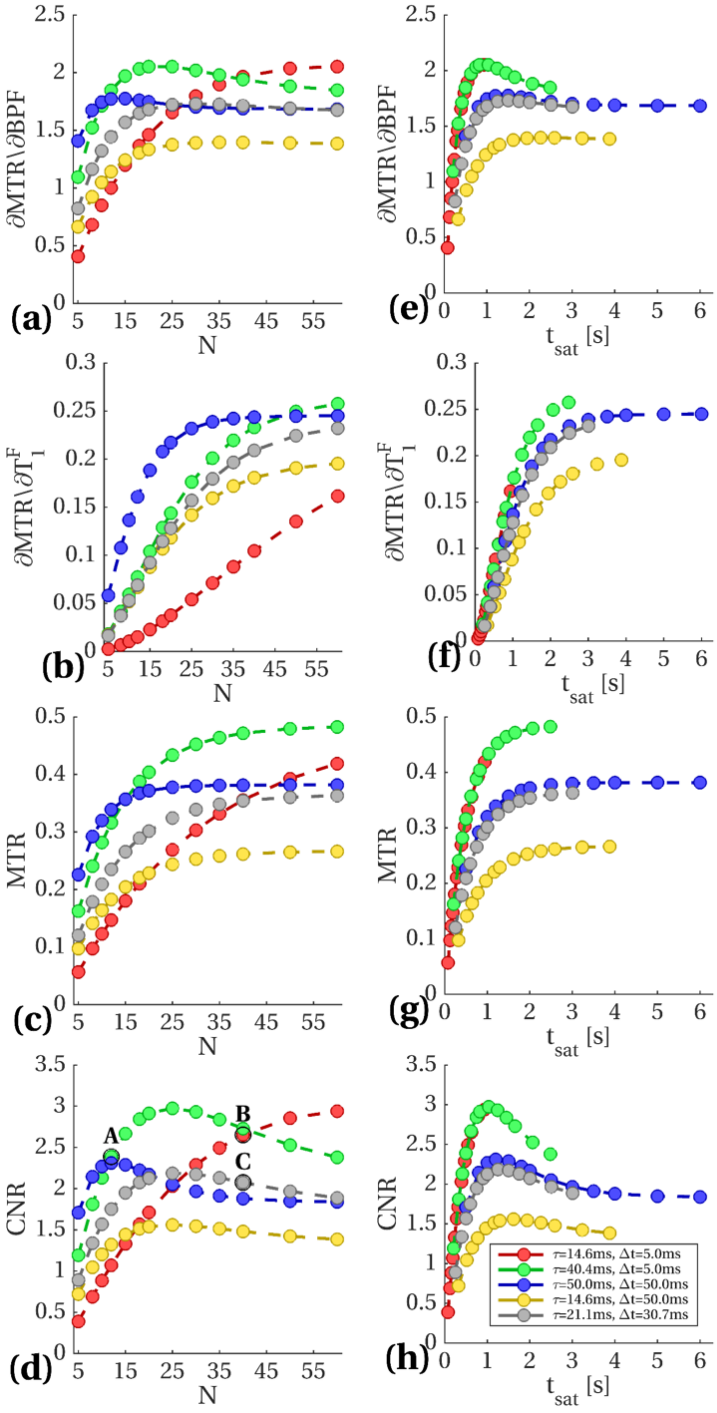

Figure A.3: Trends for sensitivity to *BPF* (**a** and **e**), sensitivity to $T_1{}^F$ (**b** and **f**), *MTR* (**c** and **g**), and *CNR* between WM and GM (**d** and **h**), for different timing configurations $\tau/\Delta t$ of the train of saturation pulses. Trends are shown both as a function of the number of pulses in the train N, and duration of the saturation train t_{sat}.

molecular content, allowing comparison between protocols of *CNR* in the resulting *MTR* maps. Figure A.4, shows CNR_{MTR} trends in BSA phantoms for the same *MTR* sequence pa-

rameters show in figure A.3d. Simulated trends of figure A.3d are qualitatively reproduced

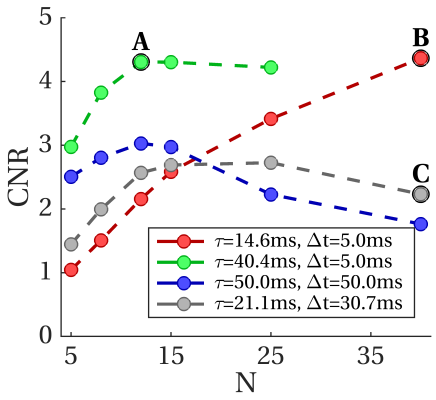

Figure A.4: CNR_{MTR} trends calculated from BSA data using the same sequence parameters considered in the simulated CNR_{MTR} trends of figure A.3d.

in the BSA phantoms experiment, confirming the validity of the simulations. Configurations labelled as A,B,C in figure A.3d in simulations are visualized in figure A.5 as *MTR* maps in a selected slice, and whole volume histograms. In the phantoms experiment *MTR CNR* can be almost doubled by optimizing parameters of the saturating train.

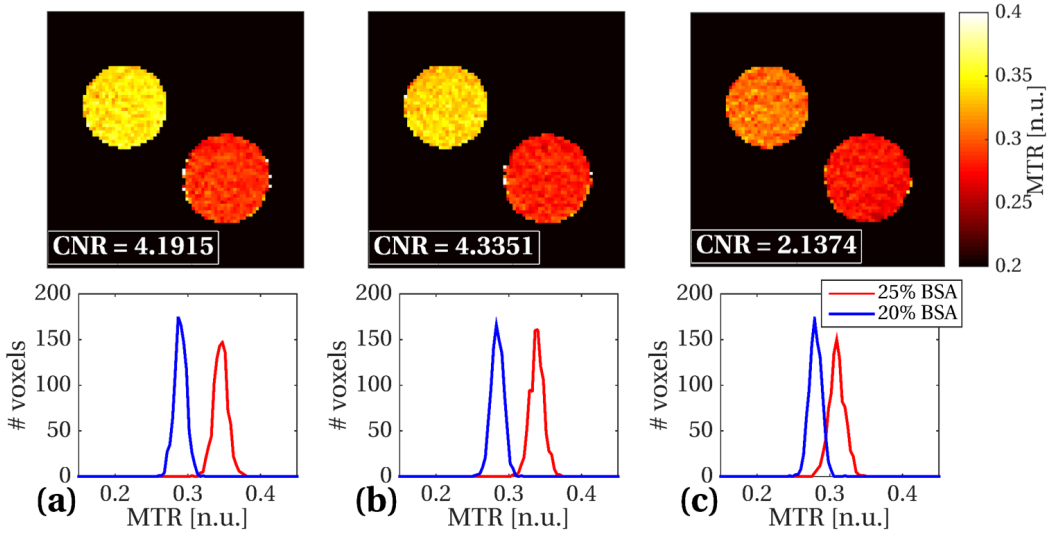

Figure A.5: Same configuration (τ, Δt, N) for a fixed pair (Δ=3.6 kHz, B_1=5.3 μT) labelled as **A**, **B**, and **C** in figure A.3d, are shown here in panels **a**, **b** and **c**. Both *MTR* map in a selected slice and whole volume *MTR* histograms are shown for the three example protocols.

To be incorporated into an MT-ZOOM-EPI sequence to be used in vivo for *MTR* protocols, also constraints on total scan time, length of saturation pulses train and feasibility of simulated combinations of $\mathbf{p}_s$ in a clinical scanner have to be taken into account at this stage.

The green and red trends shown in figure A.3, that appear to have the same effect on sen-

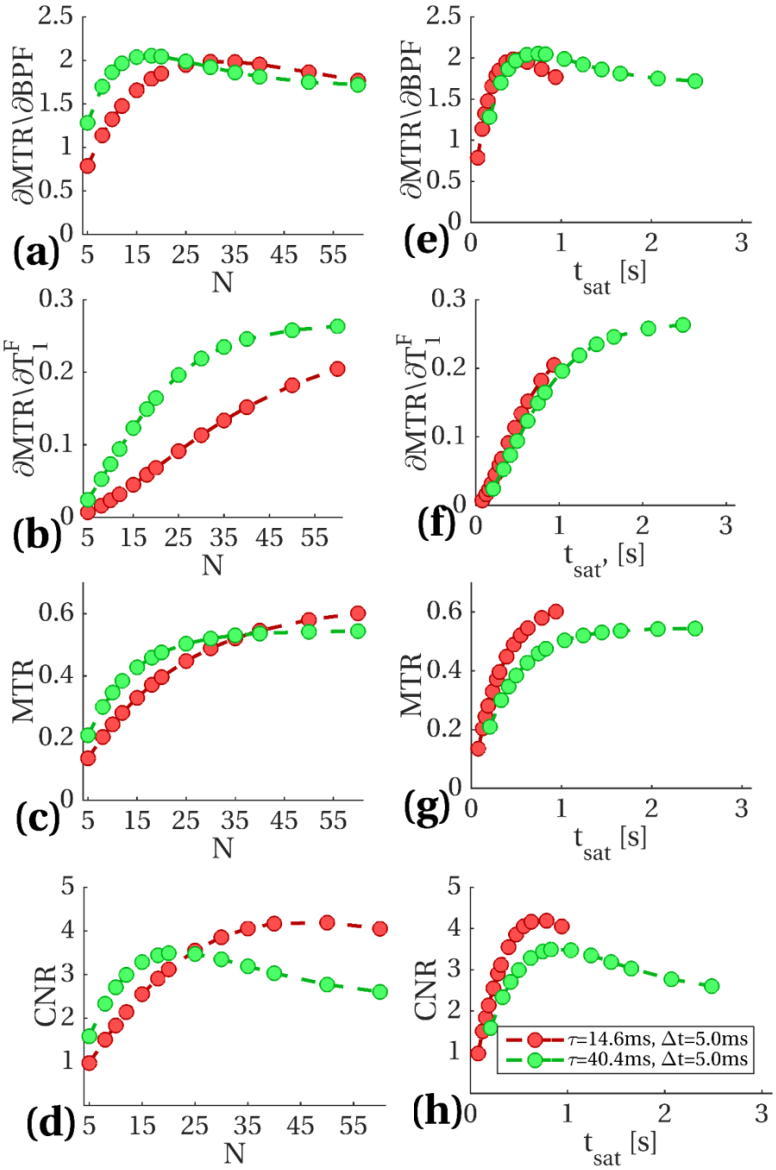

Figure A.6: The same trends as shown in figure A.3 when feasibility of combination of $\mathbf{p}_s$ for in vivo imaging is taken into account. High peak amplitude, short pulse duration, short pulse gap allow to increase $\frac{\partial MTR}{\partial BPF}$ and achieve the *CNR* peak at shorter t_{sat}, which is desirable when the *MTR* sequence is combined with cardiac gating.

sitivity and *CNR*, produce different results when constraints for in vivo imaging are taken into account. While the green trend (long pulse and short gap) produce an effective flip angle of approximatively 1800°(the maximum allowed in the scanner used in the experiment), the red trend can be further optimized by increasing B_1, as shown in figure A.6 where the maximum simulated B_1 is used (below the maximum feasible pulse amplitude, and still producing an effective flip angle lower than the upper bound). As a result, trains where

short pulse duration were used can be reproduced at higher pulse amplitude, resulting in improved $\frac{\partial MTR}{\partial BPF}$ and increased *MTR*, and hence in higher *CNR*.

The investigation into the optimization of *MTR* sensitivities to *BPF* changes showed here demonstrated that, as a general trend, short gap, high peak amplitude and short duration trains of pulses allow us to achieve high $\frac{\partial MTR}{\partial BPF}$ while $\frac{\partial MTR}{\partial T_1^F}$ is still low, and at the same time increase *MTR* value, resulting in a higher achievable *CNR* in the final *MTR* maps. For this reason, this latter configuration was used for in vivo imaging, where constraints on the duration of the train of pulses are also introduced to allow efficient cardiac gating of the sequence (see section 3.4.2.1). A summary of sequence parameters following optimization used for the in vivo *MTR* protocol is given in table 3.1.

Appendix B

Sample positioning for MRI acquisition

MRI on post mortem spinal cord samples should be performed in such a way that MRI slices can be matched to histological slices, when staining is performed at a subsequent stage on embedded samples, in order to allow accurate quantitative comparison between myelin mapping techniques from MRI and quantitative histology. It is therefore important that: (*i*) each sample can be uniquely identified in the MR images, and (*ii*) within each sample, the location of each imaging slice can be retrieved. Samples positioning and MRI acquisition should be planned accordingly for these purposes.

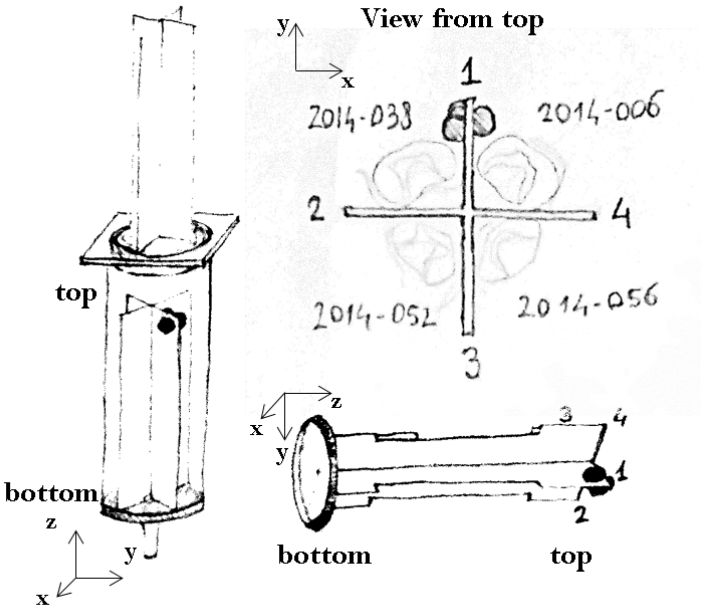

Figure B.1: Schematic representation of ex-vivo samples holder for MRI. Up to four samples can be fit in a four compartment structure. Different samples (labelled with a specific code) are positioned in each compartment defined by increasing number 1,2,3,4. MRI visible glue blobs are placed on the internal structure to ease the identification of samples in the acquired images.

To maximize the time efficiency of the protocol, more than one sample is scanned in the same exam. Moreover, samples are placed close to each other to allow further improvement of protocol time efficiency by reducing the size of the FOV. This is achieved by using the structure shown in figure B.1. Samples are placed in a four compartment plastic structure, and attached tightly to it by means of a thin thread. The structure is inserted within a cylindrical plastic tube filled with PBS, where movements are not allowed. In such a way samples can be placed close to each other, so that the size of the FOV to be used can be reduced, and hence the scan time is also minimized. Each compartment is numbered to allow the identification of the different samples placed in it, which are associated to a unique identifying code. Two MRI visible glue blobs are placed on one side of the internal plastic structure to allow each compartment, and the the relative sample, to be recognized from the acquired MRI.

Figure B.2 shows the basic operations performed in the sample positioning procedure.

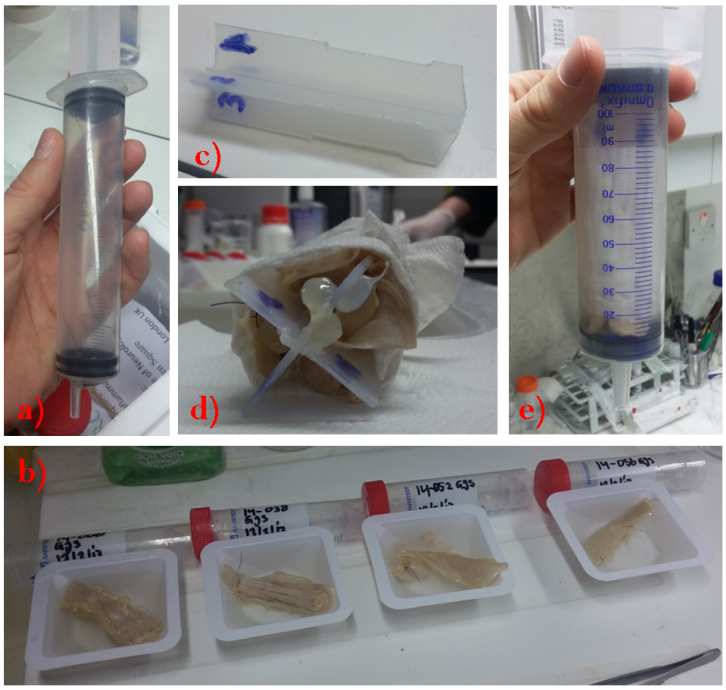

Figure B.2: Positioning of post mortem samples in the holder for MRI. (**a**) Example of the external plastic holder used to position post mortem samples; (**b**) post mortem spinal cord samples, in a PBS bath, labelled with their own identifying code prior to positioning samples in the holder; (**c**) example of the internal four compartment structure where samples are placed, with identifying numbers; (**d**) view from the top of the internal structure filled with samples, and detail of markers for identification; (**e**) example of the final holder, filled with PBS and sealed.

In order to ensure the correct matching between MRI and histological data, where slicing is

performed perpendicularly to the main sample direction, the stack of slices has to be as perpendicular as possible to all the imaged samples, and the coordinates of each slice need to be retrieved, so that their position can be mapped in the real samples before histological cutting and staining is performed. Empirically, this is ensured by acquiring a set of coronal and sagittal scans where the best angulation for all the samples is sought, as samples in the same holder share the same stack of slices planned for the quantitative MRI protocol described in table 6.2. A set of slices is then place with the same angles of the best sagittal/coronal view, and slice positions can then be readily obtained in the sagittal and coronal scans through a simple difference between slice stack centre coordinates (correcting for different image resolutions). Examples of slice position identification are given in figure B.3.

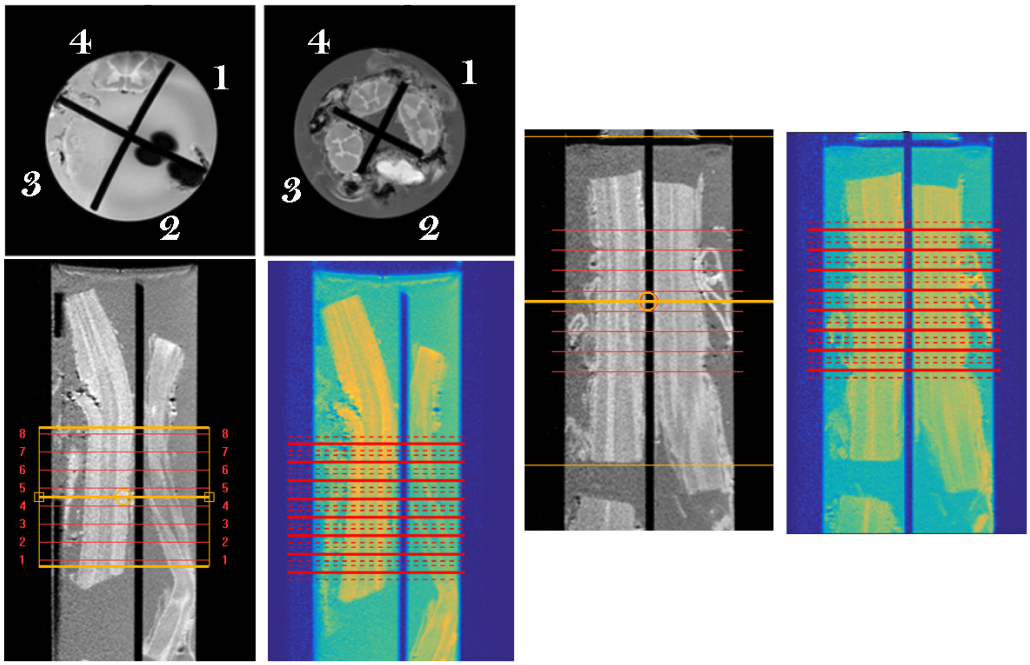

Figure B.3: Offline slice position mapping into sagittal MRI, and identification of different samples through the blob markers on the top of the holder. Following the empirical procedure described in the appendix B, slice positions of quantitative MRI protocol can be retrieved offline in the sagittal scan, as showed by the comparison with the geometry planning viewer during the MRI acquisition. The slice centres are shown with the **solid** lines, slice edges are shown with the **dashed** lines.

Bibliography

[1] Richard H Quarles, Wendy B Macklin, and Pierre Morell. Myelin formation, structure and biochemistry. Basic neurochemistry: molecular, cellular and medical aspects, 7:51–71, 2006.

[2] Bruce D Trapp and Klaus-Armin Nave. Multiple sclerosis: an immune or neurodegenerative disorder? Annu. Rev. Neurosci., 31:247–269, 2008.

[3] D Kidd, F Barkhof, R McConnell, PR Algra, IV Allen, and T Revesz. Cortical lesions in multiple sclerosis. Brain, 122(1):17–26, 1999.

[4] Hugh Kearney, David H Miller, and Olga Ciccarelli. Spinal cord MRI in multiple sclerosis —diagnostic, prognostic and clinical value. Nature Reviews Neurology, 11(6):327–338, 2015.

[5] J Sastre-Garriga, GT Ingle, M Rovaris, N Tellez, B Jasperse, DR Altmann, B Benedetti, VL Stevenson, M Cercignani, SM Leary, et al. Long-term clinical outcome of primary progressive MS: predictive value of clinical and MRI data. Neurology, 65(4):633–635, 2005.

[6] Patrick W Stroman, C Wheeler-Kingshott, M Bacon, JM Schwab, R Bosma, J Brooks, D Cadotte, T Carlstedt, Olga Ciccarelli, Julien Cohen-Adad, et al. The current state-of-the-art of spinal cord imaging: methods. Neuroimage, 84:1070–1081, 2014.

[7] CA Wheeler-Kingshott, Patrick W Stroman, JM Schwab, M Bacon, R Bosma, J Brooks, DW Cadotte, T Carlstedt, Olga Ciccarelli, Julien Cohen-Adad, et al. The current state-of-the-art of spinal cord imaging: applications. Neuroimage, 84:1082–1093, 2014.

[8] Donald W McRobbie, Elizabeth A Moore, and Martin J Graves. MRI from Picture to Proton. Cambridge university press, 2017.

[9] Robert W Brown, E Mark Haacke, Y-C Norman Cheng, Michael R Thompson, and Ramesh Venkatesan. Magnetic resonance imaging: physical principles and sequence design. John Wiley & Sons, 2014.

[10] Matt A Bernstein, Kevin F King, and Xiaohong Joe Zhou. Handbook of MRI pulse sequences. Burlington MA Elsevier Google Scholar, 2004.

[11] Richard B Buxton. Introduction to functional magnetic resonance imaging: principles and techniques. Cambridge university press, 2009.

[12] Janaka P Wansapura, Scott K Holland, R Scott Dunn, and William S Ball. NMR relaxation times in the human brain at 3.0 Tesla. Journal of magnetic resonance imaging, 9(4):531–538, 1999.

[13] William D Rooney, Glyn Johnson, Xin Li, Eric R Cohen, Seong-Gi Kim, Kamil Ugurbil, and Charles S Springer. Magnetic field and tissue dependencies of human brain longitudinal 1H2O relaxation in vivo. Magnetic Resonance in Medicine, 57(2):308–318, 2007.

[14] Nicolaas Bloembergen, Edward Mills Purcell, and Robert V Pound. Relaxation effects in nuclear magnetic resonance absorption. Physical review, 73(7):679, 1948.

[15] I Solomon. Relaxation processes in a system of two spins. Physical Review, 99(2):559, 1955.

[16] Felix Bloch. Nuclear induction. Physical review, 70(7-8):460, 1946.

[17] Henry C Torrey. Bloch equations with diffusion terms. Physical review, 104(3):563, 1956.

[18] J Hennig. K-space sampling strategies. European radiology, 9(6):1020–1031, 1999.

[19] Reuben Mezrich. A perspective on k-space. Radiology, 195(2):297–315, 1995.

[20] Jeffrey L Duerk. Principles of MR image formation and reconstruction. Magnetic resonance imaging clinics of North America, 7(4):629–659, 1999.

[21] Cynthia B Paschal and H Douglas Morris. K-space in the clinic. Journal of Magnetic Resonance Imaging, 19(2):145–159, 2004.

[22] Peter Mansfield. Multi-planar image formation using NMR spin echoes. Journal of Physics C: Solid State Physics, 10(3):L55, 1977.

[23] Michael K Stehling, Robert Turner, Peter Mansfield, et al. Echo-planar imaging: magnetic resonance imaging in a fraction of a second. Science, 254(5028):43–50, 1991.

[24] Peter Jezzard, Stuart Clare, et al. Sources of distortion in functional MRI data. Human brain mapping, 8(2-3):80–85, 1999.

[25] R Todd Constable and John C Gore. The loss of small objects in variable TE imaging: implications for FSE, RARE, and EPI. Magnetic resonance in medicine, 28(1):9–24, 1992.

[26] Klaas P Pruessmann, Markus Weiger, Markus B Scheidegger, Peter Boesiger, et al. SENSE: sensitivity encoding for fast MRI. Magnetic resonance in medicine, 42(5):952–962, 1999.

[27] Mark A Griswold, Peter M Jakob, Robin M Heidemann, Mathias Nittka, Vladimir Jellus, Jianmin Wang, Berthold Kiefer, and Axel Haase. Generalized autocalibrating partially parallel acquisitions (GRAPPA). Magnetic resonance in medicine, 47(6):1202–1210, 2002.

[28] Daniel K Sodickson and Warren J Manning. Simultaneous acquisition of spatial harmonics (SMASH): fast imaging with radiofrequency coil arrays. Magnetic Resonance in Medicine, 38(4):591–603, 1997.

[29] David A Feinberg and Kawin Setsompop. Ultra-fast MRI of the human brain with simultaneous multi-slice imaging. Journal of magnetic resonance, 229:90–100, 2013.

[30] Markus Barth, Felix Breuer, Peter J Koopmans, David G Norris, and Benedikt A Poser. Simultaneous multislice (SMS) imaging techniques. Magnetic resonance in medicine, 75(1):63–81, 2016.

[31] David J Larkman, Joseph V Hajnal, Amy H Herlihy, Glyn A Coutts, Ian R Young, and Gösta Ehnholm. Use of multicoil arrays for separation of signal from multiple slices simultaneously excited. Journal of Magnetic Resonance Imaging, 13(2):313–317, 2001.

[32] Kawin Setsompop, Borjan A Gagoski, Jonathan R Polimeni, Thomas Witzel, Van J Wedeen, and Lawrence L Wald. Blipped-controlled aliasing in parallel imaging for simultaneous multislice echo planar imaging with reduced g-factor penalty. Magnetic Resonance in Medicine, 67(5):1210–1224, 2012.

[33] Kawin Setsompop, Julien Cohen-Adad, BA Gagoski, T Raij, Anastasia Yendiki, Boris Keil, Van J Wedeen, and Lawrence L Wald. Improving diffusion MRI using simultaneous multislice echo planar imaging. Neuroimage, 63(1):569–580, 2012.

[34] Kamil Uğurbil, Junqian Xu, Edward J Auerbach, Steen Moeller, An T Vu, Julio M Duarte-Carvajalino, Christophe Lenglet, Xiaoping Wu, Sebastian Schmitter, Pierre Francois Van de Moortele, et al. Pushing spatial and temporal resolution for functional and diffusion MRI in the Human Connectome Project. Neuroimage, 80:80–104, 2013.

[35] David A Feinberg, Alexander Beckett, and Liyong Chen. Arterial spin labeling with simultaneous multi-slice echo planar imaging. Magnetic resonance in medicine, 70(6):1500–1506, 2013.

[36] Steven D Wolff and Robert S Balaban. Magnetization transfer contrast (MTC) and tissue water proton relaxation in vivo. Magnetic resonance in medicine, 10(1):135–144, 1989.

[37] Cornelia Laule, Irene M Vavasour, Shannon H Kolind, David KB Li, Tony L Traboulsee, GR Wayne Moore, and Alex L MacKay. Magnetic resonance imaging of myelin. Neurotherapeutics, 4(3):460–484, 2007.

[38] Vincent Dousset, Robert I Grossman, Karen N Ramer, Mitchell D Schnall, Lindon H Young, Francisco Gonzalez-Scarano, Ehud Lavi, and Jeffrey A Cohen. Experimental allergic encephalomyelitis and multiple sclerosis: lesion characterization with magnetization transfer imaging. Radiology, 182(2):483–491, 1992.

[39] Klaus Schmierer, Francesco Scaravilli, Daniel R Altmann, Gareth J Barker, and David H Miller. Magnetization transfer ratio and myelin in postmortem multiple sclerosis brain. Annals of neurology, 56(3):407–415, 2004.

[40] R Mark Henkelman, Xuemei Huang, Qing-San Xiang, GJ Stanisz, Scott D Swanson, and Michael J Bronskill. Quantitative interpretation of magnetization transfer. Magnetic resonance in medicine, 29(6):759–766, 1993.

[41] Clare Morrison and R Mark Henkelman. A model for magnetization transfer in tissues. Magnetic resonance in medicine, 33(4):475–482, 1995.

[42] André Pampel, Dirk K Müller, Alfred Anwander, Henrik Marschner, and Harald E Möller. Orientation dependence of magnetization transfer parameters in human white matter. NeuroImage, 114:136–146, 2015.

[43] R Mark Henkelman, Xuemei Huang, Qing-San Xiang, GJ Stanisz, Scott D Swanson, and Michael J Bronskill. Quantitative interpretation of magnetization transfer. Magnetic resonance in medicine, 29(6):759–766, 1993.

[44] John G Sled, I Levesque, AC Santos, SJ Francis, S Narayanan, Steven D Brass, DL Arnold, and GB Pike. Regional variations in normal brain shown by quantitative magnetization transfer imaging. Magnetic resonance in medicine, 51(2):299–303, 2004.

[45] A Ramani, C Dalton, DH Miller, PS Tofts, and GJ Barker. Precise estimate of fundamental in-vivo MT parameters in human brain in clinically feasible times. Magnetic resonance imaging, 20(10):721–731, 2002.

[46] John G Sled and G Bruce Pike. Quantitative interpretation of magnetization transfer in spoiled gradient echo MRI sequences. Journal of Magnetic Resonance, 145(1):24–36, 2000.

[47] Vasily L Yarnykh. Pulsed Z-spectroscopic imaging of cross-relaxation parameters in tissues for human MRI: Theory and clinical applications. Magnetic resonance in medicine, 47(5):929–939, 2002.

[48] Sharon Portnoy and Greg J Stanisz. Modeling pulsed magnetization transfer. Magnetic resonance in medicine, 58(1):144–155, 2007.

[49] Mara Cercignani and Gareth J Barker. A comparison between equations describing in vivo MT: the effects of noise and sequence parameters. Journal of Magnetic Resonance, 191(2):171–183, 2008.

[50] Daniel F Gochberg and John C Gore. Quantitative magnetization transfer imaging via selective inversion recovery with short repetition times. Magnetic resonance in medicine, 57(2):437–441, 2007.

[51] M Gloor, K Scheffler, and O Bieri. Quantitative magnetization transfer imaging using balanced SSFP. Magnetic resonance in medicine, 60(3):691–700, 2008.

[52] Dirk K Müller, André Pampel, and Harald E Möller. Matrix-algebra-based calculations of the time evolution of the binary spin-bath model for magnetization transfer. Journal of Magnetic Resonance, 230:88–97, 2013.

[53] Ewa E Odrobina, Toby YJ Lam, Teresa Pun, Rajiv Midha, and Greg J Stanisz. MR properties of excised neural tissue following experimentally induced demyelination. NMR in Biomedicine, 18(5):277–284, 2005.

[54] Klaus Schmierer, Daniel J Tozer, Francesco Scaravilli, Daniel R Altmann, Gareth J Barker, Paul S Tofts, and David H Miller. Quantitative magnetization transfer imaging in postmortem multiple sclerosis brain. Journal of magnetic resonance imaging, 26(1):41–51, 2007.

[55] Hunter R Underhill, Robert C Rostomily, Andrei M Mikheev, Chun Yuan, and Vasily L Yarnykh. Fast bound pool fraction imaging of the in vivo rat brain: association with myelin content and validation in the C6 glioma model. Neuroimage, 54(3):2052–2065, 2011.

[56] Xiawei Ou, Shu-Wei Sun, Hsiao-Fang Liang, Sheng-Kwei Song, and Daniel F Gochberg. Quantitative magnetization transfer measured pool-size ratio reflects optic nerve myelin content in ex vivo mice. Magnetic resonance in medicine, 61(2):364–371, 2009.

[57] Gunther Helms, Henning Dathe, Kai Kallenberg, and Peter Dechent. High-resolution maps of magnetization transfer with inherent correction for RF inhomogeneity and T1 relaxation obtained from 3D FLASH MRI. Magnetic resonance in medicine, 60(6):1396–1407, 2008.

[58] Nikolaus Weiskopf, John Suckling, Guy Williams, Marta M Correia, Becky Inkster, Roger Tait, Cinly Ooi, Edward T Bullmore, and Antoine Lutti. Quantitative multi-parameter mapping of R1, PD*, MT, and R2* at 3T: a multi-center validation. Frontiers in neuroscience, 7, 2013.

[59] Gunther Helms, Bogdan Draganski, Richard Frackowiak, John Ashburner, and Nikolaus Weiskopf. Improved segmentation of deep brain grey matter structures using magnetization transfer (MT) parameter maps. Neuroimage, 47(1):194–198, 2009.

[60] RS Samson, O Ciccarelli, C Kachramanoglou, L Brightman, Antoine Lutti, David L Thomas, Nikolaus Weiskopf, and CAM Wheeler-Kingshott. Tissue-and column-specific measurements from multi-parameter mapping of the human cervical spinal cord at 3T. NMR in Biomedicine, 26(12):1823–1830, 2013.

[61] AR Martin, B De Leener, J Cohen-Adad, DW Cadotte, S Kalsi-Ryan, SF Lange, L Tetreault, A Nouri, A Crawley, DJ Mikulis, et al. Clinically feasible microstructural MRI to quantify

cervical spinal cord tissue injury using DTI, MT, and T2*-weighted imaging: assessment of normative data and reliability. American Journal of Neuroradiology, 38(6):1257–1265, 2017.

[62] Gopal Varma, Guillaume Duhamel, Cedric de Bazelaire, and David C Alsop. Magnetization transfer from inhomogeneously broadened lines: a potential marker for myelin. Magnetic resonance in medicine, 73(2):614–622, 2015.

[63] Stanley J Opella and Francesca M Marassi. Structure determination of membrane proteins by NMR spectroscopy. Chemical reviews, 104(8):3587–3606, 2004.

[64] Daniel Huster, Xiaolan Yao, and Mei Hong. Membrane protein topology probed by 1H spin diffusion from lipids using solid-state NMR spectroscopy. Journal of the American Chemical Society, 124(5):874–883, 2002.

[65] Jun Hua, Craig K Jones, Jaishri Blakeley, Seth A Smith, Peter van Zijl, and Jinyuan Zhou. Quantitative description of the asymmetry in magnetization transfer effects around the water resonance in the human brain. Magnetic resonance in medicine, 58(4):786–793, 2007.

[66] G Varma, OM Girard, VH Prevost, AK Grant, G Duhamel, and DC Alsop. Interpretation of magnetization transfer from inhomogeneously broadened lines (ihMT) in tissues as a dipolar order effect within motion restricted molecules. Journal of Magnetic Resonance, 260:67–76, 2015.

[67] Olivier M Girard, Virginie Callot, Valentin H Prevost, Benjamin Robert, Manuel Taso, Guilherme Ribeiro, Gopal Varma, Novena Rangwala, David C Alsop, and Guillaume Duhamel. Magnetization transfer from inhomogeneously broadened lines (ihMT): Improved imaging strategy for spinal cord applications. Magnetic resonance in medicine, 77(2):581–591, 2017.

[68] Alan P Manning, Kimberley L Chang, Alex L MacKay, and Carl A Michal. The physical mechanism of inhomogeneous magnetization transfer MRI. Journal of Magnetic Resonance, 274:125–136, 2017.

[69] Alex Mackay, Kenneth Whittall, Julian Adler, David Li, Donald Paty, and Douglas Graeb. In vivo visualization of myelin water in brain by magnetic resonance. Magnetic Resonance in Medicine, 31(6):673–677, 1994.

[70] Saul Meiboom and David Gill. Modified spin-echo method for measuring nuclear relaxation times. Review of scientific instruments, 29(8):688–691, 1958.

[71] Kenneth P Whittall and Alexander L MacKay. Quantitative interpretation of NMR relaxation data. Journal of Magnetic Resonance, 84(1):134–152, 1989.

[72] J Hennig. Multiecho imaging sequences with low refocusing flip angles. Journal of Magnetic Resonance (1969), 78(3):397–407, 1988.

[73] Thomas Prasloski, Burkhard Mädler, Qing-San Xiang, Alex MacKay, and Craig Jones. Applications of stimulated echo correction to multicomponent T2 analysis. Magnetic resonance in medicine, 67(6):1803–1814, 2012.

[74] Thomas Prasloski, Alexander Rauscher, Alex L MacKay, Madeleine Hodgson, Irene M Vavasour, Corree Laule, and Burkhard Mädler. Rapid whole cerebrum myelin water imaging using a 3D GRASE sequence. Neuroimage, 63(1):533–539, 2012.

[75] Emil Ljungberg, Irene Vavasour, Roger Tam, Youngjin Yoo, Alexander Rauscher, David KB Li, Anthony Traboulsee, Alex MacKay, and Shannon Kolind. Rapid myelin water imaging in human cervical spinal cord. Magnetic resonance in medicine, 78(4):1482–1487, 2017.

[76] Shannon H Kolind and Sean C Deoni. Rapid three-dimensional multicomponent relaxation imaging of the cervical spinal cord. Magnetic resonance in medicine, 65(2):551–556, 2011.

[77] Aviv Mezer, Ariel Rokem, Shai Berman, Trevor Hastie, and Brian A Wandell. Evaluating quantitative proton-density-mapping methods. Human brain mapping, 37(10):3623–3635, 2016.

[78] Steffen Volz, Ulrike Nöth, Alina Jurcoane, Ulf Ziemann, Elke Hattingen, and Ralf Deichmann. Quantitative proton density mapping: correcting the receiver sensitivity bias via pseudo proton densities. Neuroimage, 63(1):540–552, 2012.

[79] Panos P Fatouros and Anthony Marmarou. Use of magnetic resonance imaging for in vivo measurements of water content in human brain: method and normal values. Journal of neurosurgery, 90(1):109–115, 1999.

[80] Neil Gelman, James R Ewing, Jay M Gorell, Eric M Spickler, and Enez G Solomon. Interregional variation of longitudinal relaxation rates in human brain at 3.0 T: relation to estimated iron and water contents. Magnetic resonance in medicine, 45(1):71–79, 2001.

[81] Tanguy Duval, Victoria Smith, Nikola Stikov, Eric C Klawiter, and Julien Cohen-Adad. Scan–rescan of axcaliber, macromolecular tissue volume, and g-ratio in the spinal cord. Magnetic resonance in medicine, 2017.

[82] Edward O Stejskal and John E Tanner. Spin diffusion measurements: spin echoes in the presence of a time-dependent field gradient. The journal of chemical physics, 42(1):288–292, 1965.

[83] Peter J Basser, James Mattiello, and Denis LeBihan. MR diffusion tensor spectroscopy and imaging. Biophysical journal, 66(1):259–267, 1994.

[84] Derek K Jones and Peter J Basser. squashing peanuts and smashing pumpkins: How noise distorts diffusion-weighted MR data. Magnetic Resonance in Medicine, 52(5):979–993, 2004.

[85] DK Jones, MA Horsfield, and A Simmons. Optimal strategies for measuring diffusion in anisotropic systems by magnetic resonance imaging. Magn Reson Med, 42(3), 1999.

[86] Derek K Jones. The effect of gradient sampling schemes on measures derived from diffusion tensor MRI: a Monte Carlo study. Magnetic Resonance in Medicine, 51(4):807–815, 2004.

[87] Peter J Basser and Carlo Pierpaoli. Microstructural and physiological features of tissues elucidated by quantitative-diffusion-tensor MRI. Journal of magnetic resonance, 213(2):560–570, 2011.

[88] Claudia AM Wheeler-Kingshott and Mara Cercignani. About axial and radial diffusivities. Magnetic resonance in medicine, 61(5):1255–1260, 2009.

[89] Eric C Klawiter, Robert E Schmidt, Kathryn Trinkaus, Hsiao-Fang Liang, Matthew D Budde, Robert T Naismith, Sheng-Kwei Song, Anne H Cross, and Tammie L Benzinger. Radial diffusivity predicts demyelination in ex vivo multiple sclerosis spinal cords. Neuroimage, 55(4):1454–1460, 2011.

[90] Sheng-Kwei Song, Jun Yoshino, Tuan Q Le, Shiow-Jiuan Lin, Shu-Wei Sun, Anne H Cross, and Regina C Armstrong. Demyelination increases radial diffusivity in corpus callosum of mouse brain. Neuroimage, 26(1):132–140, 2005.

[91] Partha P Mitra, Pabitra N Sen, Lawrence M Schwartz, and Pierre Le Doussal. Diffusion propagator as a probe of the structure of porous media. Physical review letters, 68(24):3555, 1992.

[92] Maxime Descoteaux, Rachid Deriche, Denis Le Bihan, Jean-François Mangin, and Cyril Poupon. Multiple q-shell diffusion propagator imaging. Medical image analysis, 15(4):603–621, 2011.

[93] Jens H Jensen, Joseph A Helpern, Anita Ramani, Hanzhang Lu, and Kyle Kaczynski. Diffusional kurtosis imaging: The quantification of non-gaussian water diffusion by means of magnetic resonance imaging. Magnetic resonance in medicine, 53(6):1432–1440, 2005.

[94] Erika Schneider and Gary Glover. Rapid in vivo proton shimming. Magnetic Resonance in Medicine, 18(2):335–347, 1991.

[95] Peter Jezzard and Robert S Balaban. Correction for geometric distortion in echo planar images from B0 field variations. Magnetic resonance in medicine, 34(1):65–73, 1995.

[96] Rudolf Stollberger and Paul Wach. Imaging of the active B1 field in vivo. Magnetic Resonance in Medicine, 35(2):246–251, 1996.

[97] Rolf Pohmann and Klaus Scheffler. A theoretical and experimental comparison of different techniques for B1 mapping at very high fields. NMR in Biomedicine, 26(3):265–275, 2013.

[98] Mathieu Boudreau, Christine L Tardif, Nikola Stikov, John G Sled, Wayne Lee, and G Bruce Pike. B1 mapping for bias-correction in quantitative T1 imaging of the brain at 3T using standard pulse sequences. Journal of Magnetic Resonance Imaging, 2017.

[99] Vasily L Yarnykh. Actual flip-angle imaging in the pulsed steady state: a method for rapid three-dimensional mapping of the transmitted radiofrequency field. Magnetic resonance in Medicine, 57(1):192–200, 2007.

[100] Vasily L Yarnykh. Optimal radiofrequency and gradient spoiling for improved accuracy of T1 and B1 measurements using fast steady-state techniques. Magnetic resonance in medicine, 63(6):1610–1626, 2010.

[101] Tanya Verma and Julien Cohen-Adad. Effect of respiration on the B0 field in the human spinal cord at 3T. Magnetic resonance in medicine, 72(6):1629–1636, 2014.

[102] S Johanna Vannesjo, Karla L Miller, Stuart Clare, and Irene Tracey. Spatiotemporal characterization of breathing-induced B0 field fluctuations in the cervical spinal cord at 7T. NeuroImage, 2017.

[103] David A Feinberg, JC Hoenninger, LE Crooks, L Kaufman, JC Watts, and M Arakawa. Inner volume MR imaging: technical concepts and their application. Radiology, 156(3):743–747, 1985.

[104] Patrick Le Roux, Raymond J Gilles, Graeme C McKinnon, and Pierre G Carlier. Optimized outer volume suppression for single-shot fast spin-echo cardiac imaging. Journal of Magnetic Resonance Imaging, 8(5):1022–1032, 1998.

[105] Y Luo, RA De Graaf, L DelaBarre, A Tannus, and M Garwood. BISTRO: an outer-volume suppression method that tolerates RF field inhomogeneity. Magnetic resonance in medicine, 45(6):1095–1102, 2001.

[106] Christopher J Wargo, Jay Moore, and John C Gore. A comparison and evaluation of reduced-FOV methods for multi-slice 7T human imaging. Magnetic resonance imaging, 31(8):1349–1359, 2013.

[107] BJ Wilm, Jonas Svensson, A Henning, KP Pruessmann, P Boesiger, and SS Kollias. Reduced field-of-view MRI using outer volume suppression for spinal cord diffusion imaging. Magnetic resonance in medicine, 57(3):625–630, 2007.

[108] BJ Wilm, U Gamper, A Henning, KP Pruessmann, SS Kollias, and P Boesiger. Diffusion-weighted imaging of the entire spinal cord. NMR in biomedicine, 22(2):174–181, 2009.

[109] John Pauly, Dwight Nishimura, and Albert Macovski. A k-space analysis of small-tip-angle excitation. Journal of magnetic resonance, 213(2):544–557, 2011.

[110] Emine Ulku Saritas, Charles H Cunningham, Jin Hyung Lee, Eric T Han, and Dwight G Nishimura. DWI of the spinal cord with reduced FOV single-shot EPI. Magnetic resonance in medicine, 60(2):468–473, 2008.

[111] Emine Ulku Saritas, Daeho Lee, Tolga Cukur, Ajit Shankaranarayanan, and Dwight G Nishimura. Hadamard slice encoding for reduced-FOV diffusion-weighted imaging. Magnetic resonance in Medicine, 72(5):1277–1290, 2014.

[112] MR Symms, CA Wheeler-Kingshott, GJM Parker, and GJ Barker. Zonally-magnified oblique multislice (ZOOM) EPI. In Proceedings of the 8th meeting of the International Society for Magnetic Resonance in Medicine, volume 160, 2000.

[113] Claudia AM Wheeler-Kingshott, Simon J Hickman, Geoffrey JM Parker, Olga Ciccarelli, Mark R Symms, David H Miller, and Gareth J Barker. Investigating cervical spinal cord structure using axial diffusion tensor imaging. Neuroimage, 16(1):93–102, 2002.

[114] Claudia AM Wheeler-Kingshott, Geoffrey JM Parker, Mark R Symms, Simon J Hickman, Paul S Tofts, David H Miller, and Gareth J Barker. ADC mapping of the human optic nerve: Increased resolution, coverage, and reliability with CSF-suppressed ZOOM-EPI. Magnetic resonance in medicine, 47(1):24–31, 2002.

[115] Samantha By, Robert L Barry, Alex K Smith, Bailey D Lyttle, Bailey A Box, Francesca R Bagnato, Siddharama Pawate, Seth A Smith, et al. Amide proton transfer CEST of the cervical spinal cord in multiple sclerosis patients at 3T. Magnetic Resonance in Medicine, 2017.

[116] Rebecca S Samson, Simon Lévy, Torben Schneider, Alex K Smith, Seth A Smith, Julien Cohen-Adad, and Claudia AM Gandini Wheeler-Kingshott. ZOOM or non-ZOOM? assessing spinal cord diffusion tensor imaging protocols for multi-centre studies. PloS one, 11(5):e0155557, 2016.

[117] Francesco Grussu, Torben Schneider, Hui Zhang, Daniel C Alexander, and Claudia AM Wheeler-Kingshott. Neurite orientation dispersion and density imaging of the healthy cervical spinal cord in vivo. Neuroimage, 111:590–601, 2015.

[118] Marios C Yiannakas, Francesco Grussu, Polymnia Louka, Ferran Prados, Rebecca S Samson, Marco Battiston, Daniel R Altmann, Sebastien Ourselin, David H Miller, and Claudia AM Gandini Wheeler-Kingshott. Reduced field-of-view diffusion-weighted imaging of the lumbosacral enlargement: A pilot in vivo study of the healthy spinal cord at 3T. PloS one, 11(10):e0164890, 2016.

[119] Damian J Tyler and Penny A Gowland. Rapid quantitation of magnetization transfer using pulsed off-resonance irradiation and echo planar imaging. Magnetic resonance in medicine, 53(1):103–109, 2005.

[120] Peter Gelderen, Xu Jiang, and Jeff H Duyn. Rapid measurement of brain macromolecular proton fraction with transient saturation transfer MRI. Magnetic resonance in medicine, 77(6):2174–2185, 2017.

[121] Mark A Griswold, Stephan Kannengiesser, Robin M Heidemann, Jianmin Wang, and Peter M Jakob. Field-of-view limitations in parallel imaging. Magnetic resonance in medicine, 52(5):1118–1126, 2004.

[122] P Summers, P Staempfli, T Jaermann, S Kwiecinski, and S Kollias. A preliminary study of the effects of trigger timing on diffusion tensor imaging of the human spinal cord. American Journal of Neuroradiology, 27(9):1952–1961, 2006.

[123] MC Yiannakas, H Kearney, RS Samson, Declan T Chard, Olga Ciccarelli, David H Miller, and Claudia AM Wheeler-Kingshott. Feasibility of grey matter and white matter segmentation of the upper cervical cord in vivo: a pilot study with application to magnetisation transfer measurements. Neuroimage, 63(3):1054–1059, 2012.

[124] Samantha By, Ed Mojahed, Robert L Barry, and Seth A Smith. Multiband excitation enables diffusion tensor imaging of brain stem and cervical spinal cord in clinically feasible scan times at 3T. Proceedings of the 24th meeting of the International Society for Magnetic Resonance in Medicine, 4405, 2016.

[125] Nikola Stikov, Jennifer SW Campbell, Thomas Stroh, Mariette Lavelée, Stephen Frey, Jennifer Novek, Stephen Nuara, Ming-Kai Ho, Barry J Bedell, Robert F Dougherty, et al. In vivo histology of the myelin g-ratio with magnetic resonance imaging. Neuroimage, 118:397–405, 2015.

[126] Jennifer SW Campbell, Ilana R Leppert, Sridar Narayanan, Tanguy Duval, Julien Cohen-Adad, G Bruce Pike, and Nikola Stikov. Promise and pitfalls of g-ratio estimation with MRI. arXiv preprint arXiv:1701.02760, 2017.

[127] SH Koenig, RD Brown, M Spiller, and N Lundbom. Relaxometry of brain: why white matter appears bright in MRI. Magnetic resonance in medicine, 14(3):482–495, 1990.

[128] Neil Gelman, James R Ewing, Jay M Gorell, Eric M Spickler, and Enez G Solomon. Interregional variation of longitudinal relaxation rates in human brain at 3.0 T: relation to estimated iron and water contents. Magnetic resonance in medicine, 45(1):71–79, 2001.

[129] Kevin D Harkins, Junzhong Xu, Adrienne N Dula, Ke Li, William M Valentine, Daniel F Gochberg, John C Gore, and Mark D Does. The microstructural correlates of T1 in white matter. Magnetic resonance in medicine, 75(3):1341–1345, 2016.

[130] Josef Vymazal, Andrea Righini, Rodney A Brooks, Margherita Canesi, Claudio Mariani, Marco Leonardi, and Gianni Pezzoli. T1 and T2 in the brain of healthy subjects, patients

with parkinson disease, and patients with multiple system atrophy: relation to iron content 1. Radiology, 211(2):489–495, 1999.

[131] Elizabeth Henderson, Graeme McKinnon, Ting-Yim Lee, and Brian K Rutt. A fast 3D look-locker method for volumetric T1 mapping. Magnetic resonance imaging, 17(8):1163–1171, 1999.

[132] AJ Freeman, PA Gowland, and P Mansfield. Optimization of the ultrafast look-locker echo-planar imaging T1 mapping sequence. Magnetic resonance imaging, 16(7):765–772, 1998.

[133] Evan K Fram, Robert J Herfkens, G Allan Johnson, Gary H Glover, John P Karis, Ann Shimakawa, Tom G Perkins, and Norbert J Pelc. Rapid calculation of T1 using variable flip angle gradient refocused imaging. Magnetic resonance imaging, 5(3):201–208, 1987.

[134] Sean CL Deoni, Brian K Rutt, and Terry M Peters. Rapid combined T1 and T2 mapping using gradient recalled acquisition in the steady state. Magnetic Resonance in Medicine, 49(3):515–526, 2003.

[135] Nikola Stikov, Mathieu Boudreau, Ives R Levesque, Christine L Tardif, Joëlle K Barral, and G Bruce Pike. On the accuracy of T1 mapping: searching for common ground. Magnetic resonance in medicine, 73(2):514–522, 2015.

[136] Christopher P Gilmore, Gabriele C DeLuca, Lars Bö, Trudy Owens, James Lowe, Margaret M Esiri, and Nikos Evangelou. Spinal cord neuronal pathology in multiple sclerosis. Brain Pathology, 19(4):642–649, 2009.

[137] Christopher P Gilmore, Lars Bö, Trudy Owens, James Lowe, Margaret M Esiri, and Nikos Evangelou. Spinal cord gray matter demyelination in multiple sclerosis a novel pattern of residual plaque morphology. Brain pathology, 16(3):202–208, 2006.

[138] CP Gilmore, JJG Geurts, N Evangelou, JCJ Bot, RA Van Schijndel, PJW Pouwels, F Barkhof, and L Bö. Spinal cord grey matter lesions in multiple sclerosis detected by post-mortem high field MR imaging. Multiple Sclerosis Journal, 15(2):180–188, 2009.

[139] Peter Bede, Arun LW Bokde, Susan Byrne, Marwa Elamin, Andrew J Fagan, and Orla Hardiman. Spinal cord markers in ALS: diagnostic and biomarker considerations. Amyotrophic Lateral Sclerosis, 13(5):407–415, 2012.

[140] Volker Dietz and Armin Curt. Neurological aspects of spinal cord repair: promises and challenges. The Lancet Neurology, 5(8):688–694, 2006.

[141] Dean M Wingerchuk, Vanda A Lennon, Claudia F Lucchinetti, Sean J Pittock, and Brian G Weinshenker. The spectrum of neuromyelitis optica. The Lancet Neurology, 6(9):805–815, 2007.

[142] Seth A Smith, Richard AE Edden, Jonathan AD Farrell, Peter B Barker, and Peter Van Zijl. Measurement of T1 and T2 in the cervical spinal cord at 3 Tesla. Magnetic resonance in medicine, 60(1):213–219, 2008.

[143] Lin-Ching Chang, Cheng Guan Koay, Peter J Basser, and Carlo Pierpaoli. Linear least-squares method for unbiased estimation of T1 from SPGR signals. Magnetic resonance in medicine, 60(2):496–501, 2008.

[144] Vasily L Yarnykh. Optimal radiofrequency and gradient spoiling for improved accuracy of T1 and B1 measurements using fast steady-state techniques. Magnetic resonance in medicine, 63(6):1610–1626, 2010.

[145] Yoojin Lee, Martina F Callaghan, and Zoltan Nagy. Analysis of the precision of variable flip angle T1 mapping with emphasis on the noise propagated from RF transmit field maps. Frontiers in Neuroscience, 11, 2017.

[146] RJ Ordidge, P Gibbs, B Chapman, MK Stehling, and P Mansfield. High-speed multislice T1 mapping using inversion-recovery echo-planar imaging. Magnetic resonance in medicine, 16(2):238–245, 1990.

[147] Stuart Clare and Peter Jezzard. Rapid T1 mapping using multislice echo planar imaging. Magnetic resonance in medicine, 45(4):630–634, 2001.

[148] David G Norris. Adiabatic radiofrequency pulse forms in biomedical nuclear magnetic resonance. Concepts in Magnetic Resonance Part A, 14(2):89–101, 2002.

[149] Mark Jenkinson, Peter Bannister, Michael Brady, and Stephen Smith. Improved optimization for the robust and accurate linear registration and motion correction of brain images. Neuroimage, 17(2):825–841, 2002.

[150] Mark Jenkinson and Stephen Smith. A global optimisation method for robust affine registration of brain images. Medical image analysis, 5(2):143–156, 2001.

[151] Shani Ben-Amitay, Derek K Jones, and Yaniv Assaf. Motion correction and registration of high b-value diffusion weighted images. Magnetic resonance in medicine, 67(6):1694–1702, 2012.

[152] Benjamin Leener, Gabriel Mangeat, Sara Dupont, Allan R Martin, Virginie Callot, Nikola Stikov, Michael G Fehlings, and Julien Cohen-Adad. Topologically preserving straightening of spinal cord MRI. Journal of Magnetic Resonance Imaging, 2017.

[153] Derek K Jones and Peter J Basser. squashing peanuts and smashing pumpkins: How noise distorts diffusion-weighted MR data. Magnetic Resonance in Medicine, 52(5):979–993, 2004.

[154] VS Fonov, Arnaud Le Troter, Manuel Taso, Benjamin De Leener, G Lévêque, M Benhamou, Michaël Sdika, Habib Benali, P-F Pradat, D Louis Collins, et al. Framework for integrated MRI average of the spinal cord white and gray matter: The MNI–Poly–AMU template. Neuroimage, 102:817–827, 2014.

[155] Benjamin De Leener, Simon Lévy, Sara M Dupont, Vladimir S Fonov, Nikola Stikov, D Louis Collins, Virginie Callot, and Julien Cohen-Adad. SCT: Spinal cord toolbox, an open-source software for processing spinal cord MRI data. Neuroimage, 145:24–43, 2017.

[156] Ferran Prados, M Jorge Cardoso, Marios C Yiannakas, Luke R Hoy, Elisa Tebaldi, Hugh Kearney, Martina D Liechti, David H Miller, Olga Ciccarelli, Claudia AM Gandini Wheeler-Kingshott, et al. Fully automated grey and white matter spinal cord segmentation. Scientific Reports, 6, 2016.

[157] Kenneth O McGraw and Seok P Wong. Forming inferences about some intraclass correlation coefficients. Psychological methods, 1(1):30, 1996.

[158] Patrick E Shrout and Joseph L Fleiss. Intraclass correlations: uses in assessing rater reliability. Psychological bulletin, 86(2):420, 1979.

[159] David C Zhu and Richard D Penn. Full-brain T1 mapping through inversion recovery fast spin echo imaging with time-efficient slice ordering. Magnetic resonance in medicine, 54(3):725–731, 2005.

[160] Greg J Stanisz, Ewa E Odrobina, Joseph Pun, Michael Escaravage, Simon J Graham, Michael J Bronskill, and R Mark Henkelman. T1, T2 relaxation and magnetization transfer in tissue at 3T. Magnetic resonance in medicine, 54(3):507–512, 2005.

[161] Hanzhang Lu, Lidia M Nagae-Poetscher, Xavier Golay, Doris Lin, Martin Pomper, and Peter van Zijl. Routine clinical brain MRI sequences for use at 3.0 Tesla. Journal of Magnetic Resonance Imaging, 22(1):13–22, 2005.

[162] Mitsunori Makino, Kentaro Mimatsu, Haruhiko Saito, Nobuo Konishi, and Yoshio Hashizume. Morphometric study of myelinated fibers in human cervical spinal cord white matter. Spine, 21(9):1010–1016, 1996.

[163] F Grussu, T Schneider, RL Yates, M Tachrount, J Newcombe, H Zhang, DC Alexander, GC DeLuca, and CAM Wheeler-Kingshott. Histological metrics confirm microstructural characteristics of NODDI indices in multiple sclerosis spinal cord. In Proc Intl Soc Mag Reson Med, volume 23, pages 0909–0909. International Society for Magnetic Resonance in Medicine (ISMRM) 23rd Scientific Meeting and Exhibition, 2015.

[164] T Duval, S Lévy, N Stikov, J Campbell, A Mezer, T Witzel, B Keil, V Smith, LL Wald, E Klawiter, et al. g-ratio weighted imaging of the human spinal cord in vivo. NeuroImage, 145:11–23, 2017.

[165] Alex K Smith, Richard D Dortch, Lindsey M Dethrage, and Seth A Smith. Rapid, high-resolution quantitative magnetization transfer MRI of the human spinal cord. NeuroImage, 95:106–116, 2014.

[166] Aurélien Massire, Manuel Taso, Pierre Besson, Maxime Guye, Jean-Philippe Ranjeva, and Virginie Callot. High-resolution multi-parametric quantitative magnetic resonance imaging of the human cervical spinal cord at 7T. NeuroImage, 143:58–69, 2016.

[167] Jürgen Finsterbusch, Falk Eippert, and Christian Büchel. Single, slice-specific z-shim gradient pulses improve T2*-weighted imaging of the spinal cord. Neuroimage, 59(3):2307–2315, 2012.

[168] Joëlle K Barral, Erik Gudmundson, Nikola Stikov, Maryam Etezadi-Amoli, Petre Stoica, and Dwight G Nishimura. A robust methodology for in vivo T1 mapping. Magnetic resonance in medicine, 64(4):1057–1067, 2010.

[169] Edwin D Becker, James A Ferretti, Raj K Gupta, and George H Weiss. The choice of optimal parameters for measurement of spin-lattice relaxation times. II. comparison of saturation recovery, inversion recovery, and fast inversion recovery experiments. Journal of Magnetic Resonance (1969), 37(3):381–394, 1980.

[170] Robert J Ogg and Peter B Kingsley. Optimized precision of inversion-recovery T1 measurements for constrained scan time. Magnetic resonance in medicine, 51(3):625–630, 2004.

[171] Dan Ma, Vikas Gulani, Nicole Seiberlich, Kecheng Liu, Jeffrey L Sunshine, Jeffrey L Duerk, and Mark A Griswold. Magnetic resonance fingerprinting. Nature, 495(7440):187–192, 2013.

[172] Peter Bede, Arun LW Bokde, Susan Byrne, Marwa Elamin, Andrew J Fagan, and Orla Hardiman. Spinal cord markers in ALS: diagnostic and biomarker considerations. Amyotrophic Lateral Sclerosis, 13(5):407–415, 2012.

[173] Volker Dietz and Armin Curt. Neurological aspects of spinal-cord repair: promises and challenges. The Lancet Neurology, 5(8):688–694, 2006.

[174] Dean M Wingerchuk, Vanda A Lennon, Claudia F Lucchinetti, Sean J Pittock, and Brian G Weinshenker. The spectrum of neuromyelitis optica. The Lancet Neurology, 6(9):805–815, 2007.

[175] Christopher P Gilmore, Ian Donaldson, Lars Bö, Trudy Owens, J Lowe, and Nikos Evangelou. Regional variations in the extent and pattern of grey matter demyelination in multiple

sclerosis: a comparison between the cerebral cortex, cerebellar cortex, deep grey matter nuclei and the spinal cord. Journal of Neurology, Neurosurgery & Psychiatry, 80(2):182–187, 2009.

[176] Hiroshi Tsukagoshi, Nobuo Yanagisawa, Kimio Oguchi, Kazuro Nagashima, and Toshikazu Murakami. Morphometric quantification of the cervical limb motor cells in controls and in amyotrophic lateral sclerosis. Journal of the neurological sciences, 41(3):287–297, 1979.

[177] Sven Jarius and Brigitte Wildemann. AQP4 antibodies in neuromyelitis optica: diagnostic and pathogenetic relevance. Nature Reviews Neurology, 6(7):383–392, 2010.

[178] Xiawei Ou, Shu-Wei Sun, Hsiao-Fang Liang, Sheng-Kwei Song, and Daniel F Gochberg. Quantitative magnetization transfer measured pool-size ratio reflects optic nerve myelin content in ex vivo mice. Magnetic resonance in medicine, 61(2):364–371, 2009.

[179] Mara Cercignani, Mark R Symms, Klaus Schmierer, Philip A Boulby, Daniel J Tozer, Maria Ron, Paul S Tofts, and Gareth J Barker. Three-dimensional quantitative magnetisation transfer imaging of the human brain. Neuroimage, 27(2):436–441, 2005.

[180] Vasily L Yarnykh and Chun Yuan. Cross-relaxation imaging reveals detailed anatomy of white matter fiber tracts in the human brain. Neuroimage, 23(1):409–424, 2004.

[181] D Tozer, A Ramani, GJ Barker, GR Davies, DH Miller, and PS Tofts. Quantitative magnetization transfer mapping of bound protons in multiple sclerosis. Magnetic resonance in medicine, 50(1):83–91, 2003.

[182] Giovanni Giulietti, Marco Bozzali, Viviana Figura, Barbara Spanò, Roberta Perri, Camillo Marra, Giordano Lacidogna, Franco Giubilei, Carlo Caltagirone, and Mara Cercignani. Quantitative magnetization transfer provides information complementary to grey matter atrophy in Alzheimer's disease brains. Neuroimage, 59(2):1114–1122, 2012.

[183] Seth A Smith, Xavier Golay, Ali Fatemi, Asif Mahmood, Gerald V Raymond, Hugo W Moser, Peter van Zijl, and Greg J Stanisz. Quantitative magnetization transfer characteristics of the human cervical spinal cord in vivo: application to adrenomyeloneuropathy. Magnetic resonance in medicine, 61(1):22–27, 2009.

[184] Alex K Smith, Richard D Dortch, Lindsey M Dethrage, and Seth A Smith. Rapid, high-resolution quantitative magnetization transfer MRI of the human spinal cord. NeuroImage, 95:106–116, 2014.

[185] Vasily L Yarnykh. Fast macromolecular proton fraction mapping from a single off-resonance magnetization transfer measurement. Magnetic resonance in medicine, 68(1):166–178, 2012.

[186] Richard D Dortch, Adrienne N Dula, Ke Li, Jane A Hirtle, Catherine E Frame, Pooja Gaur, John C Gore, and Seth A Smith. Quantitative magnetization transfer imaging of human cervical spinal cord at 7 Tesla. Proceedings of the 20th meeting of the International Society for Magnetic Resonance in Medicine, 614, 2012.

[187] Clare Morrison, Greg Stanisz, and R Mark Henkelman. Modeling magnetization transfer for biological-like systems using a semi-solid pool with a super-Lorentzian lineshape and dipolar reservoir. Journal of Magnetic Resonance, Series B, 108(2):103–113, 1995.

[188] Steven M Kay. Statistical signal processing. Estimation Theory, 1, 1993.

[189] Mara Cercignani and Daniel C Alexander. Optimal acquisition schemes for in vivo quantitative magnetization transfer MRI. Magnetic resonance in medicine, 56(4):803–810, 2006.

[190] Daniel C Alexander. A general framework for experiment design in diffusion MRI and its application in measuring direct tissue-microstructure features. Magnetic Resonance in Medicine, 60(2):439–448, 2008.

[191] Ke Li, Zhongliang Zu, Junzhong Xu, Vaibhav A Janve, John C Gore, Mark D Does, and Daniel F Gochberg. Optimized inversion recovery sequences for quantitative T1 and magnetization transfer imaging. Magnetic resonance in medicine, 64(2):491–500, 2010.

[192] Jingyi Xie, Daniel Gallichan, Roger N Gunn, and Peter Jezzard. Optimal design of pulsed arterial spin labeling MRI experiments. Magnetic resonance in medicine, 59(4):826–834, 2008.

[193] Ives R Levesque, John G Sled, Sridar Narayanan, Paul S Giacomini, Luciana T Ribeiro, Douglas L Arnold, and G Bruce Pike. Reproducibility of quantitative magnetization-transfer imaging parameters from repeated measurements. Magnetic resonance in medicine, 64(2):391–400, 2010.

[194] Marco Battiston, Francesco Grussu, James Fairney, Ferran Prados, Sebastien Ourselin, Mara Cercignani, Claudia AM Gandini Wheeler-Kingshott, and Rebecca S Samson. In vivo quantitative magnetisation transfer in the cervical spinal cord using reduced field-of-view imaging: A feasibility study. 24th Annual Meeting of ISMRM, 2016.

[195] Ivan Zelinka. SOMA self-organizing migrating algorithm. In New optimization techniques in engineering, pages 167–217. Springer, 2004.

[196] Daniel C Alexander. A general framework for experiment design in diffusion MRI and its application in measuring direct tissue-microstructure features. Magnetic Resonance in Medicine, 60(2):439–448, 2008.

[197] RS Samson, MR Symms, M Cercignani, DJ Tozer, and PS Tofts. Optimisation of quantitative magnetization transfer (qMT) sequence acquisition parameters. In Proceedings of the 14th Annual Meeting of ISMRM, page 2493, 2006.

[198] Ives R Levesque, John G Sled, and G Bruce Pike. Iterative optimization method for design of quantitative magnetization transfer imaging experiments. Magnetic resonance in medicine, 66(3):635–643, 2011.

[199] S Santis, Yaniv Assaf, Christopher John Evans, and Derek K Jones. Improved precision in CHARMED assessment of white matter through sampling scheme optimization and model parsimony testing. Magnetic resonance in medicine, 71(2):661–671, 2014.

[200] Mathieu Boudreau, Nikola Stikov, and G Bruce Pike. B1-sensitivity analysis of quantitative magnetization transfer imaging. Magnetic Resonance in Medicine, 2017.

[201] Neil A Harrison, Ella Cooper, Nicholas G Dowell, Georgia Keramida, Valerie Voon, Hugo D Critchley, and Mara Cercignani. Quantitative magnetization transfer imaging as a biomarker for effects of systemic inflammation on the brain. Biological psychiatry, 78(1):49–57, 2015.

[202] RD Dortch, EB Welch, JC Gore, and SA Smith. Quantitative magnetizaton transfer imaging of human cervical spinal cord at 3T. 28th Annual Meeting of ISMRM, 2010.

[203] Gabriele C DeLuca, Rose Alterman, Jenny L Martin, Arunesh Mittal, Samkeliso Blundell, Shannon Bird, Harry Beale, Lai San Hong, and Margaret M Esiri. Casting light on multiple sclerosis heterogeneity: the role of HLA-DRB1 on spinal cord pathology. Brain, 136(4):1025–1034, 2013.

[204] Francesco Grussu, Torben Schneider, and Carmen Tur. Neurite dispersion: a new marker of multiple sclerosis spinal cord pathology? Annals of Clinical and Translational Neurology, 2017.

[205] Joost CJ Bot, Frederik Barkhof, Geert Lycklama à Nijeholt, Dirkjan van Schaardenburg, Alexandre E Voskuyl, Herman J Ader, Jolanda AL Pijnenburg, Chris H Polman, Bernard MJ Uitdehaag, Erik GJ Vermeulen, et al. Differentiation of multiple sclerosis from other inflammatory disorders and cerebrovascular disease: value of spinal MR imaging. Radiology, 223(1):46–56, 2002.

[206] Frederik Barkhof. The clinico-radiological paradox in multiple sclerosis revisited. Current opinion in neurology, 15(3):239–245, 2002.

[207] Joseph CJ Bot, Erwin LA Blezer, Wouter Kamphorst, Geert J Lycklama a Nijeholt, Herman J Ader, Jonas A Castelijns, Elisabeth Bergers, Rivka Ravid, Chris Polman, and Frederik Barkhof. The spinal cord in multiple sclerosis: relationship of high-spatial-resolution quantitative MR imaging findings to histopathologic results. Radiology, 233(2):531–540, 2004.

[208] Eric C Klawiter, Robert E Schmidt, Kathryn Trinkaus, Hsiao-Fang Liang, Matthew D Budde, Robert T Naismith, Sheng-Kwei Song, Anne H Cross, and Tammie L Benzinger. Radial diffusivity predicts demyelination in ex vivo multiple sclerosis spinal cords. Neuroimage, 55(4):1454–1460, 2011.

[209] JP Mottershead, K Schmierer, M Clemence, JS Thornton, F Scaravilli, GJ Barker, PS Tofts, J Newcombe, ML Cuzner, RJ Ordidge, et al. High field MRI correlates of myelin content and axonal density in multiple sclerosis. Journal of neurology, 250(11):1293–1301, 2003.

[210] Hui Zhang, Torben Schneider, Claudia A Wheeler-Kingshott, and Daniel C Alexander. NODDI: practical in vivo neurite orientation dispersion and density imaging of the human brain. Neuroimage, 61(4):1000–1016, 2012.

[211] Cornelia Laule, Andrew Yung, Vlady Pavolva, Barry Bohnet, Piotr Kozlowski, Stanley A Hashimoto, Stephen Yip, David KB Li, and GR Wayne Moore. High-resolution myelin water imaging in post-mortem multiple sclerosis spinal cord: A case report. Multiple Sclerosis Journal, 22(11):1485–1489, 2016.

[212] C Laule, E Leung, D KB Li, AL Traboulsee, DW Paty, AL MacKay, and G RW Moore. Myelin water imaging in multiple sclerosis: quantitative correlations with histopathology. Multiple Sclerosis Journal, 12(6):747–753, 2006.

[213] Mark D Does. Multi-exponential relaxationanalysis (MERA) toolbox, version2. 2014.

[214] Evan P Minty, Thorarin A Bjarnason, Cornelia Laule, and Alex L MacKay. Myelin water measurement in the spinal cord. Magnetic resonance in medicine, 61(4):883–892, 2009.

[215] Adrienne N Dula, Daniel F Gochberg, Holly L Valentine, William M Valentine, and Mark D Does. Multiexponential T2, magnetization transfer, and quantitative histology in white matter tracts of rat spinal cord. Magnetic resonance in medicine, 63(4):902–909, 2010.

[216] Kathryn L West, Nathaniel D Kelm, Robert P Carson, Daniel F Gochberg, Kevin C Ess, and Mark D Does. Myelin volume fraction imaging with MRI. NeuroImage, 2016.

[217] DJ Tozer, GR Davies, DR Altmann, DH Miller, and PS Tofts. Correlation of apparent myelin measures obtained in multiple sclerosis patients and controls from magnetization transfer and multicompartmental T2 analysis. Magnetic resonance in medicine, 53(6):1415–1422, 2005.

[218] Klaus Schmierer, Claudia AM Wheeler-Kingshott, Daniel J Tozer, Phil A Boulby, Harold G Parkes, Tarek A Yousry, Francesco Scaravilli, Gareth J Barker, Paul S Tofts, and David H Miller. Quantitative magnetic resonance of postmortem multiple sclerosis brain before and after fixation. Magnetic resonance in medicine, 59(2):268–277, 2008.

[219] Christoph Birkl, Christian Langkammer, Nicole Golob-Schwarzl, Marlene Leoni, Johannes Haybaeck, Walter Goessler, Franz Fazekas, and Stefan Ropele. Effects of formalin fixation and temperature on MR relaxation times in the human brain. NMR in Biomedicine, 29(4):458–465, 2016.

[220] Yoram Cohen, Debbie Anaby, and Darya Morozov. Diffusion MRI of the spinal cord: from structural studies to pathology. NMR in Biomedicine, 30(3), 2017.

[221] Mara Cercignani, Mark R Symms, Maria Ron, and Gareth J Barker. 3D MTR measurement: from 1.5T to 3.0T. Neuroimage, 31(1):181–186, 2006.